X-ray Beam Modelling

In Radiotherapy :

The Effect of Lung Inhomogeneities

A thesis
submitted in fulfilment
of the requirements for the Degree
of
Doctor of Philosophy in Physics
at the
University of Waikato

by
PETER EDWIN METCALFE

University of Waikato
1990

Thank you to my darling Tracy

THESIS ERRATUM

1. Page 22 paragraph 1 replace the words
   "slightly non - Gaussian"
   with
   "non - Gaussian"

2. Page 30 paragraph 6 after the words
   "Linacs have a smaller virtual source size (approximately 3 mm) than isotope machines. This means that they produce a sharper dose fall off in the penumbra."
   include a new sentence which reads
   "The penumbra advantage of linacs over Cobalt machines is lost at high energies as the increase in electron range broadens the penumbra width."

3. Page 36 The key in Figure 2.5 should include information about the keV of each scan line ie. from top to bottom 64, 71 and 75 keV.

4. Page 64 paragraph 2 replace the words
   "The number of electrons..."
   with
   "The change in spectrum of electrons..."

5. Page 78 equation 3.12. There is an extra set of brackets missing around the second and third terms of the indices above the exponential.

6. Page 101 paragraph 2 replace the sentence
   "This method shows the closest agreement to the experimental points of any of the methods discussed."
   with
   "This method shows the closest agreement to the experimental points of any of the methods discussed except for the Batho (TPR) method which shows similar accuracy."

ABSTRACT

A lung phantom consisting of epoxy resin based analogs is developed in-house and a quality assurance method, which compares experimental CT numbers with theoretical CT numbers calculated from electronic cross sections, is described. Currently used photon beam inhomogeneity correction models and their inadequacies are discussed. The methods studied include Batho and Equivalent Tissue-Air-Ratio corrections. For a 10 MV high energy photon beam the mean difference in central axis depth dose in the lung phantom for these methods is 8.8% and 3.5%, respectively (for a 5 x 5 cm field). The differences in the beam profiles at an off-axis distance of 5 cm is 12.6% for both methods (for a 10 x 10 cm field).

A unified three-dimensional superposition approach to dose calculations used in treatment planning of a polyenergetic 10 MV photon beam in radiotherapy is developed. This radiotherapy X-ray beam computation method involves an electron gamma shower (EGS) Monte Carlo generated surface polyenergetic dose spread array (PDSA), which describes the energy spread from a point interaction source. This is superposed with the relative reduction in polyenergetic total energy released per unit mass (TERMA) as the beam traverses tissue.

By comparing primary PDSAs produced at different radiological depths, the effect of beam hardening on the PDSA has been quantified. Calculations show the mean electron range due to the surface 10 MV primary PDSA is 6.67 mm and the mean electron range of the beam hardened primary PDSA is 8.24 mm. In comparison a 3 MV primary monoenergetic dose spread array (MDSA) has a much smaller mean electron range of 4.81 mm.

The effect of using a beam hardened PDSA for superposition is also studied. The mean percentage difference between depth dose curves obtained using superposition of a surface and a beam hardened PDSA is only 0.1%. The mean percentage difference from experimental data for these superposition curves is 1.2% down to 20 cm in a homogeneous phantom. The superposition process is shown to be forgiving to spectral differences in the PDSA but sensitive to spectral changes in the TERMA.

A method of scaling PDSAs to account for lung inhomogeneities is introduced which shows good agreement with experimental and Monte Carlo results in the lung phantom. The mean difference in central axis depth dose in the lung phantom for this method is 2.0% for a 5 x 5 cm field. The differences in lung for the beam profile at an off-axis distance of 5 cm is 4.3% for a 10 x 10 cm field.

PREFACE

Computer generated treatment plans are produced for each cancer patient, prior to treatment with radiotherapy X-ray beams. These plans show isodose distributions which are overlayed on patient axial cross sections to give the Radiotherapist a clear indication of dose to the tumour and surrounding structures.

In radiotherapy treatment planning it is necessary to calculate X-ray dose distributions with accuracy. Incorrect predictions lead to sub-optimum treatment which can result in radiation induced complications such as lung pneumonitus and bone marrow suppression. In this thesis methods are introduced which reduce the errors involved in the computerised radiotherapy planning process.

The interaction properties of radiotherapy X-ray beams are dealt with in chapter 1. Included in this chapter is information about lateral electron disequilibrium as this is essential to the discussion of beam models which follow. In chapter 2 the experimental methods developed to study the accuracy of beam models are outlined. This chapter includes a discussion of the in-house manufacture of epoxy resin based tissue analogs, computed tomography (CT) quantitative analysis of the analogs, and their construction into dosimetry phantoms. The work contained in this chapter has been published in part (Metcalfe *et al* 1988, Metcalfe *et al* 1990a).

Chapter 3 includes a review of currently used photon beam models and their inadequacies. The inhomogeneity correction methods studied in this chapter include effective depth, Batho and Equivalent Tissue-Air-Ratio corrections. This work has been published in part (Metcalfe and Beckham 1988, Metcalfe and Battista 1988).

In chapter 4 the author introduces a photon beam computing method which is based on superposition mathematics and accounts for charged particle transport. Included is a detailed analysis of the effect of beam spectrum and lung inhomogeneities on the accuracy of the method. The method displays excellent accuracy in both homogeneous and heterogeneous media. Work contained in this chapter has been published in part (Metcalfe *et al* 1989, Metcalfe *et al* 1990b). Associated work in this area which the candidate has had significant input into, includes Murray *et al* (1989), Hoban *et al* (1990a) and Harper *et al* (1990).

While the research described in this thesis was being carried out the following papers were prepared:

Metcalfe P.E., Beckham W.A. (1988). Radiotherapy planning accuracy in terms of C.T. numbers and inhomogeneity correction techniques. *Aust. Rad.*, **23(3)**, 371-379.

Metcalfe P.E., Beckham W.A., Long B.H., Battista J.J. (1988). The effect of patient density variation on radiotherapy dose calculations. *Aust. Phys. Eng. Sci. Med.*, **11(3)**, 107-115.

Metcalfe P.E., Battista J.J. (1988). Accuracy of inhomogeneity corrections in lung irradiated with high energy X-rays. *Aust. Phys. Eng. Sci. Med.*, **11(2)**, 67-75. This paper received the annual Kenneth Clarke award for the most significant contribution to the journal of the Australasian Physical and Engineering Sciences in Medicine.

Metcalfe P.E., Hoban P.W., Murray D.C., Round W.H. (1989). Modelling polychromatic high energy photon beams by superposition. *Aust. Phys. Eng. Sci. Med.*, **12(3)**, 138-149.

Metcalfe P.E., Hoban P.W., Harper N.R., Murray D.C., Round W.H. (1990a). The production of body analog materials for use in medical radiation physics. *Aust. Phys. Eng. Sci. Med.*, **13(3)**, 117-128.

Metcalfe P.E., Hoban P.W., Murray D.C., Round W.H. (1990b). Beam hardening of 10 MV radiotherapy X-rays: Analysis using a convolution/superposition method. *Phys. Med. Biol., in-print*, **35**.

All of the publications mentioned above have been accepted for publication. These are included in Appendix 3 of the thesis. Parts of the work contained in this thesis have also been reported by the author at the following conferences:

Metcalfe P.E., Beckham W.A., Long B.H., Battista J.J. (1987). Computation of radiotherapy dose distributions: The influence of accurate C.T. densitometry and inhomogeneity corrections. *Canadian Association of Physics Congress, Toronto. (Abstract in Physics in Canada Journal)*, **43(3)**.

Metcalfe P.E., Beckham W.A., Long B.H., Battista J.J. (1987). Quality assurance of CT densitometry for radiotherapy dose calculations. *American Association of Physicists in Medicine, Detroit. (Abstract G5 in Med. Phys.)*, **14(3)**.

Metcalfe P.E., Battista J.J. (1987). Accuracy of inhomogeneity corrections in lung irradiated with high energy X-rays. *American Association of Physicists in Medicine, Detroit. (Abstract G6 in Med. Phys.)*, **14(3)**.

Metcalfe P.E., Beckham W.A., Long B.H., Battista J.J. (1987). Improved radiotherapy dose accuracy: The influence of accurate CT densitometry and inhomogeneity corrections. *Aust. Phys. Eng. Sci. Med. Conference, Auckland. (Abstract in Proceedings).*

Metcalfe P.E., Hoban P.W., Round W.H. (1988). Improved accuracy of high energy computerised dose calculations using superposition. *Aust. Phys. Eng. Sci. Med. Conference Brisbane. (Abstract in Proceedings).*

Metcalfe P.E., Hoban P.W., Murray D.C., Round W.H. (1989). The production of body analogs and their use in radiation dosimetry. *Aust. Phys. Eng. Sci. Med. Conference, Hamilton. (Abstract in Proceedings).*

Metcalfe P.E., Hoban P.W., Murray D.C., Round W.H. (1990). Beam hardening of 10 MV radiotherapy X-rays: Analysis using a convolution/superposition method. *Aust. Phys. Eng. Sci. Med. Conference, Adelaide. (Abstract in Proceedings).* This presentation received the inaugural Varian award for the most significant presentation at the conference on the subject of radiotherapy.

ACKNOWLEDGEMENTS

The candidate is grateful to Dr. Howell Round for providing the highest quality supervision. Howell encouraged my initial enrollment, worked through many of the problems which arose during the project, and his suggestions enhanced the manuscript and subsequent publications.

The candidate is grateful to Professor Bruce Liley and Dr. Evan Bydder who have always been supportive during many years of study at the University of Waikato.

The cooperation of members of the Waikato Hospital Scientific and Information Service Department is acknowledged; ie. Mr. Martin Pracy, Mr. George Coalter, Mr. Nigel Harper and particularly Mr. Wayne Beckham.

As the project progressed it became increasingly reliant on computer programming for the development and implementation of EGS Monte Carlo simulations. I am grateful for the support in this area provided by David Murray as this was crucial to the success of the project.

The author is grateful to Peter Hoban for his outstanding assistance in providing rigorous mathematical description of the superposition models.

The TTPS project was funded by the Cancer Society of New Zealand (National, Waikato and Bay of Plenty Divisions) and the Waikato Hospital. Although the author of this thesis received no direct funding for his research from these bodies he is grateful for their support of the project, as this provided him with the expertise and equipment to enhance his own research. The TTPS project has in turn benefited from the findings reported in this thesis.

The most rewarding part of the project has been the friendship which has developed within the research group. Thank you - Peter, David, and Howell for your help.

CONTENTS

2. Experimental Methods

3. Photon Beam Models

4. Modelling Dose Distribuions From 10 MV X-rays: Analysis Using a Convolution/Superposition Method

5. Summary and Future Projects

Appendices

LIST OF TABLES

LIST OF FIGURES

Quote:

"In short, primary and scatter dose models assume that electron equilibrium exists. Consequently, the results of dose computations at interfaces, at beam boundaries, at inhomogeneity boundaries, and in regions near small structures may be in significant error due to considerable departures from electron equilibrium."

Mohan and Chui (1985a)

LIST OF SYMBOLS

A	Mass number; the number of protons and neutrons in an element.
α	Coefficients used to define the profile shape in the beam's penumbral region.
CF	Correction factor; multiplication factor which converts dose in a homogeneous medium to dose at the same point in an inhomogeneous medium.
D	Absorbed dose; energy transferred from charged particles to a medium per unit mass.
D_{max}	Maximum dose within the medium due to a field of ionizing radiation.
%D	Percentage dose; ratio of dose at a depth to dose at D_{max}, expressed as a percentage.
D_i	Dose at point in an inhomogeneous medium.
D_h	Dose at a point in a homogeneous medium.
D_{med}	Dose within a medium.
$\bar{d}'$	Radiological depth; depth scaled along a ray by the mean density.
E	Energy.
E_k	Kinetic energy.
f	Source surface distance; distance from the beams source to the surface of a medium.
ϕ	Photon fluence; the number of photons which cross a unit cross sectional area.
Ψ	Energy fluence; photon fluence multiplied by energy.
F_{KN}	Klein Nishina factor for Compton scattering.
F_{umbral}	Off-axis ratio in the umbral part of the beam profile.
$F_{penumbra}$	Off-axis ratio in the penumbral part of the beam profile.
F_n	Fraction of photons in the nth spectral component of a spectrum.
G	Energy deposition kernel describing energy spread from an interaction site.
H_p	Dose spread function; describing the spread of energy from an interatction site.
K	Kinetic energy released per unit mass.
L	Restricted linear stopping power.
M	Electrometer reading of charge collected in an ionization chamber; including correction for pressure and temperature.
μ	Linear attenuation coefficient.
$< n >$	Expected number of photons scattered into a solid angle.
N_{gas}	Cavity gas calibration factor.
N_{CT}	CT number in Hounsfield units.
ΔN_{CT}	Difference between calculated CT number and measured CT number.
p	Geometric penumbral width.

P_{wall}	Ionization chamber wall correction factor; corrects for differences between chamber wall and phantom material.
P_{repl}	Ionization chamber replacement correction factor; corrects for dose gradient and chamber air cavity effects.
P_{ion}	Ionization chamber correction for ion recombination losses.
Q	Charge produced in air by ionizing radiation.
R_γ	Experimental regression line gradient for bone analog substances.
R_σ	Ratio of the electron cross section of water to that of a substance.
r'	Effective beam radius as defined in the ETAR correction method.
r_{eff}	Effective charged particle range.
ρ	Mass density.
ρ_e	Electron density.
ρ_e^w	Relative electron density; electron density of a substance expressed as a ratio of the electron density of water.
$\bar{\rho}$	Mean density along a ray.
$\bar{\rho}'$	Weighted density along a ray.
S	Linear stopping power.
σ	Atomic cross section.
σ_e	Electron cross section.
T	Total energy released per unit mass.
X	Exposure; charge collected in air divided by the mass of air.
y_{eff}	Effective charge particle lateral range.
z_{eff}	Effective charged particle longitudinal range.
Z	Atomic number; number of protons in an atom.
Z_{eff}	Effective atomic number.
Z_{eff}^w	Effective atomic number expressed as a ratio to that of water.

CHAPTER 1

THE INTERACTION OF PHOTONS WITH TISSUE

1.1 INTRODUCTION

The processes involved in the interaction of radiotherapy photon and electron beams with matter are discussed in this chapter. In section 1.2 the properties of the electron at relativistic velocities are described, as this has an impact on the interaction processes which occur between X-ray photons and electrons. The different photon interaction processes which are dominant at radiotherapy X-ray beam energies are each discussed in section 1.3. These interactions are photoelectric absorption, Compton scattering and pair production.

Such X-ray interactions cause electrons to be set in motion. Electrons then interact with other electrons and this leads to energy being absorbed in the medium. The collisional and radiative energy loss mechanisms of electrons are described in section 1.4. In section 1.5 the concepts of photon fluence, energy release, and energy absorption per unit mass (or dose) are discussed. The location at which an X-ray interacts with matter and the location at which the resulting dose is absorbed are not the same. This is discussed and a qualitative model is presented which shows how electron ranging leads to *lateral electron disequilibrium.*

1.2 THE ELECTRON BEAM AT RELATIVISTIC VELOCITIES

The physics of the electron beam at relativistic velocities is explained here, as it has some bearing on the characteristics of the photon beam once it leaves the medical linear accelerator exit port for patient treatment. When electrons are accelerated to relativistic velocities the mass m, and energy E, at a relativistic velocity are related as postulated by Einstein's theory of relativity (1905), such that

$$E = mc^2 \qquad (1.1)$$

where c is the speed of light.

Hence the kinetic energy E_k given to an electron accelerated in a linear accelerator waveguide is

$$E_k = mc^2 - m_0c^2 \qquad (1.2)$$

where m_0 is the electron rest mass and is equal to (9.11×10^{-31} kg). By rearranging (1.2) then

$$m = m_0 + \frac{E_k}{c^2} \quad . \tag{1.3}$$

The particles mass m is related to m_0 by

$$m = \frac{m_0}{\left(1 - \frac{v^2}{c^2}\right)^{\frac{1}{2}}} \quad , \tag{1.4}$$

where v is the velocity of the particle. By rearranging (1.4) then

$$v = c\left(1 - \frac{m_0^2}{m^2}\right)^{\frac{1}{2}} \tag{1.5}$$

To acquire a feeling for the quantities involved when dealing with linear accelerators, let us apply the above equations to a typical electron energy. By applying (1.3) to a 3 MeV electron beam (remember that 1 MeV = 1.602×10^{-13} Joules), the result is that the electron acquires a mass $m = 6.9m_0$. By applying (1.5) the velocity of the electron $v = 0.989c$, which is close to the velocity of light.

1.3 PHOTON INTERACTION PROCESSES

Once electrons have been accelerated to these velocities within the linear accelerator waveguide then they strike a target, and a broad spectrum of photons is emitted due to *bremsstrahlung* production as detailed in section 1.4. The resultant photon beam is a narrow bullet-shaped lobe of photons which is reshaped by a beam flattening filter to produce the characteristic photon beam evident at the linear accelerator exit port. These photons then traverse air in a tightly defined beam and strike the patient. This is when any one of the following interactions occur.

At very low energies there is some classical scattering which is referred to as *coherent* or *Rayleigh* scattering, whereby elastic collisions occur between photons and electrons. This phenomenon is only important at photon energies which are lower than those relevant to radiotherapy beam energies discussed in this thesis, so the process is not discussed here.

For details refer to Johns and Cunningham (1983). The three photon interaction types of relevance at energies used in radiotherapy are discussed as follows.

1.3.1 Photoelectric Absorption

In this process all of the photon's energy is transmitted to a bound electron such that (Meredith and Massey 1977) :

$$h\nu = W + \frac{1}{2} m v^2 \qquad (1.6)$$

where $h\nu$ is the initial photon energy, h is Planck's constant and ν is the photon frequency, W is the electron binding energy and $(1/2)mv^2$ is the kinetic energy given to the electron. Shown in Figure 1.1 is a description of the photoelectric process using the Böhr model of the atom. The X-ray strikes an outer or inner shell electron and all of the X-ray's energy is absorbed by the electron which escapes its shell. If an inner shell electron is involved then it is replaced by an outer shell electron. This electron in turn emits some energy in the form of a photon whose energy is characteristic of the energy difference between the two shells. This radiation is known as *Characteristic Radiation*. However for tissue-type low atomic number materials this energy difference is so small (eg. for Carbon it is 0.3 keV) that it is absorbed locally in closely neighbouring atoms.

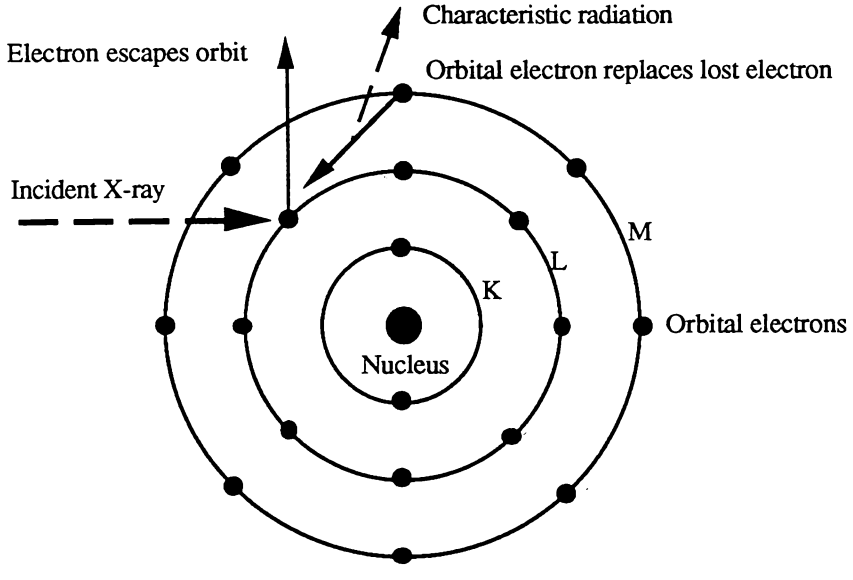

Figure 1.1: The Photoelectric absorption process shown for an inner shell electron. An incident X-ray with energy $h\nu$ interacts with a bound inner shell electron and the X-ray gives up all of its energy. The inner shell electron escapes its orbit and it may be replaced by an outer shell electron. A photon is then given off whose energy is characteristic of the energy difference between the two shells.

1.3.2 Compton Scattering

Compton scattering, which occurs at higher energies, is important at the beam energies used for radiation therapy. The interaction is shown in Figure 1.2. It involves some energy transfer from the incident photon which has an initial energy $h\nu$ to an electron which recedes from its orbit with energy E, and the photon is scattered at a new angle with energy $h\nu'$. As energy is conserved, the energy E given to the electron (assuming the electron binding energy is negligible) is equal to the electron kinetic energy, E_k, such that

$$E_k = h\nu - h\nu' \quad . \tag{1.7}$$

Since the electron may have a velocity approaching c, by using the relativistic expressions in (1.2) combined with (1.4) then (1.7) can be modified to

$$E_k = m_0 c^2 \left\{ \frac{1}{\left(1 - \frac{v^2}{c^2}\right)^{\frac{1}{2}}} - 1 \right\} \tag{1.8}$$

Now let us denote the momentum of the incident photon by **p**, and the magnitude of the momentum by p, then

$$p = mv = \frac{h\nu}{c} \quad . \tag{1.9}$$

Similarly, denote the momentum of the recoil photon by **p'** and the magnitude of the momentum by p', where

$$p' = \frac{h\nu'}{c} \quad . \tag{1.10}$$

Also let us denote the momentum of the recoil electron by **q**. As **p**, **p'** and **q** are all vectors and momentum is conserved, then for the vectors shown in Figure 1.2:

$$\mathbf{q} = \mathbf{p} - \mathbf{p'} \tag{1.11}$$

and

$$q^2 = p^2 + (p')^2 - 2\,(\mathbf{p}\cdot\mathbf{p}) \quad . \tag{1.12}$$

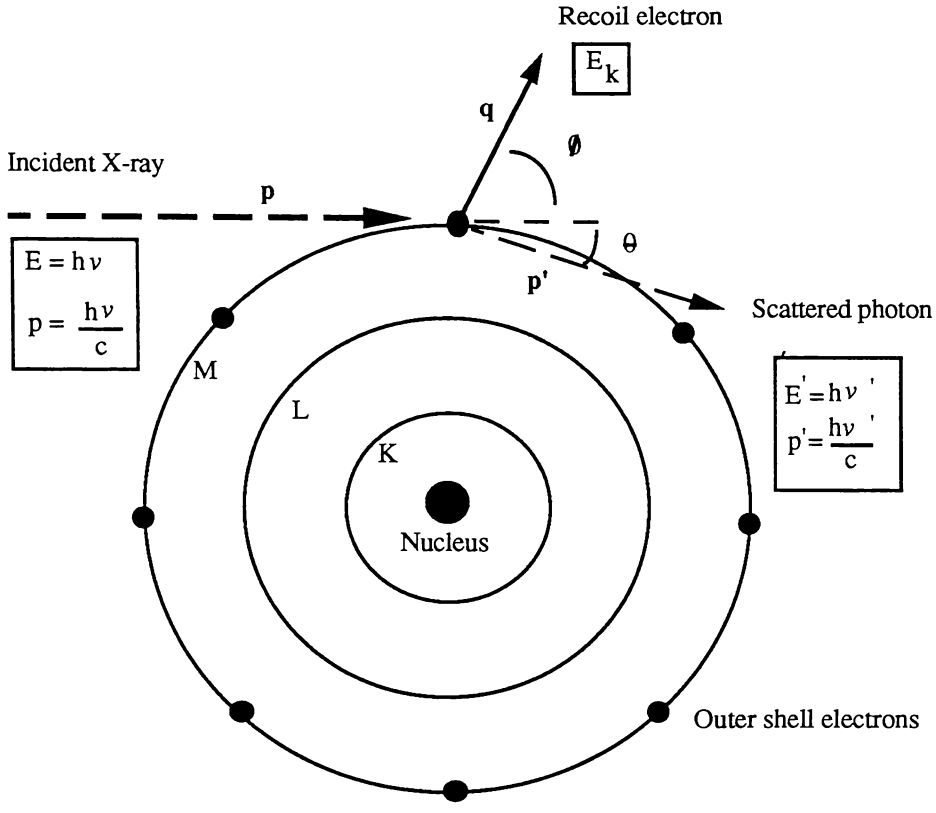

Figure 1.2: The Compton scattering process. An incident photon with energy E = hν and momentum of magnitude p = hν/c interacts with a free electron giving it an energy E_k and momentum q. The recoil electron is scattered at an angle ϕ and escapes its orbit. The incident photon gives up some energy to the recoil electron and the rest of the energy goes to the scattered photon which has energy E = hν' and momentum p' = hν'/c. The amount of energy given the electron and recoil photon depends on the angle of photon scatter θ. (Johns and Cunningham 1983) .

By vector analysis and proof, Johns and Cunningham (1983) give the following equations which show that the kinetic energy E_k given to the recoil electron, and the energy hν' given to the scattered photon are dependent on θ, the angle of recoil photon scatter:

$$E_k = h\nu \left(\frac{\alpha (1 - \cos \theta)}{1 + \alpha (1 - \cos \theta)} \right) , \qquad (1.13)$$

and as

$$h\nu ' = h\nu - E_k , \qquad (1.14)$$

then by substituting (1.13) into (1.14) and simplifying

$$h\nu' = h\nu \left(\frac{1}{1 + \alpha (1 - \cos \theta)} \right) \tag{1.15}$$

where

$$\alpha = \frac{h\nu}{m_0 c^2} \tag{1.16}$$

Note that α is the ratio of photon energy $h\nu$ to electron rest energy m_0c^2, where

$$m_0c^2 = 0.511 \text{ [MeV]} \quad . \tag{1.17}$$

In this thesis MeV is the unit used to refer to either a monenergetic beam of this energy or the mean energy of a polyenergetic beam. This unit is often shortened to MV as this is used to denote the peak energy of a polyenergetic X-ray beam (Johns and Cunningham 1983).

Figure 1.3 shows the energy given to recoil electrons and recoil photons from a 3 MeV incident photon. The energy depends on the recoil photon scatter angle. The graph was obtained by applying (1.13) and (1.15) to 3 MeV photons for different angles of θ. The resulting energy of the photon and recoil electron are plotted.

The cross-section σ represents the area that an interaction centre (electron, atom or nucleus) presents to the radiation (units cm^2 or barns $=10^{-28}$ m^2). The number of photons crossing normal to a unit area is denoted by fluence, Φ (units cm^{-2}). For an incident fluence Φ and a scattering cross section σ the expected number of photons scattered per scattering centre is given by $< n >$, where

$$< n > = \sigma\Phi \quad . \tag{1.18}$$

The probability that a photon will be scattered through an angle θ into a unit solid angle, is the *differential cross section per unit solid angle* $d\sigma/d\Omega$. This is illustrated in Figure 1.4.

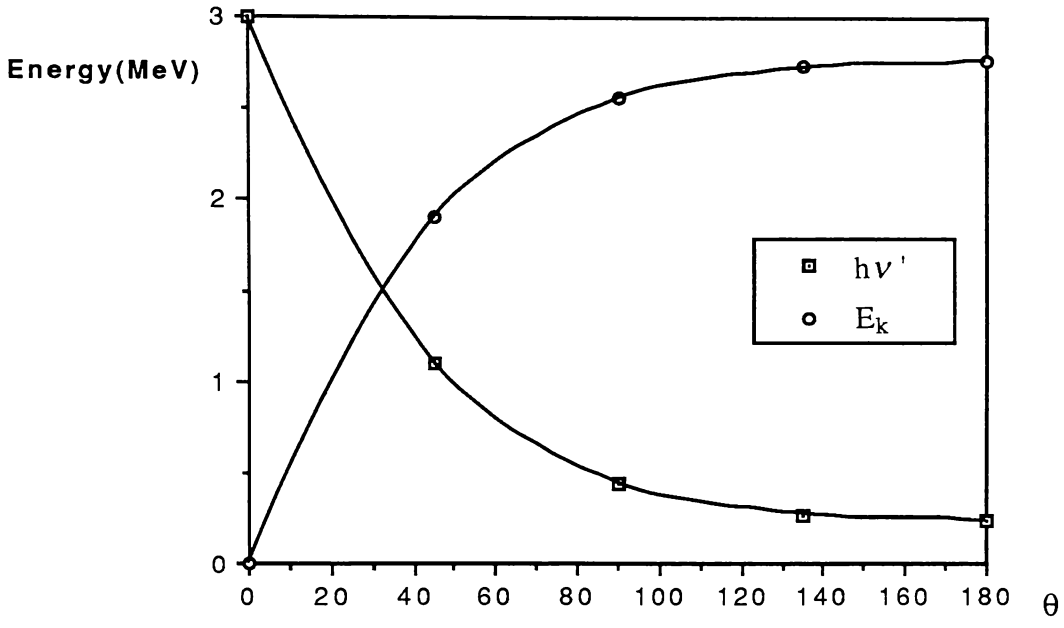

Figure 1.3: Graph showing the amount of energy given to an electron and photon from an incident 3 MeV photon. The energy depends on the angle of photon scatter θ. For example, from data shown in the graph, the interaction of an incident photon with an electron which causes the photon to scatter at $\theta = 45^0$ will produce a scattered photon of energy $h\nu' = 1.104$ MeV and a recoil electron of energy $E_k = 1.896$ MeV.

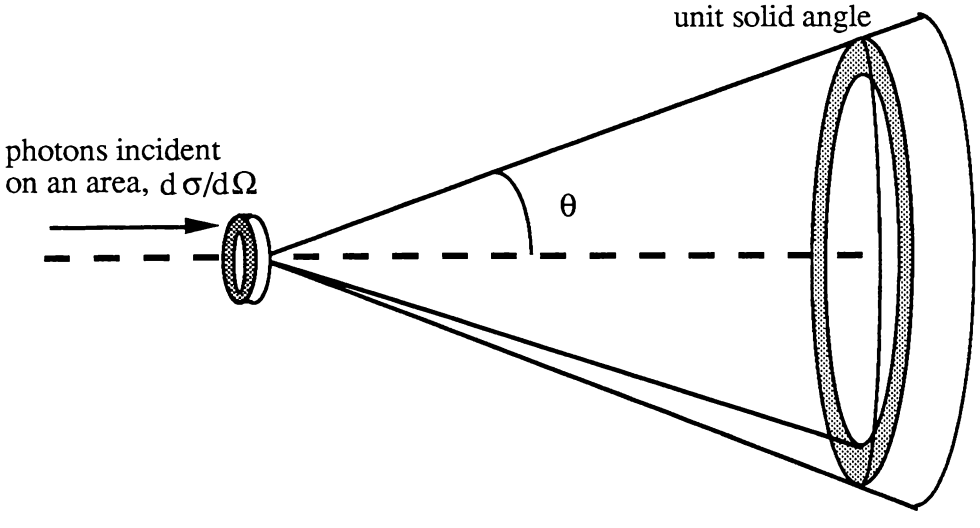

Figure 1.4: Differential cross section per unit solid angle $d\sigma/d\Omega$. A group of photons scattered by an interaction such as a Compton interaction with an electron are scattered at an angle θ.

Klein and Nishina (1929) determined by quantum mechanical analysis that this probability for Compton interactions is given by (Heitler 1960):

$$\frac{d\sigma}{d\Omega} = \left(\frac{d\sigma_0}{d\Omega}\right) F_{KN} \quad , \tag{1.19}$$

where $d\Omega$ is

$$d\Omega = 2\pi \sin\theta \, d\theta \quad . \tag{1.20}$$

The term, $d\sigma_0/d\Omega$ is the classical scattering expression (Johns and Cunningham 1983), such that

$$\frac{d\sigma_0}{d\Omega} = \frac{r_0^2}{2} (1 + \cos^2\theta) \quad , \tag{1.21}$$

where r_0 is the classical electron radius such that:

$$r_0 = \frac{k\, e^2}{m_0\, c^2} = 2.81794 \times 10^{-15} \text{ m} \tag{1.22}$$

where $k = 8.9875 \times 10^9$ m^2c^{-2}. The term F_{KN} is the Klein-Nishina factor and is given by (Klein and Nishina 1929):

$$F_{KN} = \left(\frac{1}{1 + \alpha (1 - \cos\theta)}\right)^2 \left(1 + \frac{\alpha^2 (1 - \cos\theta)^2}{(1 + \alpha (1 - \cos\theta)) (1 + \cos^2\theta)} \right) \quad . \tag{1.23}$$

The energy transfer cross section for recoil electrons σ_{tr}, is the fraction of the incident photon energy transferred to recoil electrons per scattering centre. The differential energy transfer cross section $d\sigma_{tr}/d\Omega$, is given by (Johns and Cunningham 1983):

$$\frac{d\sigma_{tr}}{d\Omega} = \frac{d\sigma_0}{d\Omega} (F_{KN}) \left(\frac{\alpha (1 - \cos\theta)}{1 + \alpha (1 - \cos\theta)}\right) \quad . \tag{1.24}$$

For the case of an incident 3 MeV photon beam, (1.19), (1.21) and (1.24) have been applied and the results are plotted in Figure 1.5 to show the classical and Compton cross sections for scattered photons and electrons.

The total cross section is represented by

$$\sigma = \int_{\theta=0}^{\theta=\pi} \left(\frac{d\sigma_0}{d\Omega} \right) (F_{KN}) (2 \pi \sin \theta) \, d\theta \quad . \tag{1.25}$$

This integral represents the equivalent of the total area under the graph for the differential cross section, $d\sigma/d\Omega$, plotted in figure 1.5. Integral solutions to this equation have been solved elsewhere (Johns and Cunningham 1983, Heitler 1960).

Note that all the previous equations assume that electrons are *free*, whereas they are in fact bound. An approximate solution to this problem can be obtained by including an incoherent scattering function S(x,z) which accounts for the electrons that do not escape due to their binding energy. Extensive tables of S(x,z) have been produced by Hubbell *et al* (1975). However, for energies above 500 keV where Compton interactions dominate this is a negligible effect (Johns and Cunningham 1983).

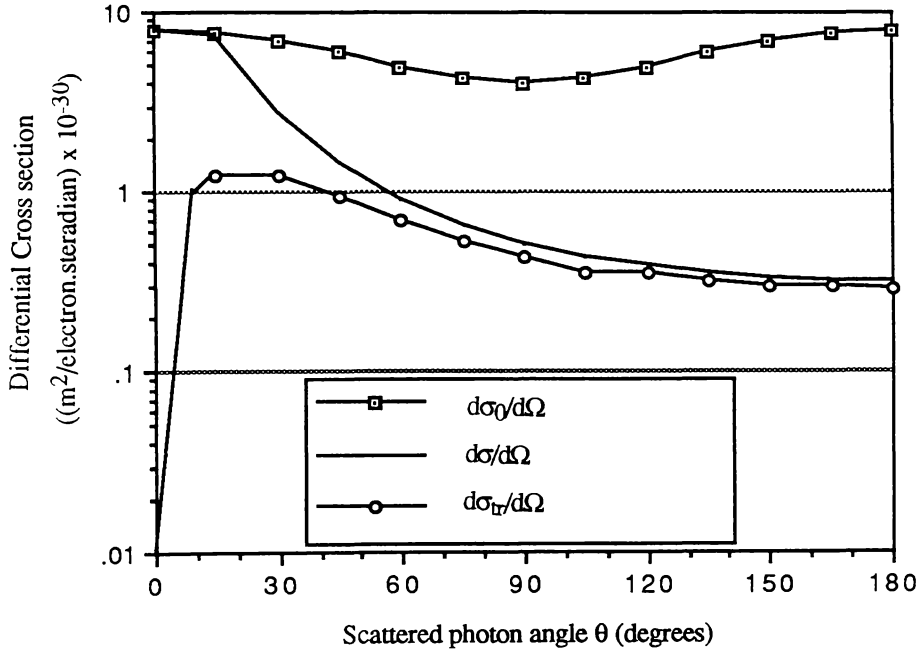

Figure 1.5: Graph showing the differential cross section $d\sigma$ per unit solid angle $d\Omega$ plotted against angle of photon scatter θ. Data shown in the graph includes the classical differential cross section per unit solid angle $d\sigma_0/d\Omega$, the Compton scattered photon differential cross section per unit solid angle $d\sigma/d\Omega$, and the Compton recoil electrons differential cross section per unit solid angle $d\sigma_{tr}/d\Omega$.

1.3.3 Pair Production

When the energy of an incident photon is greater than 1.022 MeV the photon may be absorbed through the mechanism of pair production.

The pair production process is a striking comfirmation of Einstein's equation (1.1). The mass m of the electron is 9.11×10^{-31} kg and the speed of light is approximately 3×10^{8} ms^{-1}; thus

$$E = mc^2 = (9.11 \times 10^{-31}\text{kg})\,(3 \times 10^{8}\ \text{ms}^{-1})\ [\text{Joules}] \quad , \tag{1.26}$$

and by converting from Joules to MeV then

$$E = \frac{8.2 \times 10^{-14}\ [\text{Joules}]}{1.6 \times 10^{-13}\ [\text{Joules/MeV}]} = 0.511\ [\text{MeV}] \quad . \tag{1.27}$$

The energy equivalent of one electronic mass unit as shown in (1.27) is 0.511 MeV and as two charged particles are formed, the threshold energy required of the photon is 2 x (0.511) MeV = 1.022 MeV. The mechanism is described in Figure 1.6 which shows the incident photon colliding with the nucleus and a positron-electron pair being formed.

A threshold energy of 1.022 MeV is required by the photon for it to interact with the nucleus and convert some energy to mass in the form of a positive electron (positron) and negative electron of mass equally shared and total energy exceeding 0.511 MeV. As positrons are extremely unstable and have a positive charge then they quickly interact with another electron giving off two photons each of 0.511 MeV energy. This radiation is called *annihilation radiation* .

Also shown in Figure 1.6 is triplet production. This is a similar interaction to pair production only the interaction occurs with the field of an electron rather than in the field of the nucleus. Three particles are involved: the original electron, a created electron and a created positron. The threshold for this interaction occurring is 2.044 MeV. Triplet production is usually a small component compared to pair production and is usually included with pair production when the cross sections for this interaction are discussed.

Note that energy and charge are conserved between the photon, electron and positron but momentum is not conserved between the three particles as some momentum is given to the nucleus. Because the nucleus attains some of the collision's momentum, it is difficult to

analyse the collision in detail as the exact angular deviation of the positron and electron are unknown. The differential cross section for the production of an electron-positron pair has been shown by Heitler (1960) to be approximately equal to

$$\frac{d\kappa}{d\Omega} = \frac{Z^2}{137}\frac{r_0^2}{2\pi} m_0^2 c^4 F_{pair} , \qquad (1.28)$$

the term, F_{pair} is a complicated function of momentum, energy and angle of projection of the positron and the electron, and $d\Omega$ is the solid angle into which the photon is projected.

Shown in Figure 1.7 is the total cross section κ plotted as a function of energy for two elements; oxygen (the atomic number Z = 8) and calcium (Z = 20). Note that the pair production cross section increases with atomic number of the element. The increase is approximately proportional to Z^2.

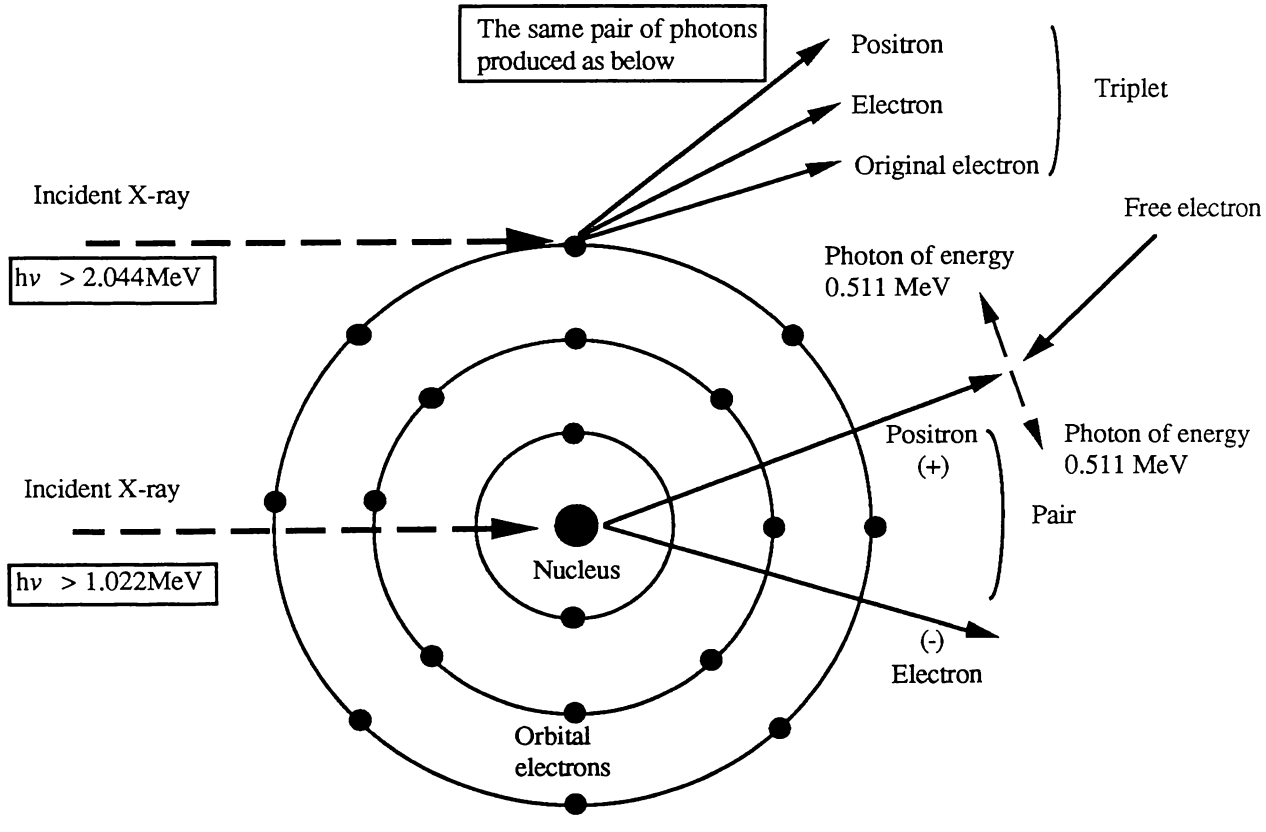

Figure 1.6: The absorption of photons by the pair and triplet production processes. The incident photons require an energy of 1.022 and 2.044 MeV respectively. In each case a positron-electron pair is produced. The positron then interacts with a free electron and the result is two 0.511 MeV photons.

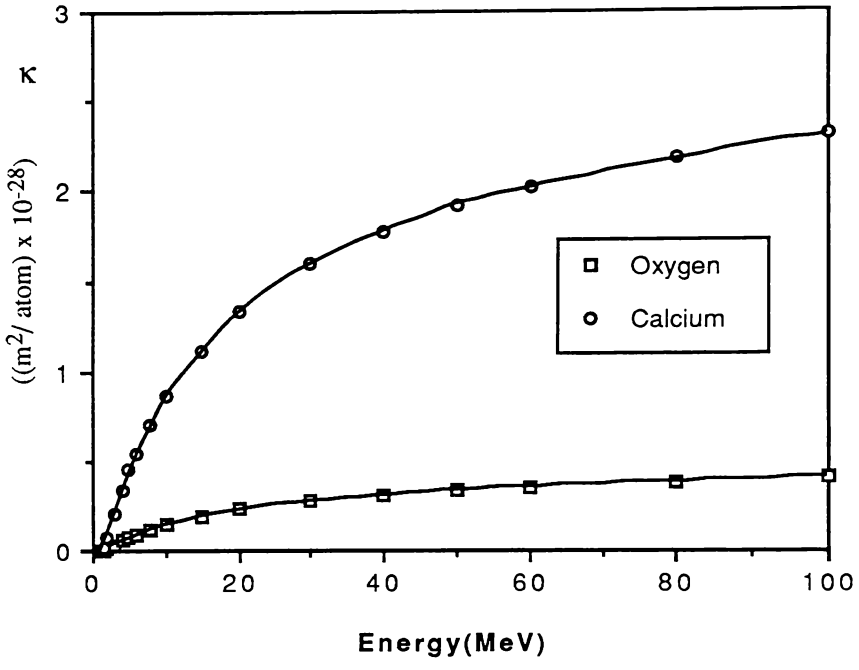

Figure 1.7: Total of pair and triplet cross sections, κ. The cross sections for the elements oxygen (which has an atomic number Z = 8) and calcium (which has an atomic number Z = 20) are plotted against energy in MeV on the horizontal axis. Note the cross section increases with energy and atomic number (Data from Johns and Cunningham 1983, Appendix A3).

1.3.4 The Relative Importance Of Each Process

The contribution of each interaction process to the total photon beam attenuation can be determined and this depends on the energy of the photon beam. In this section, the probability of photon beam removal is defined and this term's relationship to atomic cross sections is discussed.

The probability of photon removal, by either absorption or scatter, per unit path length is defined as the *linear attenuation coefficient* μ, which is usually defined in units of cm^{-1}. The equivalent mass independent quantity is the *mass attenuation coefficient* μ/ρ, which has units of cm^2g^{-1}. These quantities are derived from atomic cross sections as follows. If B is the number of interaction centres per unit volume, Φ is the fluence and defining σ as the cross section per atom, then the number of interactions N per unit path length dz is equal to (Greening 1981):

$$N = B \sigma \Phi \, dz \quad . \tag{1.29}$$

The fractional change in fluence , $d\Phi/\Phi$, is therefore

$$\frac{d\Phi}{\Phi} = -B\,\sigma\,dz \quad , \tag{1.30}$$

and as the number of interaction centres per unit volume B multiplied by the cross section per atom σ is equal to the linear attenuation coefficient μ, then by replacing $B\sigma$ with μ in (1.30),

$$\frac{d\Phi}{\Phi} = -\mu\,dz \quad . \tag{1.31}$$

Integrating both sides of (1.31) then gives

$$\ln \Phi = -\mu z + c \tag{1.32}$$

where c is a constant. Now taking exponentials of both sides of (1.32) and using the boundary condition $\Phi(0) = \Phi_0$ the fluence at depth z is given by

$$\Phi(z) = \Phi_0 e^{-\mu z} \quad . \tag{1.33}$$

The total linear attenuation coefficient is the sum of the attenuation coefficients due to coherent (coh), photoelectric (τ), Compton (σ), and pair production (κ) processes. Therefore the total linear attenuation coefficient is given by :

$$\mu = \mu_{coh} + \mu_\tau + \mu_\sigma + \mu_\kappa \quad , \tag{1.34}$$

and the mass attenuation coefficient is:

$$\frac{\mu}{\rho} = \frac{\mu_{coh}}{\rho} + \frac{\mu_\tau}{\rho} + \frac{\mu_\sigma}{\rho} + \frac{\mu_\kappa}{\rho} \quad , \tag{1.35}$$

where

$$\tau = \tau_a + \tau_s : \quad \sigma = \sigma_a + \sigma_s : \quad \kappa = \kappa_a + \kappa_s \quad . \tag{1.36}$$

The subscripts a and s denote absorption and scatter processes and are only significant for Compton interactions (Johns and Cunningham 1983).

The relationship between the linear attenuation coefficient μ and cross section σ is (Greening 1981):

$$\mu = \frac{N_A \rho \sigma}{A} \quad , \tag{1.37}$$

where, N_A, is Avogadro's number (6.022×10^{-23} mol^{-1}), ρ is the mass density (for oxygen $\rho = 1.332 \times 10^{-3}$ g.cm^{-3}), and A is the mass number (for oxygen A = 16). The conversion from σ to μ using (1.37) for oxygen is therefore

$$\mu = \frac{(6.022 \times 10^{23})(1.332 \times 10^{-3})}{16} \sigma = (5 \times 10^{19})\sigma \quad [\text{cm}^{-1}] \tag{1.38}$$

and

$$\frac{\mu}{\rho} = \frac{\mu}{1.332 \times 10^{-3}} \quad [\text{g.cm}^{-2}] \quad . \tag{1.39}$$

Figure 1.8 shows the relationship of atomic cross sections of component interactions including coherent, photoelectric, Compton and pair production versus energy for the element oxygen. Data for the graph was obtained from detailed tables of these coefficients (Johns and Cunningham 1983, Appendix A4). Note the dominance of classical scattering at very low energies then photoelectric absorption dominates at slightly higher energies.

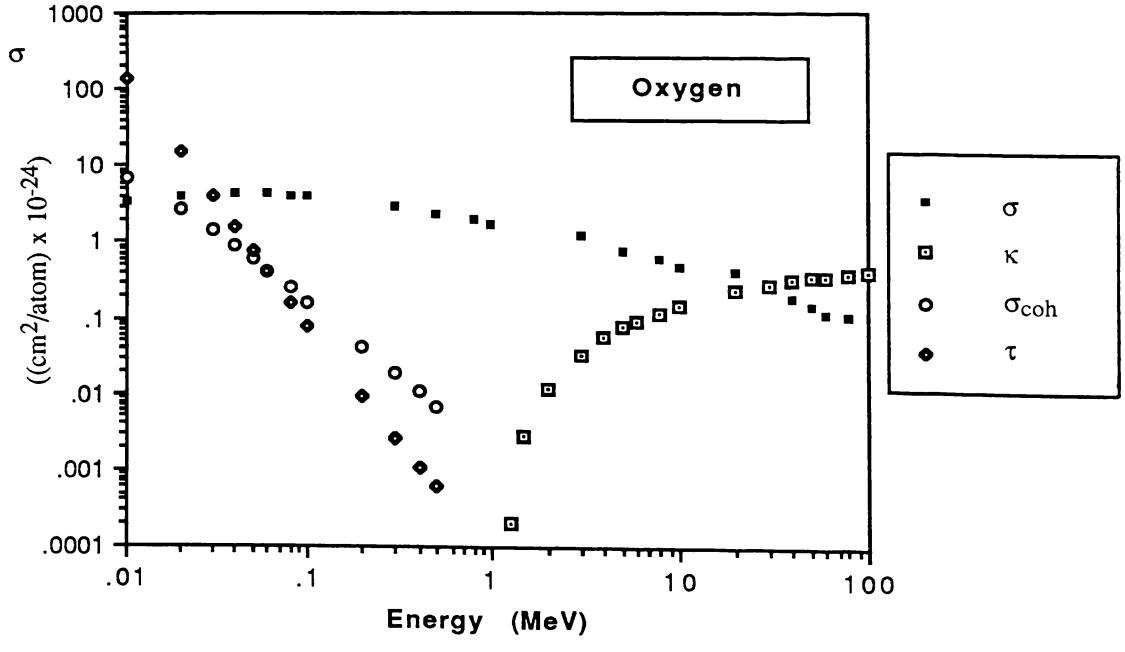

Figure 1.8: The relationship of atomic cross sections of component interactions including, photoelectric τ, Compton σ_C, and pair production κ, versus energy for the element Oxygen. The coherent scattering cross section σ_{coh} is also included for interest. Data for the graph was obtained from detailed tables of these coefficients (Johns and Cunningham 1983, Appendix A4).

This is succeeded by Compton scattering which dominates over the range of energies most commonly used in radiotherapy applications and finally pair production dominates. By applying (1.38) to the data provided in Figure 1.8 linear attenuation coefficients are produced. These are plotted against energy in Figure 1.9 for the element oxygen.

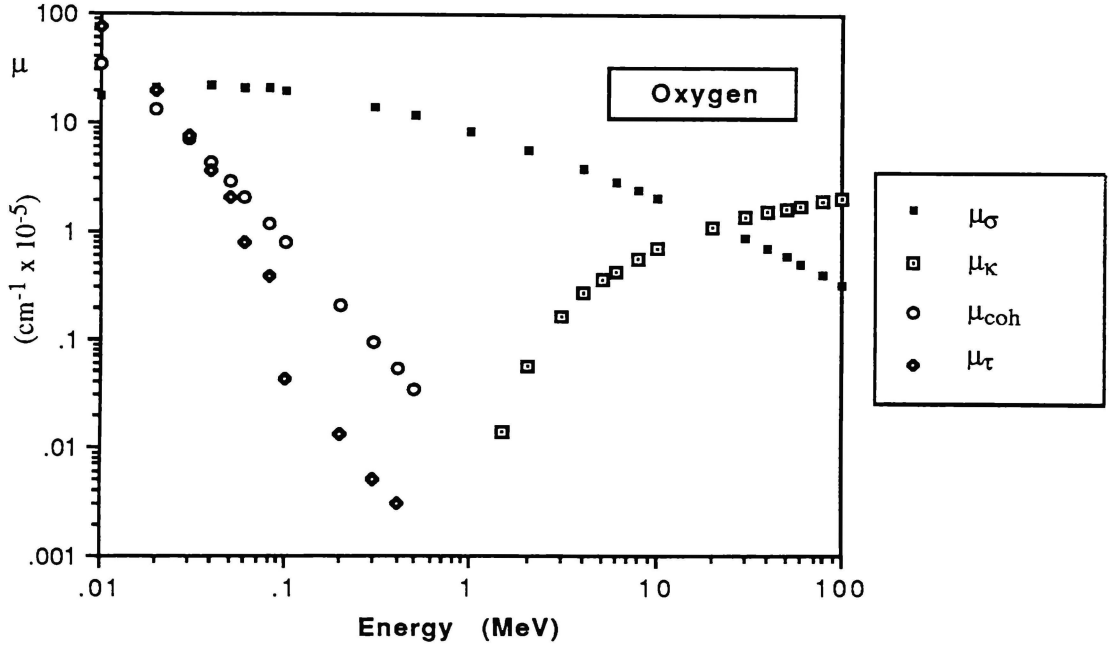

Figure 1.9: The relationship between linear attenuation coefficients of component interactions including coherent μ_{coh}, photoelectric μ_{τ}, Compton μ_{σ}, and pair production μ_{κ}. The values are plotted as a function of energy for the element oxygen.

Using (1.39) the data used in Figure 1.9 is converted to mass attenuation coefficients and these are plotted as a function of energy as shown in Figure 1.10 for the element oxygen. Also shown on this graph is total mass attenuation coefficient versus energy. This is the sum of the component coefficients at a specific energy.

Not all energy is always transferred from photons to charged particles. The average energy transferred from the photons to charged particles is $\bar{E}_{tr}$, and the mass energy transfer coefficient is defined as

$$\frac{\mu_{tr}}{\rho} = \frac{\mu}{\rho}\left(\frac{\bar{E}_{tr}}{h\nu}\right) . \qquad (1.40)$$

For high energy beams not all the energy transferred is absorbed and some is re-radiated as bremsstrahlung. The average absorbed energy $\bar{E}_{ab}$, is also referred to elsewhere as $\bar{E}_{en}$. This quantity has an associated mass energy absorption coefficient which is related to the transfer coefficient by

$$\frac{\mu_{ab}}{\rho} = \frac{\mu_{tr}}{\rho}\left(\frac{\bar{E}_{ab}}{\bar{E}_{tr}}\right) = \frac{\mu_{tr}}{\rho}(1-g) \quad , \tag{1.41}$$

where g is the fraction of charged particle energy converted to bremsstrahlung. For energies less than about 10 MeV the bremsstrahlung production is negligible (in atomic number materials that are similar to tissue). Therefore g approximately equals zero, and

$$\frac{\mu_{tr}}{\rho} = \frac{\mu}{\rho}\left(\frac{\bar{E}_{tr}}{h\nu}\right) \approx \frac{\mu_{ab}}{\rho} \quad \text{for tissue when} \quad h\nu \leq 10\,\text{MeV} \tag{1.42}$$

The mass energy transfer coefficient using (1.40) for a 3 MeV photon in tissue is :

$$\frac{\mu_{tr}}{\rho} = 0.03359\ g^{-1}cm^2\ x\left(\frac{1.74\ MeV}{3\ MeV}\right) = 0.01948\ [g^{-1}cm^2] \quad . \tag{1.43}$$

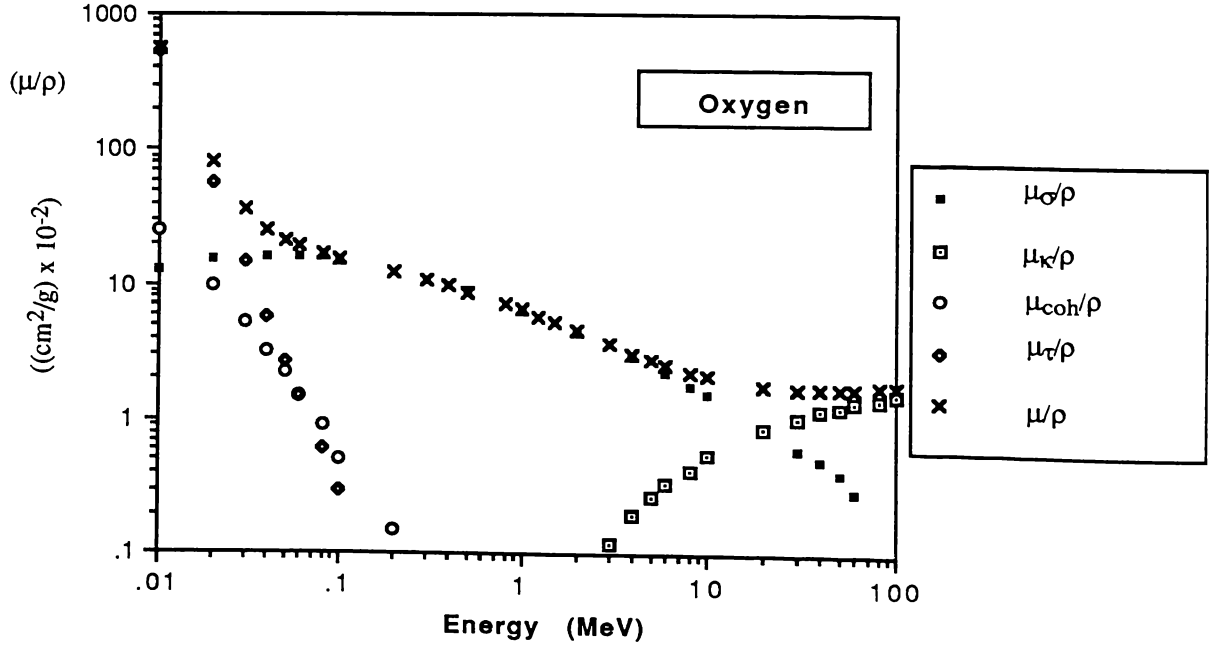

Figure 1.10: The relationship between mass attenuation coefficients of component interactions including coherent μ_{coh}/ρ, photoelectric μ_{τ}/ρ, Compton μ_{σ}/ρ, and pair production μ_{κ}/ρ, and total μ/ρ. Plotted as a function of energy for the element oxygen.

Figure 1.11 shows the relationship of the mass attenuation coefficients, mass energy absorption coefficients, and mass energy transfer coefficients versus energy for water. Data for the graph was obtained from detailed tables of these coefficients. Note the subtle difference shown on the graph between the energy transfer and energy absorption coefficients at high energy. This is due to bremsstrahlung production becoming more significant at high energies.

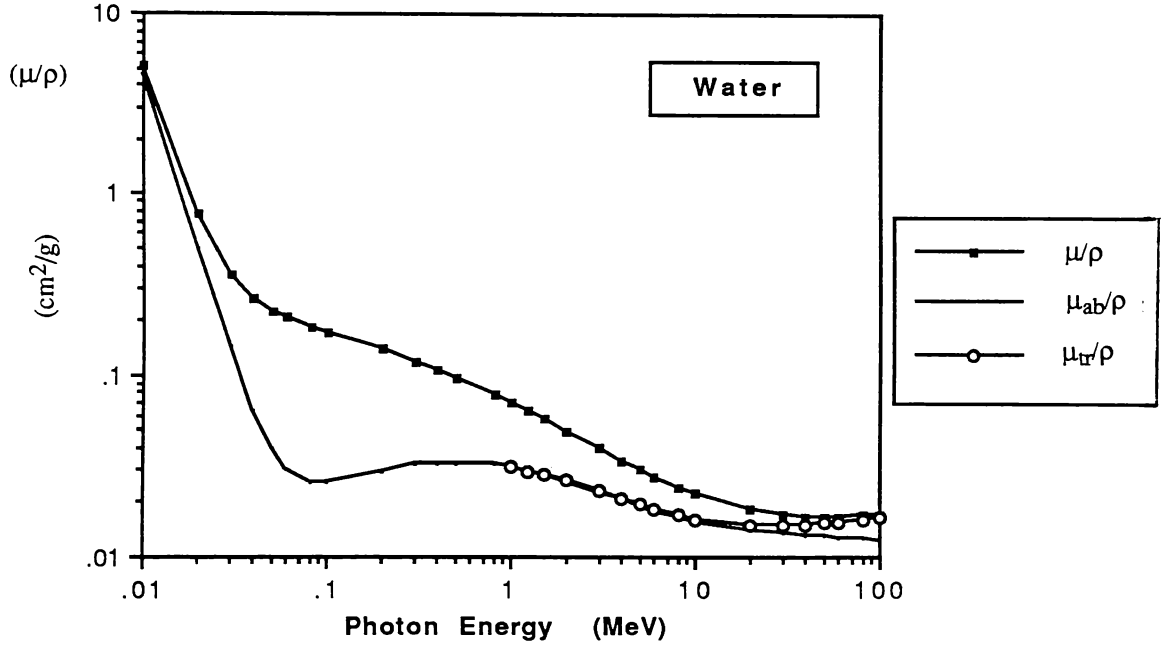

Figure 1.11: Mass attenuation coefficient μ/ρ, mass energy absorption coefficient μ_{ab}/ρ, and mass energy transfer coefficient μ_{tr}/ρ, versus energy for water. Data for the graph was obtained from detailed tables of these coefficients (Johns and Cunningham 1983, Appendix A3).

Where the percentage contribution of each process to attenuation is calculated for a monoenergetic 3 MeV photon beam as

$$\frac{\mu_\sigma}{\rho} = 0.03347 \quad , \quad \frac{\mu_\kappa}{\rho} = 0.0012 \quad , \quad \frac{\mu}{\rho} = 0.03359 \quad [g^{-1}\,cm^2] \quad . \tag{1.44}$$

This shows that the majority of attenuation at this energy is due to Compton interaction processes, that is 97%, and the remainder of the interactions, 3%, are due to pair production processes. The calculation (1.44) shows that at this energy Compton interactions are dominant and pair production only contributes a small amount to the interaction process,

hence any Compton interaction model will closely approximate the total energy transfer process at this energy.

1.4 ELECTRON INTERACTIONS

When an X-ray photon interacts with a medium, any one of the three major photon interaction processes previously outlined may occur. These interactions result in charged particles, electrons or positrons, *ranging* from the original site of photon interaction. The term *ranging* is used to describe the process whereby electrons travel from their site of photon-electron interaction and undergo multiple electron-electron and electron-nucleus interactions prior to coming to rest, having deposited energy along their track.

It is the subsequent multiple interactions of the electrons with atomic nuclei or bound atomic electrons which leads to the atomic ionization and excitation processes responsible for biological damage to the cell.

Once electrons have been set in motion by one of the previously described photon interaction processes, they range from the site of initial interaction and are themselves subject to absorption and scattering processes. Interactions occur with nuclei, the most common interaction is *Coulomb scattering*. *Radiative collisions,* those that produce Bremsstrahlung photons, can occur with nuclei or atomic electrons.

1.4.1 Collisional Energy Loss

Collisions which cause electron energy loss are of major interest as these events give rise to deposition of energy. Collisional energy loss occurs when a ranging electron interacts with an atomic electron as shown in Figure 1.12 and this results in either excitation or ionization of the atom. In general this process is closely modelled by a free electron collision. This is because the outer shell electrons are loosely bound and the most frequent interaction involves a small energy transfer to the orbital electron.

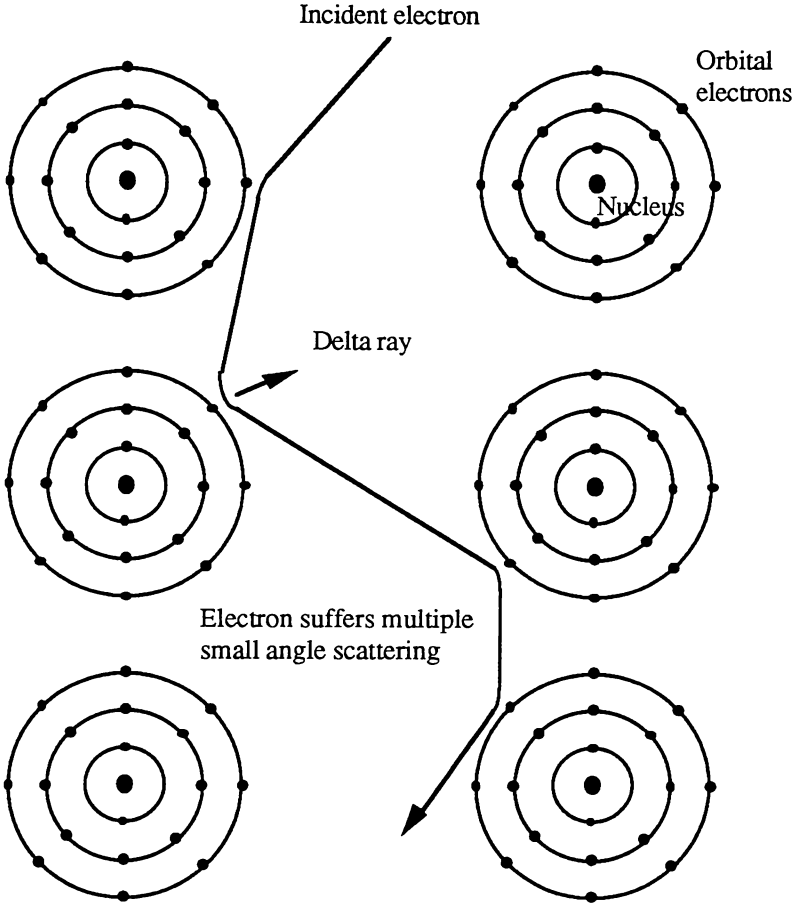

Figure 1.12: The track of an incident electron through a series of atoms. This results in either excitation or ionization of the atom. In general this process is closely modelled by a free electron collision. This is because the outer shell electrons are loosely bound and the most frequent interaction involves a small energy transfer to the orbital electron. Hence multiple small angle scattering occurs and the cross sections for ionization are large. This is the dominant scattering mechanism in tissue. In some interactions an orbital electron may be given enough energy to escape and itself interact elsewhere. Such an electron is referred to as a delta ray.

1.4.2 Radiative Energy Loss (Bremsstrahlung Production)

A collision between an electron and an atom which results in energy in the form of photon radiation is called a *radiative energy loss* and the process is shown in Figure 1.13. *Bremsstrahlung* photons are emitted when an electron interacts with the coulomb field of the nucleus. Therefore the probability of such an interaction is higher if the distance of the electron's approach to the atom is less than the atomic radius. The maximum energy of the bremsstrahlung can be no more than the peak electron energy and a spectrum of photon energies below this value is produced.

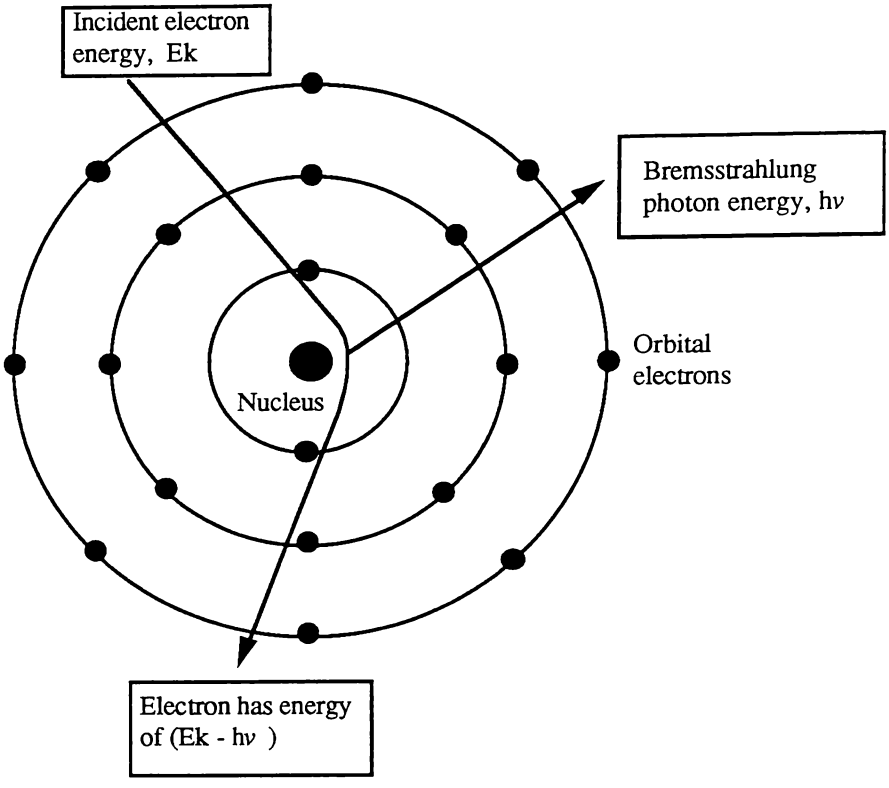

Figure 1.13: Bremsstrahlung photons are emitted when an electron interacts with the coulomb field of the nucleus. The electron continues with its energy reduced to Ek - hν, where hν is the energy lost to the photon.

The energy loss due to production of photons per unit path length z, from electrons of energy $E = h\nu_{max}$, where ν is the bremsstrahlung frequency, is given approximately by the following relationship (Klevenhagen 1985)

$$\frac{dE}{dz} = 4Z^2 \frac{N}{137} r_0^2 E \frac{183}{Z^{1/3}} \quad , \qquad (1.45)$$

where Z is the atomic number, N is the number of nuclei per unit volume and r_0 is the classical radius of the electron.

1.4.3 Electron Stopping Powers

Energy transferred from the electron to the medium by collisional or radiative processes is quantified by the use of stopping powers. The rate of energy loss per unit path length, dE/dz, defined in (1.45) is the *linear stopping power,* referred to as S, and to make this quantity mass independent the *mass stopping power* S/ρ is defined. The *total mass*

stopping power is equal to the sum of the collisional S_{col}/ρ stopping power and radiative mass stopping power S_{rad}/ρ (Klevenhagen 1985):

$$\frac{S_{tot}}{\rho} = \left(\frac{S_{rad}}{\rho}\right) + \left(\frac{S_{coll}}{\rho}\right) \text{ [MeV cm}^2 \text{ g}^{-1}\text{]} \quad . \tag{1.46}$$

Tables of stopping powers are available (Berger and Seltzer 1966). The collisional stopping power is usually represented by a special case called the restricted stopping power L. This is because if enough energy is imparted in the collision to the atomic electron, then it has sufficient energy to itself cause ionization. This electron is often referred to as a *delta ray* (see Figure 1.12). The delta ray in turn interacts with electrons which deposit their energy at a point remote from its original position. The actual energy at a point is therefore defined as the energy transferred by secondary electrons of energy less than a specific value defined as Δ. The *linear restricted stopping power*, also known as the *linear energy transfer* L, is therefore the energy loss per unit path length in which the energy loss per collision is less than Δ. Note that if there is no restriction placed on the energy loss then, ($L = L_{\infty} = S_{coll}$). The restricted mass stopping power is therefore defined as

$$\left(\frac{L}{\rho}\right) = \left(\frac{S_{coll}}{\rho}\right)_{\Delta} \tag{1.47}$$

where Δ is the cut off energy below which electrons are scored as though they deposit their energy at this point. This parameter is typically set at 100 keV as the range of electrons in water at such a low energy is less than 1mm.

1.4.4 Electron Scattering Powers

The approach put forward by Fermi (Klevenhagen 1985) to model the predominant multiple small angle scattering which characterises the electron beam was to formulate scatter distribution functions for lateral displacement and angular deflection. Fermi's original method assumed the electron energy remained constant with depth. Eyges (1948) provided a modified solution to account for beam energy degradation. Though this is an approximation, the theory works well and successful *computerised electron pencil beam planning models* such as those employed by Hogstrom (1985) are based on the Fermi-Eyges scattering theory. Complex beam situations can be reasonably accurately modelled using the pencil beam approach (Hoban 1988, Coalter 1984, Perry and Holt 1980, Jette 1984a and 1984b).

There are some situations where the failure of the method to model large angle scattering causes errors. These problems are addressed by Brahme *et al* (1981) and Lax (1986). This group are producing slightly non-Gaussian shaped pencil beams by using Monte Carlo techniques.

1.5 FLUENCE, KERMA AND ABSORBED DOSE

Photon fluence, KERMA and absorbed dose are defined by the International Commission of Radiation Units, ICRU#19 (1971), as follows.

1.5.1 Fluence

Photon fluence, dN/da, is the number of photons which cross a unit cross-sectional area. Therefore the *photon fluence*, Φ, and *energy fluence*, Ψ, are defined respectively by (1.48) and (1.49) as

$$\Phi = \frac{dN}{da} \tag{1.48}$$

and

$$\Psi = \frac{dN}{da} h\nu = \Phi h\nu \tag{1.49}$$

1.5.2 KERMA

The **K**inetic **E**nergy **R**eleased in a medium per unit **MA**ss or *KERMA*, K, represents the average energy transferred from the photon to the charged particle $d\bar{E}_{tr}$, per unit mass dm, at the site of interaction. Therefore

$$K = \frac{d\bar{E}_{tr}}{dm} \quad . \tag{1.50}$$

As KERMA is the kinetic energy released then it is equal to the energy fluence, Ψ, multiplied by the coefficient of energy transfer μ_{tr}/ρ. Therefore

$$K = \Psi\left(\frac{\mu_{tr}}{\rho}\right) \tag{1.51}$$

and by applying (1.49) then:

$$K = \Phi(h\nu)\left(\frac{\mu_{tr}}{\rho}\right) . \qquad (1.52)$$

As pointed out by Attix (1979), the KERMA can be partitioned into two components: the energy transferred to charged particles K_{col}, and the energy transferred which results in radiative energy is K_{rad}. Therefore

$$K = K_{col} + K_{rad} = \left(\frac{\mu_{ab}}{\mu_{tr}}\right)K + \left(\frac{\mu_{tr} - \mu_{ab}}{\mu_{tr}}\right)K . \qquad (1.53)$$

1.5.3 Absorbed Dose

The energy absorbed by a medium per unit mass, or *absorbed dose* D, represents the average energy transferred from the charged particle to the medium $d\bar{E}_{ab}$, per unit mass dm, where dm is large enough to prevent stochastic variations (Greening 1981), such that

$$D = \frac{d\bar{E}_{ab}}{dm} . \qquad (1.54)$$

1.5.4 Lateral Electron Disequilibrium

1.5.4.1 Discussion

The general phenomenon of electron equilibrium has been discussed by (Dutriex *et al* 1965,1966). This work looked at this effect at air/tissue interfaces. The phenomenon of *lateral electron disequilibrium* has been experimentally characterised by other researchers (Kornelson and Young 1982, Young and Kornelson 1983, Mackie *et al* 1985a). These authors tend to have relied on the following explanation for their results. Due to electrons ranging longitudinally and laterally from the site of photon interactions, the site of energy deposition (dose) is different from the site of energy release (KERMA).

If the beam width is greater than the lateral range of the electrons set in motion, then near the centre of the beam the same aggregate electron energy enters a dose site as leaves the site. In this case *lateral charged particle equilibrium* or *lateral electron equilibrium* is said to exist (note usually most of the charged particles are electrons). A simple model of the

phenomenon is sketched in Figure 1.14 which shows that disequilibrium occurs near the edge of photon beams.

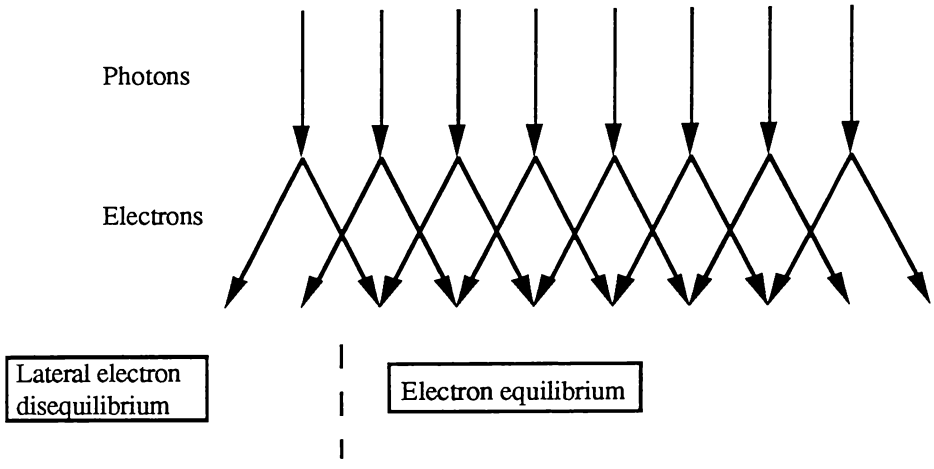

Figure 1.14: Geometry of electron disequilibrium, this is a simplified model of how electrons ranging away from the photon interaction site will produce regions of lateral disequilibrium at the beam edge. (Johns and Cunningham (1983)).

In a lower density medium, the electron range is extended. At high energies the lateral range of some of the electrons exceeds half the field width (eg.10 MV X-rays, 5 x 5 cm field in lung). In this situation electron lateral disequilibrium extends across the entire field width. This leads to a dose void along the central axis. For larger field sizes (eg. 10 x 10 cm) the disequilibrium still occurs but is restricted to the penumbral region. The experimental effects of this phenomenon are discussed in chapters 3 and 4. But a more detailed explanation of *lateral electron disequilibrium* is included as follows.

1.5.4.2 Monte Carlo Dotplot description of Lateral Electron Disequilibrium

When a photon interacts in a medium a series of secondary processes is initiated. Electrons and positrons (charged particles) are set in motion and their energy is imparted to individual atoms as they track through the medium. Delta ray, bremsstrahlung or annihalation events may occur during the electron's tracking process.

The *range* of an electron is defined here as the displacement of the electron from the interaction site at the end of its track. Defining the *lateral range* as the displacement of this track from the x axis and the *longitudinal range* as the displacement in the z axis (see Figure 1.15) then the range of the electron depends on the incident photon energy, recoil electron angle and number of interaction centres along the track (ie. this in turn depends on the electron density and atomic number of the media).

Shown in Figure 1.15 is the results of a simulation of an electron set in motion by an incident 10 MeV photon in media of electron density equal to 0.3. The simulation was generated by using the dotplot option of the electron gamma shower (EGS) Monte Carlo code (Murray 1990). Note the electron longitudinal range is 2.0 cm and the lateral range is 2.3 cm.

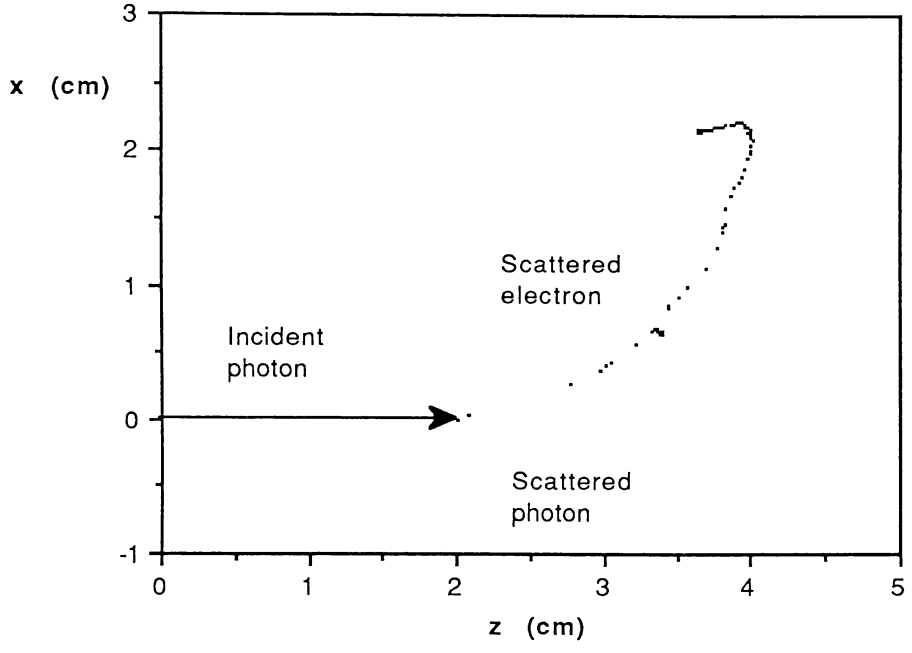

Figure 1.15: Dotplot of a 10 MeV photon interacting with an electron in media of electron density equal to 0.3. The initial energy given to the recoil electron is 3.402 MeV and its kinetic energy is 2.891 MeV (because its original energy in orbit is 0.511 MeV). The energy of the scattered photon is 7.109 MeV. Note that every time the random number is changed a different sequence of events will occur, one scenario has been followed by choosing one random number for the initial event.

Shown in Figure 1.16 is a series of electron tracks (shown in red) which have been generated by forcing 50 photons to interact at the same position. The incident photon paths have been removed from the plots so that the reader can concentrate on the electron tracks without confusion. A polyenergetic spectrum representative of that produced by a 10 MV X-ray machine has been used for the EGS simulation (Mohan and Chui 1985b). Note that a number of electrons stream to a lateral position beyond the 2.5 cm radius which has been marked on the graph and very few electrons range back toward the central area of the pencil beam. Also of interest are the small dots which appear scattered a long way from the interaction site, these are due to scattered photons interacting and producing low energy electrons which deposit their energy locally.

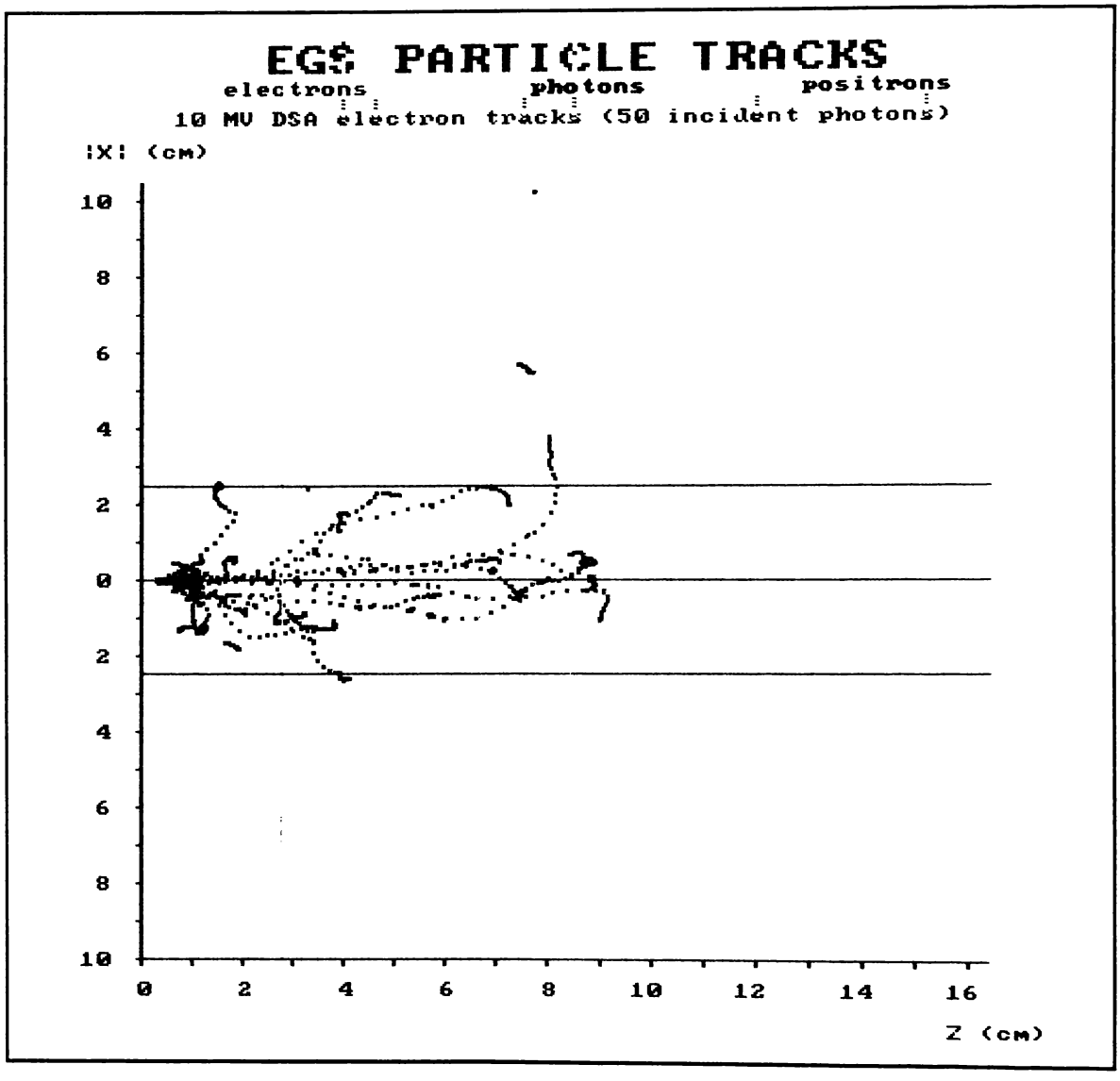

Figure 1.16: Dotplot of a 50 photons interacting with a electrons in an 0.3 density media. The photons are from a polyenergetic spectrum which is typical of that encountered with 10 MV radiotherapy X-ray beams (Mohan and Chui 1985b). The electron tracks are shown in red and a positron track is shown in green.

1.5.4.2 Mathematical Explanation of Lateral Electron Disequilibrium

When considering the energy E deposited to a point (x, y) due to all other points in the beam (x', y') within a rectangular field of dimensions X by Y as shown in Figure 1.17. Then for *lateral electron equilibrium* to exist the energy deposited at point (x, y) from points (x', y') should equal the energy released from point (x, y). This can be shown as follows.

The energy deposited at (x, y) due to energy released at (x', y') depends on the radial distance from interaction to deposition site, therefore

$$E(x, y; x', y') = E[(x - x')^2 + (y - y')^2]^{1/2} \qquad (1.55)$$

The total energy deposited due to the lateral electron range component at (x, y) is mainly due to electrons ranging from upstream at z, however if one just considers the lateral component of this electron spread, then a two-dimensional expression which is a requirement for lateral equilibrium to exist at (x, y) is that energy deposited at (x, y) due to interactions within the field envelope X,Y, is equal to the energy deposited at (x, y) if the field were infinite, therefore

$$\int_0^X \int_0^Y E(x, y; x', y')dx'dy' = \int_{-\infty}^{\infty} \int_{-\infty}^{\infty} E(x, y; x', y')dx'dy' \qquad (1.56)$$

When *electron lateral disequilibrium* exists some of the energy does not fall within the field envelope and (1.56) is not satisfied, such that

$$\int_0^X \int_0^Y E(x, y; x', y')dx'dy' < \int_{-\infty}^{\infty} \int_{-\infty}^{\infty} E(x, y; x', y')dx'dy' \qquad (1.57)$$

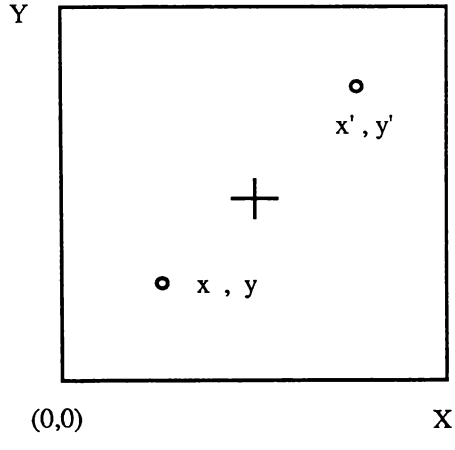

Figure 1.17: Beams eye view of field dimensions used when defining (1.55), (1.56) and (1.57).

CHAPTER 2

EXPERIMENTAL METHODS

2.1 INTRODUCTION

The equipment employed, adapted or manufactured for use in experiments outlined in the thesis, is discussed in this chapter.

The main features of different radiotherapy machines used to treat patients, and equipment used for radiotherapy treatment planning is reviewed in section 2.2. In section 2.3 the properties of available body analogs are quantified. The materials used to manufacture the low density (lung density 0.2) two lung phantom used in subsequent experiments are in this group of compounds.

In section 2.4 the in-house production of epoxy resin based body analogs is outlined. A quality assurance method which uses computed tomography (CT) scan data to analyse the efficacy of these analogs is also outlined in section 2.4. Several phantoms produced using this material are described and these include the medium density (lung density 0.3) two lung phantom used extensively in subsequent experiments.

The monitoring equipment used in subsequent experiments is discussed in section 2.5. This includes ionization chamber and diode detectors, precision drive and electrometer control equipment. An analysis is also included in section 2.5 which establishes the accuracy of using a Baldwin Farmer-type ionization chamber in low density media.

2.2 RADIOTHERAPY TREATMENT AND PLANNING MACHINES

2.2.1 Teletherapy Machines

For the treatment of deep seated tumours, high energy photon beams with deep penetration characteristics are required. Early methods of producing high energy beams for medical applications employed Cobalt-60 and Caesium-137 sources produced in nuclear reactors. The Cobalt-60 machine of the type developed by Johns *et al* (1952, 1959) became the most popular due to its higher specific activity, enabling a large source activity (5000 Curies) to be packed into a small cylinder (approximately 15 mm diameter). This ensures a penumbral definition and dose rate which is superior to other isotope machines (such as Caesium-137).

The Cobalt-60 machine is used widely in radiotherapy applications and new units are still marketed. Despite its single rather low photon energy (1.25 MeV), it is often regarded as a more reliable unit than its main competitor the linear accelerator. This is because it requires minimal "down-time" due to the relative simplicity of design.

2.2.2 Medical Linear Accelerators

The evolution of the medical linear accelerator (linac) was a direct result of radar development work which culminated in the production of microwave generators in the form of magnetrons and klystrons. These devices are capable of establishing intense electromagnetic fields in microwave cavities. This enables the acceleration of electrons to relativistic velocities when incorporated with suitable waveguide structures. Figure 2.1 shows a photograph of a linac (Clinac 18). Further details of operation and technical apects can be obtained elsewhere (Slater 1948, Karzmark and Perring 1973, Karzmark 1984).

Linacs are the modality of choice for the production of high energy X-rays in radiotherapy applications. These units are becoming increasingly more popular than Cobalt-60 teletherapy units as they have the following advantageous features:

(1) Multiple electron and photon energies are available which allow the physician to tailor treatment to the required treatment depth. A modern linac is usually capable of producing two different photon and five different electron energies.

(2) The dose rates (1 to 5 Gy per minute) are higher than isotope machines . This enables shorter treatment times and longer target (**S**ource) to patient (**S**urface) **D**istances, SSDs, to be used. The longer distances ensure less beam divergence and slower fall off in the percentage depth dose.

(3) Linacs have a smaller virtual source size (approximately 3 mm) than isotope machines. This means that they produce a sharper dose fall off in the penumbra.

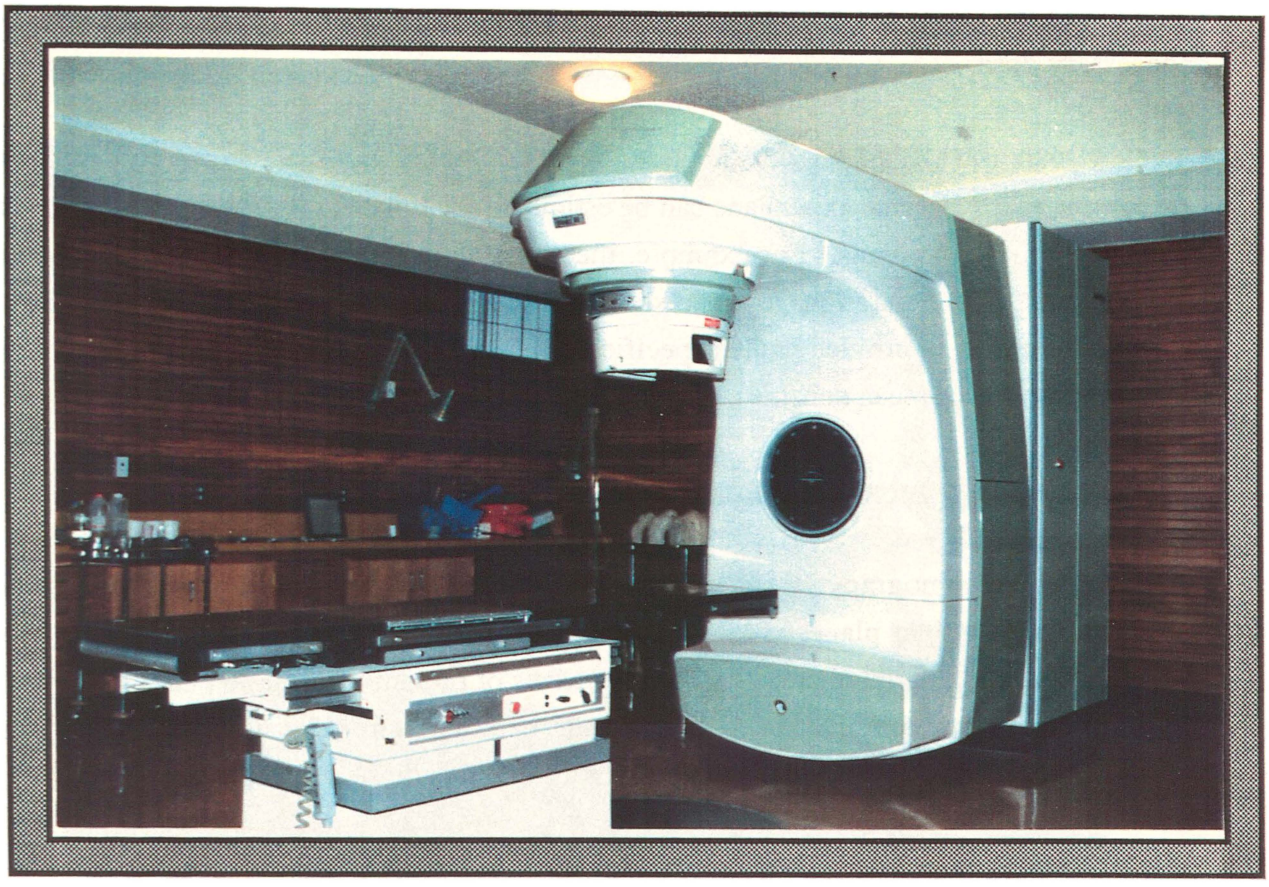

Figure 2.1: Photograph of a medical linear accelerator. This model is a "Varian Clinac 18". It is situated in a treatment room at the Waikato Hospital radiotherapy centre. This linac is capable of producing 10 MV X-rays and 6, 9, 12, 15, 18 MeV electrons at a dose rate of between 1 and 5 Gy per minute. The machine's centre of rotation (isocentre) is at 100 cm SSD.

2.2 3 Radiotherapy Planning Methods

2.2.3.1 External Patient Contours

There are several ways of obtaining patient external contour shape. These include outline formers such as flexicurves and porcupines, dynamic contour scanners, and photogrammetry. These methods do not provide information about internal body structures (Bleehen *et al* 1983, Mould 1981).

2.2.3.2 X-ray Simulators and Ultrasound

The X-ray simulator is used by the planning radiographer and radiotherapist prior to patient treatment. Simulators are diagnostic X-ray machines that provide geometric movements which mimic (simulate) those of the therapy machines. As such they provide the clinician with an X-ray "beam's eye view" of the tumour and surrounding structures, so that accurate

treatment to the target can be acheived while radiation sensitive structures are spared any unnecessary dose.

By using anatomical land marks and lead markers, the position of internal anatomical structures in the transverse axial plane can be estimated. Ultrasound is used to augment this information for some plans. For example, the chest wall is often ultrasound scanned to ascertain chest wall separation (ie. the distance between lungs and external body contour). These methods do not provide patient specific information about electron densities of these structures, and hence mean densities (derived from patient surveys) have to be assigned.

2.2.3.3 X-ray Computed Tomography

X-ray computed tomograpy (CT) scanners provide high contrast X-ray pictures in the transverse axial patient plane (Hounsfield 1973, Brooks and DiChiro 1975). CT is the modality of choice for radiotherapy planning in terms of providing accurate internal/external contour information, combined with an accurate map of electron densities (as outlined in sections 2.4 and 2.5). The CT scanner used for tests in this thesis was a Siemens DRH.

2.2.3.4 Nuclear Magnetic Resonance Imaging

Nuclear magnetic resonance image (MRI) scans do not provide electron density information and there are some image distortion problems with these scans. One advantage, however, is that MRI provides better tumour definition for many tumour types and hence the target volume can be more accurately specified. Current research is therefore involved with overlaying the MRI tumour information onto the CT electron density image (Frass *et al* 1987).

2.2.3.5 Radiotherapy Planning Computers

Using the image information collected from the above methods, the planning radiographer enters the patient cross sections onto a planning computer and a two-dimensional patient treatment plan is generated. The plan consists of an isodose distribution (see chapter 3) overlayed on the patient structures and clearly shows the dose to the target volume. The radiotherapist then reviews the plan and decides whether it is providing the required dose distribution. This is all done prior to patient treatment to ensure the dose distribution delivered to the patient will be adequate. Three-dimensional display of treatment plans have been developed using wire frame, surface rendering and beams eye view techniques (Mohan 1989, Gotein *et al* 1983). Shown in Figure 2.2 is a photograph of the Theraplan treatment

planning system which employs features common to many other systems. The hardware features which are common to radiotherapy planning computers are shown in Figure 2.3.

Figure 2.2: Photograph of the Theraplan treatment planning system which was commissioned by the author in 1989 at the Waikato Hospital Radiotherapy Centre.

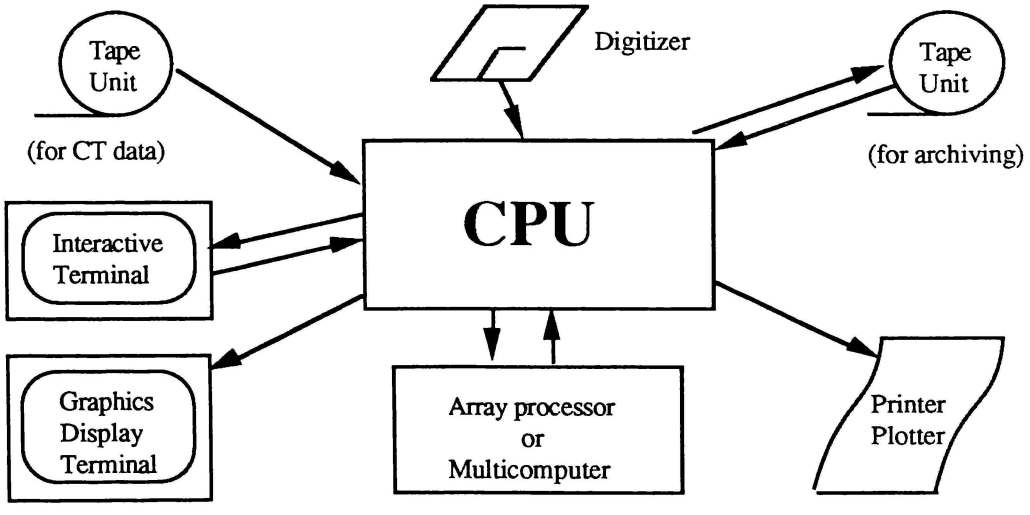

Figure 2.3: Schematic block diagram showing the common features of radiotherapy planning computers. The planning radiographer interacts with the computer by input of patient and beam data. The computer generates radiotherapy plans with isodose distributions overlayed on the internal patient structures.

2.3 AVAILABLE BODY ANALOGS

2.3.1 Discussion

In order to produce suitable radiotherapy dosimetry phantoms a number of materials were examined. These included "off the shelf" materials which are discussed in this section and analogs which were manufactured "in-house" as discussed in section 2.3.

2.3.2 Computed Tomography Calibration Methods

Calibration plots for a Siemens DRH CT scanner, as shown in Figure 2.4, were obtained from data included in Table 2.1. In this case because the elemental composition of some of the elements is unknown (eg. the cork) the electron density relative to water ρ_e^w is assumed to be related to mass density ρ by the equation

$$\rho_e^w \approx \rho \quad . \tag{2.1}$$

The relationship of CT number N_{CT} to electron density relative to water is quasi-independent of beam energy only if the effective atomic number Z_{eff}^w of the substance matches that of water (and hence soft tissues). This assumption is shown to be valid for the lung analogs made of cork because the cork data points conform to the Hounsfield regression line fit shown in Figure 2.4. The cork analog sample of 0.2 density is of particular interest because this material is used to form the low density two lung phantom used extensively in subsequent experiments. Notice that this sample lies on the Hounsfield regression line. This proves that although the elemental composition is unknown, the effective atomic number of this sample is very close to that of water. Hence the radiation properties of this sample at high X-ray energies is likely to closely model those of lung.

For the other compounds of different atomic number (polystyrene, acrylic, ertalyte and delrin) the electron densities are calculable since the chemical formula and mass density are available. Electron densities and effective atomic numbers were calculated for such compounds, using the formulae of McCullough and Holmes (1985). The results of calculations for the samples are provided in columns 3 and 4 respectively of Table 2.1.

Bone exhibits extra photoelectric absorption due to its higher atomic number (ie. higher than other body tissues). Bone analogs have been investigated here using liquid solutions with various concentrations of monohydrogen di-potassium phosphate (K_2HPO_4). The method

used to ascertain the electron densities and effective atomic numbers from the solution concentrations also followed the guidelines of McCullough and Holmes (1985), and the results are listed in Table 2.1. The samples listed in Table 2.1 were studied on a Siemens DRH CT scanner and their CT numbers N_{CT} were recorded when samples of each material were placed in the centre of a 30 cm cylindrical CT phantom and scanned.

Due to a change in the primary beam attenuation filter of the scanner X-ray tube (from 0.4 to 0.2 mm Copper) the opportunity arose to examine the effect of tube kilovoltage on sample calibration. Three effective energies were studied (75, 71 and 64 keV) as determined by the use of *effective keV liquids* (White and Speller 1980). It was found that the change in X-ray spectra had little effect on the soft tissue analog calibration lines as shown in Figure 2.4, but it had a more significant effect on the bone analog line gradients (see Figure 2.5). This is attributed to the enhanced photoelectric effect observed in samples of greater atomic number when beam energy is reduced (Henson and Fox 1984).

Compound (formula) [conc.]	ρ	ρ_e^w	Z_{eff}	Z_{eff}^w
air	0.0012	0.0012	7.55	1.02
cork+	0.2	0.2	7.4	1.0
cork	0.4	0.4	7.4	1.0
cork	0.5	0.5	7.4	1.0
polystyrene (C_8H_8)+	1.04	1.01	5.70	0.77
acrylic $(C_5H_4O_2)$	1.19	1.16	7.55	1.02
ertalyte $(C_5H_4O_2)$	1.29	1.31	6.59	0.89
delrin (CH_2O)	1.41	1.36	6.96	0.94
(K_2HPO_4) [75 mg/ml]	1.06	1.05	8.51	1.15
(K_2HPO_4) [180 mg/ml]	1.13	1.11	9.55	1.29
(K_2HPO_4) [250 mg/ml]	1.18	1.15	10.06	1.36
(K_2HPO_4) [325 mg/ml]	1.23	1.19	10.51	1.42
(K_2HPO_4) [400 mg/ml]	1.27	1.23	10.88	1.47

Table 2.1: Mass density, electron density, and effective atomic number relative to water for samples scanned by a Siemens DRH CT scanner at nominal energies of 64, 71 and 75 keV.

+ These are the materials used in the low density two lung cork phantom A which is shown in Figure 2.6.

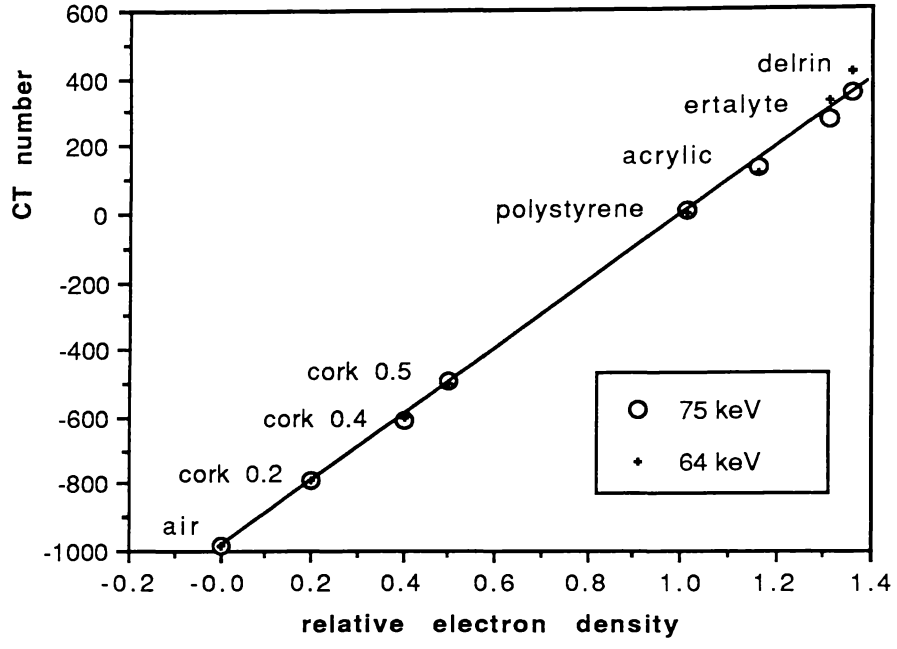

Figure 2.4: Calibration line of CT number versus relative electron density for commercially available materials scanned on a Siemens DRH CT scanner at nominal energies of 64 and 75 keV.

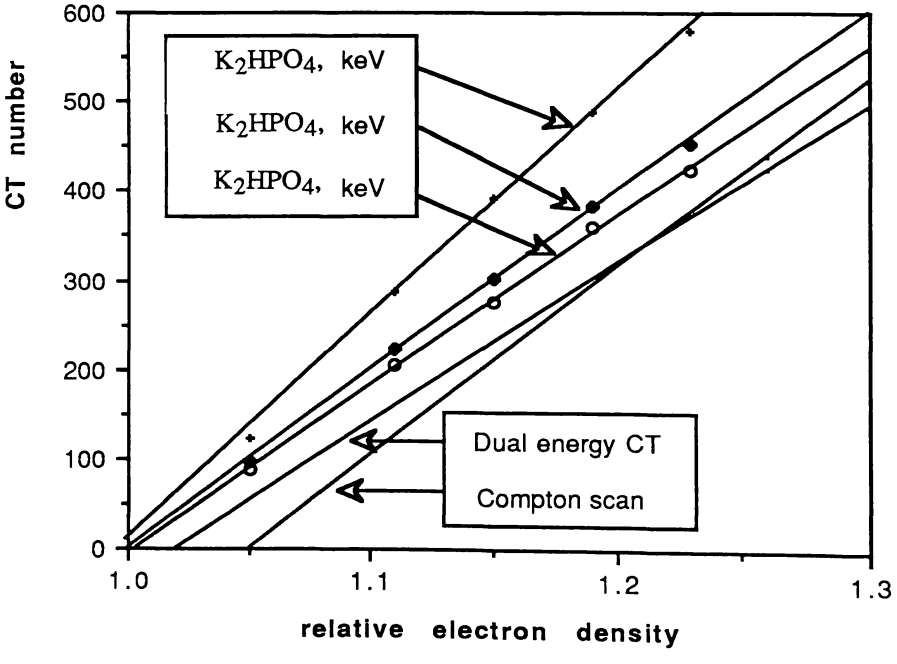

Figure 2.5: Calibration line of CT number versus relative electron density for the liquid bone analog material, di-potassium phosphate solution (K_2HPO_4), compared to in vivo data obtained using other scanner methods (dual energy CT and Compton scan). The dual energy CT line was obtained from Henson and Fox (1984) and the Compton scan data was obtained from Battista and Bronskill (1981).

A graph of N_{CT} versus ρ_e^w is provided in Figure 2.5 for the liquid bone analog materials. A search for *in vivo* data of bone calibration lines to compare with the liquid analogs revealed two lines of interest. This data was obtained independently by Compton scanning (Battista and Bronskill 1981) and a dual photon CT method (Henson and Fox 1984). Intercomparison of the plots for the K_2HPO_4 liquids with this data is also shown in Figure 2.5. The comparison of data shown on the graph indicates that the K_2HPO_4 compound closely models the slope of the *in vivo* data. The offset relative to the in vivo data is in part due to uncertainties in the experimental data of 5% for the dual photon case and 10% for the Compton scan data.

In Figure 2.5 it is evident that the intercepts of the K_2HPO_4 lines are very close to (1, 0). It is suggested that this is representative of the bone line, as a bone density increase is probably accompanied by an increase in bone mineral content. Note also that the gradient of the bone line is greater than that of the tissue line. This is due to more photoelectric absorption from the high atomic number materials. The result is greater X-ray absorption and hence higher CT numbers with respect to electron density.

Examination of the horizontal axis of Figure 2.5 also shows that data for the liquid analogs is limited to a maximum electron density level of $\rho_e^w = 1.23$. This is because the solutions become saturated above this level.

The results in Figure 2.5 also show variation of N_{CT} with beam energy and suggest that a *periodic calibration* technique or continuous *on-line calibrations* will ensure that a change in effective energy is accounted for by the recalibration. CT calibration using an on-line method is discussed elsewhere (Metcalfe *et al* 1988).

By fitting regression equations to the lines in Figure 2.5 for the K_2HPO_4 samples at different energies. The data are represented by

$$\rho_e^w = R_\gamma\left(\frac{1}{1000} N_{CT}\right) + 1 \quad , \tag{2.2}$$

where R_γ denotes the experimental regression line gradient for bone type substances. The regression equations are useful for radiotherapy planning purposes as these equations are used to convert from CT number to relative electron density for bone-type substances (Metcalfe and Beckham 1988, McCullough and Holmes 1985).

2.3.3 The Two Lung Cork Phantom

The *two lung cork phantom* produced is shown in Figure 2.6. It has been used extensively in radiotherapy dosimetry tests (Metcalfe and Beckham 1988, Metcalfe and Battista 1988, Metcalfe *et al* 1988, Hoban *et al* 1990a). Some of these results are described in chapters 3 and 4 of this thesis. The phantom was built from components included in the CT analysis described in the previous section. It consists of 3 mm polystyrene slabs of density $\rho_e^w = 1.01$ to simulate tissue and 6 mm cork slabs of density $\rho_e^w = 0.2$ to simulate lung.

The density of the cork ($\rho_e^w = 0.2$) is at the low end of the likely scale of lung densities when considering the mean density is approximately $\rho_e^w = 0.3$ for a sample of patients, with a variation from about 0.2 to 0.5. The range within an individual patient's lung can also vary between 0.2 and 0.5 due to inspiration and blood pooling (Van Dyk *et al* 1979, Van Dyk *et al* 1982).

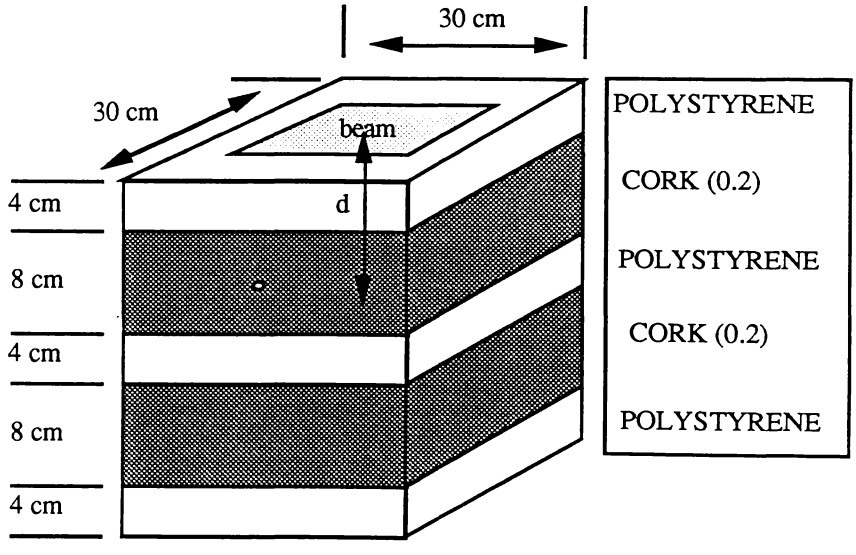

Figure 2.6: The construction details of the Metcalfe two lung cork phantom known as *phantom A* used in experiments outlined in chapters 3 and 4. The cork layers were laminated from 6 mm thick sheets and the polystyrene was laminated from 3 mm sheets. An ionization chamber is placed in custom drilled holes within the polystyrene and cork slabs for dose measurements.

2.4 THE IN-HOUSE PRODUCTION OF BODY ANALOGS

2.4.1 Reason for In-House Manufacture

Because the density of the cork in the two lung cork phantom is at the low end of the density range for lung it accentuates the effect of lateral electron disequilibrium. The dose perturbation effects are representative of likely dose distributions in large areas of lung. A drawback with the cork was that a detailed chemical analysis was not available. The CT scan analysis however (see Figure 2.4) showed the constituents were suitable as lung analog material because the lung data points fell on the regression line for tissue like materials. Therefore the effective atomic number of this material is very close to that of patient lung.

To have the added flexibility of being able to tailor the exact density, atomic number and shape of a phantom has obvious advantages, and the use of polystyrene and cork does not give one this flexibility. Therefore in-house manufacture of lung, tissue and bone analogs for dosimetry phantoms was undertaken. The manufacturing and quality assurance methods developed for this process are explained in this section.

The cost of these analog materials in 30 x 30 x 1 cm layers was quoted as NZ$560 per muscle or lung slab and NZ$920 per bone slab, (commercial supplier - REM New Zealand Ltd., agents for Radiation Measurements Inc., Middleton Wisconsin, U.S.A., 1989). If purchased from the commercial supplier the analog material for the two lung phantom would have cost NZ$15680 (ie. 28 slabs x NZ$560 per slab). This cost was considered to be excessive considering the large amount of material which was required for the phantoms.

In contrast, in-house manufacture is relatively inexpensive. The cost for materials including resins, moulds and equipment to manufacture the analogs in-house is about NZ$45 per slab. The cost to produce the two lung phantom in-house was 28 slabs x $45 = $1260.

The in-house manufacture of solid bone analogs is just as advantageous as that of solid lung analogs. This is because no suitable solid analogs exist for bone that are commercially available. In fact delrin, ertalyte and teflon are poor bone analogs as their atomic numbers are much less than that of *in vivo* bone.

The effective atomic number of the liquid analog K_2HPO_4 closely matches *in vivo* bone (see Figure 2.5) and these analogs are therefore suitable for CT calibration tests, liquid analogs are less suitable for use in radiotherapy phantoms. This is because they have to be

housed in the required phantom shape by a vessel which cannot itself perturb the radiation beam. This practical problem is the main drawback when liquid analogs are considered for use in multiple slab radiotherapy phantoms.

2.4.2 Materials and Methods

Bone, muscle and lung epoxy resin based analogs were produced for use as dosimetry phantom material. The recipes and methods of White *et al* (1977, 1986) have been followed in the manufacture of these substances. A method has been developed by White (1977, 1978) to show that the radiation properties of these analogs match closely those of their respective equivalent human tissues. The mass stopping powers S/ρ, and mass attenuation coefficients μ/ρ, of these substances match those of their human tissue equivalents to within 3% over the X-ray energy range of 0.1 to 10 MeV (White *et al* 1977, 1986).

Tables 2.2, 2.3, and 2.4 show the constituent elements required for production of bone, muscle and lung analog material respectively. Included in the tables are the codes which White *et al* use to refer to these materials.

The apparatus used for the manufacture of bone, muscle and lung analogs is shown in Figure 2.7. It consists of a powerful electric mixer (an electric drill motor) which turns a mixing propeller within a reaction vessel. The vacuum is provided by a pump, which is able to maintain a vacuum of 0.001 Torr. This is connected to the top of the reaction vessel by a flexible hose. An electric drill motor is connected to the mixing propeller by a connecting rod which feeds through a glass stirring gland. The gland is sealed with glycerol and the reaction vessel has a ground glass edge which means it can be vacuum sealed with grease. The apparatus is housed in a fume cupboard because the epoxy resin hardeners are extremely toxic.

The ingredients are weighed on a percentage by mass basis. All ingredients are poured into the reaction vessel and are given a thorough manual mix. The reaction vessel is then attached to the mixing device. Automatic mixing is applied for a further 3 minutes and then the vacuum is applied to the reaction vessel. The pressure reduction in the vessel causes the fluid to foam up in the vessel, but the rotating blades break the resulting foam to release the trapped gases. This prevents bubbles forming in the mix. Mixing for 20 minutes under vacuum is essential to remove all the bubbles. The vacuum is then released and the mixing is stopped. The reaction vessel is then removed from the mixing device and the mixture is poured into the mould.

The mixture settles in the mould and is left for 24 hours to harden. Complete curing is achieved by heating the analogs in an oven at 70 degrees Celsius for two hours. At this stage the analog is set and can be removed from its mould. If the mixture is not the desired shape then it can be reheated to 70 degrees Celsius, in which case it becomes flexible and can be reset to the desired shape. If the mixture is not of the correct thickness it can be successfully faced off using a conventional milling machine.

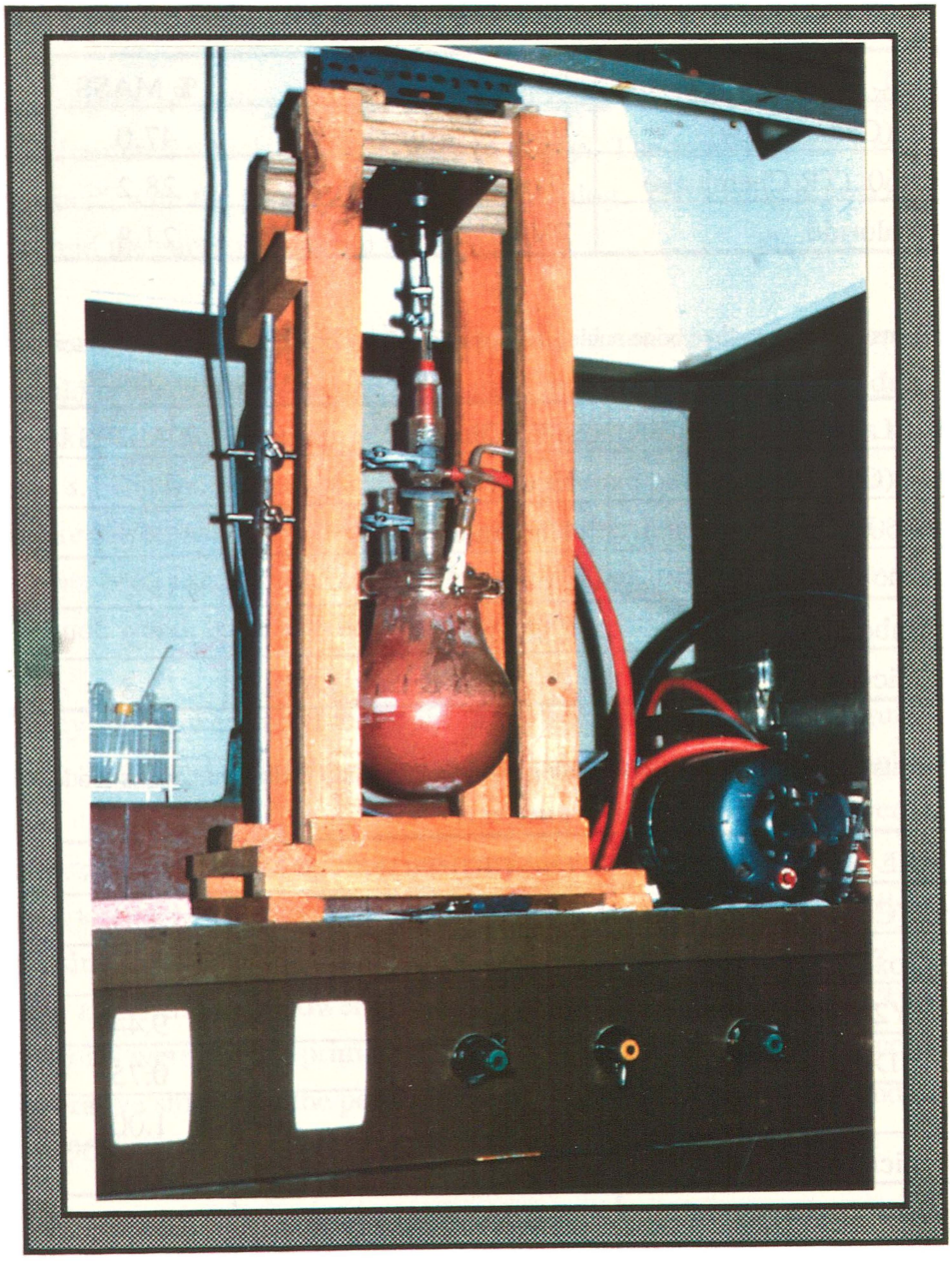

Figure 2.7: Photograph showing the mixing and vacuum apparatus used for the in-house manufacture of body analogs. The electric drill which is shown at the top of the frame is attached to a glass stirring rod which feeds through a glass-to-glass stirring gland. The vacuum within the reaction vessel is maintained by the pump shown at the right of the frame. The assembly is housed in a fume cupboard because of the toxic fumes from the hardeners which are emitted during the de-gassing process.

The lung analog is made using the same process, except the vacuum is not applied. The mixture is simply poured into moulds and gently rises due to the expanding agent (Dow Corning 1107) which blows hydrogen bubbles into the mixture. The number and size of gas spaces left in the lung analog is reduced by the surfactant (Dow Corning 200/50). The type of MgO used is critical to the process. The more pure grades of MgO tend to collapse the mixture (White *et al* 1986). The MgO found most suitable was "laboratory grade MgO heavy". The curing process for the lung analog was supplemented by placing the material in an oven at 70 degrees Celsius for two hours.

MATERIAL AND (SUPPLIER)	DESCRIPTION	% MASS
Araldite F (Ceiba Geigy)	Epoxy Resin	47.0
Synolide 960 (TR Chemicals)	Hardener	28.2
Polyvinylchloride	PVC Powder	24.8

Table 2.2: Ingredients used to produce bone analog material for X-ray beam simulations (Whites code IB1).

MATERIAL AND (SUPPLIER)	DESCRIPTION	% MASS
Araldite F (Ceiba Geigy)	Epoxy Resin	47.5
Synolide 960 (TR Chemicals)	Hardener	28.5
Polyethylene	Powder 50 μm	15.0
Calcium Cabonate	$CaCO_3$ powder	6.2
Phenolic micro balloons	PMS low density powder	2.8

Table 2.3: Ingredients used to produce muscle analog material for X-ray beam simulations (code MS 10).

MATERIAL AND (SUPPLIER)	DESCRIPTION	% MASS
Araldite F (Ceiba Geigy)	Epoxy Resin	33.71
Araldite epoxide 8	Hardener control	16.85
Araldite HY2996	Hardener	9.44
DC1107 (BDH chemicals)	Expander	0.75
DC 200/50	Surfactant	1.00
Phenolic micro balloons	PMS low density powder	4.42
Polyethylene	Particulate filler powder	15.00
Magnesium Oxide	Particulate filler powder	18.83

Table 2.4: Ingredients used to produce lung analog material for X-ray beam simulations (code LN 10/75).

2.4.3 Moulds, Analogs and Phantoms

The moulds used to produce slab phantom material are constructed from acrylic and are screwed together such that the ends can be disassembled as shown in Figure 2.8. This helps in the release process, as does the addition of "mould release". To remove the analogs from the mould the sides are removed from the moulds and a chisel is used to gently prize the rest of the analog from the base of the mould. The use of a hammer to dislodge the analogs from the moulds is not recommended as the analogs tend to shatter or crack.

Another mould releasing process was developed for the lung analogs, since they use a different hardener which does not release easily. The moulds were lined with "laboratory bench paper", with the plastic side facing the analog. The analog is removed from the mould once set and the paper peels from the analog.

Moulds for anthropomorphic and large cylindrical analog phantoms were formed by using a heat mould process which is commonly used in radiotherapy planning departments to create face masks for radiation therapy patients. A mould produced by this method is shown in Figure 2.8. The mould material is "cellulose acetate butyrate" and this is vacuum moulded into the required shape by using a dummy former. In this case a Rando phantom cross section has been used as the dummy former. Other formers which have been successfully used include wood, large acrylic cylinders and plaster casts.

Acrylic cylinders were used to mould the CT phantoms shown in Figure 2.9. The moulds are 1 mm thick acrylic and these are retained permanently around the analogs as the thin layer is found not to affect CT numbers. The long cylinders produced were used as the solid constituents of a Cann phantom (Cann and Gennant 1980). The bone analog has also been useful in testing the accuracy of electron beam algorithms which until recently have been tested using substances such as teflon or lead which do not exactly model the electron stopping and scattering powers of electron beams (Cygler *et al* 1987). Though electron beam studies were not the primary aim of this thesis, the material produced has been used in a collaborative study into the perturbation of electron beams by bone and air cavities (Hoban *et al* 1990b).

Build up caps for ionization chambers were also made using muscle analog material. The mould used consists of a thin plastic bottle as shown in Figure 2.9. This is filled with analog material and then an aluminium ionization chamber former is used to create the desired space for ionization chambers. To enable easier release, the former is fitted into a thin rubber sheath (commonly used to water proof ionization chambers). When the analog

has set hard the aluminium former plus rubber sheath are readily removed leaving an excellent fit for real ionization chambers to slot into. This process is also repeated in any slab phantom sections which need to house ionization chambers.

Build up caps were produced out of muscle analog material to collect TARs for high energy beams as outlined in chapter 3 (see Figure 3.8). The alternative method usually employed is to mill build up caps out of acrylic (as polystyrene tends to be hard to mill in a lathe) and drill out a space for the ionization chamber. The new build up caps produced were not only more tissue equivalent but they were also much easier to make by the moulding process described earlier.

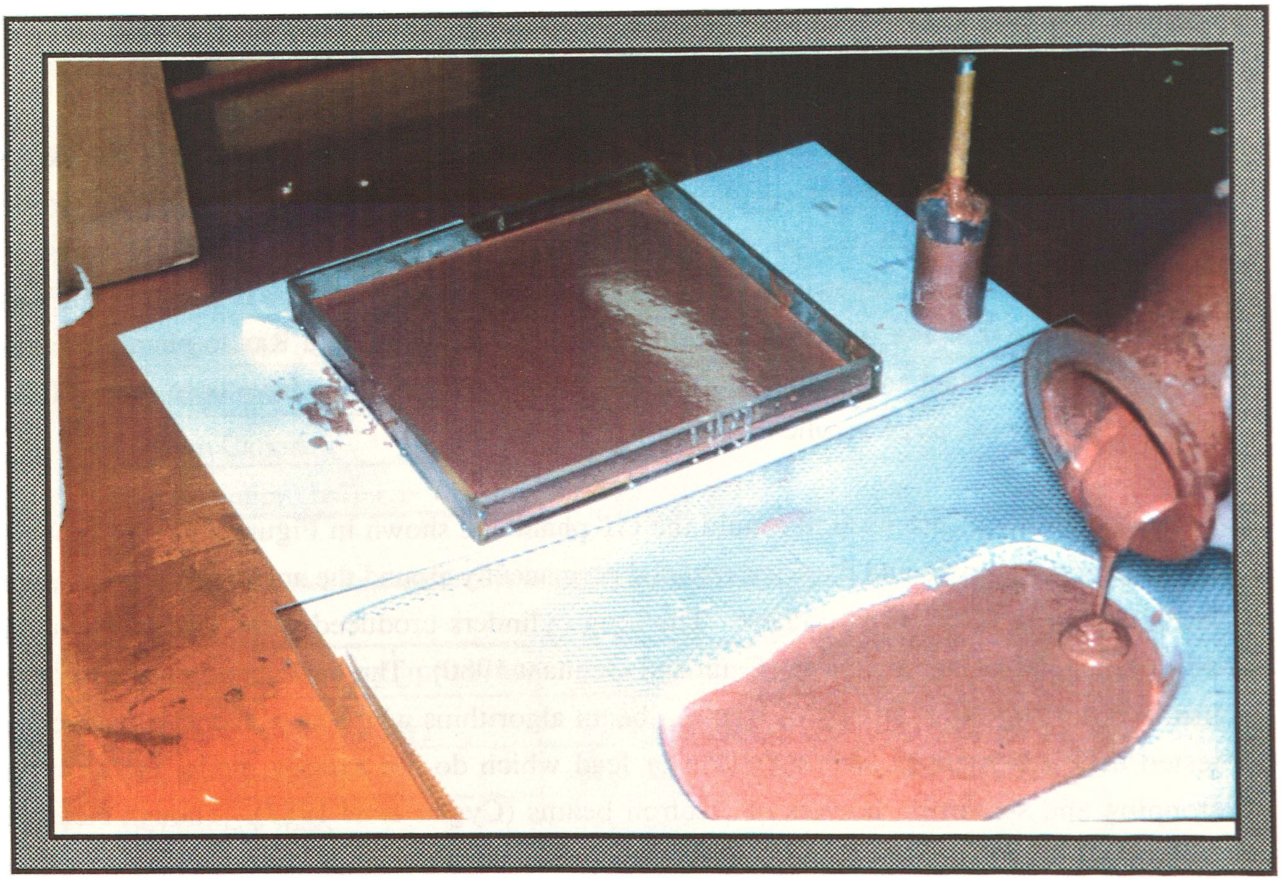

Figure 2.8: Photograph showing muscle analog (MS10) mixture being poured into moulds.

Centre - shows a mould made out of acrylic sheets which are screwed together and can easily be disassembled. The moulds for lung analogs were also lined with laboratory bench paper as this aided the release process.

Lower right - shows an anthropomorphic phantom and mould produced from a Rando phantom slice as a former around cellulose acetate butyrate. The heat moulding device used to form the mould is commonly available in most radiotherapy planning departments as the device is used to form face masks used to aid immobilisation during radiotherapy treatment.

Top right - shows a build-up cap being produced in a plastic bottle. A rubber sheathed aluminium former can be seen protruding from the top of the mould.

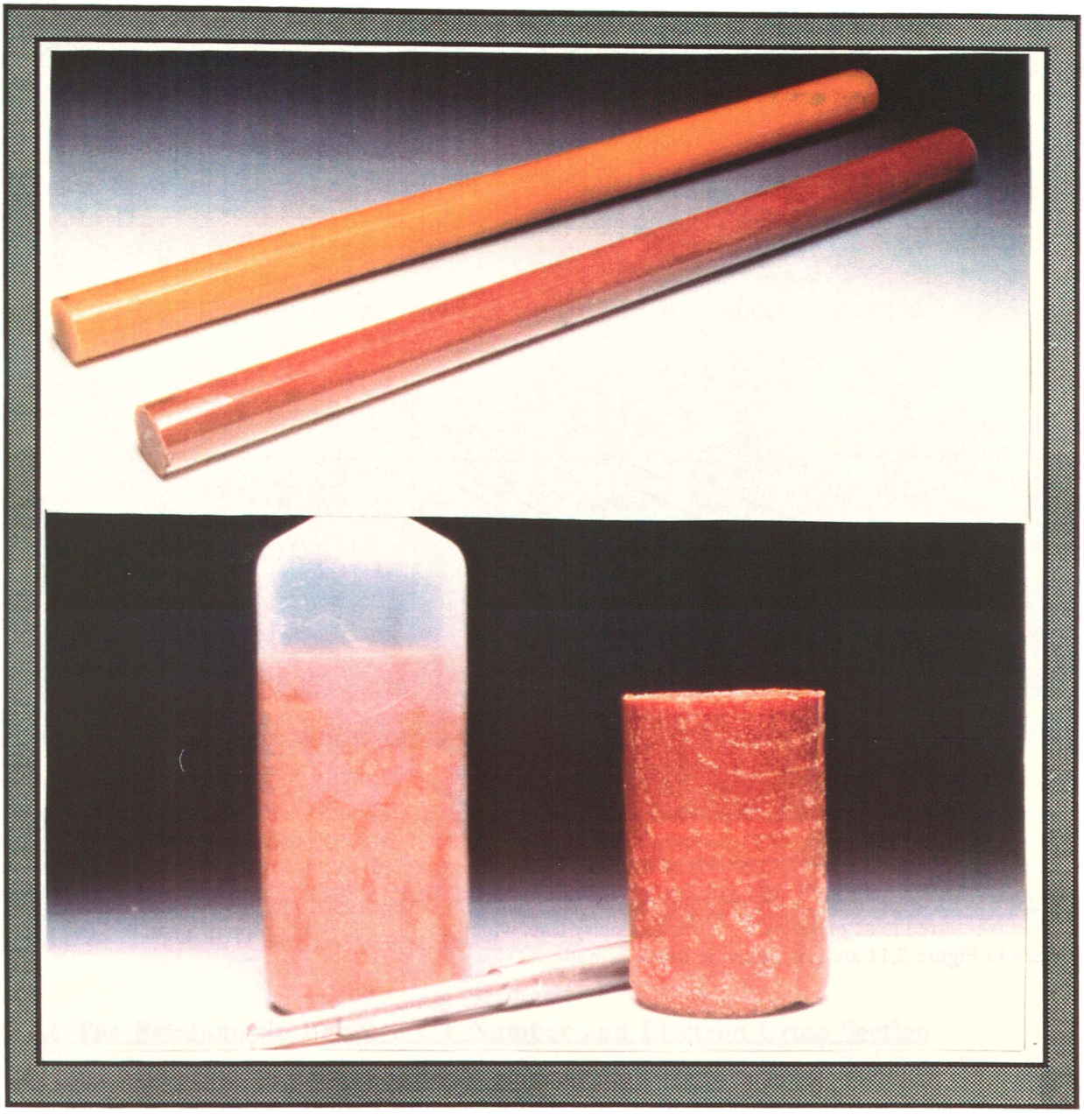

Figure 2.9: A selection of phantoms produced in different shapes.

Top - cylindrical phantoms formed in thin acrylic pipes for use as radiotherapy phantoms and CT phantoms. The thin 1 mm acrylic pipes which house the analogs were retained. The yellow cylinder is the bone analog IB1 and the brown cylinder is the muscle analog MS10 (see White *et al* 1975, for codes)

Bottom - build up cap for a Baldwin Farmer ionization chamber made from MS10. Left - the mixture sets in the mould, right - the build up cap is shown removed from the mould, centre - the aluminum former which is used to shape the ionization chamber insert.

2.4.4 The Two Lung Analog Phantom

The *two lung analog phantom* produced is shown in Figures 2.10 and 2.11. It has been used extensively in X-ray radiotherapy dosimetry tests as described in chapters 3 and 4 of this thesis, where it is referred to as *phantom B*. It consisted of 10 mm muscle slabs (ρ_e^w = 1.02) to simulate muscle and 20 mm lung slabs of density (ρ_e^w = 0.28) to simulate lung. It has the same geometric dimensions as the cork-polystyrene phantom mentioned previously, however the density of the lung analog (ρ_e^w = 0.28) is closer to the mean lung density (ρ_e^w = 0.3) which has been reported for a sample of patients by Van Dyk *et al* (1982).

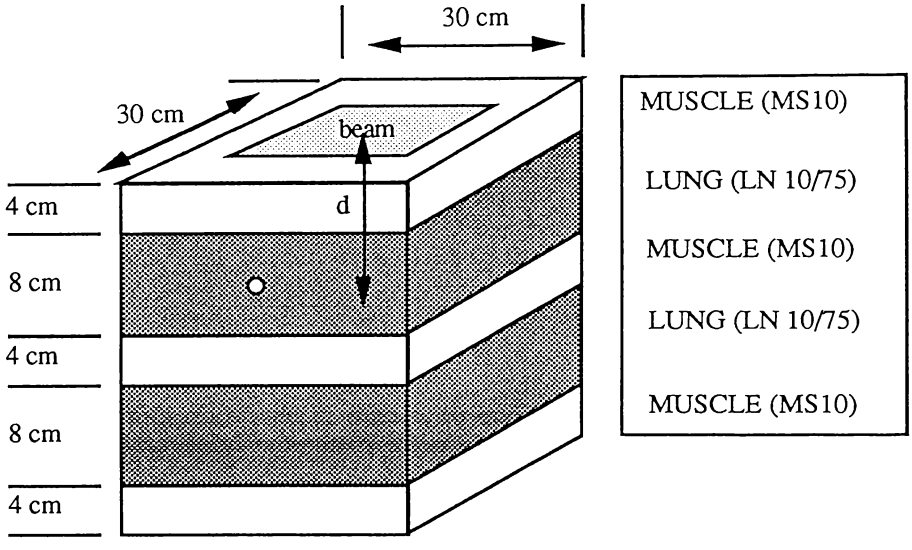

Figure 2.10: Schematic of the two lung analog slab phantom consisting of muscle and lung analog slabs. This is referred to as *phantom B* in the dosimetry tests which are described in chapters 3 and 4. The wings seen in Figure 2.11 are not shown in this schematic.

2.4.5 CT Quality Assurance Of Body Analog Composition

To ensure the analogs manufactured closely match the elemental compositions of their respective tissues and therefore the radiation properties required, a convenient quality assurance method which uses CT analysis has been developed. Using the method described below, experimental CT numbers for analogs are compared with the theoretical CT numbers calculated using elemental compositions of White *et al* (1977,1986). This is a convenient and accurate method of quality assurance which entails no laboratory chemical analysis.

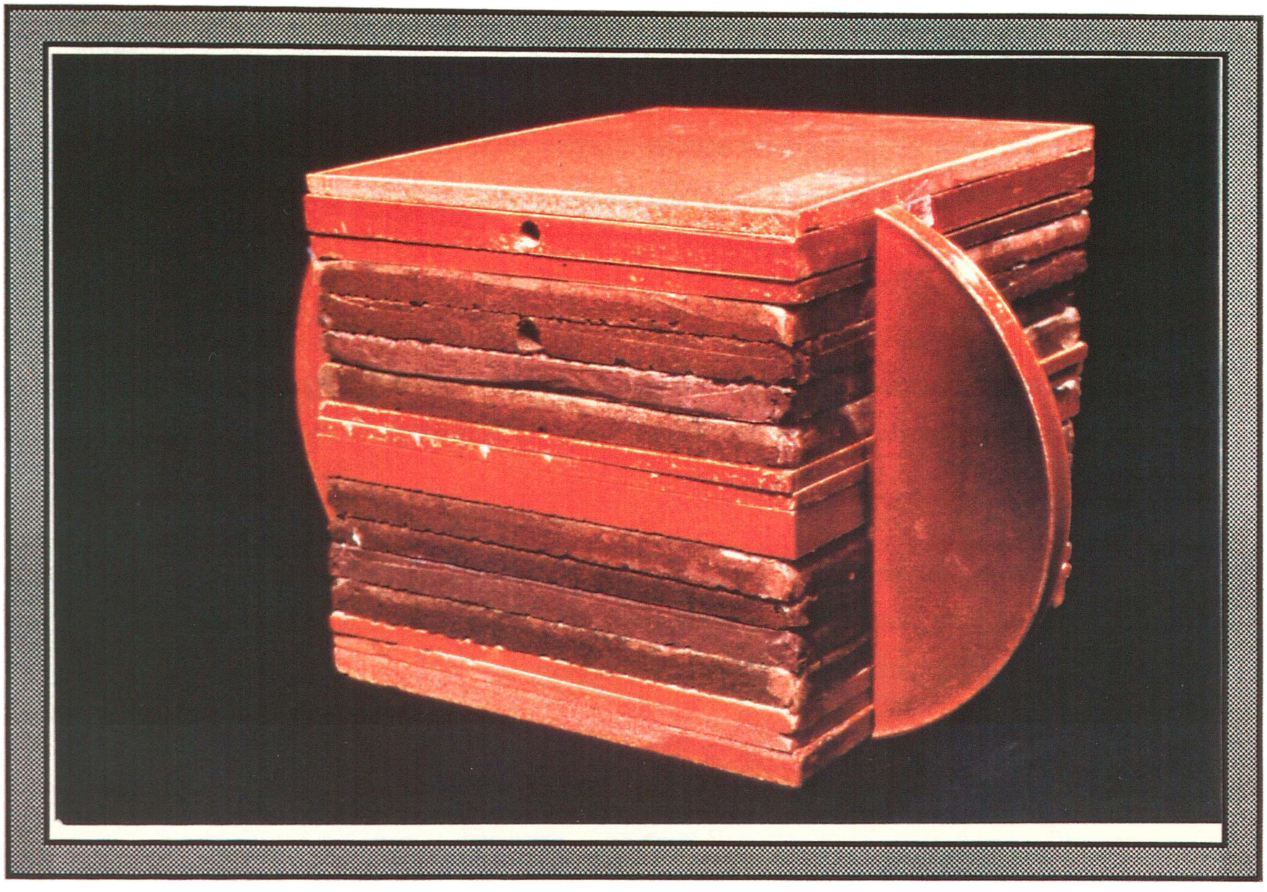

Figure 2.11: Photograph of the two lung analog slab *phantom B* consisting of muscle and lung analog slabs and muscle wings which reduce artifacts when the phantom is CT scanned. The phantom is generally used under the radiotherapy beam without the wings. It is also useful to be able to CT scan the phantom as some commercial correction methods will only work when CT data is input (eg. The Theraplan E-TAR method outlined in chapter 3). Because the wings give the phantom a more body like shape they help prevent CT artifacts when CT scans of the phantom are required.

2.4.6 The Relationship Between CT Number and Electron Cross Section

In order to understand the calculations used in this quality assurance exercise, a theoretical way of calculating the expected CT numbers is presented below. The relationship defined by Hounsfield (1973) between CT number N_{CT}, and linear attenuation coefficient μ, is

$$N_{CT} = \frac{1000(\mu_s - \mu_w)}{\mu_w} \quad , \qquad (2.3)$$

where μ_s is the linear attenuation coefficient for a substance at a specific energy and μ_w is the linear attenuation coefficient of water at this energy.

The product of electron density ρ_e (electrons cm^{-3}), and total electron cross section σ_e (cm^2/electron), is equal to μ (McCullough 1975, Geise and McCullough 1977):

$$\mu = \rho_e \sigma_e \quad , \tag{2.4}$$

where σ_e is the sum of component electron cross sections due to Rayleigh scattering σ_R, photoelectric absorption σ_τ, Compton scattering σ_c, and pair production σ_κ, such that

$$\sigma_e = \sigma_R + \sigma_\tau + \sigma_c + \sigma_\kappa \quad . \tag{2.5}$$

The pair production term can be neglected as at diagnostic CT energies of less than 100 keV there is no such contribution (since 1.022 MeV is required) but it is included here for completeness.

Now let ρ_{es} and ρ_{ew} be the electron density of a substance and of water respectively. Also defining σ_{es} and σ_{ew} as the total electron cross sections of a substance and of water respectively, then substituting (2.4) into (2.3) gives

$$N_{CT} = \frac{1000(\rho_{es}\sigma_{es} - \rho_{ew}\sigma_{ew})}{\rho_{ew}\sigma_{ew}} \quad , \tag{2.6}$$

and this is equivalent to

$$\frac{\rho_{es}}{\rho_{ew}} = \frac{\sigma_{ew}}{\sigma_{es}}\left(\frac{N_{CT}}{1000} + 1\right) \quad . \tag{2.7}$$

The term ρ_{es}/ρ_{ew} is the electron density of a substance relative to that of water, commonly called the relative electron density ρ_e^w. The ratio σ_{ew}/σ_{es} has been defined by Battista and Bronskill (1981) as the ratio of electron cross sections R_σ:

$$R_\sigma = \frac{\sigma_{ew}}{\sigma_{es}} = \frac{(\sigma_R + \sigma_\tau + \sigma_c + \sigma_\kappa)_w}{(\sigma_R + \sigma_\tau + \sigma_c + \sigma_\kappa)_s} \quad . \tag{2.8}$$

Therefore (2.7) can be written as

$$\rho_e^w = R_\sigma\left(\frac{N_{CT}}{1000} + 1\right) \tag{2.9}$$

or

$$N_{CT} = \frac{1000}{R_\sigma}(\rho_e^w - R_\sigma) \quad . \tag{2.10}$$

To calculate R_σ using known elemental data, some terms first have to be defined.

For an ith element within a compound consisting of N components it can be seen from (2.4) that

$$\left(\frac{\mu}{\rho}\right)_i = \left(\frac{\rho_{es}\sigma_{es}}{\rho}\right)_i \quad , \tag{2.11}$$

and rearranging (2.11) gives

$$(\sigma_{es})_i = \left(\frac{\mu}{\rho}\right)_i \left(\frac{\rho}{\rho_{es}}\right)_i \tag{2.12}$$

Where ρ is the mass density and therefore ρ_{es}/ρ, is the number of electrons per gram otherwise known as the mass electron density N_g (McCullough 1975):

$$N_g = \left(\frac{\rho_{es}}{\rho}\right)_i = N_A\left(\frac{Z}{A}\right)_i \quad , \tag{2.13}$$

thus

$$\left(\frac{\rho}{\rho_{es}}\right)_i = \frac{1}{N_A}\left(\frac{A}{Z}\right)_i \quad . \tag{2.14}$$

Substituting (2.14) into (2.12) gives

$$(\sigma_{es})_i = \frac{1}{N_A}\left(\frac{\mu}{\rho}\right)_i \left(\frac{A}{Z}\right)_i \quad . \tag{2.15}$$

Defining $(\sigma_{es})_s^{eff}$ as the effective cross section for a substance of different elemental compositions of mass fraction f_i, then

$$(\sigma_{es})_s^{eff} = \sum_{i=1}^{N} f_i\,(\sigma_{es})_i \quad , \tag{2.16}$$

therefore from substituting (2.15) into (2.16):

$$(\sigma_{es})_s^{eff} = \left[\frac{1}{N_A} \sum_{i=1}^{N} f_i \left(\frac{\mu}{\rho}\right)_i \left(\frac{A}{Z}\right)_i \right]_s \qquad (2.17)$$

Remembering from (2.8) that R_σ is the ratio of cross sections, then

$$R_\sigma = \frac{(\sigma_{es})_w^{eff}}{(\sigma_{es})_s^{eff}} \quad , \qquad (2.18)$$

and substituting (2.17) into (2.18) gives

$$R_\sigma = \frac{\left[\sum_{i=1}^{N} f_i \left(\frac{\mu}{\rho}\right)_i \left(\frac{A}{Z}\right)_i \right]_w}{\left[\sum_{j=1}^{N} f_j \left(\frac{\mu}{\rho}\right)_j \left(\frac{A}{Z}\right)_j \right]_s} \quad . \qquad (2.19)$$

Data for the fractional elemental compositions f_i for analogs and human tissue is given in Table 2.5. Values of $(\mu/\rho)_i$ were estimated for bone and muscle analogs at 71 keV using data from Jackson and Hawkes (1981). Values of $(A/Z)_i$ were obtained from the periodic table for chemical elements. Values of R_σ calculated for body analogs and their equivalent human tissues using (2.19) are presented in Table 2.6.

Now that a method for calculating R_σ has been presented then the only unknown in (2.10) is ρ_e^w. Knowing ρ and the atomic composition then ρ_e^w has been calculated (Henson 1989):

$$\rho_e^w = \frac{N_A \rho}{\rho_{ew}} \left[\sum_{j=1}^{N} f_j \left(\frac{Z}{A}\right)_j \right]_s \quad , \qquad (2.20)$$

where N_A is 6.023×10^{23} mol^{-1} and ρ_{ew} is 3.33×10^{23} cm^{-3}, then

$$\rho_e^w = 1.81\, \rho \left[\sum_{j=1}^{N} f_j \left(\frac{Z}{A}\right)_j \right]_s \qquad (2.21)$$

The values of ρ_e^w for the body analogs and their equivalent human tissues are presented in Table 2.6. Another quantity of interest in assessing the radiation properties of analogs is the effective atomic number. This is assessed by using an adaptation of the methods developed by McCullough and others (McCullough 1975, McCullough and Holmes 1985, Geise and McCullough 1977) as follows.

The effective atomic number can be derived from (McCullough and Holmes 1985):

$$Z_{eff} = \left(\sum_{i=1}^{q} \alpha_i (Z_i)^a \right)^{\frac{1}{a}} , \qquad (2.22)$$

where the exponent a accounts for photoelectric effects at CT energies. The value of a = 2.94 is used in the calculations to conform with other publications (McCullough and Holmes 1985). The coefficient α_i in (2.22) can be calculated by (McCullough and Holmes 1985):

$$\alpha_i = \frac{n_i Z_i}{\sum_{j=1}^{q} (n_j Z_j)} . \qquad (2.23)$$

The quantity n_i is the relative number of the ith element in the substance (ie. the empirical formula). But to use (2.22) directly from values of constituent fraction by mass f_i then α_i needs to be determined in terms of f_i. The derivation is as follows.

Describing f_i in terms of n_i, then

$$f_i = \frac{n_i A_i}{\sum_{j=1}^{q} n_j A_j} \qquad (2.24)$$

and therefore

$$n_i = f_i \left(\sum_{j=1}^{q} n_j A_j \right) \frac{1}{A_i} . \qquad (2.25)$$

Substituting (2.25) into (2.23) then

$$\alpha_i = \frac{f_i\left(\sum_{j=1}^{q} n_j A_j\right)\frac{1}{A_i} Z_i}{\sum_{j=1}^{q}\left(f_j\left(\sum_{k=1}^{q} n_k A_k\right)\frac{1}{A_j}\right) Z_j} , \qquad (2.26)$$

but as

$$\sum_{j=1}^{q} n_j A_j = \sum_{k=1}^{q} n_k A_k , \qquad (2.27)$$

then (2.23) can be replaced by

$$\alpha_i = \frac{f_i\left(\frac{Z}{A}\right)_i}{\sum_{j=1}^{q} f_j\left(\frac{Z}{A}\right)_j} . \qquad (2.28)$$

Using (2.22) combined with (2.28) values of Z_{eff} have also been calculated for both analogs and human tissues as shown in Table 2.6.

Values of N_{CT} calculated using (2.10) are shown in Tables 2.7 for one nominal CT energy, 71 keV. The samples were also scanned and calculations were carried out at a nominal CT energy of 64 keV, similar data was obtained. In the interest of brevity the data collected at 64 keV is not reported here. Using the compositions of human bone, tissue and lung provided in the literature (White *et al* 1977, Woodard and White 1986), (2.10) has been used once again to calculate the N_{CT} values expected for human tissue. Comparison of analog CT numbers and human tissue CT numbers in the table serves to show that at these energies the CT numbers of the analogs very closely match the CT numbers of the tissues for which they are substitutes.

ANALOG/TISSUE	ELEMENT AND (% f_i)
bone analog	H(7.90), C(63.79), N(4.23), O(9.88), Cl(14.20)
human bone	H(8.67), C(13.00), N(3.6), O(66.40), S(0.46), P(2.43), Ca(4.96), (Na, Mg, K, Trace)
muscle analog	H(9.15), C(70.66), N(4.28), O(13.34), Cl(0.11), Ca(2.46)
human muscle	H(10.20), C(14.30), N(3.40), O(71.00), K(0.40),Na(0.10), (P, S, Cl, Trace)
lung analog	H(8.36), C(60.41), N(1.67), O(17.33), Cl(0.15), Si(0.72), Mg(11.36)
human lung	H(10.30), C(10.1), N(2.90), O(75.50), Na(0.20), P(0.20), S(0.30), Cl(0.30)

Table 2.5: The percentage by mass compositions (%f_i) for bone, muscle and lung analog and human tissue respectively. These are the values used in (2.19), (2.21) and (2.22) to calculate the ratio of cross sections, relative electron density, and effective atomic number, respectively as presented in Table 2.6. Elemental compositions are based on data from White *et al* (1977, 1986) and Woodard and White (1986).

SAMPLE	ρ	ρ_e^w	R_σ (71 keV)	Z_{eff}	Z_{eff}^w
bone analog^{++}	1.16	1.14	0.9130	9.26	1.25
human bone	1.12	1.10	0.8982	9.32	1.26
muscle analog	1.03	1.02	0.9860	7.39	1.00
human muscle	1.05	1.04	0.9965	7.45	1.01
lung analog	0.30	0.28	0.9879	7.51	1.01
human lung	0.30	0.30^{+}	0.9963	7.59	1.02

Table 2.6: Mass density, relative electron density, ratio of cross sections and effective atomic numbers for body analogs and tissue. Values of mass density were obtained by weighing the samples. Using (2.19) and (2.21) values for the ratio of cross sections and relative electron density have been calculated for analogs and human tissue. The values of Z_{eff} have been calculated using (2.22) combined with (2.28) for analog and human tissue.

$^{+}$ Electron density based on patient survey by Van Dyk *et al* (1982).

$^{++}$ An example of how to calculate the values shown in row 1 for bone analog is provided in Appendix 1.

An example of how to calculate the values shown in row 1 of Table 2.6 for bone analog is provided in Appendix 1. This is also included for the convenience of readers who may wish to repeat the procedure with other analogs or *in vivo* human data. It is important to note that the composition of real inner bone outlined in Table 2.5 (row 2) is used for the calculation of N_{CT} in Table 2.7 (row 2). This data is based on the estimate of White *et al* (1977) that inner bone has an average composition of 22.4% hard bone and 77.6% red marrow.

To ensure the analog mix is close to the analog composition expected, samples of the analog are scanned using a Siemens DRH CT scanner and the results of the experimental CT numbers obtained are shown in column 3 of Table 2.7.

SAMPLE	N_{CT}^{THEORY}	$N_{CT}^{EXPERIMENT}$	ΔN_{CT}
bone analog	222++	229 (238)	7
human bone	224	236+	12
muscle analog	34	16	18
human muscle	44	30	1
lung analog	- 716	-720 (-718)	4
human lung	-699	-711+	12

(Units - Hounsfield units HU)

Table 2.7: CT numbers for analogs and human tissue have been calculated and measured. CT numbers were calculated using (2.19) and (2.10), (column 2). These are compared with CT numbers measured on a Siemens DRH CT scanner at a nominal energy of 71 keV (column 3). The numbers in brackets refer to commercial samples from RMI which were tested, and the CT numbers show good agreement with the samples produced in-house.

+ The human bone data and human lung data was obtained by sampling 5 patients whose bone and lung regions were CT scanned. The relative electron density was then calculated using (2.9). It is recognised that bone density and composition varies greatly depending on site and patient. However the pelvic region is a frequent site for Radiotherapy treatment so this was the bone area which was surveyed for the data presented in column 3.

++ An example calculation of theoretical CT number for bone analog is also provided in Appendix 1.

The ΔN_{CT} value in column 4 of Table 2.7 presents the differences in Hounsfield units between the calculated and measured N_{CT} numbers, where

$$\Delta N_{CT} = | N_{CT}^{THEORY} - N_{CT}^{EXPERIMENT} | \qquad (2.29)$$

If this ΔN_{CT} difference is divided by the usual range of Hounsfield numbers between air and bone from -1000 to +1000, then the difference in percentage terms can be estimated as

$$\%\Delta N_{CT} = \frac{\Delta N_{CT}}{2000} \times 100\% \ . \qquad (2.30)$$

When comparing the the analogs a worst difference of (ΔN_{CT} = 18HU) was obtained. This is a $\%\Delta N_{CT}$ of 0.9%. Therefore the experimentally determined N_{CT} values shown in column 3 of Table 2.7 measured on the CT scanner are very close to the theoretically predicted N_{CT} values. Hence if the compound composition is known and the nominal

energy of the CT beam is estimated, using the nominal keV liquid method of White and Speller (1980), then the expected value of N_{CT} can be calculated. This estimate of CT number agrees closely with the samples scanned, and therefore the analogs produced closely match the elemental compositions expected using the original composition data.

The same procedure has been used for real body tissues. The N_{CT} values for real tissues also match closely those for their respective analogs. Comparing the CT numbers in the rows in Table 2.7 also shows there is a close match between the CT numbers of the tissues and their matching analogs.

Shown in Figure 2.12 is the muscle and lung analog data along with the Hounsfield regression line. By examining Tables 2.1 and 2.6 it is apparent that Z_{eff} for both these substances is similar to water (Z_{eff} = 7.4). As atomic cross section depends on Z_{eff} (McCullough 1975, Mitchell and Johnson 1989) then these substances present a similar atomic cross section to the scanner and hence the absorption properties are similar. Because the Hounsfield line characterises those substances with water like properties in terms of effective atomic number this means the CT number of these analogs is very close to the Hounsfield line.

The solid bone analog data point is shown in Figure 2.13 along with the regression lines for K_2HPO_4 liquid bone analog and the in vivo Compton scan data (as previously presented in Figure 2.5). The solid bone analog point is slightly below the K_2HPO_4 line. This is because the liquid analog data has a slightly higher effective atomic number than the solid analog of the same electron density (see data in Tables 2.1 and 2.6 for these analogs).

Also shown in Figure 2.13 is the Hounsfield regression line. Note all the bone analog data is above the Hounsfield line. This is because the bone analogs have a higher Z_{eff} than water and hence their cross section is greater. This leads to a higher CT number per electron density than with water like substances. Because the cross section affects the linear attenuation coefficient (see 2.4) then for a given electron density the linear attenuation coefficient of bone is higher than that of water-type substances. Because CT number is proportional to linear attenuation coefficient (see (2.3)), the CT number is greater also.

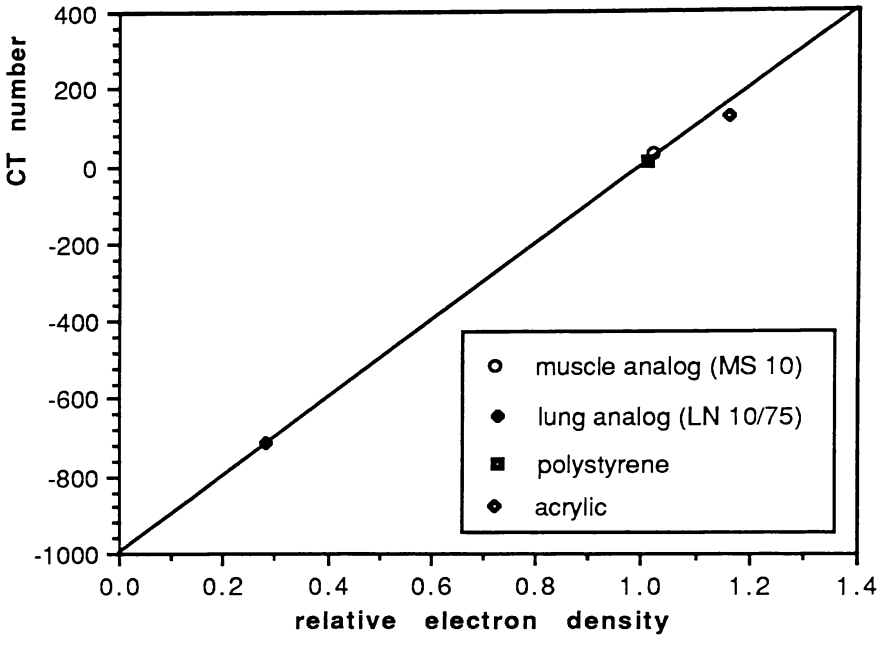

Figure 2.12: The CT number versus relative electron density for in-house manufactured body analogs compared with some other substances. The CT numbers were measured on a Siemens DRH CT scanner at 71 keV. The continuous line is the Hounsfield line. Included also for interest are some commercially available materials commonly used as radiotherapy dosimetry phantoms. The polystyrene has a very slightly lower electron density than muscle analog whereas acrylic has a higher electron density.

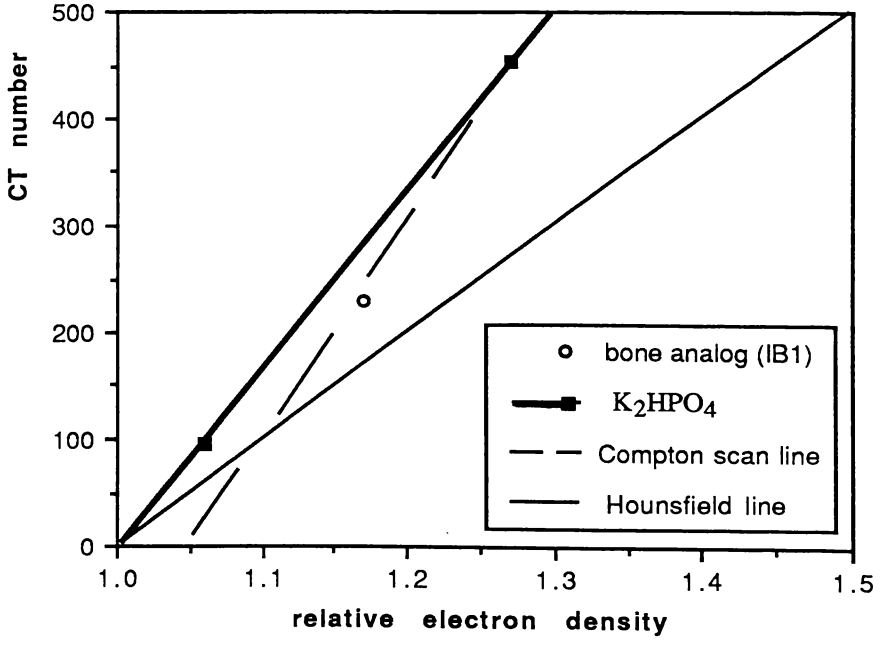

Figure 2.13: The CT number versus relative electron density for the in-house manufacured bone analog compared with the liquid bone analog (K_2HPO_4) scanned at 71 keV. Also shown is the in vivo Compton scan line published by Battista and Bronskill (1981). The Hounsfield line is also shown for interest as the gradient of this line is much less than that of the bone and bone analog lines.

2.5 MODES OF X-RAY DETECTION

2.5.1 Ionization Chambers

The SI unit of absorbed dose D is the Gray (Gy), (ICRU#19 1971):

$$1\ [\mathrm{Gy}] = 1\ [\mathrm{Jkg}^{-1}]\ . \tag{2.31}$$

Instead of measuring absorbed dose directly, the proportional relationship between charge induced in air by ionizing radiation, and absorbed dose is utilised. The charge collection instrument is called an ionization chamber. The principle of operation is the collection of all the charges created by direct ionization within a gas (usually air) through the application of an electric field. The drift of the positive and negative charges represented by the ions and electrons constitutes an electric current. If a given volume of gas is undergoing steady state irradiation, the rate of formation of ion pairs is constant. For a small test volume of gas, this rate of formation will be exactly balanced by the rate at which ion pairs are lost from the volume either by recombination, diffusion or migration from the volume. Under the conditions that recombination is negligible and all the charges are efficiently collected the steady state current which is produced is an accurate measure of the rate at which the ion pairs are formed within the volume.

Exposure X is measured in terms of charge (Coulombs) per unit mass of air (kg), such that

$$X = \frac{dQ}{dm}\ . \tag{2.32}$$

It is fortunate that the amount of energy required to induce one ionization in air is constant over a wide range of electron energies (ICRU#31 1979, ICRU#33 1980). It is approximately equal to 33.7 eV per ion pair produced, which relates to 33.7 Joules per Coulomb (JC^{-1}).

Thimble type ionization chambers are the most frequently used dosimeters in medical radiation physics at present. This is because of their ease of use combined with a wealth of information about their properties. These chambers are of cylindrical geometry. The outer shell of the cylinder is operated at ground potential and a central conducting rod conducts the applied voltage, or vise versa. In this case a field that varies inversely with radius is created in the air space between the electrodes.

The most common form of chamber used in radiation dosimetry is the "Baldwin Farmer-type" chamber. The Baldwin Farmer-type chamber used here for measurements in inhomogeneities such as cork and lung analog phantoms is a Nuclear Enterprises-type 2571. This has a 0.6 ml thimble volume, an aluminium central electrode and a graphite outer electrode. A PTW+ chamber used for water depth dose measurements is also of the thimble type. This has a flexible rubber waterproof cover and a small 0.1 ml thimble volume.

Parallel plate chambers with thin front entrance windows are suitable for measurements in build up regions but are less ideal for in water measurements as the shape of these devices tends to perturb the water medium during dynamic depth dose and profile collections. Measurements in inhomogeneous slabs are also difficult as often these chambers are mounted on substantial slabs of material (such as acrylic), whereas ideally the chamber should be housed in a slab of similar material to that of the rest of the phantom. Maucari and Kase (1987) have got around this problem by mounting chambers in suitable lung analog slabs.

2.5.2 Ionization Chamber Measurements in Low Density Media

The most accurate estimate of absorbed dose from ionization chamber charge measurements is obtained by using one of the currently adopted dosimetry protocols. In Australasia the currently accepted protocol is the IAEA protocol (IAEA 1987, NRL 1989) which is very similar to a previous protocol which is still the USA standard. The document is known as TG 21 (AAPM Topic Group TG 21 1983). With the aid of these protocols one is able to predict absorbed dose to a homogeneous water medium D_{med}, to an accuracy of 2%. A complete review by Rogers and Ross (1988) points out the minor influences such as humidity effects, and other assumptions which lead to this 2% error margin. The absorbed dose conversion from charge as described by TG 21 and other protocols includes the following chamber corrections:

$$D_{med} = M\, N_{gas} \left(\frac{\bar{L}}{\rho}\right)^{med}_{gas} P_{ion}\, P_{wall}\, P_{repl} \quad . \tag{2.33}$$

The term M is the electrometer reading corrected to standard temperature and pressure (STP) and N_{gas} is the cavity gas calibration factor as derived in TG 21 and allocated by the standardising laboratory to each specific chamber (further details of its derivation are not relevant here). $(\bar{L}/\rho)$ is the restricted stopping power as discussed earlier in chapter 1.

+ Chamber type and supplier - PTW Freiburg micro-ionization chamber, Gamma Sonics Inc.

The term P_{ion} corrects for ion recombination losses. In liquid filled ion chambers it is impossible to achieve saturation as outlined in articles by Wickman (1974a, 1974b) and Bydder *et al* (1988). However for air filled ionization chambers this process has been quantified in detail by Boag (1950, 1952a, 1952b). For air filled ionization chambers ion saturation is achieved provided a bias voltage of above about 200 volts is applied.

The term P_{wall} defined in (2.33) takes account of the differences in wall to phantom composition and is equal to

$$P_{wall} = \frac{[\,\alpha\,(\bar{L}/\rho)^{wall}_{air}\,(\bar{\mu}_{en}/\rho)^{med}_{wall} + (1-\alpha)\,(\bar{L}/\rho)^{air}_{med}\,]}{(\bar{L}/\rho)^{med}_{air}}\ , \qquad (2.34)$$

where $\bar{L}/\rho$ is the ratio of mean restricted mass stopping powers and μ_{en}/ρ is the average mass energy absorption coefficient. The term α is the fraction of ionizations in the detector cavity caused by electrons from the chamber wall and $(1 - \alpha)$ is the fraction of ionizations in the cavity caused by electrons from the surrounding medium.

The term P_{repl} is the replacement correction which accounts for dose gradient and chamber air cavity effects. The term P_{repl} is actually due to two effects. These are the gradient correction P_{grad} due to the air cavity, and P_{flue} which accounts for disturbances in electron fluence caused by the replacement of the phantom material by the detection device:

$$P_{repl} = P_{grad}\,P_{flue}\ . \qquad (2.35)$$

P_{grad} is negligible for Baldwin Farmer probes in photon beams (AAPM Topic Group TG 21 1983). The term P_{flue} can have a small effect when measurements in low density media in disequilibrium situations are undertaken (Rice *et al* 1988). Hence this parameter is discussed in some detail in the following analysis.

Percentage depth dose %D, is the ratio, expressed as a percentage of absorbed dose at depth d to maximum dose in the medium D_{max}, at the depth d_{max}, (see also (3.1)). To ascertain the %D values in chapters 3 and 4 of this thesis the ratio expressed as a percentage of electrometer meter readings M (units Coulombs) at d to that at d_{max}, is actually recorded. The following analysis validates this simplification.

Specifying the maximum dose in a homogeneous medium as $D_{med,hom,max}$, and denoting the dose at depth d of measurement in a heterogeneous phantom as $D_{med,het}$. Then

$$\%D = \frac{D_{med,het}}{D_{med,hom,max}} \times 100\% \quad , \tag{2.36}$$

therefore the %D at a point employing (2.33) is

$$\%D = \frac{M_{med,het}\, N_{gas}\, (\bar{L}/\rho)_{gas}^{med,het}\, P_{ion}\, P_{wall,het}\, P_{grad,het}\, P_{flue,het}}{M_{med,hom,max}\, N_{gas}\, (\bar{L}/\rho)_{gas}^{med,hom}\, P_{ion}\, P_{wall,hom}\, P_{grad,hom}\, P_{flue,hom}} \quad . \tag{2.37}$$

This relationship can be significantly simplified when the following information is considered.

The terms N_{gas} and P_{ion} in the numerator and denominator of (2.37) are equal for homogeneous and heterogeneous media and therefore cancel each other out. This is because these factors are chamber dependent and do not depend on the phantom material. Provided the elemental composition of the low density media and high density media are similar then the L/ρ terms are equivalent and they cancel also. As discussed earlier in sections 2.3 and 2.4, this is the case.

The number of electrons produced by the detector wall is negligible and is also likely to be independent of material density (AAPM TG 21 1983, Mauceri and Kase 1987, Rice *et al* 1988) hence the P_{wall} terms are likely to be identical and they cancel also. The P_{grad} effect is also negligible for photon beams (according to TG 21 $P_{grad} = 0.99$ for a Baldwin Farmer thimble chamber).

This leaves the P_{flue} ratios. The ratio $P_{flue,het}/P_{flue,hom}$ accounts for differences in electron fluence in a chamber in a heterogeneous medium versus a homogeneous medium. Appendix 2 deals with detailed estimates of the P_{flue} ratio. According to the calculations in Appendix 2 the greatest variation of P_{flue} from unity in low density 0.2 cork is 2% ($P_{flue,het}/P_{flue,hom} = 0.98$) and in 0.3 lung analog the variation from unity is 1% ($P_{flue,het}/P_{flue,hom} = 0.99$).

This author considers the magnitude of $P_{flue,het}/P_{flue,hom}$ will vary depending on the position within the slab geometry because the contribution to the lung dose is due to interactions in the overlaying tissue as well as lung (Hoban *et al* 1990a, Figure 5). Hence the effective field radius will change depending on lung position. Therefore it is wise to consider the ratio to be approximately unity in heterogeneous and homogeneous situations. Then one is left with the following simplification of (2.37), that is

$$\%D = \frac{M_{med,het}}{M_{med,hom,max}} \times 100\% \quad . \qquad (2.38)$$

This is the relationship used to calculate %D presented in the graphs in chapters 3 and 4. This method is consistent with previous publications in the literature (eg. Cunningham 1982, Kornelson and Young 1982, Mackie *et al* 1985b, Metcalfe and Beckham 1988, Rice *et al* 1989).

Monte Carlo simulations carried out in chapter 4 also show good agreement with the experimental %D measurements. The mean in-lung differences between the experimental measurements obtained using (2.38) and Monte Carlo simulations are only 1.6% in the 0.3 density lung analog material (see section 4.7 and Figure 4.21 for details). These results further confirm the accuracy of using (2.38) to assess %D in the inhomogeneous phantoms in regions of electronic disequilibrium.

2.5.3 Semiconductor Detectors

In radiation detector applications requiring extremely good spatial resolution the semi-conductor detector has advantages because the solid medium of the junction is approximately 1000 times more dense than that of a gaseous medium. This means the detector volume can be extremely small and sufficient ion pairs are still produced for an adequate electric current to flow.

For radiation applications the diode is usually used in photovoltaic mode. In this mode the junction electrodes are left open and no external bias is applied. The diode biases itself in the forward direction so that if no radiation is applied the net current is zero and an open circuit voltage is developed.

The electric field which exists in a semi-conductor junction causes any electrons which are created in or near the junction to be swept towards the n-type material and any holes are swept toward the p-type material. The region is then called a depletion region because the number of electrons and holes is decreased. Hence any electron-hole pairs which are created in this region by ionizing radiation are swept from the region by an electric field and their motion causes a current to flow. The current is monitored by an electrometer.

The diode depletion region contains silicon which has a high atomic number (Z = 14) compared to air (Z = 7.55). This causes an enhanced response to photoelectric beam

components but fortunately the effect is only significant at low energies where the diode over-responds to the photoelectric beam component, eg. Caesium-137, 662 keV (Metcalfe 1988). Special backscatter filtered designs are now available to help reduce the effect (Rikner 1983, Rikner *et al* 1985, Grussell and Rikner 1984). Although higher energy beams do have low energy components these are not significant enough to effect the diodes depth dose response in the range of energies predominantly discussed in this thesis, that is 1.25 MeV to 15 MV. The depth dose curves collected under beams within this energy range using a semiconductor detector (a Therados p-type diode detector of sensitive volume 2.5 x 2.5 x 0.1mm) were almost identical to those collected using ionization chambers.

2.5.4 Thermoluminescent Dosimeters

The advantage of Thermoluminescent dosimeters (TLDs) is that they have no wire connections, and as such can be easily placed at sites in patients or phantoms which are not accessible by ionization chambers and diodes which require connections to an electrometer.

In TLD materials X-ray energy is absorbed and energetic secondary electrons excite atomic electrons to move from the filled band to the conduction band. A proportion of these excited electrons fall back to energy levels called traps where they are held, the amount of electrons which fall into traps being proportional to the amount of incident radiation. When the material is heated (to typically 400 degrees Celsius) these electrons acquire enough thermal energy to escape back into the conduction band where they fall back into holes in the filled band, while giving off energy in the form of visible photons. This light emission is proportional to the amount of initial radiation and can be accurately monitored by a photomultiplier. Hence the term "thermo" as in heat is applied and "luminescent" as in light is emitted.

Radiation dose is ascertained by comparing the response associated with an unknown absorbed dose to the response of TLD material from the same batch which is given a known absorbed dose, termed a calibration dose.

A so called "background" correction is usually required. This usually shows in the form of the pure annealed powder needing a background subtraction of between 0.3 and 0.5 mGy. This may be due to a surface friction phenomenon called triboluminescence (Cameron *et al* 1968) or perhaps incomplete emptying of all the electron traps during the annealing process.

For absorbed dose experiments a variety of TLD material configurations are available such as disks, chips and powder (eg. lithium fluoride (LiF) powder with a crystal diameter

between 0.05-0.2mm). Powder is the most convenient form provided a constant sample volume can be dispensed as then only one calibration is required for the whole batch of powder. In contrast the chips and disks have to be individually calibrated then re-annealed, re-irradiated and read (the assumption of no change in sensitivity between anneals is invoked). Also, sufficient powder can often be loaded at a site to ensure that several readings can be obtained and the average of these readings can be used for better statistical accuracy (15 mg per anneal sample, 75 mg per sample capsule, hence 5 samples per capsule). In contrast chips and disks provide only one readout per sample.

There are several alternative compounds available as T.L.D. materials, such as calcium sulphate (very sensitive but a high atomic number) and lithium borate (low atomic number but very hygroscopic). However, lithium fluoride (TLD 100) has many attractive features including an atomic number ($Z = 8$), which is very close to water ($Z = 7.4$). This gives it dose response linearity over a wide energy range (above approximately 100 keV). It also displays total dose linearity of response from 0.05 to 10 Gy independent of dose rate (Cameron *et al* 1968). The phosphor is not light sensitive (unlike sodium chloride) and the long half life of its high temperature traps (0.5, 7 and 80 years) ensure that fading is insignificant. Provided the powder is kept more than 24 hours to remove any low energy traps (which have half lives of 5 minutes and 10 hours) then readings over several weeks after this time will provide identical results (Metcalfe 1982).

The following details relate to the specific system used at Waikato Hospital. A batch of TLD material is placed in a container and all the electrons are emptied from the traps by a process referred to as annealing. This consists of a high temperature (400 degrees Celsius for 1 hour) followed by a low temperature of (80 degrees for 16 hours) anneal.

The TLD reader (Pitmans instrument, Toledo TLD reader) is set up to deliver a pre-heat cycle to remove low energy traps and then the reading cycle begins. At this stage a photomultiplier measures the quantity of light emitted from the sample and converts this to an electric current which is integrated during the heat cycle and is digitally displayed on the unit.

2.5.5 Film Densitometry

For photon beams in water a large amount of off-axis data is accessible by driving detectors (ion chambers or semi-conductors) to any three dimensional position in a liquid medium. However, for low density media solid slab phantoms are employed simply because no low

density liquid medium is available (or indeed known to exist). Collection of central axis depth dose data and off-axis profiles by using ionization chambers is quite laborious, as after each discrete reading is taken the probe is re-positioned within the phantom and another reading is recorded. An alternative technique is to sandwich a radiation sensitive film between phantom material and expose this parallel or perpendicular to the beam central axis.

The film (Kodak XTL-2) when developed shows a degree of film blackening known as the film optical density which is determined by the transmission of infra red light through the film.

For electron beams and indeed other photon beams (eg. Caesium-137) the optical density depth curves do not exactly match the depth dose curves and sensitometric correction is invoked by applying a ratio correction between the depth dose curves found using another detector (such as an ionization chamber) to the depth density curves obtained using film. A possible reason for the phenomenon is reciprocity failure (Hine and Brownell 1956) due to the film response in high dose rate gradient regions.

The perturbation of the results by the high atomic number silver film emulsion has been shown to be insignificant (Klevenhagen 1981) due to the very thin layer of this material. In practice using unwrapped film (light sealed within the phantom) helps avoid electron tunnelling which can occur along any air bubbles which may lie between the film and the film wrap. A Therados film densitometer with 2 mm spot size and an infra red sensitive window was used for the film profile measurements reported in chapters 3 and 4.

2.5.6 Electrometers and Precision Control

The following equipment was available at Waikato Hospital for measuring dose distributions in a water tank and on X-ray film. Precision three dimensional position control ($\pm$ 0.1mm) is provided by a radiation field analyzer device (Therados radiation field analyzer RFA3). This has an on board electrometer which records relative dose levels for pulsed beams. This is achieved by having a difference circuit which compares the signals from two detectors (the field and reference detector).

An electrometer (Therados RDM2A) is also used with single detectors for charge collection measurements. All diodes and ion chambers previously mentioned can be interfaced to both these electrometer devices. The diodes are used in open circuit with these electrometers whereas a bias plate voltage of 200 or 400 volts is applied to the ionization chamber devices. Figures 2.14 and 2.15 show the main components of this combined water phantom, precision control and dose logging system.

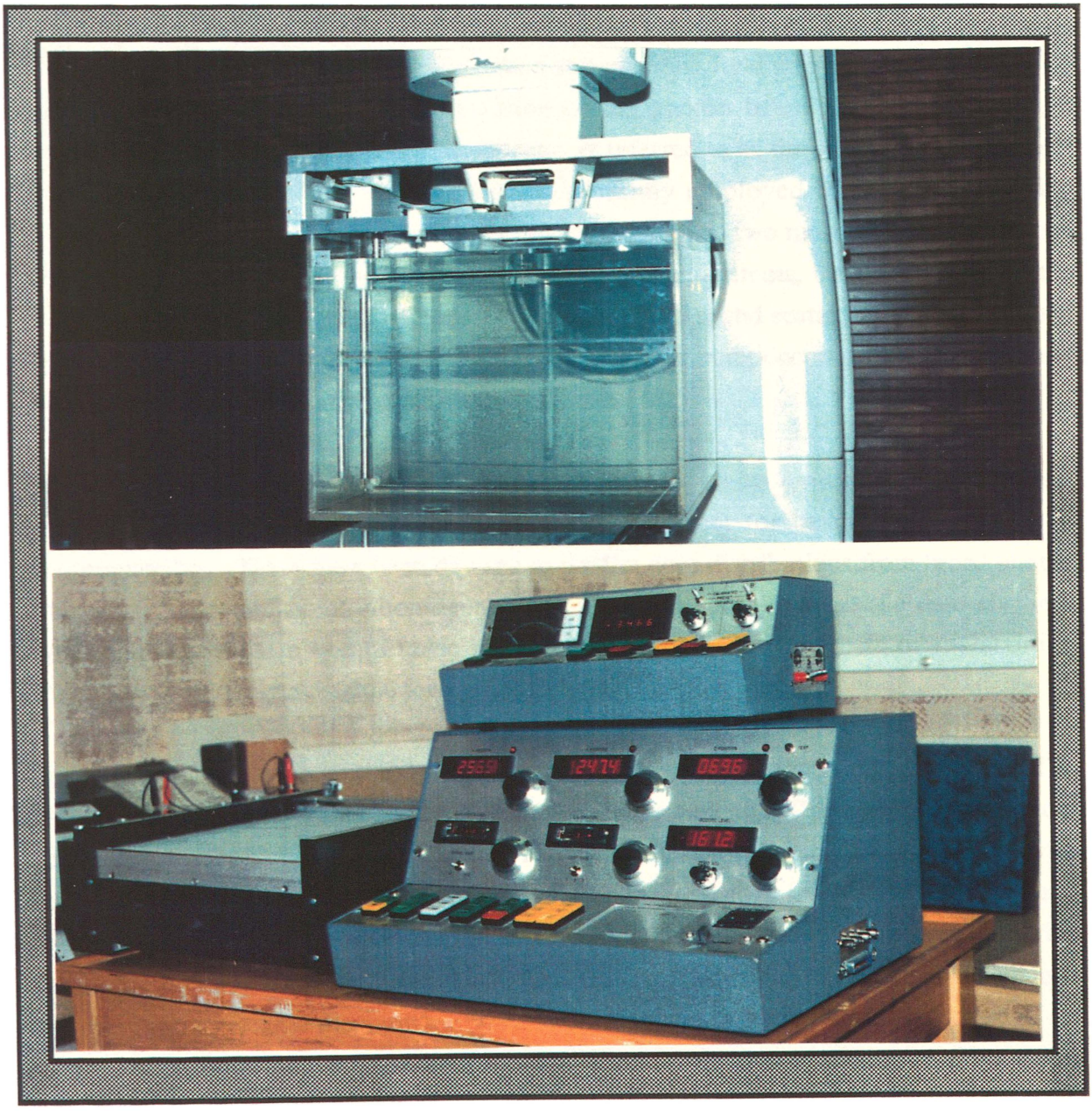

Figure 2.14: Top - photograph of the Therados RFA3 plotting tank placed under the Clinac 18 and filled with water.

Figure 2.15: Bottom - photograph of the Therados RFA3 electrometer and precision control system and the Therados RDM2A electrometer system (the smaller unit) used for absolute charge collection measurements. The RDM2A electrometer records charge measurements in the range between 10^{-12} and 2×10^{-7} Coulombs.

CHAPTER 3

PHOTON BEAM MODELS

3.1 INTRODUCTION

In this chapter some aspects of the more common semi-empirical methods used to calculate dose are considered. Beam conventions such as equivalent field size and field co-ordinates are defined in section 3.2. Representation of the photon beam by a primary photon component and a scattered photon component is referred to as the scatter function model (Meredith and Neary 1944). This model is currently employed in computer planning software as used by most commercial planning systems. The two most popular commercial planning systems in use today, the Target and Theraplan systems, both use a form of the scatter function model by employing tissue-air-ratios (TARs) and scatter-air-ratios (SARs) to represent the beam's primary and secondary photon scatter components. These concepts are defined and discussed in section 3.3.

Existing commercial radiotherapy computer planning systems employ so called "semi-empirical approximations" (Cunningham 1987) to correct for beam traversal through inhomogeneities. These have been devised to predict dose distributions from broad photon beams in and around body inhomogeneities of various complexities. To date all these algorithms represent a compromise of dose accuracy in the interests of maintaining reasonably short computing time for routine radiotherapy planning.

The accuracy of several semi-empirical methods were tested in two lung phantoms. The results are presented in this chapter. The equivalent pathlength (E-depth) methods show inaccuracy at all energies tested. Some TAR methods show reasonable agreement with dosimetry results at 1.25 MeV beam energy, but larger errors are observed in the lung phantom at higher photon energies (10 and 15 MV) as discussed in section 3.4. In this section the E-depth, Batho and equivalent-TAR (E-TAR) algorithm assumptions which lead to these errors are also discussed. The most important assumption is that there is no electron disequilibrium, and this leads to significant errors in dose prediction accuracy at high X-ray energies.

3.2 DEFINING BEAM CONVENTIONS

3.2.1 Field Co-ordinates

In this section the field co-ordinate conventions used in this thesis and by other researchers are discussed. A cartesian co-ordinate system is selected for this explanation, with (x, y, z) axis orientations shown in Figure 3.1. Source-surface distance (SSD) is represented by the symbol f, and depth in phantom is represented by z or d depending upon the original author's nomenclature.

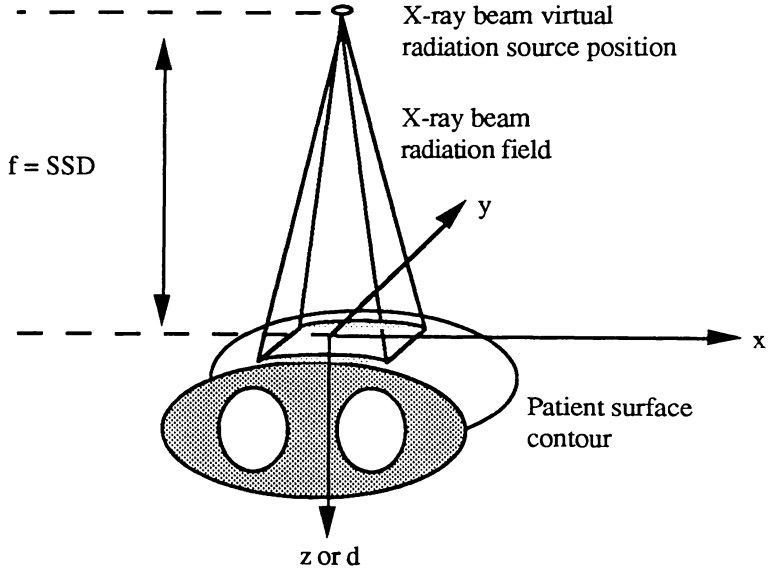

Figure 3.1: The co-ordinate framework used by various authors to define the X-ray beam position relative to the patient.

3.2.2 Equivalent Field Size

The equivalent field is defined as that standard field which has the same central-axis depth dose characteristics as a given non-standard field. The equivalent field method is based on the assumption that it is possible to associate the depth dose characteristics of any rectangular shaped field to that of an equivalent square or equivalent circle (Clarkson 1941, Jones 1949, Day 1950). Tables relating rectangular fields to equivalent square and equivalent circular fields are available (BJR Supp.17 1983).

In this text, field size will usually be referred to by using the parameter S, which represents the general parameter "field size". The conversion of this size parameter S to the side length s of an equivalent square or to an equivalent radius r is trivial using the afore mentioned tables.

3.2.3 Percentage Depth Dose

Absorbed dose D is the mean energy absorbed $d\bar{E}_{ab}$ in a medium per unit mass dm due to electron interactions (see (1.54)). The dose can be calculated from measured data by using the dosimetry protocols outlined in section 2.5 (AAPM TG 21 1983, IAEA 1987).

A reference dose is usually determined at the depth d_{max} of maximum dose on the beam central axis, where the dose is represented as $D(d_{max}, f, S)$ or D_{max}. The dose within the body is then considered for computer treatment planning calculations in terms of percentage dose %D, which is the ratio, expressed as a percentage, of the absorbed dose at a point to the dose at D_{max}. The relationship is functionally related to depth d in the medium, field size at the surface S and SSD f (see also Figure 3.2 for further explanation of percentage depth dose):

$$\%D(d, f, S) = \frac{D(d, f, S)}{D(d_{max}, f, S)} \times 100\% \quad . \tag{3.1}$$

Knowing the value of absorbed dose at a point, for example D_{max}, and percentage depth dose information, then the absorbed dose at any other central axis point can be calculated as

$$D(d, f, S) = \frac{\%D(d, f, S)}{100} D(d_{max}, f, S) \quad . \tag{3.2}$$

The central axis percentage dose is often plotted against depth as this indicates the penetration properties of the beam as shown in Figure 3.3. This type of curve is commonly referred to as a percentage depth dose curve.

3.2.4 Beam Profiles

When a detector is scanned at a depth d_{ref} along either the x or y axis, a beam profile is formed. These cross plot profiles are generally normalised to unity at the centre of the field, thus an off-axis ratio (OAR) for each off-axis distance x is obtained. Dose at any point on the profile can be calculated using the depth dose at central axis and the OAR. The dose at a point $D(d_{ref}, x, y, f, S)$ is given by

$$D(d_{ref}, x, y, f, S) = OAR(d_{ref}, x, y, f, S) \times \frac{\%D(d_{ref}, 0, 0, f, S)}{100} \times D(d_{max}, 0, 0, f, S) \quad . \qquad (3.3)$$

The profile consists of two distinct regions as indicated in Figure 3.4. The umbral region A is where the beam is unaffected by the collimators and the penumbral region B is where the beam is affected by the field defining collimators, the finite size of the source, and lateral electron disequilibrium.

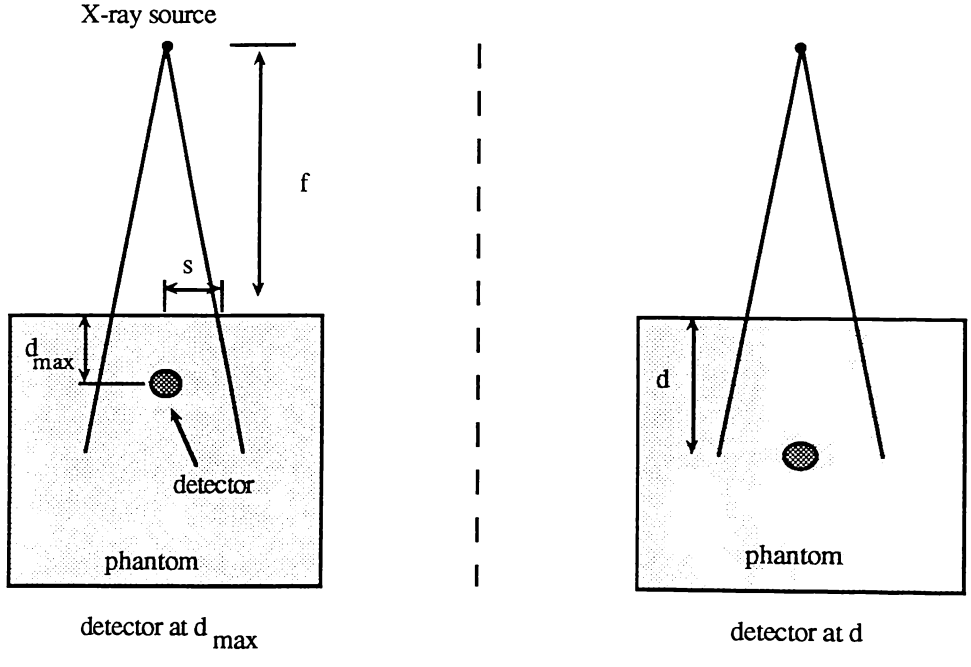

Figure 3.2: Schematic showing the definition of percentage depth dose. The SSD is constant but the source detector distance changes. Percentage depth dose varies depending on beam energy, SSD and phantom material. The phantom material is usually water, but it may also be a solid slab phantom of the type outlined in section 2.4.

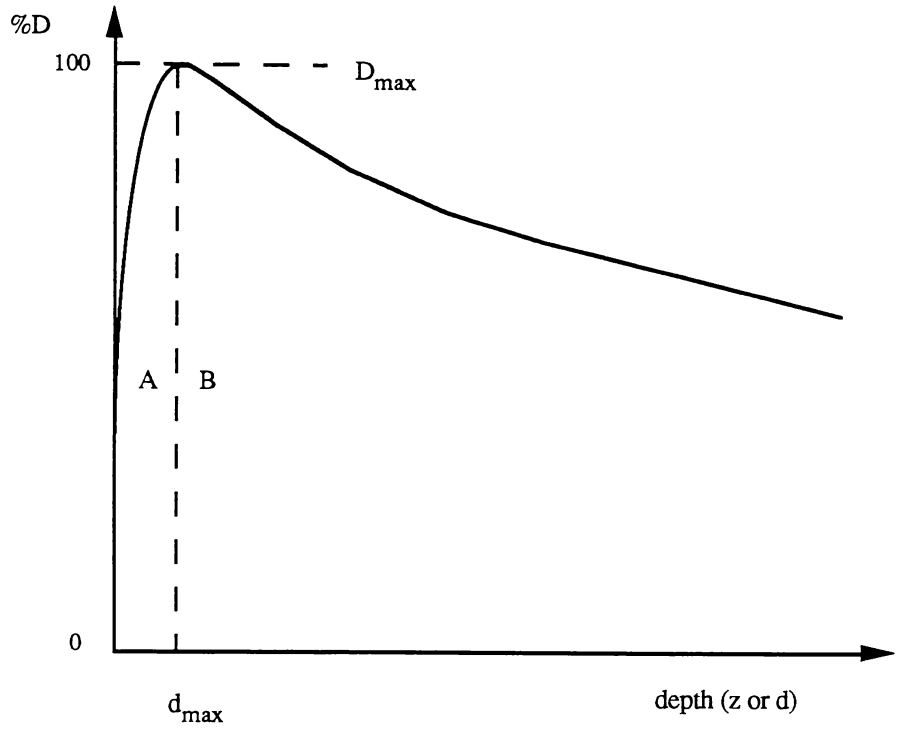

Figure 3.3: Percentage depth dose curve typical of a radiotherapy X-ray beam. A is the dose build up region and B is the dose fall off region.

3.2.5 Beam Isodose Curves

When points of equal dose are joined together, an isodose curve is produced. These curves are used for visualising dose distributions on patient contours. This is because the dose to many points in a patient need to be assessed and compared to the dose at a reference point (usually d_{max}). A series of isodose curves for a range of different doses, such as %D of 90, 70, 50, 30 and 10%, can be combined to form an isodose chart or isodose distribution. This form of display is convenient since the distribution gives a map of the dose contours in one plane of a radiation beam. Two isodose distributions are shown in Figures 3.5(a) and (b) for two X-ray beams of different energy. Figure 3.5(a) shows an isodose distribution for a 1.25 MeV Cobalt-60 beam (at 80 SSD). Figure 3.5(b) shows the distribution for a 10 MV X-ray beam produced by a linear accelerator (at 100 SSD). The deeper penetration of the 10 MV isodose curves compared to the 1.25 MeV curves is due to the higher photon energy and longer SSD of the 10 MV beam.

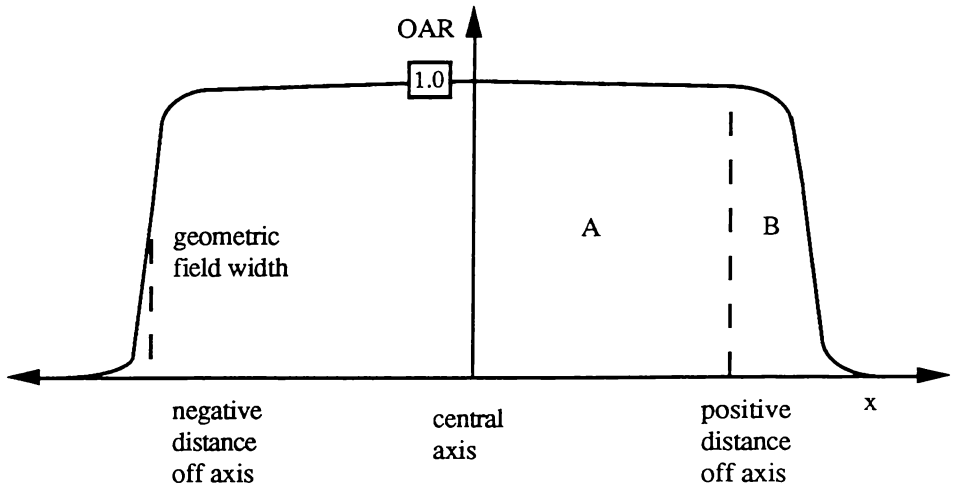

Figure 3.4: Profile of an X-ray beam taken by scanning across the x or y axis of the field, region A defines the umbral region and B is the penumbral region. The geometric field width usually coincides with the 0.5 level of the profile.

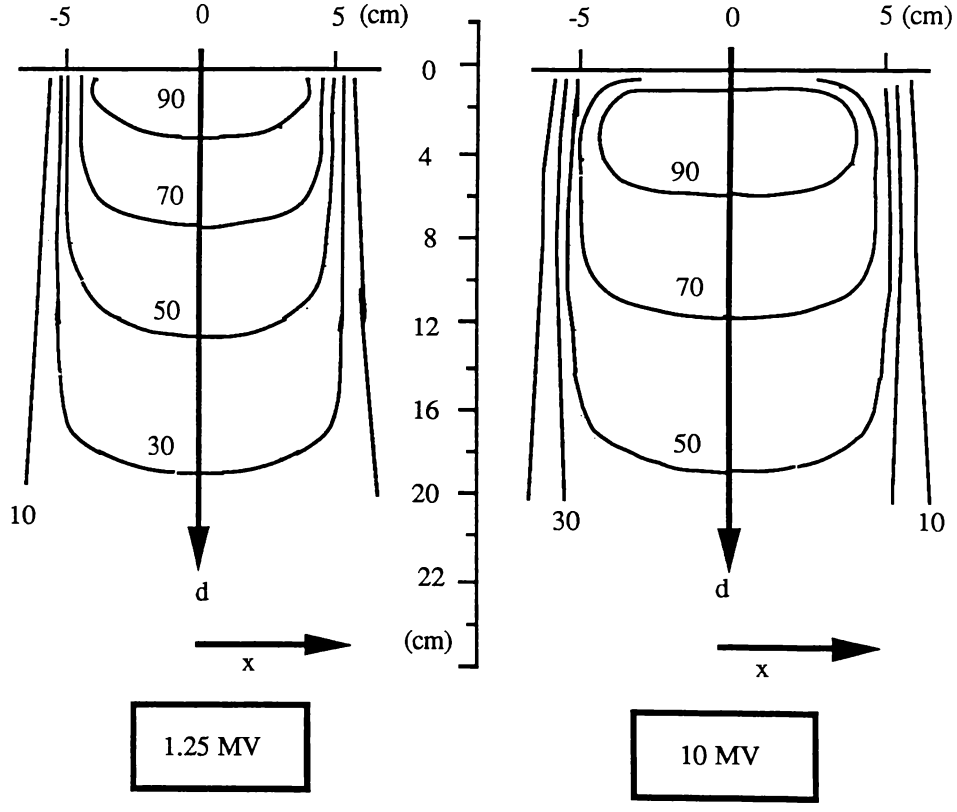

Figure 3.5: Isodose distributions for 1.25 MeV and 10 MV photon beams. The 90, 70, 50, 30, 10% isodose levels are shown

(a) Left - isodose distribution for a 1.25 MeV photon beam produced by a Cobalt-60 beam.

(b) Right - isodose distribution for a 10 MV photon beam produced by a linear accelerator.

3.3 SCATTER FUNCTIONS

3.3.1 Tissue-Air-Ratios and Scatter-Air-Ratios

To represent the scatter contributions at different depths, the concepts of tissue-air-ratio (TAR) and scatter-air-ratio (SAR) have been introduced (Johns and Cunningham 1983). These are just scatter functions expressed as ratios.

The tissue-air-ratio (TAR) is defined (ICRU#23 1973, ICRU#24 1976) as the ratio of absorbed dose at a given point in a phantom to the absorbed dose that would be measured at the same point in free air within a volume of phantom material which is just large enough to provide electron equilibrium at the point of measurement. Figure 3.6 is a schematic diagram of how the TARs are derived. In practice TARs are calculated by taking the ratio of ionization chamber readings in tissue and air (with appropriate build up caps added to the chamber). The TAR is defined as

$$TAR(d, S) = \frac{D\ (tissue, d, S)}{D\ (air, d, S)} \quad . \tag{3.4}$$

The scatter function model (Meredith and Neary 1944) divides dose into two components, the dose at a point due to primary photons D_{prim}(tissue, d, S), and the dose at a point due to scattered photons D_{scat}(tissue, d, S). The separation of scatter and primary components of dose is achieved by an approximation process whereby extrapolation of dose versus field size data back to a zero area is attempted (see Figure 3.7). Using the TAR framework representation of the scatter function model, then

$$TAR(d, S) = \frac{D_{prim}(tissue, d, S)}{D(air, d, S)} + \frac{D_{scat}(tissue, d, S)}{D(air, d, S)} \quad . \tag{3.5}$$

The first term on the right side of (3.5) defines the zero area tissue-air-ratio TAR(d, 0) and the second term defines the scatter-air-ratio SAR(d, S) for the field size S. The SAR at a given point in a medium is defined (BJR Supp. 17 1983) as the ratio of absorbed dose due to scattered photons at a point in tissue to the absorbed dose due to all photons in air. The increase in SAR with field size is due to an increase in scatter dose, and this is represented by the differential scatter-air-ratio (dSAR), which is the scatter dose component at a point due to scattering from a volume element remote from the point's position. Accurate experimental measurement of dSARs is difficult due to the small dose differences which need to be detected (Wong *et al* 1981). Therefore, analytical methods for estimating dSAR

have been developed Cunningham (1972, 1982), Wood (1981), Sontag (1979), and Wong and Henkelman (1982, 1983).

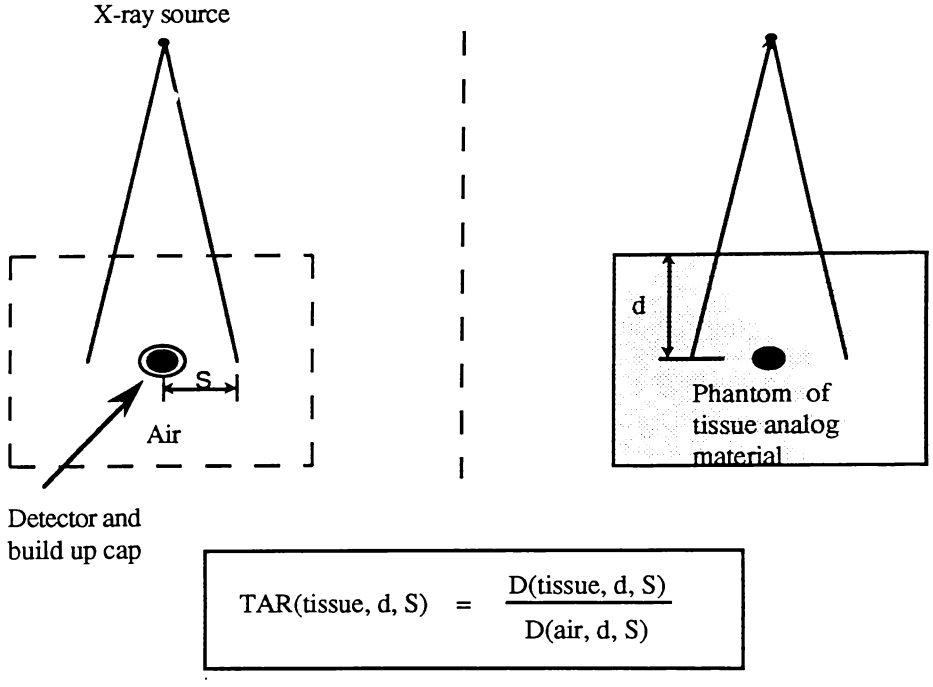

Figure 3.6: Schematic diagram which explains the definition of tissue-air-ratio (TAR). Dose readings are taken with an ionization chamber in air with a build up cap (left) and in a medium (right). The ratio of the tissue and air readings are then calculated to give the TAR.

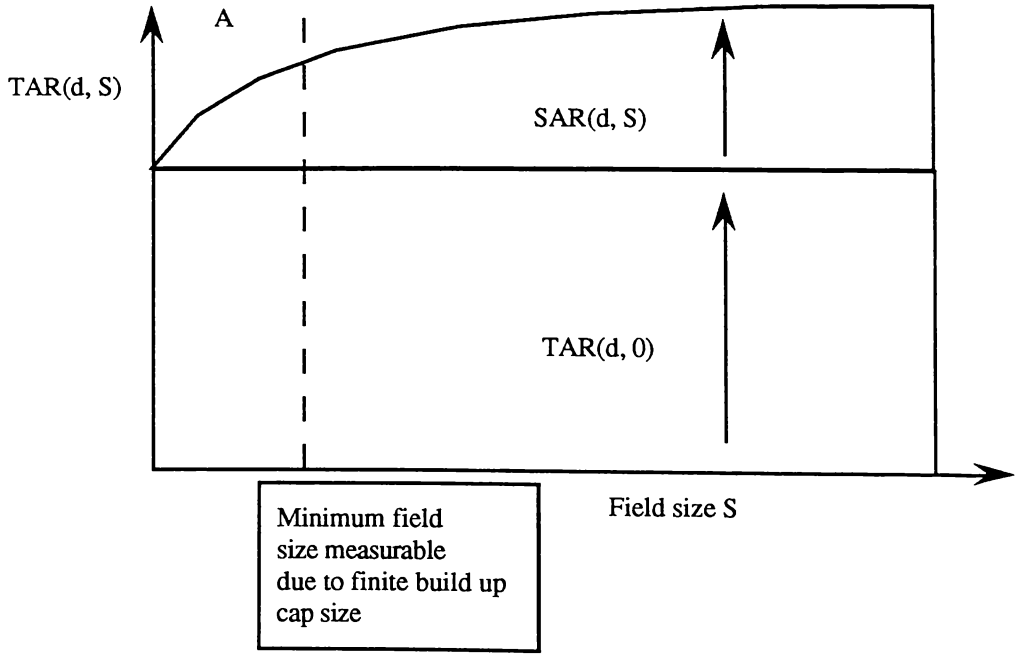

Figure 3.7: Graphical representation of how TARs and SARs are related with respect to field size. The TAR(d, S) is equal to the sum of the TAR(d, 0) and the SAR(d, S). Region A is where the field size is smaller than the diameter of the build up cap (eg. for a 10 MV beam this is about 5 x 5 cm) and extrapolation of TARs back to zero field area is required to get the TAR(d, 0).

Terms in (3.5) can be rewritten as

$$TAR(d, S) = TAR(d, 0) + SAR(d, S) \quad . \tag{3.6}$$

In practice SARs cannot be measured directly because the primary and scatter dose components cannot be separated. Rearranging (3.6) gives an expression for evaluating SARs provided the TAR(d, S) and TAR(d, 0) are known:

$$SAR(d, S) = TAR(d, S) - TAR(d, 0) \quad . \tag{3.7}$$

Figure 3.7 shows how TAR and SAR values are derived from graphs of scatter versus field size. In an attempt to define TAR(d, 0) the TAR values are normalised to unity for a zero field size, but at high photon energies an exact value of TAR(d, 0) is impossible to obtain, because a measurement of dose for a field size closely approaching zero is not possible. In this situation an extrapolation of data from measurements at finite field sizes back to a zero field size is required. In fact the smallest field size which can be measured for a 10 MV beam in water is about 5 cm because the build up region required for electron equilibrium is 2.1 cm and the diameter of the chamber is 6 mm.

The TAR values obtained by experimental measurements for a 10 MV photon beam are shown in Figure 3.8. These results were obtained by taking the ratio of dose readings in air with a build up cap to the dose in tissue simulated by a slab phantom (both made of muscle analog material as described in chapter 2). The graphed results demonstrate the difficulty of obtaining TAR(d, 0) at high photon energies when extrapolating back from a field size of 5 x 5 cm.

The TAR(d, 0) is supposed to represent the dose deposition from the beam which is due to primary photons only. This is clearly not accurately definable, as shown in Figure 3.8, for high energy beams in particular where extrapolation back to the zero area causes errors. It is impossible to verify the position of the TAR(d, 0) line since extrapolation cannot be avoided (Van Dyk 1977, Johns and Cunningham 1983). The extrapolation is done as though the curve carries on as it does for larger fields, where electronic equilibrium exists. However, readings are not taken at smaller field sizes because equilibrium does not exist. The radial build up factors shown in Appendix 2 (Figure A2.1) in fact show a much steeper drop off in dose to this region than is indicated by the extrapolation line shown in Figure 3.8.

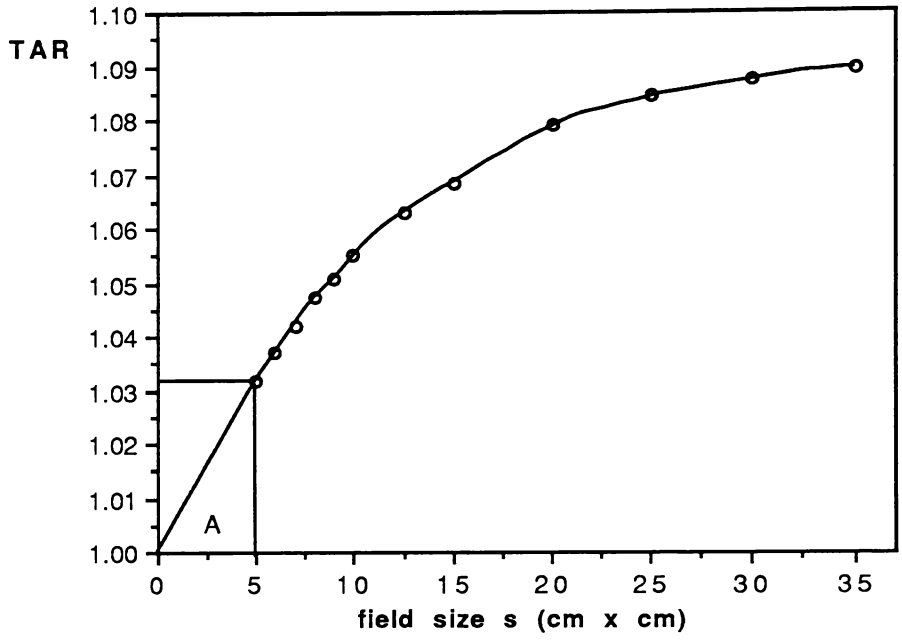

Figure 3.8: Tissue-air-ratios (TARs) obtained for a 10 MV photon beam. These were obtained by taking ionization chamber readings in a muscle analog build up cap and slabs which were produced by the process outlined in chapter 2. Because the minimum field size for measurement is about 5 x 5 cm then the line is extrapolated in Region A.

3.3.2 Tissue-Phantom-Ratios

The tissue-phantom-ratio (TPR) is defined as the ratio of absorbed dose at any given point to the absorbed dose at the same distance from the source, but with the surface of the phantom moved so that this point is at a specified reference depth d_{ref} (see Figure 3.9):

$$TPR(d, S) = \frac{D(tissue, d, S)}{D(tissue, d_{ref}, S)} \quad . \tag{3.8}$$

The tissue-maximum-ratio (TMR) is a special case of the TPR where the specified reference depth is at d_{max} (BJR Supp. 17 1983):

$$TMR(d, S) = \frac{D(tissue, d, S)}{D(tissue, d_{max}, S)} \quad . \tag{3.9}$$

The majority of radiotherapy treatment plans use a common point of origin within the patient. This form of planning is known as isocentric planning and the beams are referred to as isocentric beams. The TAR, TPR and TMR concepts are useful when planning with

isocentric beams as dose ratios at different depths are provided directly, and these quantities have been shown to be relatively independent of SSD (Johns *et al* 1958, Gupta and Cunningham 1966). The TAR does not however provide a solution to the problem of accurately separating scatter and primary photon components, and this separation is not even addressed in the definition of TPRs and TMRs.

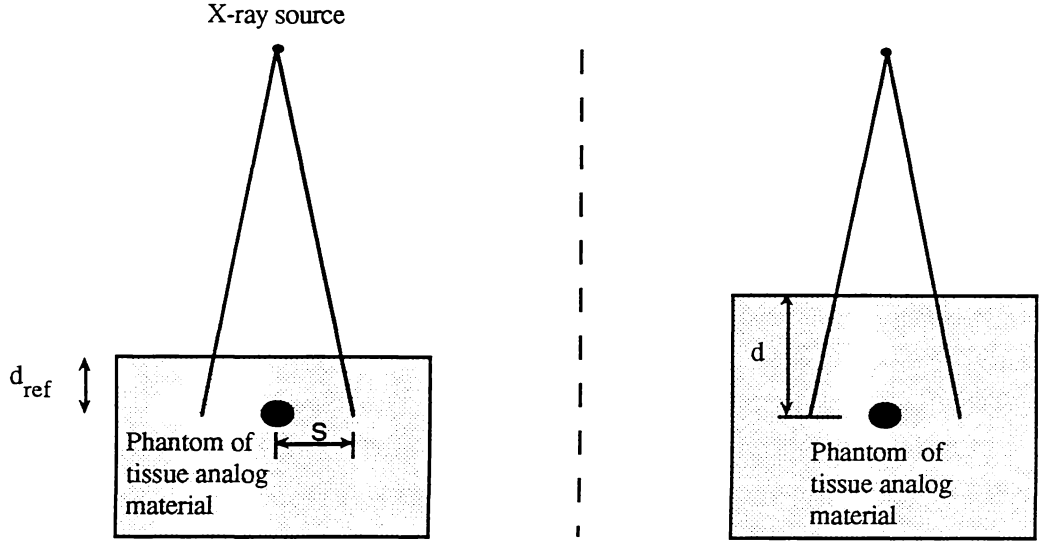

Figure 3.9: Definition of the TPR. The dose reading taken in a phantom at depth d is taken as a ratio to the reading taken in a phantom at a reference depth d_{ref}. The phantom consists of water or tissue analog.

One of the reasons that range scaling methods based on the scatter function models do not work well in small field low density situations (see section 3.4) is that the extrapolated part of the TAR curve is used. This is used because the effective field width calculated in low density regions is less than the width at which electron disequilibrium occurs. The problem only occurs for high energy beams when the lateral electron range exceeds the effective field half-width.

3.3.3 Off-Axis Ratios

The scatter function model used by the Theraplan treatment planning system to calculate dose to points off the beam central axis has been described by Cunningham (1987), Johns and Cunningham (1984) and Theraplan (1989). The dose to a point is defined as

$$D(\text{tissue}, d, x) = [\, D(\text{air}, d, 0) \times F(\text{air}, d, x) \times TAR(d, 0)] + SAR(d, S) \quad (3.10)$$

where D(tissue, d, x) is the dose to a point which is a distance x off axis in tissue, and the term F(air, d, x) is defined by Khan *et al* (1986) as the "off-axis ratio of the quasi-primary beam dose profile". This simply means that the TAR and SAR components are separated in the calculation of dose as shown in (3.10). The umbral region of the beam profile has been previously defined in section 3.2.4. To calculate the off-axis ratio in the umbral part of the profile (F_{umbral}) as shown in Figure 3.4, the assumption of radial symmetry is made and therefore by definition

$$F_{umbral}(\text{air}, d, x) = F_{umbral}(\text{air}, d, r) \quad . \quad (3.11)$$

This simplification means that any differences in the beam's transverse and radial profiles are not accounted for. In practice, however, differences in these profiles are very small. For the Theraplan system only primary beam profiles in the umbral region at four depths are stored. Results in the umbral region show good agreement with experiment at all depths, so the selection of four depths appears to be adequate to model umbral shape in homogeneous media.

3.3.4 Penumbral Forming Functions

In the rapidly changing beam penumbral region the Theraplan system uses an empirical fit to the rapidly changing profile shape. This is called a penumbral forming function. With reference to Figure 3.10 a fit can be produced in homogeneous phantoms by the following empirical equations:

$$F_{penumbra}(\text{air}, d_{ref}, x) = 1 - \frac{1}{2} e^{\left(\frac{-\alpha_1}{p}\right)\left(\frac{W_d}{2}\right) - |x|} \quad \text{for } |x| \le \frac{W_d}{2} \quad , \quad (3.12)$$

and

$$F_{penumbra}(\text{air}, d_{ref}, x) = t + \left(\frac{1}{2} - t\right) e^{\left(\frac{-\alpha_2}{p}\right)\left(|x| - \left(\frac{W_d}{2}\right)\right)} \quad \text{for } |x| \ge \frac{W_d}{2} \quad , \quad (3.13)$$

where $|x|$ is the absolute value of the off-axis distance x, $W_d/2$ is the half-width of the beam at depth d_{ref} and t is the collimator transmission factor. The distance p is the width of the penumbra predicted using geometrical assumptions only to calculate the beam divergence

from a finite source size s (ie. the distance from A to C in Figure 3.10). Denote f as the SSD and f_c as the source collimator distance. Then the geometrical penumbral width p is

$$p = \frac{s(f - f_c)}{f_c} \quad . \tag{3.14}$$

Note that α_1 and α_2 are the constants which determine the shape of the penumbra as shown in Figure 3.12. What is not pointed out in the original references and is shown in (3.12) and (3.13) is that only one reference depth, d_{ref}, is chosen to represent the penumbral shape at all depths. This leads to practical problems in obtaining a good penumbral match at all depths.

Another major problem with the empirical method is that electron ranging (a mechanism which contributes to the penumbral shape) also varies greatly in inhomogeneous situations. Hence the penumbra gets broader in low density inhomogeneous media. The penumbral forming function stays constant and this causes errors in the penumbral part of the field profiles, as discussed in the next section.

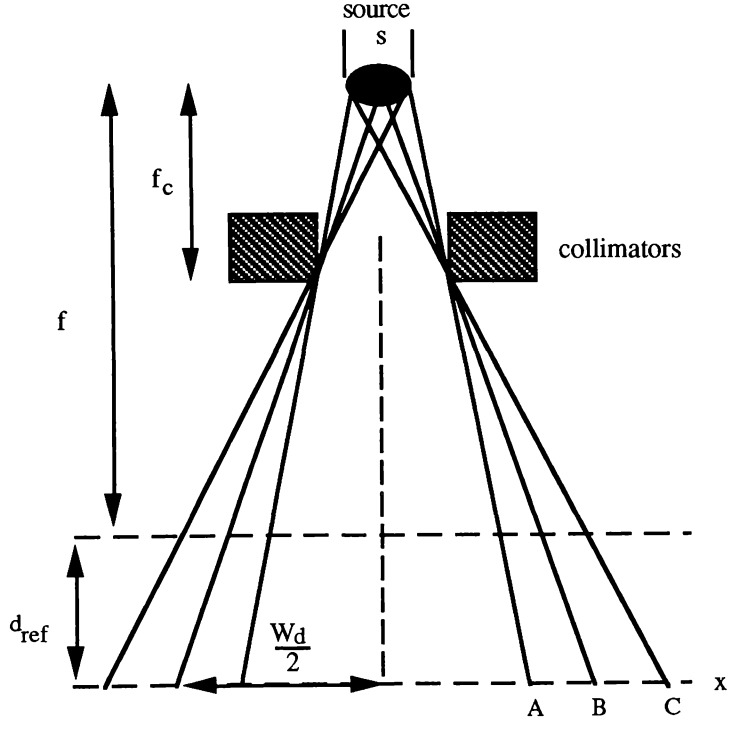

Figure 3.10 (a): Diagram showing the geometric effect on penumbra produced by finite source size and beam defining collimators. The positions A, B and C are referenced on the profile shown in Figure 3.10(b).

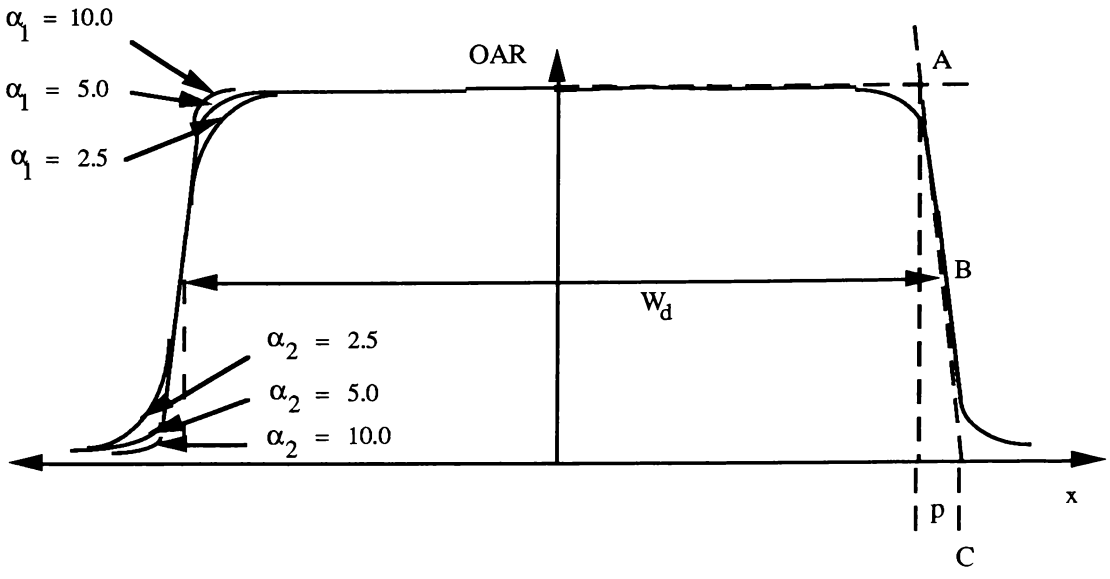

Figure 3.10 (b): Profile of an X-ray beam taken by scanning across the x axis of the field. The dashed line defined by ABC is the effect caused by finite source size and beam divergence. The rounded corners of the profile are caused by electron ranging. Empirical methods model the shape of these curves: The lower the values of α in (3.12) and (3.13) the more rounded the curves become. No attempt is made to alter the empirical forming function when a different density medium is traversed.

3.4 X-RAY INHOMOGENEITY CORRECTIONS IN LUNG

3.4.1 INTRODUCTION

In this section dosimetry results obtained using two different "two lung" phantoms are compared with dose computations produced by equivalent pathlength and scatter function (TAR) scaling methods. In each subsection the theory behind each correction method is presented and then the experimental accuracy of each method in one or both of the two lung phantoms is presented.

As mentioned previously, existing commercial radiotherapy computer planning systems employ so called "semi-empirical approximations" (Cunningham 1987). To date all these algorithms represent a compromise to dose accuracy in the interests of maintaining the reasonably short computing time required for routine radiotherapy planning.

Of the semi-empirical methods tested in the two lung phantom geometry, the equivalent pathlength methods show inaccuracy at all energies tested. Some TAR methods show reasonable agreement with dosimetry results at 1.25 MeV beam energy, but significant differences (as high as 16.4 %) were observed in one of the lung phantoms at a higher photon energy (15 MV). The Batho and equivalent-TAR (E-TAR) algorithm assumptions which lead to these errors are discussed. The most important assumption is that there is no

electron disequilibrium, and this leads to significant errors in dose prediction accuracy at high X-ray energies.

3.4.2 EXPERIMENTAL METHODS

This section quantifies errors in dose computation which occur in lung by comparing dose computations with dosimetry results in two "two-lung" models shown in Figures 2.6 and 2.13. The dimensions of both phantoms are the same, and these are based on geometric sizes derived from a patient lung sample carried out by Van Dyk (1983). This arrangement approximates the situation of a therapy beam laterally traversing the chest wall and lungs in the patient thorax region.

The density of the materials used in the phantom have been accurately measured using gravitometric and CT techniques to minimise the uncertainty in dose caused by inaccurate density assessment. Detail of the density analysis is included in sections 2.3 and 2.4. The main difference in the two phantoms is that the lung density of phantom A is 0.2, where as the lung density of phantom B is 0.3.

Effective depth (E-depth), Batho (TPR), Batho (dSAR), and equivalent-TAR (E-TAR) scaling correction methods were used on several different computers running different software implementations at Hospital and University institutes. Details of computers used are outlined in Table 3.1. Comparisons between experimental data and data produced using the algorithms were made for three X-ray energies on three different X-ray machines (1.25 MeV Theratron 80, 10 MV Varian Clinac 18, and 15 MV Siemens Mevatron). Measurements were made along the beam central axis (depth dose) and across the beam central axis (profiles). Dosimetry was performed by placing an ionization chamber at various positions in the two lung sandwich phantoms, which were constructed from cork/polystyrene (phantom A) and lung/muscle analog (phantom B) respectively.

Correction method (reference)	Beam energies (MeV) / (MV)	Computer hardware	Computer software (reference)	Lung phantom
E-depth (Milan and Bentley 1974)	1.25, 10	DEC PDP 11/34	Edinburgh Algorithms (Redpath 1977)	A
Batho (TPR) (El-Khatib and Battista 1984)	15	DEC VAX 780	Alberta Treatment Plan (Battista *et al* 1984)	A
E-TAR (Yakiwczuk 1987)	15	DEC VAX 780	Alberta Treatment Plan (Battista *et al* 1984)	A
Batho (dSAR) (Wong and Henkelman 1983)	1.25, 10	DEC PDP 11/73	Theratronics Theraplan (Theraplan 1990)	A, B
E-TAR (Sontag 1979)	1.25, 10	DEC PDP 11/73	Theratronics Theraplan (Theraplan 1990)	A, B

Table 3.1: Summary of inhomogeneity correction methods, computer software/hardware and phantom types used in appraisal of dose accuracy within lung phantoms in this section.

Ionization measurements were performed at two participating institutions: the Cross Cancer Institute (CCI) and the Waikato Hospital Radiotherapy Centre (WHRC). The 1.25 MeV and 10 MV data were obtained at the WHRC, with a Baldwin Farmer type (Nuclear Enterprises, 0.6 ml, 2571 graphite) ionization chamber, in cork with a relative electron density of 0.2 and in lung analog (LN 10/75) with a relative electron density of 0.3. The 15 MV readings were recorded using a Baldwin farmer type (Capintec, PR-06, 0.65ml) ionization chamber. All "in-lung" measurements were recorded without a build up cap, in order to avoid inducing a false electronic equilibrium.

Depth dose readings using ionization chambers were obtained by placing the chamber in a layer of material, then taking a charge reading. The charge reading was then normalised to the charge reading at d_{max}, then the chamber was "stepped" through the phantom by placing it in each respective layer and repeating the process.

Profile results using the ionization chamber were obtained by placing the lung phantom on a trolley which was placed in the Therados RFA3 plotting tank as shown in Figure 3.11. The chamber and phantom were scanned across the beam and ionization readings were recorded at discrete off-axis locations. Precise location of the chamber with respect to the beam was maintained using the Therados controls. Considering the analysis in section 2.5.2 and Appendix 2 the ionization chamber data points reported on the graphs in chapters 3 and 4 are accurate to within 2% for the two lung phantom tests.

Because of the order in which experiments were carried out it was not possible to test all energies and all correction methods with both phantoms. For example the Batho (TPR) method was not tested at 10 MV because the beam energies available at the CCI were 1.25 MeV and 15 MV. Also, these tests were carried out prior to the lung/muscle analog phantom construction. Comparisons of other correction methods at the 1.25 MeV beam energy are likewise only presented for the cork/polystyrene phantom because the cobalt-60 machine was de-commissioned at WHRC prior to the lung/muscle analog phantom construction. The lung/muscle analog phantom was however tested for all algorithms except Batho (TPR) at the beam energy of 10 MV.

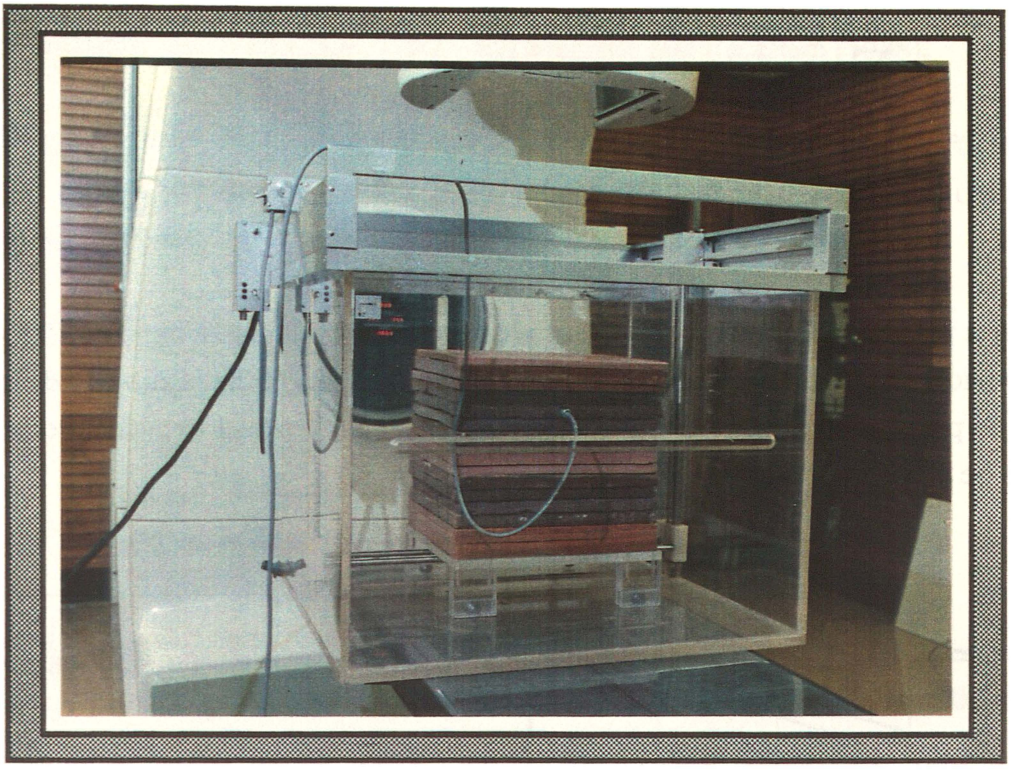

Figure 3.11: Photograph of the trolley which was used in the Therados plotting tank to obtain profile data. The ionization chamber is placed in the phantom and the phantom is placed on the trolley. The chamber and phantom are then scanned across the beam on the trolley using the Therados motor controls.

3.4.3 EQUIVALENT PATHLENGTH METHODS

3.4.3.1 Ray Tracing

Using standard ray tracing the radiological beam depth $\bar{d}'$ is the geometric depth scaled by the average relative electron density $\bar{\rho}$ lying along a beam ray where the geometric path length is d, such that

$$\bar{d}' = d\,\bar{\rho} \quad . \tag{3.15}$$

If $\bar{\rho}$ is considered to be the mean pathlength then for N voxels along the ray path as shown in Figure 3.12, ρ is defined as

$$\bar{\rho} = \frac{1}{N}\sum_{i=1}^{N}\rho_i \quad . \tag{3.16}$$

It is also possible to give a preferential weighting factor to some voxels, such that

$$\bar{\rho}' = \frac{\sum_{i=1}^{N} f_i \rho_i}{\sum_{i=1}^{N} f_i} , \qquad (3.17)$$

where f_i is the weighting factor. For example Mackie (1985) and Hoban *et al* (1990a) use this approach to add extra weighting to the interaction voxel in the scaling of dose spread arrays. In practice the ray trace is usually from the centre of voxel 1 to the centre of voxel i. This can be accounted for by a method shown in Figure 3.12.

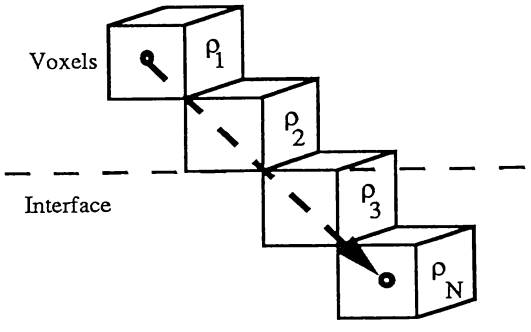

The equation for a ray trace through a discrete number of voxels of density ρ_i and each given a weight f_i, is given by

$$\bar{\rho}' = \frac{\sum_{i=1}^{N} f_i \rho_i}{\sum_{i=1}^{N} f_i} ,$$

where normally $f_i = 0.5$ for i = 1 and i = N because there is only traversal of half the first and last voxel, and $f_i = 1.0$ for all the other voxels. However any f_i can be modified to give the voxel extra weight. In particular $f_i > 0.5$ when i = 1.

In practice the ray trace is usually from the centre of voxel 1 to the centre of voxel i. If we add for example the ability to weight the first voxel with a function f_i then

$$\bar{\rho}' = \frac{0.5 f_1 \rho_1 + \left[\sum_{i=2}^{N-1} \rho_i \right] + 0.5 \rho_N}{0.5 + (N-2) + 0.5} .$$

Figure 3.12: Explanation of ray tracing whereby the radiological path is found by calculating the mean weighted density between voxels.

3.4.3.2 Effective Depth Correction

This method represents one of the first attempts to correct for photon beam interactions with inhomogeneous media. Details of the method are outlined elsewhere; Milan and Bentley

(1973), Redpath (1977), Metcalfe (1982), and Metcalfe and Beckham (1988).

Correction methods are compared in terms of inhomogeneity correction factors (CF), which relate the dose in an inhomogeneous medium D_i to the dose in an all water homogeneous medium D_h, such that

$$D_i = D_h(d', r) \tag{3.18}$$

and

$$CF = \frac{D_i}{D_h} \quad \text{or} \quad D_i = (CF) \times D_h \tag{3.19}$$

This approach is a convenient way of adjusting doses in a homogeneous medium (which are precalculated by the multiplicative correction factor CF) to give an estimate of the degree of perturbation due to interaction with the inhomogeneous media. In the E-depth correction method CF is a simple ratio of dose at the radiological depth d' as calculated using (3.15) to dose at the the geometrical depth d in water. Also included is an inverse square correction to account for the point of calculation change in d' relative to d. The expression is

$$CF = \frac{D_h(\bar{d}', r)}{D_h(d, r)} \left(\frac{f + \bar{d}'}{f + d} \right)^2 \tag{3.20}$$

In this method only the attenuation of the primary photon beam is scaled correctly. The result is a consistent overprediction of lung dose because this method only scales depth dose data and does not attempt to correct for secondary interactions. For example, there is a lack of back scatter in the lung medium and there is no attempt to correct for this.

Figures 3.13 -3.38 show percentage depth dose and profile curves for correction methods compared with those obtained using experimental measurements. Included in each caption of the figures are quantified differences between experimental data and the correction method. For assessing the mean percentage difference (MPD) between simulation and experimental depth dose curves the following equation is used:

$$MPD = \frac{\sum_{n=1}^{N} \left[\left(\left| \frac{\%D_S - \%D_E}{\%D_E} \right| \right) \times 100\% \right]}{N}, \tag{3.21}$$

where $\%D_S$ is the percentage depth dose calculated by the simulation and $\%D_E$ is the experimentally measured percentage depth dose. N is the number of sample points beyond d_{max}. This avoids any mismatch in the build up region which may be due to electron contamination. This difference is more relevant to the comparisons in chapter 4 where contamination free data is available in the build up region.

For assessing the mean percentage difference between simulation and experimental depth dose measurements within the lung regions (MPDL), then (3.21) is modified whereby only sample points within lung are used in the equation:

$$MPDL = \frac{\sum_{n=1}^{N_L}\left[\left(\left|\frac{\%D_{SL} - \%D_{EL}}{\%D_{EL}}\right|\right) x\ 100\%\right]}{N_L} , \qquad (3.22)$$

where N_L is the number of sample points within the lung regions. $\%D_{SL}$ is the percentage depth dose due to the simulation within the lung regions and $\%D_{EL}$ is the percentage depth dose due to experiment within the lung regions.

The maximum percentage difference (MAXPD) between simulation and experimental depth dose measurements is defined as

$$MAXPD = MAX\left(\left|\frac{\%D_S - \%D_E}{\%D_E}\right| x\ 100\%\right) , \qquad (3.23)$$

where MAX refers to the maximum difference found among the sets of data.

Figures 3.13 and 3.14 show comparisons of experimental depth dose versus E-depth prediction for 5 x 5 cm and 10 x 10 cm fields at 1.25 MeV. Figures 3.15 and 3.16 represent the comparison of a 10 MV beam of size 5 x 5 cm and 10 x 10 cm respectively. Note comparison of depth dose curves in Figures 3.14 and 3.16 show the 1.25 MeV beam is in more error than the 10 MV beam for the 10 x 10 cm field size. This is because the larger backscatter component in the lower energy beam is not being accounted for by this method of correction. However, at the smaller 5 x 5 cm field size the results at 10 MV as shown in Figure 3.15 are in greater error than those for the 1.25 MeV beam (Figure 3.13). Hence the trend has been reversed, due to another phenomenon called lateral electron disequilibrium (as described in section 1.5) which manifests itself for high energy beams in low density media.

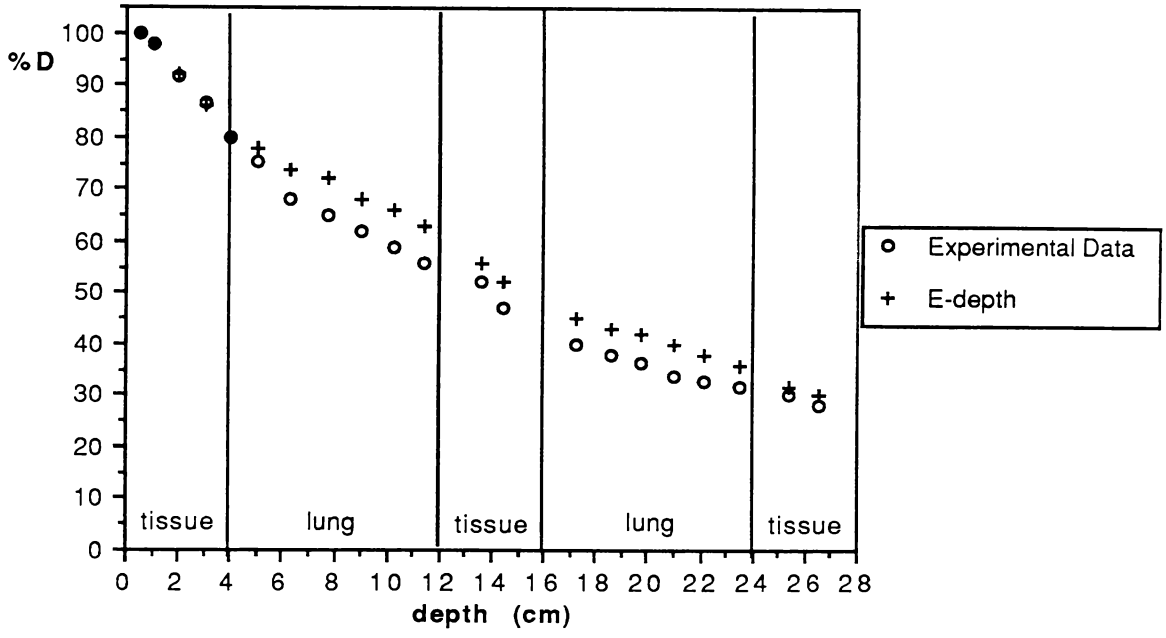

Figure 3.13: Depth dose plots of E-depth correction and experimental measurements:
Beam energy 1.25 MeV, field size 5 x 5 cm, phantom A.
Mean difference 8.4%, mean lung difference 11.9%, maximum difference 17.6%.

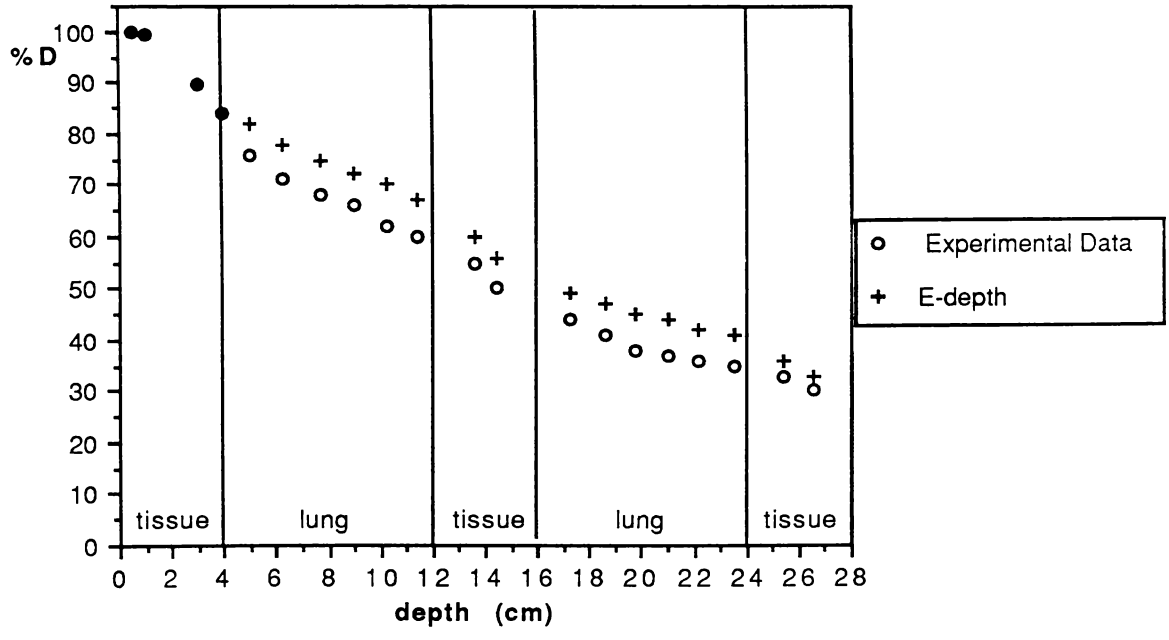

Figure 3.14: Depth dose plots of E-depth correction and experimental measurements:
Beam energy 1.25 MeV, field size 10 x 10cm, phantom A.
Mean difference 11.1%, mean lung difference 13.2%, maximum difference 18.9%.

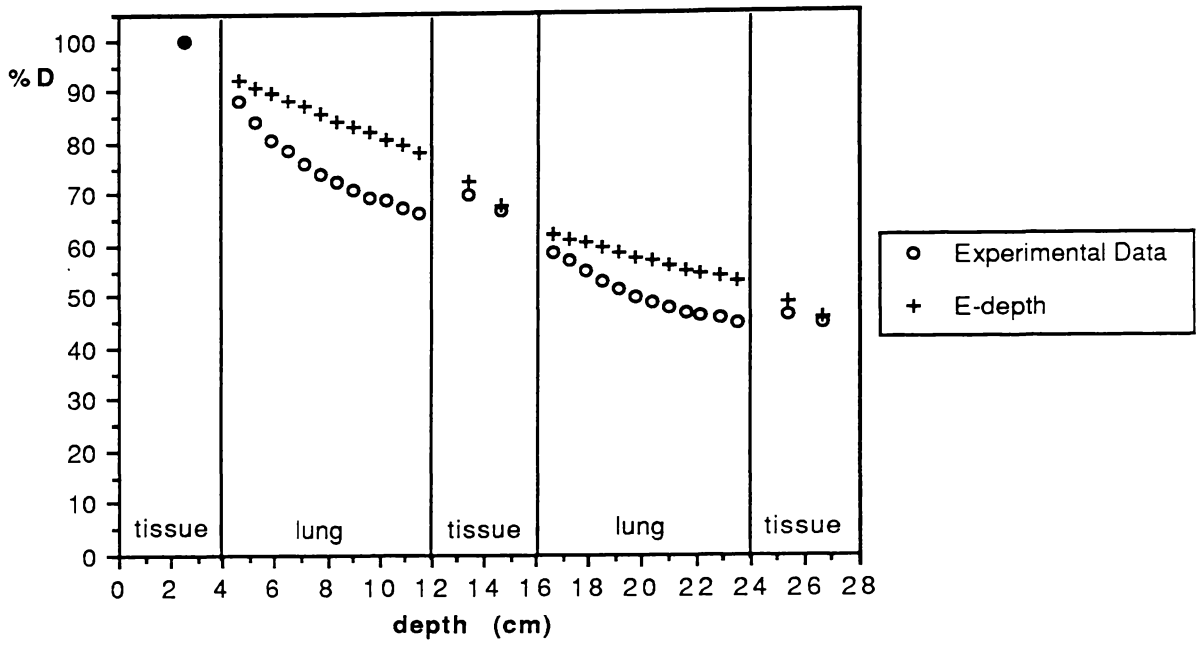

Figure 3.15: Depth dose plots of E-depth correction and experimental measurements:
Beam energy 10 MV, field size 5 x 5 cm, phantom A.
Mean difference 12.2%, mean lung difference 14.3%, maximum difference 18.4%.

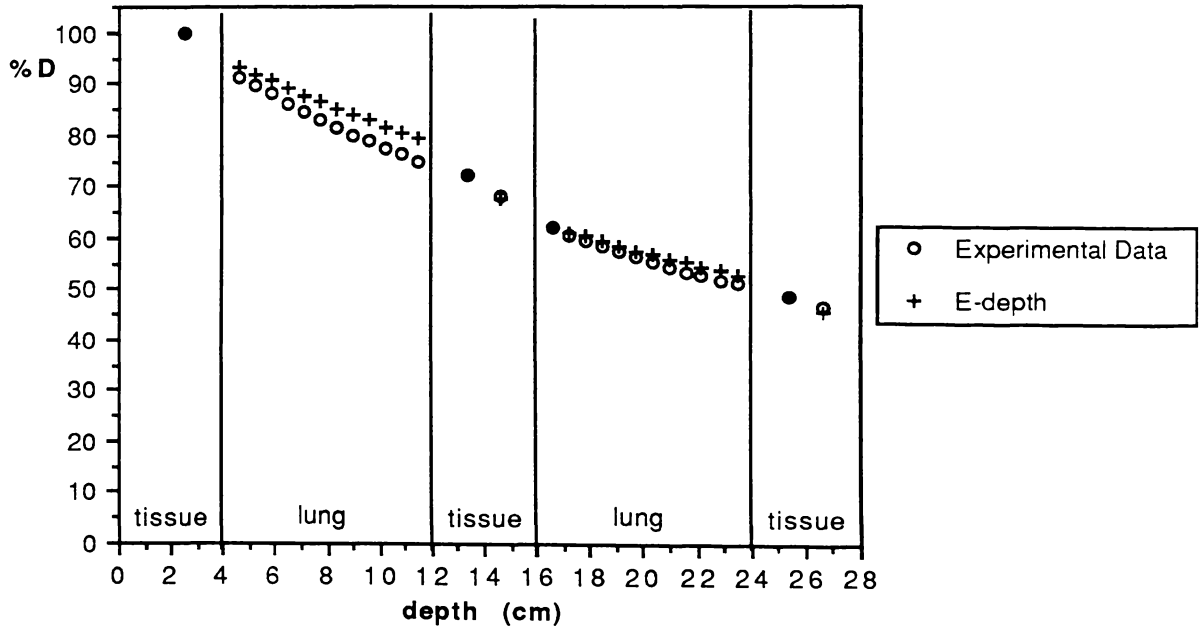

Figure 3.16: Depth dose plots of E-depth correction and experimental measurements:
Beam energy 10 MV, field size 10 x10 cm, phantom A.
Mean difference 2.7%, mean lung difference 3.2%, maximum difference 5.7%.

3.4.4 TISSUE-AIR-RATIO SCALING METHODS

3.4.4.1 Batho Corrections

The Batho power law method of dose computation uses tissue-air-ratios raised to an exponent based on density differences. The method corrects for changes in primary photon fluence and approximates scattered radiation effects. The inhomogeneity is assumed to be a slab extending well beyond the beam boundaries (Batho 1964), such that

$$CF = \left(\frac{TAR(d_1, r)}{TAR(d_2, r)} \right)^{1-\rho_2} , \qquad (3.24)$$

where ρ_2 is the density of the inhomogeneous medium overlying the water medium, d_1 is the distance from the top of the inhomogeneity to point p_2 and d_2 is the distance from the bottom of the inhomogeneity to point p_2 (see Figure 3.17). As noted by others (Wong and Henkelman 1983), a fundamental derivation of the power law equation, even in Batho's original paper, was not presented. Despite this, experimental results from several papers and this thesis show the method is reasonably accurate for a 1.25 MeV beam.

The original method only calculated dose beyond inhomogeneities, but Sontag and Cunningham (1977) subsequently extended the technique to include calculation of dose within inhomogeneities, such that

$$CF = [TAR(d_1, r)]^{\rho_2 - 1} . \qquad (3.25)$$

Therefore, as a general case, within and beyond inhomogeneities the correction method can be described by (El-Khatib and Battista 1984):

$$CF = \frac{[\, TAR\,(d_1,\ r\,)]^{\rho_2 - \rho_1}}{[\, TAR\,(d_2,\ r\,)\,]^{1-\rho_1}} , \qquad (3.26)$$

where ρ_1 is the relative electron density of medium 1, ρ_2 is the relative electron density of medium 2, d_1 is the distance from the calculation point to the top of the inhomogeneity, d_2 is the distance from the calculation point to the skin surface and r is the beam radius at depth of calculation point (see Figure 3.17).

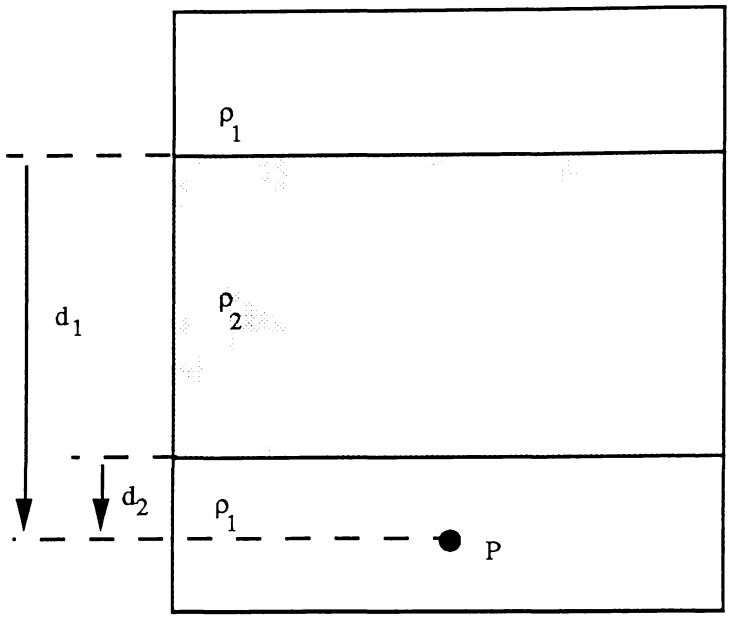

Figure 3.17: Geometrical parameters used in the Batho power law correction methods.

The first technique experimentally appraised in this section, at 1.25 MeV and 15 MV, is based on a further small modification by El-Khatib and Battista (1984) which appears to improve the accuracy of this method within lung by using tissue-phantom-ratios (TPRs) to replace the TARs in (3.26). Because of this modification the method is known as the Batho (TPR) method. Therefore (3.26) becomes

$$CF = \frac{[\ TPR\ (d_1,\ r\ )]^{\rho_2 - \rho_1}}{[\ TPR\ (d_2,\ r\ )\ ]^{1-\rho_1}} \quad . \tag{3.27}$$

The Batho (TPR) prediction versus experimental results are compared in Figures 3.18 and 3.19, showing results for 5 x 5 cm and 10 x 10 cm fields at 1.25 MeV. Note at this energy most data points fall close to the experimental results. This shows the improved scatter correction of this method over the E-depth method. This method looks quite accurate at low energies. At 15 MV for the 10 x 10 cm field size in Figure 3.21 the depth dose agreement is also good, yet at 5 x 5 cm, 15 MV (Figure 3.20) the error once again is extremely large (notably in the first lung region). This is due to the inability of the method to account for regions of lateral electron disequilibrium.

The second Batho correction appraised at 1.25 MeV and 10 MV in this section, is based on a method developed by Wong and Henkelman. The method is known as the "Batho differential scatter-air-ratio method" or Batho (dSAR) method. It is given this name because of its similarities in functional form to the original dSAR method developed by Beadoin and

described by Cunningham (1972). This method is supposed to employ an improved system of coping with the scatter correction. It is important to note however that only first scatter is considered in this correction method, and no account is taken of the multiple scatter contribution. For details of the method refer to Wong and Henkelman's paper (1982).

The Batho (dSAR) correction and experimental results are compared in Figures 3.22 and 3.23, showing results for 5 x 5 cm and 10 x 10 cm fields at 1.25 MeV. Note at this energy most data points fall well outside the experimental data points and this method shows little improvement in accuracy over the E-depth method.

The error using this method is perhaps due to it considering first scatter only, whereas multiple scatter is a major contributor to dose at any point at 1.25 MeV beam energy. At 10 MV for the 10 x 10 cm field size (Figure 3.25) the depth dose agreement is good, possibly because at this energy the contribution from multiple scatter is less. Yet once again for the 5 x 5 cm field size at 10 MV beam energy the error is extremely large (see Figure 3.24) due to the inability of the method to account for regions of lateral electron disequilibrium. The error is not quite as large as that for the Batho (TPR) method at 15 MV (Figure 3.21), because as the beam energy is reduced the lateral electron disequilibrium effect is reduced.

Another effect which can reduce the, disequilibrium induced, percentage depth dose void is the density of the lung. The lung analog phantom B (lung density 0.3) was used for depth dose data collection at 10 MV. Graphs of percentage depth dose for this phantom are compared with the Batho (dSAR) correction method as shown in Figures 3.26 and 3.27, respectively. Note that the error is still large, although not as great as for the lower density lung phantom.

Cross plot profiles produced using an ionization chamber, film and TLD in the mid-depth of the first lung for a 10 x 10 cm field size at 10 MV are shown in Figure 3.28 for phantom A and Figure 3.29 for phantom B. Profile data collected using the E-TAR and Batho corrections are also presented on these graphs, although at this stage we will only consider the Batho data as the E-TAR data is considered in section 3.4.4.2. The experimental profiles are more rounded in the penumbral part than the Batho data. This is due to the effect of electron ranging. Differences of 15.0% occur in the penumbral region of the profile. This shows the excellent results presented for the central axis (see Figure 3.25 and 3.27) are somewhat misleading because electron equilibrium is achieved in the central axis for large field sizes, but this is not matched in the penumbral region and large errors occur in this region for the Batho (dSAR) method.

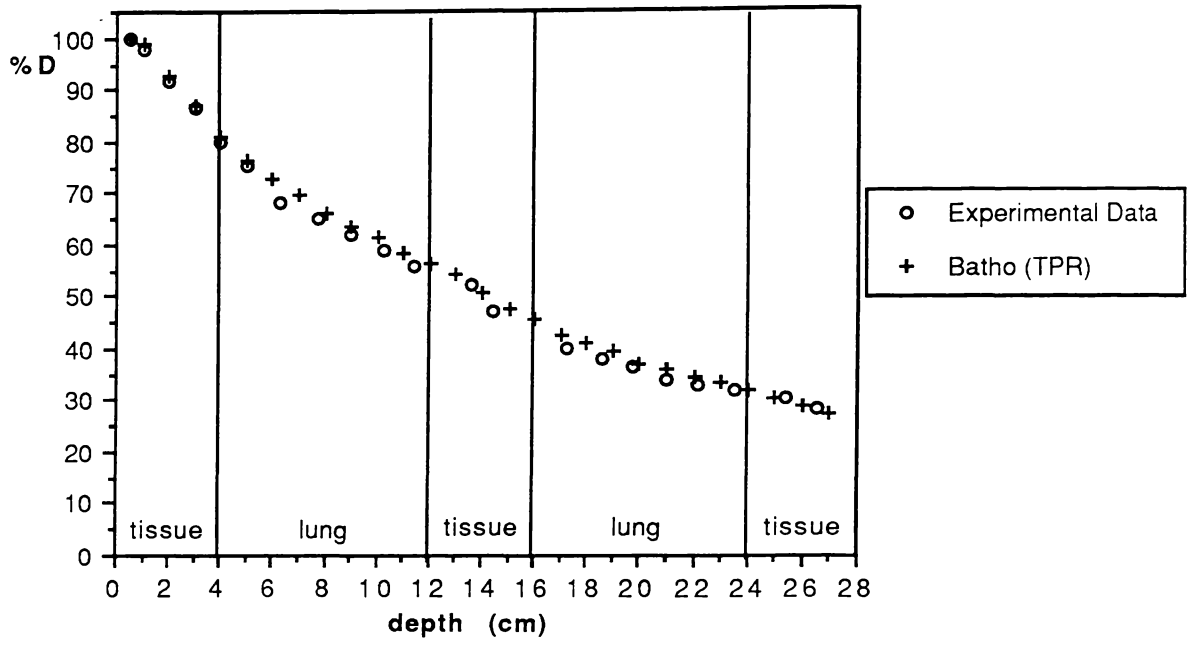

Figure 3.18: Depth dose plots of Batho (TPR) and experimental measurements:
Beam energy 1.25 MeV, field size 5 x 5 cm, phantom A.
Mean difference 2.5%, mean lung difference 3.4%, maximum difference 5.3%.

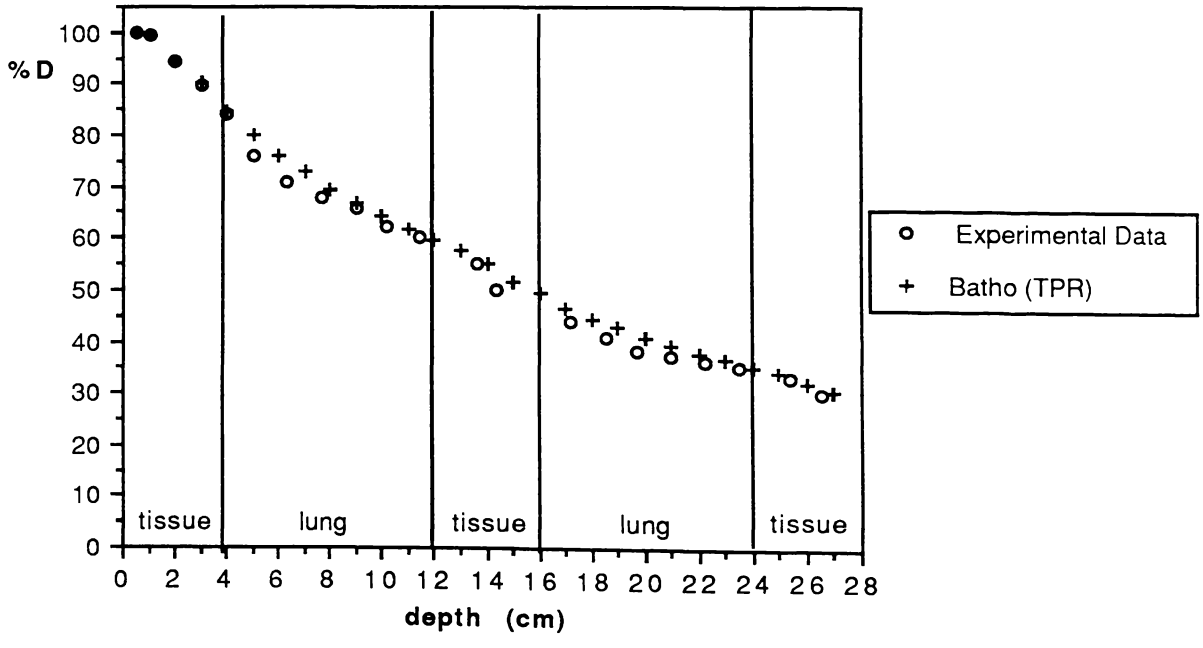

Figure 3.19: Depth dose plots of Batho (TPR) and experimental measurements:
Beam energy 1.25 MeV, field size 10 x 10 cm, phantom A.
Mean difference 2.9%, mean lung difference 3.8%, maximum difference 6.8%.

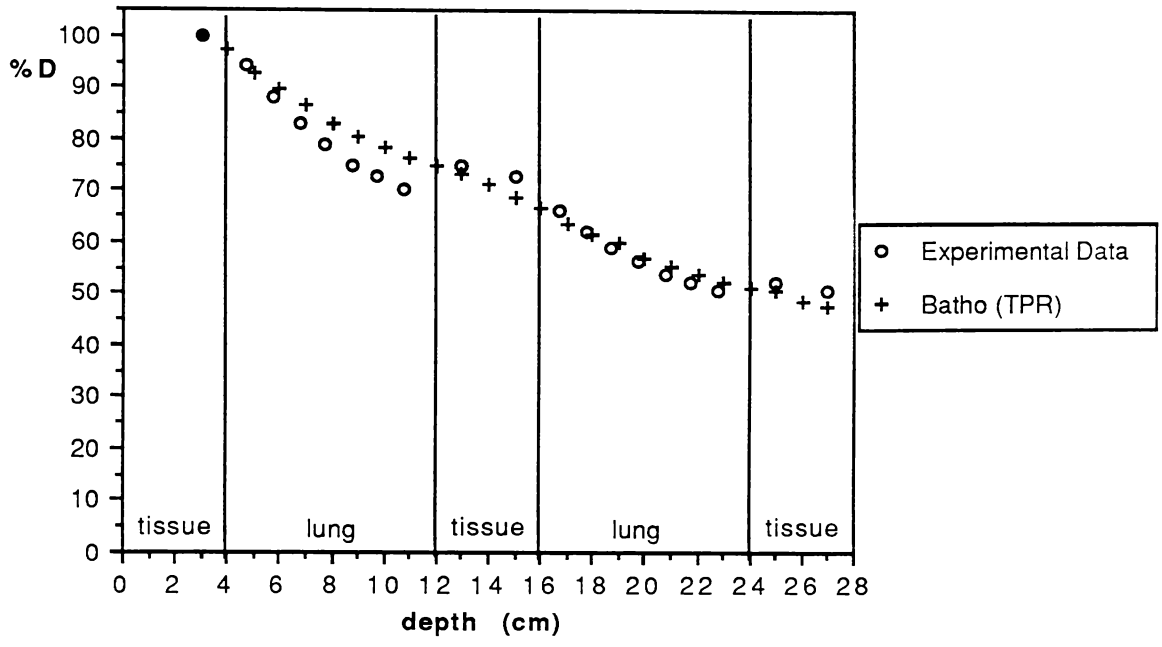

Figure 3.20: Depth dose plots of Batho (TPR) and experimental measurements:
Beam energy 15 MV, field size 5 x 5 cm, phantom A.
Mean difference 4.0%, mean lung difference 4.2%, maximum difference 9.4%.

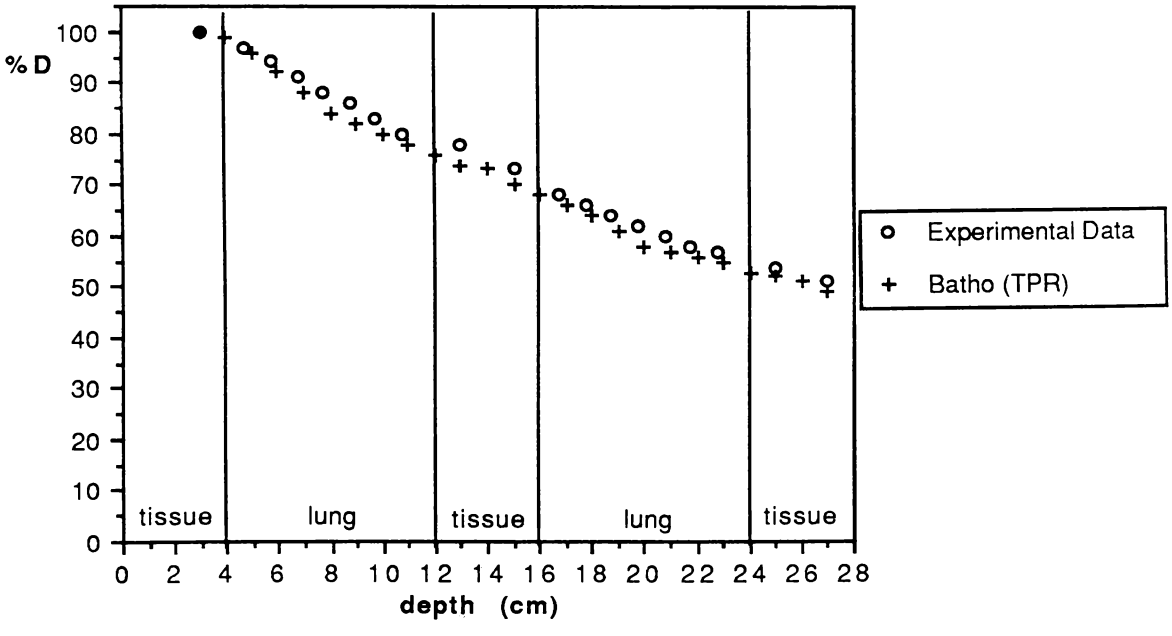

Figure 3.21: Depth dose plots of Batho (TPR) and experimental measurements:
Beam energy 15 MV, field size 10 x 10 cm, phantom A.
Mean difference 1.0%, mean lung difference 0.9%, maximum difference 3.9%.

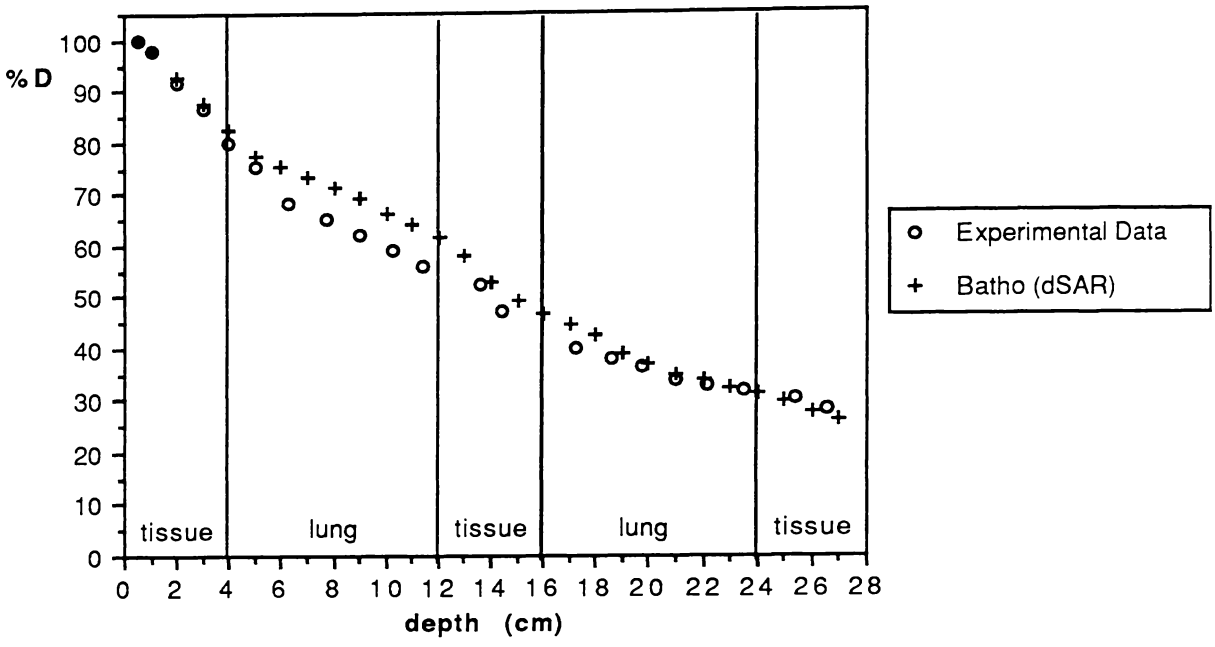

Figure 3.22: Depth dose plots of Batho (dSAR) and experimental measurements:
Beam energy 1.25MeV field size 5 x 5 cm, phantom A.
Mean difference 5.5%, mean lung difference 7.4%, maximum difference 12.5%.

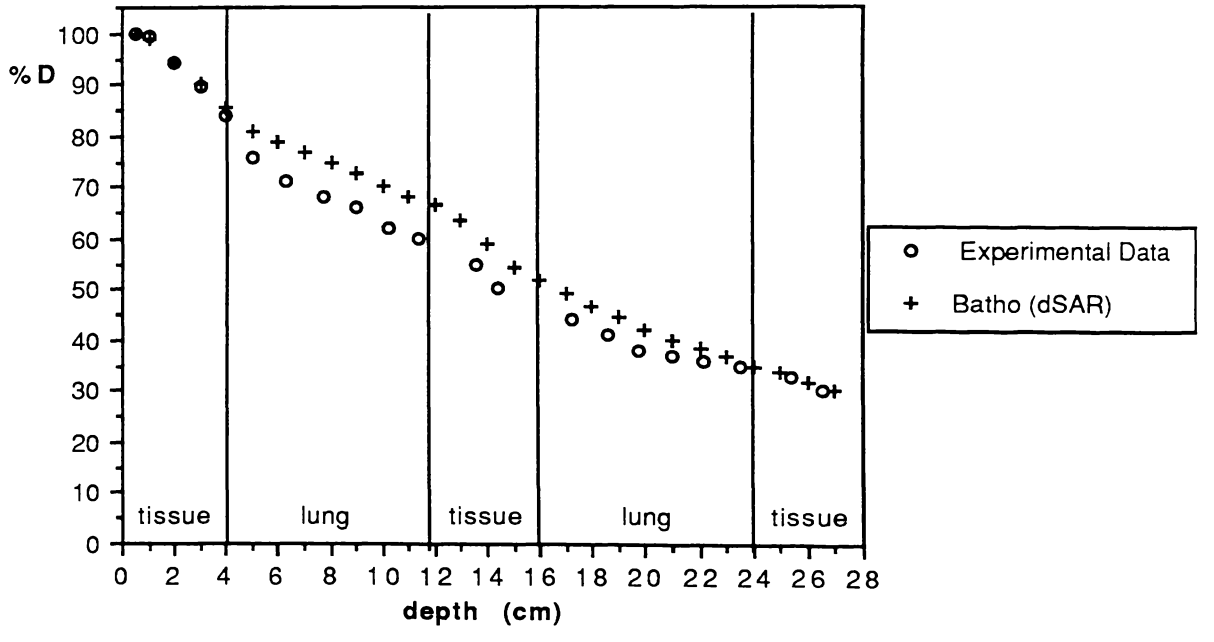

Figure 3.23: Depth dose plots of Batho (dSAR) and experimental measurements:
Beam energy 1.25 MeV, field size 10 x 10 cm, phantom A.
Mean difference 6.9%, mean lung difference 11.2%, maximum difference 14.0%.

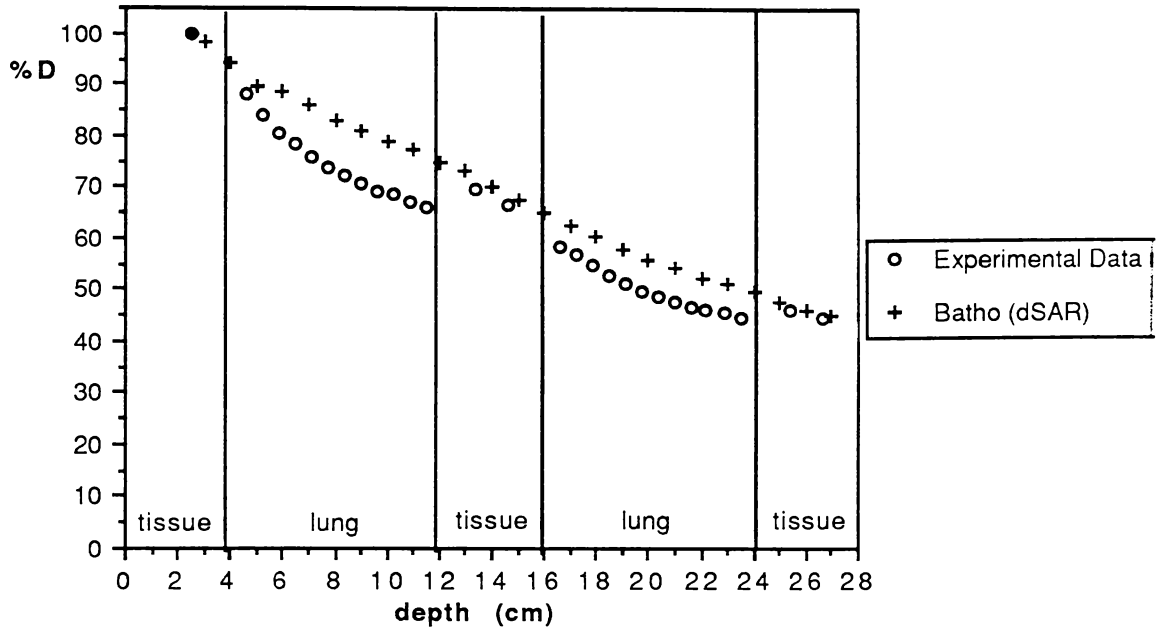

Figure 3.24: Depth dose plots of Batho (dSAR) correction and experimental measurements:
Beam energy 10 MV, field size 5 x 5 cm, phantom A.
Mean difference 10.4, mean lung difference 12.1%, maximum difference 15.9%.

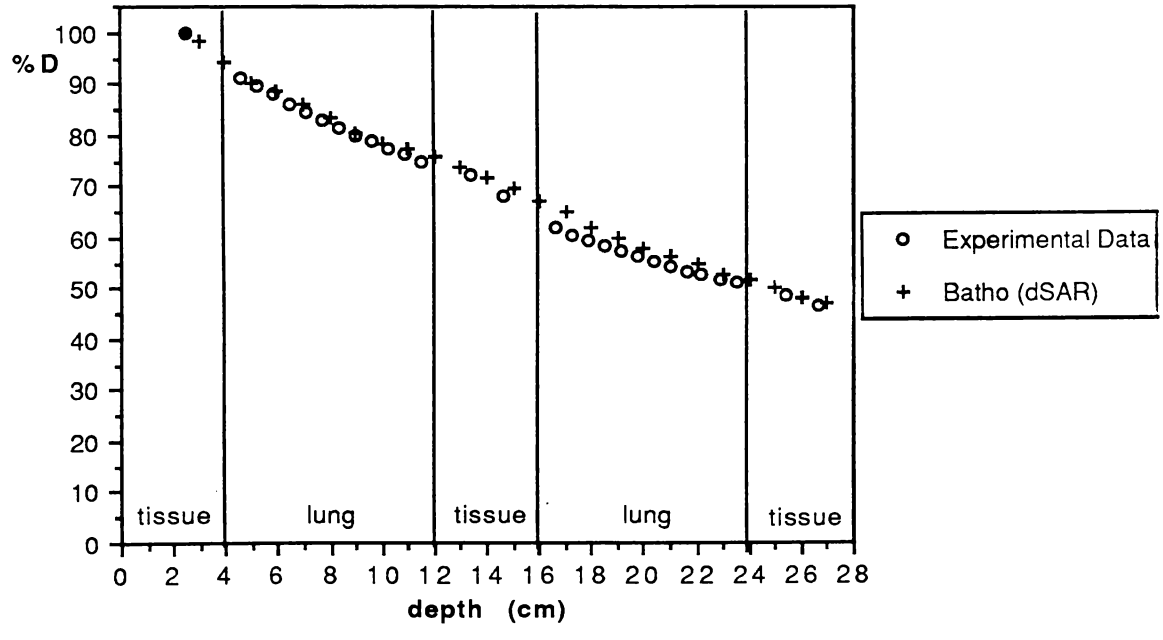

Figure 3.25: Depth dose plots of Batho (dSAR) and experimental measurements:
Beam energy 10 MV, field size 10 x 10 cm, phantom A.
Mean difference 2.5%, mean lung difference 2.8%, maximum difference 7.4%.

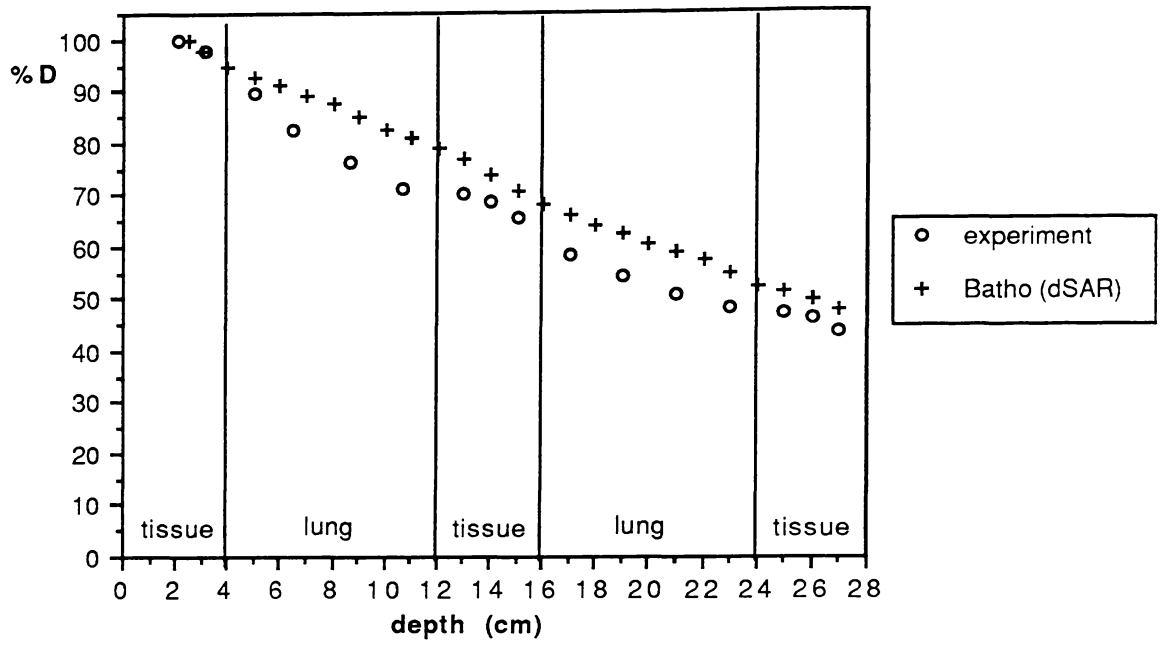

Figure 3.26: Depth dose plots of Batho (dSAR) correction and experimental measurements:
Beam energy 10 MV, field size 5 x 5 cm, phantom B.
Mean difference 8.8%, mean lung difference 12.3%, maximum difference 16.4%.

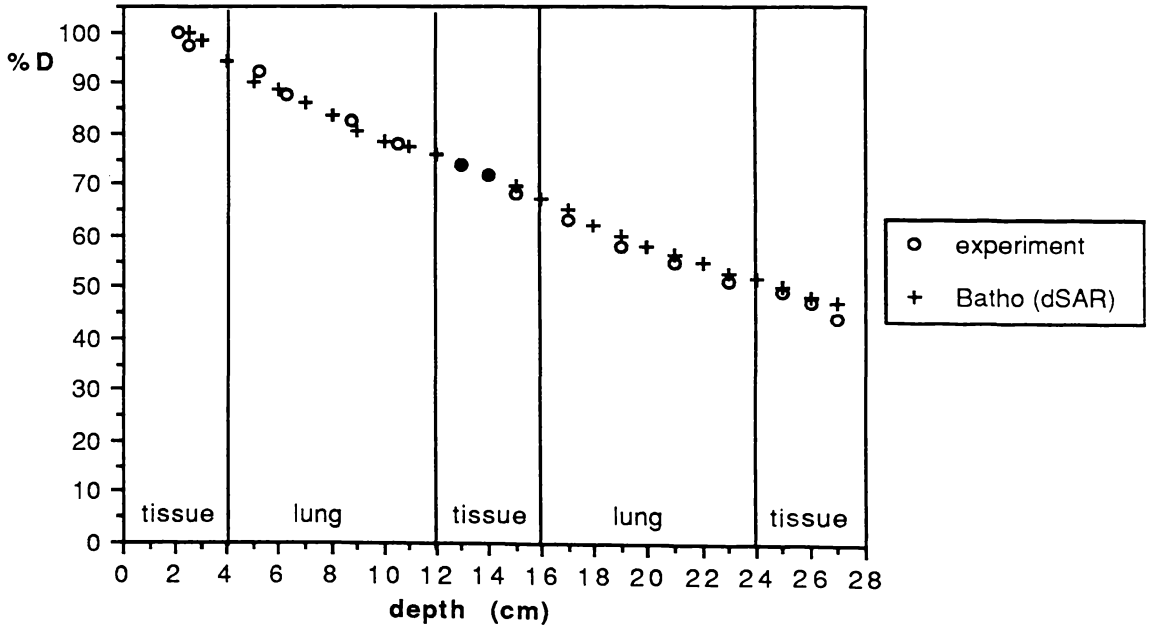

Figure 3.27: Depth dose plots of Batho (dSAR) correction and experimental measurements:
Beam energy 10 MV, field size 10 x 10 cm, phantom B.
Mean difference 2.0%, mean lung difference 2.2%, maximum difference 6.8%.

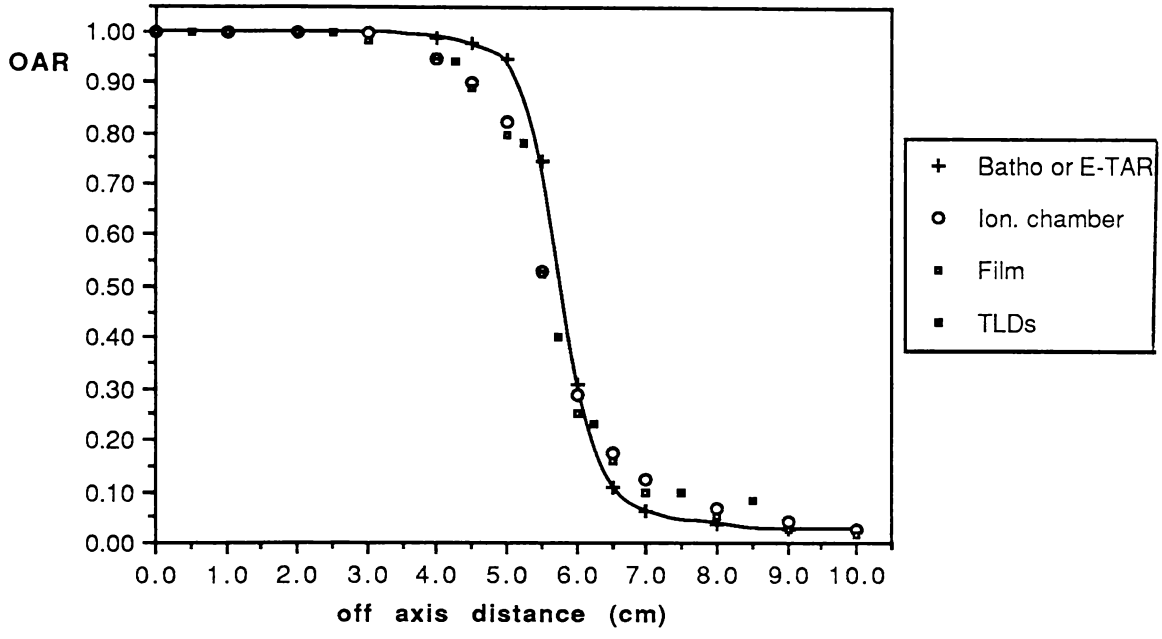

Figure 3.28: Dose profile OARs versus off axis distance as predicted by Batho and E-TAR: Measured at 8 cm depth, mid lung, with an ionization chamber, film and TLDs: Beam energy 10 MV, field size 10 x 10 cm, phantom A, difference at 5 cm is 15.0%.

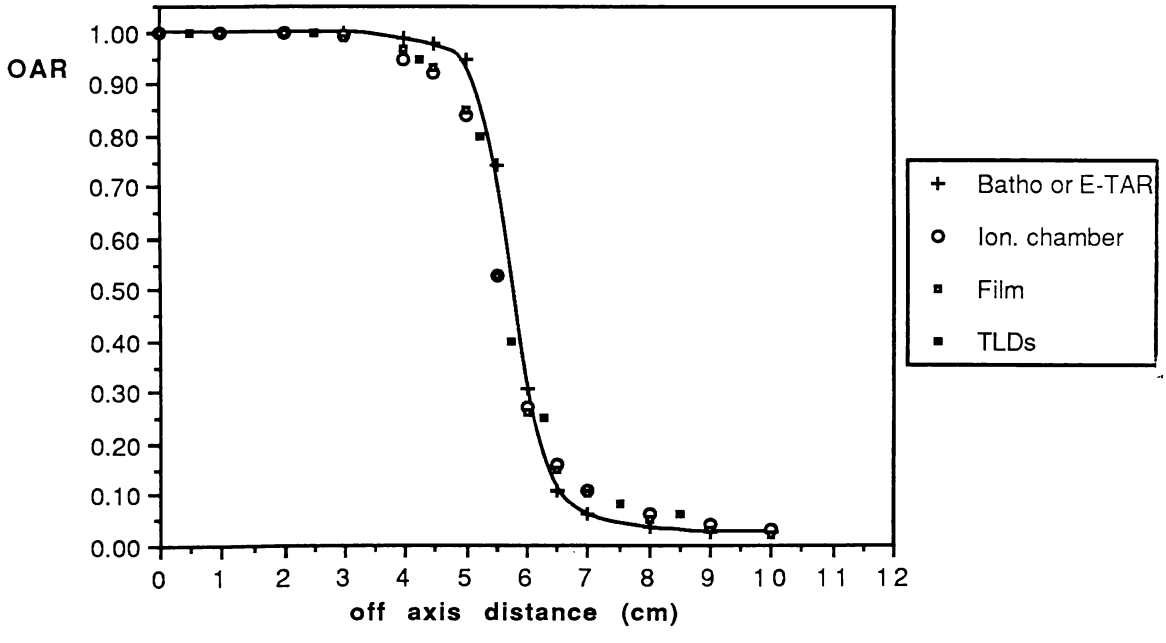

Figure 3.29: Dose profile of off axis ratio versus off axis distance as predicted by Batho and E-TAR: Measured at 8 cm depth, mid lung, with ionization chamber, film and TLDs: Beam energy 10MV, field size 10 x 10 cm, phantom B, difference at 5 cm is 12.6%.

3.4.4.2 The Equivalent Tissue-air-ratio Correction (E-TAR)

The Equivalent tissue-air-ratio (E-TAR) method developed by Sontag and Cunningham (1978) was the first algorithm which attempted to correct for the scattered radiation component by using multiple slice CT pixel density information. This was achieved by scaling the beam size in proportion to the lateral electron density distribution and associated photon scattering. At present, it is the "benchmark" to which other algorithms are compared since it is the most advanced algorithm commercially implemented and shows a good compromise between dose accuracy and speed of computation .

This algorithm relies on O'Connor's range scaling theorem (1957) which predicts that the dose to a point in a unit density medium is the same as the dose to a point in a non-unit density medium provided the beam radius (r) and depth (d) are appropriately scaled. The inhomogeneity correction factor is defined using the E-TAR method as:

$$CF = \frac{TAR(\bar{d}', \tilde{r}')}{TAR(d, r)} \quad . \tag{3.28}$$

The derivation of suitable ways to scale the effective depth $\bar{d}'$ and effective radius r' to account for primary and scatter contributions is as follows. The effective depth $\bar{d}'$ is simply found using (3.16). But as the scatter increases with beam size, the beam radius is scaled in a complicated fashion in an attempt to account for the relative "scattering power" of neighbouring voxels to the dose voxel in question. In principle, to do this in three-dimensions

$$\tilde{r}' = r\,\tilde{\rho} \tag{3.29}$$

where

$$\tilde{\rho} = \frac{\sum_i \sum_j \sum_k \rho_{ijk} W_{ijk}}{\sum_i \sum_j \sum_k W_{ijk}} \quad . \tag{3.30}$$

The term ρ_{ijk} is the density of the voxel element and W_{ijk} is the weighting factor of the ijk voxel set equal to the differential scatter-air-ratio (dSAR) of that voxel.

The E-TAR algorithm is three-dimensional in conception but only two-dimensional in

implementation. The three-dimensional summation of W_{ijk} has not been attempted as it is considered too time consuming for available computing resources. Hence present day commercial implementations use a two-dimensional simplification of the method, relying on the "assumption" of separability :

$$W_{ijk} = W_k W_{ij} \quad , \tag{3.31}$$

where a simplified two-dimensional weighted mean density is calculated at an effective scattering slice. The term $\tilde{\rho}$ of (3.30) is expressed by the following approximation

$$\tilde{\rho} \approx \frac{\sum_i \sum_j W_{ij} \left(\sum_k \rho_{ijk} W_k \right)}{\sum_i \sum_j W_{ij} \left(\sum_k W_k \right)} \tag{3.32}$$

and

$$\tilde{\rho} \approx \frac{\sum_i \sum_j W_{ij} \left[\dfrac{\sum_k \rho_{ijk} W_k}{\sum_k W_k} \right]}{\sum_i \sum_j W_{ij}} \quad , \tag{3.33}$$

where

$$\tilde{\rho}_{ij} = \frac{\sum_k \rho_{ijk} W_k}{\sum_k W_k} \quad . \tag{3.34}$$

The derivation of W_k involves some approximations as discussed by the authors (Sontag 1979, Sontag and Cunningham 1978). For the final step which is carried out for each point of the calculation, the origin of the co-ordinates is shifted to the point of calculation and an effective density is calculated for that point:

$$\tilde{\rho} \approx \frac{\sum_i \sum_j \tilde{\rho}_{ij} \, W_{ij}(z_{eff})}{\sum_i \sum_j W_{ij}(z_{eff})} \quad . \tag{3.35}$$

The term z_{eff} is the "effective distance" away from the plane of calculation at which the resultant densities $\tilde{\rho}_{ij}$ are located. Details of the derivation of z_{eff} involves some approximations as discussed by the authors (Sontag 1979, Sontag and Cunningham 1978).

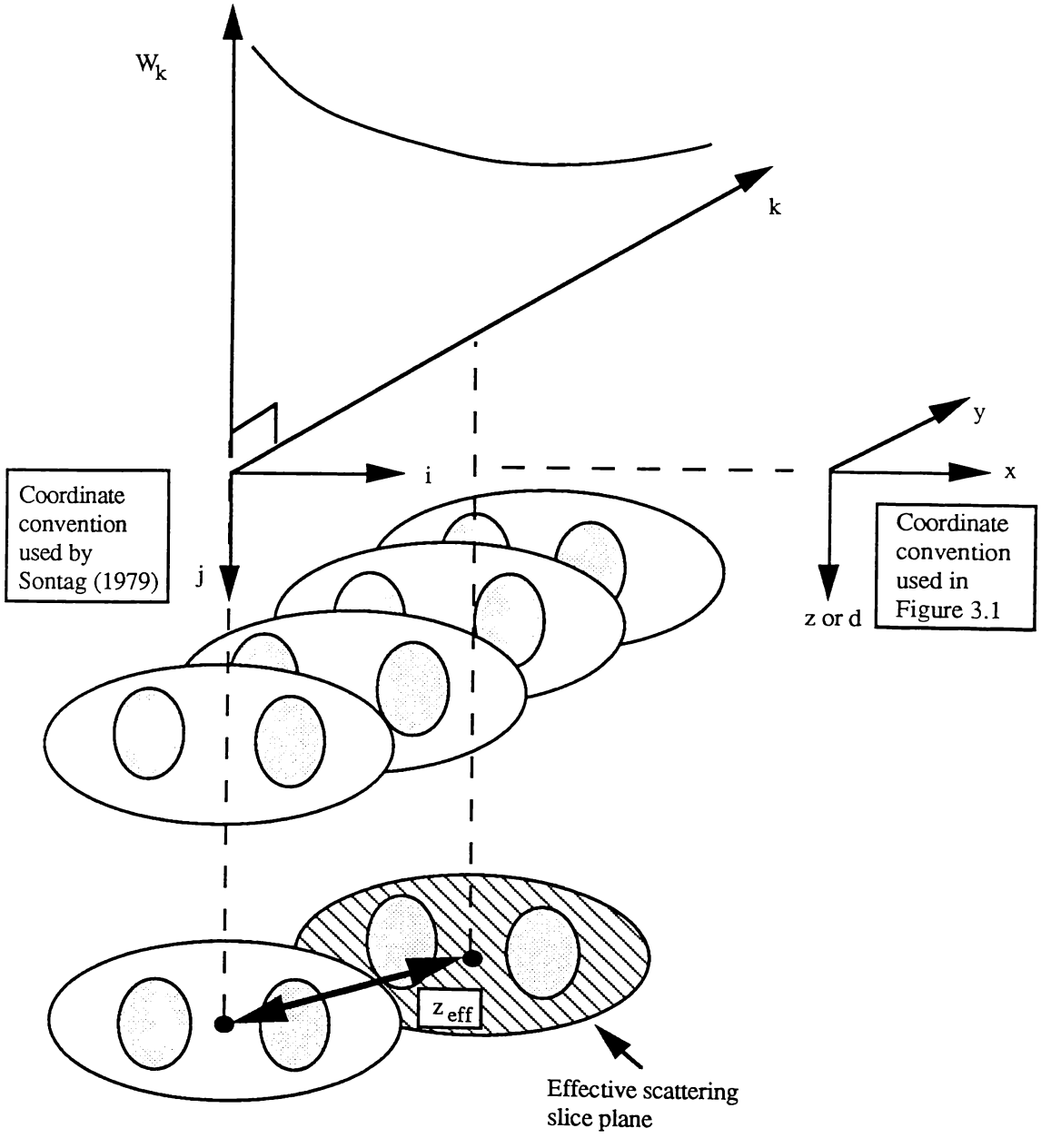

Figure 3.30: In the E-TAR correction method a weighted slice is calculated in a plane at a distance z_{eff} from the primary slice of calculation. The Sontag (1979) co-ordinate convention has been followed for (3.28)-(3.35) and this co-ordinate convention along with that used in Figure 3.1 is shown here.

Regardless of its two or three-dimensional implementation, however, the accuracy of the algorithm relies on the calculation of weighting factors. The calculation of W_{ij} includes the consideration of first and multiple scattering, separated into first and multiple scatter components (ie. the first and multiple scatter components of dSARs).

The E-TAR correction and experimental data are presented in Figures 3.31 and 3.32. These figures show results for 5 x 5 cm and 10 x 10 cm fields at 1.25 MeV. Note at this energy most data points fall close to the experimental data points. This method shows the closest agreement to the experimental points of any of the methods discussed.

At 10 MV for the 10 x 10 cm field size the depth dose agreement is also good (see Figure 3.34). Yet once again for the 5 x 5 cm field size at 10 MV beam energy the error is extremely large due to the inability of the method to account for regions of lateral electron disequilibrium (see Figure 3.35).

Another effect which can reduce the disequilibrium induced percentage depth dose void is the density of the lung. Once again data is collected in the lung analog phantom B (lung density 0.3) under the 10 MV X-ray beam. Graphs of percentage depth dose for this phantom are compared with the E-TAR correction method as shown in Figures 3.35 and 3.36, respectively. Note the error is still large although not as great as for the lower density lung phantom.

Cross plot profiles produced using an ionization chamber, film and TLDs in the middle of the first lung for a 10 x 10 cm field size at 10 MV are shown in Figure 3.28 for phantom A and Figure 3.29 for phantom B. Included in these graphs are the OARs which are predicted using E-TAR. The experimental profiles are more rounded in the penumbral part, due to the effect of electron ranging. The differences at an off-axis distance of 5 cm in the penumbral region is 15.0% for phantom A and 12.6% for phantom B. Note the OAR profiles are identical to the Batho results when normalised to the centre of the field. This is because the same OARs and penumbral forming function methods (as discussed in section 3.3) are used.

Data was also collected under a 15 MV beam using phantom A, as shown in Figure 3.37 for a 5 x 5 cm field and Figure 3.38 for a 10 x 10 cm field. The agreement with experiment is good for the 10 x 10 cm field. The E-TAR corrected data shows a large difference from the experimental data in the lung region (MLD = 8.2%) for the 5 x 5 cm field. The difference is more than that encountered at lower energies, because electron ranging is greater at high energies and this leads to the electron disequilibrium effect being increased.

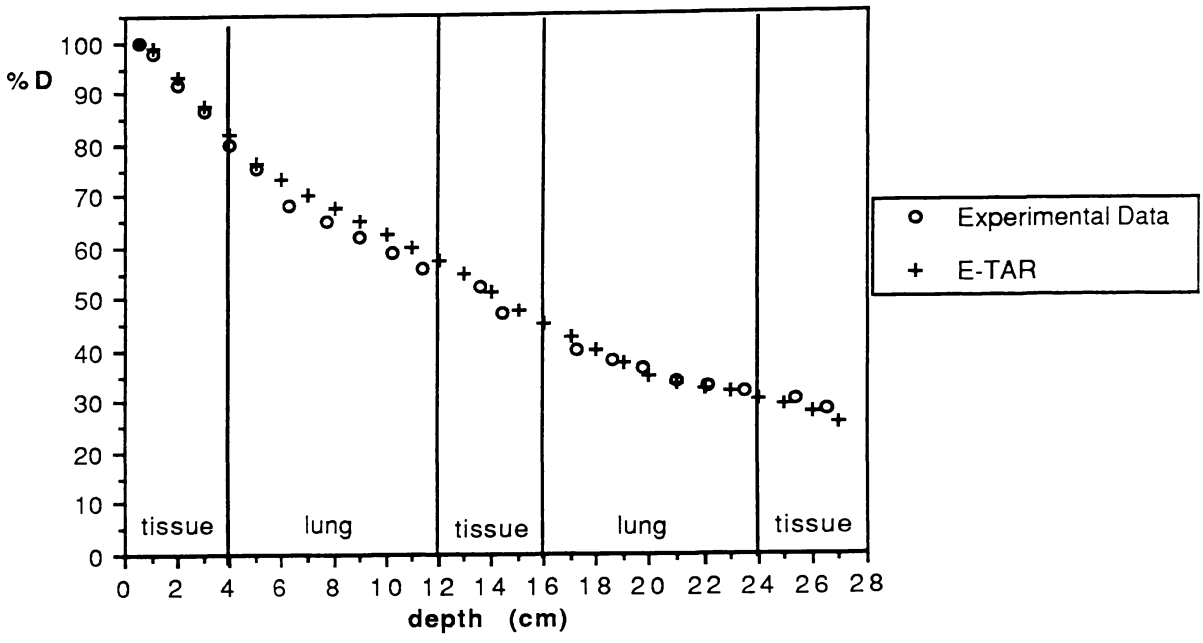

Figure 3.31: Depth dose plots of E-TAR and experimental measurements:
Beam energy 1.25 MeV, field size 5 x 5 cm, phantom A.
Mean difference 3.1%, mean lung difference 3.3%, maximum difference 6.6%.

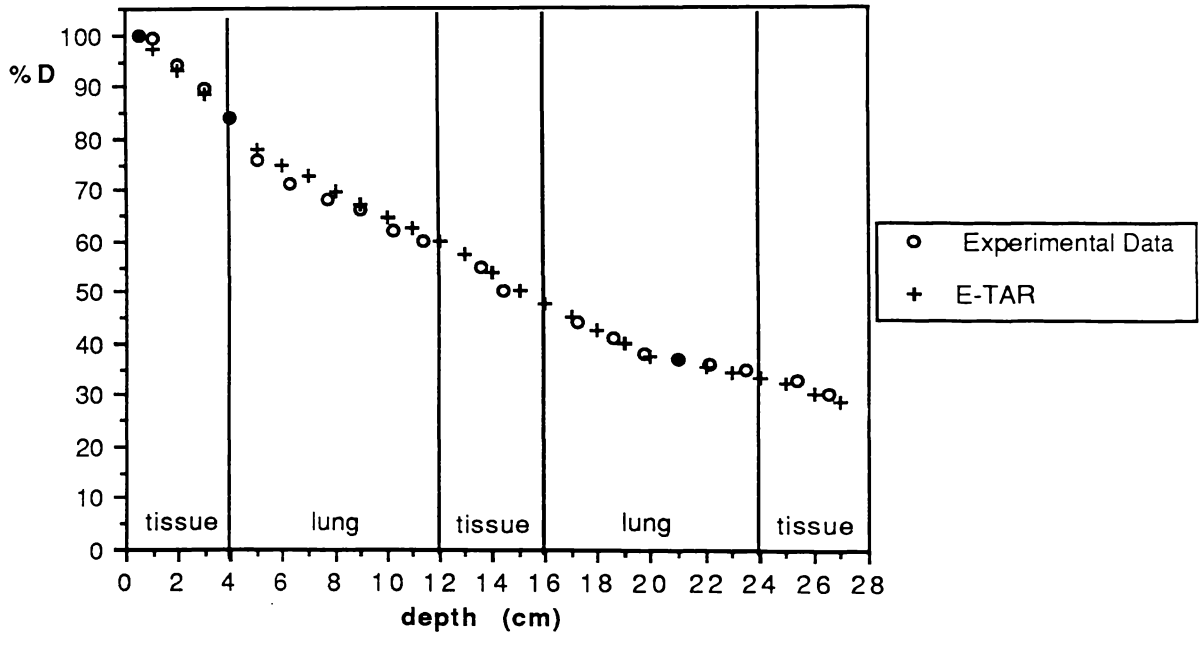

Figure 3.32: Depth dose plots of E-TAR and experimental measurements:
Beam energy 1.25 MeV, field size 10 x 10 cm, phantom A.
Mean difference 3.0%, mean lung difference 4.0%, maximum difference 5.6%.

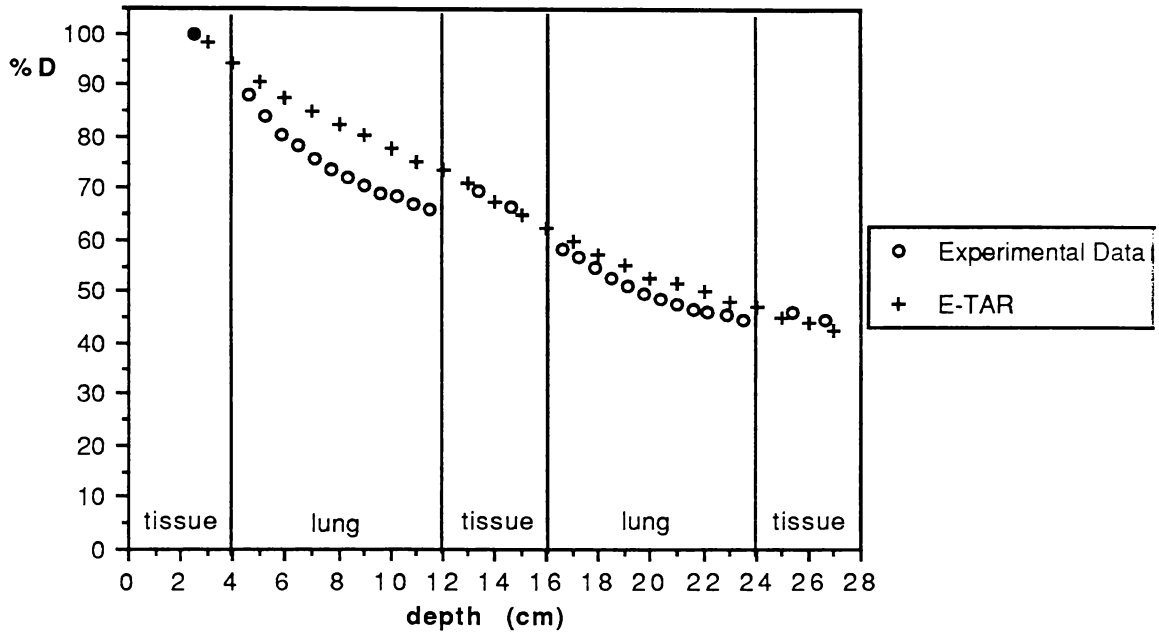

Figure 3.33: Depth dose plots of E-TAR and experimental measurements:
Beam energy 10 MV, field size 5 x 5 cm, phantom A.
Mean difference 6.3%, mean lung difference 6.3%, maximum difference11.3%.

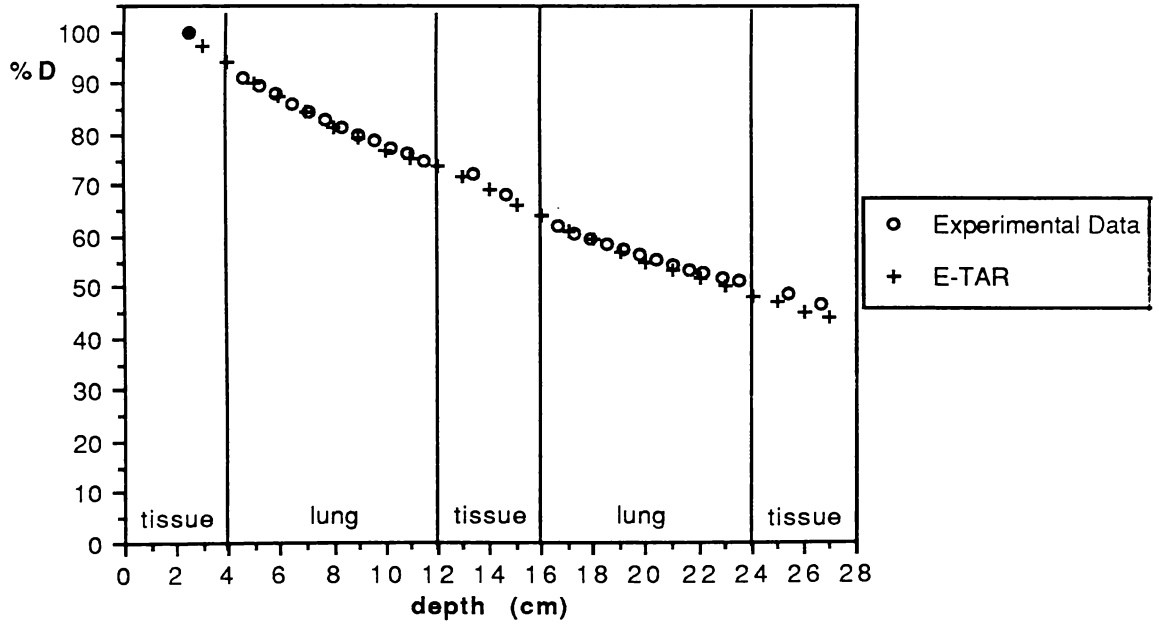

Figure 3.34: Depth dose plots of E-TAR correction and experimental measurements:
Beam energy 10 MV, field size 10 x 10 cm, phantom A.
Mean difference 1.7%, mean lung difference 1.0%, maximum error 9.8%.

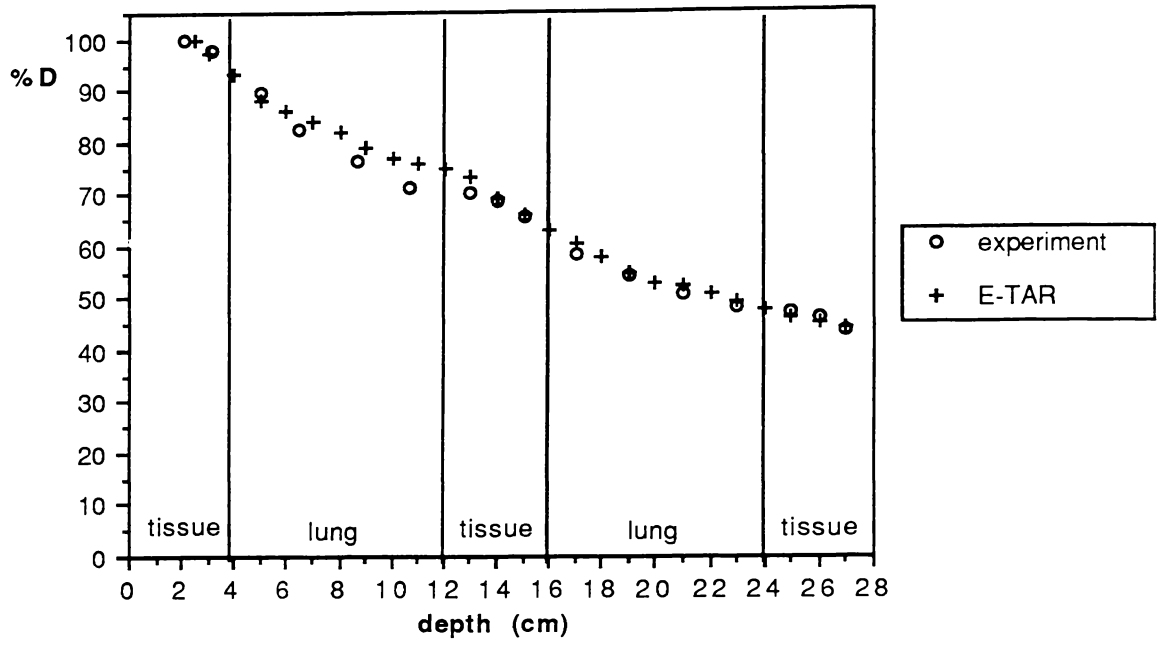

Figure 3.35: Depth dose plots of E-TAR correction and experimental measurements:
Beam energy 10 MV, field size 5 x 5 cm, phantom B.
Mean difference 3.5%, mean lung difference 3.5%, maximum difference 7.6%.

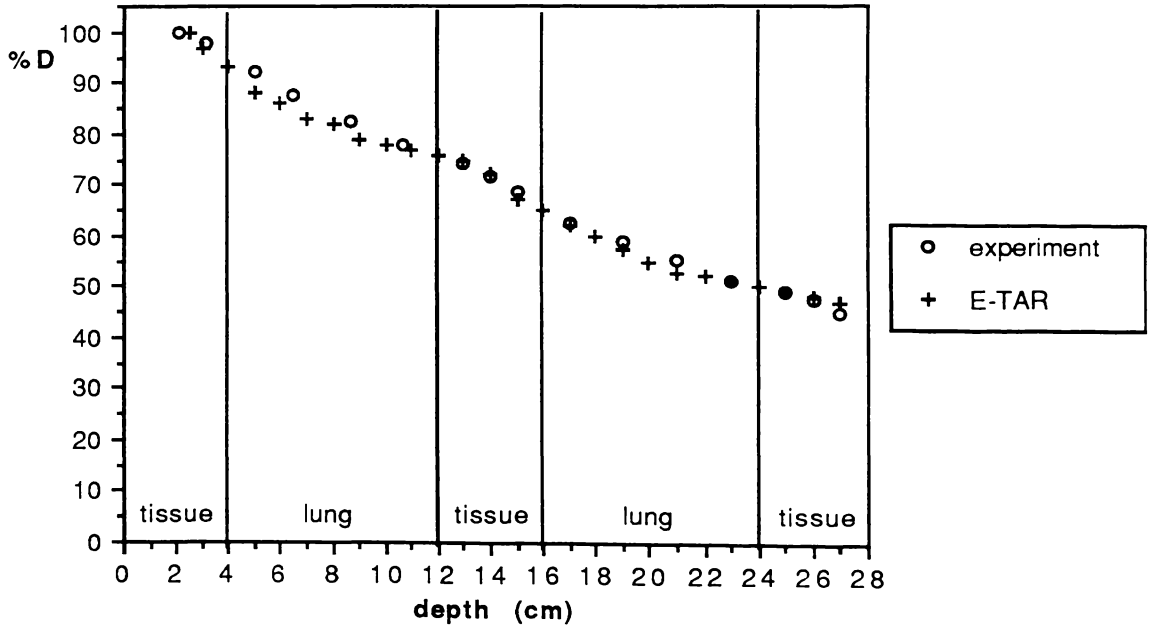

Figure 3.36: Depth dose plots of E-TAR correction and experimental measurements:
Beam energy 10 MV, field size 10 x 10 cm, phantom B.
Mean difference 3.5%, mean lung difference 4.1%, maximum difference 6.9%.

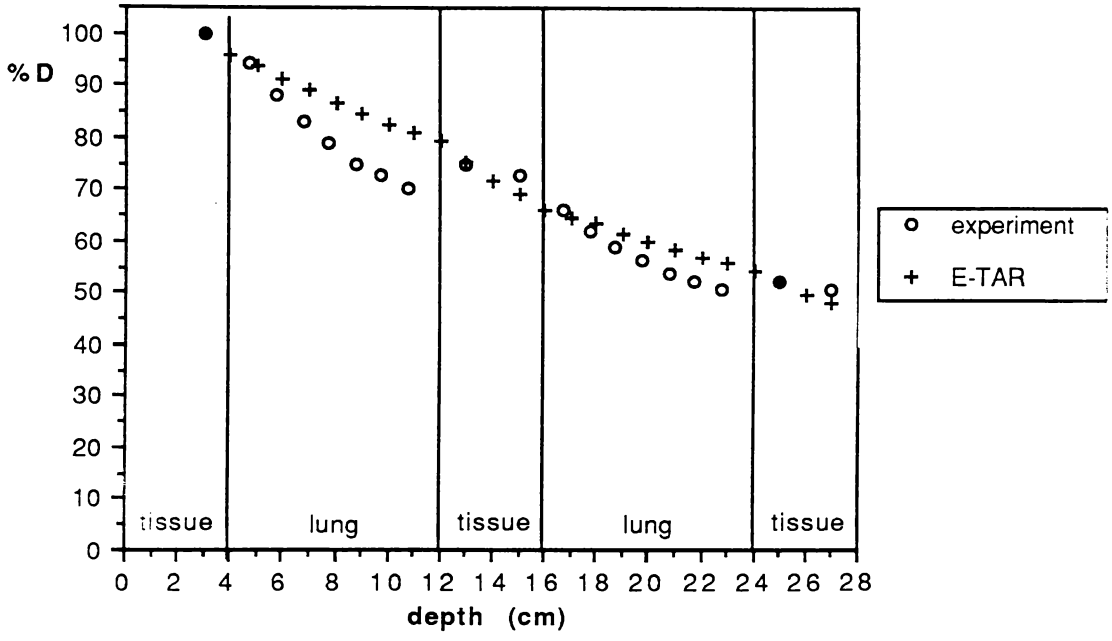

Figure 3.37: Depth dose plots of E-TAR correction and experimental measurements:
Beam energy 15 MV, field size 5 x 5 cm, phantom A.
Mean difference 6.7%, mean lung difference 8.2%, maximum difference 16.4%.

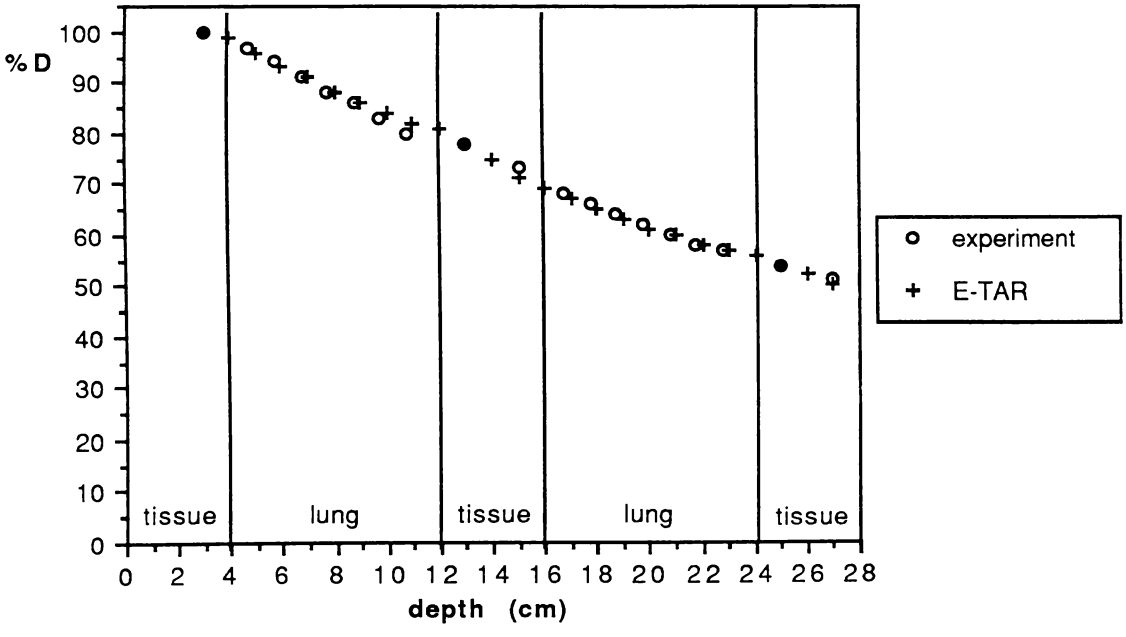

Figure 3.38: Depth dose plots of E-TAR correction and experimental measurements:
Beam energy 15 MV, field size 10 x10 cm, phantom A.
Mean difference 1.0%, mean lung difference 1.1%, maximum difference 3.7%.

3.5 CONCLUSIONS

The accuracy of inhomogeneity corrections in a two lung phantom geometry has been discussed. The photon beam methods reviewed in this chapter show inaccuracy in lung, because they fail to account for charged particle transport (ie. electron disequilibrium). The E-depth correction shows large differences (MPD about 10%) for the majority of beam energies and field sizes tested. This is because the method fails to model photon scatter and charged particle transport.

In the interests of brevity the tests performed in the penumbral region using the E-depth method are not presented here. However, similar errors to those found using TAR methods were encountered. This is because "in-water" data is used in the penumbral region (Pracy 1988), and the lateral shape of the penumbra is not altered with density changes.

The Batho and E-TAR corrections show small differences (MPD about 3%) in the central axis depth dose regions of 10 x 10 cm field sizes even at 10 MV. This is because these methods account for photon scatter in their scaling procedures. However, the Batho and E-TAR methods display large differences in their off-axis profiles. The percentage difference at an off-axis distance of 5 cm in a lung phantom (density 0.3) is 12.6% for a 10 x 10 cm field at 10 MV. This is because these methods use penumbral forming functions which fail to account for loss of electronic equilibrium at the penumbral edge of the beam.

The failure to account for charged particle transport leads to electron disequilibrium extending to the centre of the field for 5 x 5 cm fields tested. This leads to MPDs in the central axis of between 3.5 an 6.3% for E-TAR at 10 MV and between 8.8% and 10.0% for Batho (dSAR) at 10 MV. The differences depend on the field size, phantom type, beam energy and correction method employed.

The guideline for dose accuracy recommended by ICRU#24 (1976) is that total error in dose delivered be less than 5% and the contibution to this error from beam models be less than 2%. Therefore in terms of this guideline all methods reviewed are inadequate in the central axis region for 5 x 5 cm fields in lung, and are inadequate in the penumbral region in lung for 10 x 10 cm fields.

CHAPTER 4

MODELLING DOSE DISTRIBUTIONS FROM 10 MV X-RAYS: ANALYSIS USING A CONVOLUTION/SUPERPOSITION METHOD

4.1 INTRODUCTION

In this chapter a dose calculation method for use in planning radiotherapy treatments with polyenergetic high energy photon beams is presented. It uses a "superposition" or "convolution" technique. Similar techniques used by other researchers are reviewed in section 4.2. The approach used here involves calculating the dose in a medium from a photon beam by convolving a dose spread function with a TERMA function at all points in a medium. The dose spread function describes how energy released at a point is spatially distributed about that point. The TERMA function describes the spatial distribution of energy removal from the beam throughout the medium. The two functions are approximated by arrays of data for computation purposes, these are referred to as the dose spread array (DSA) and TERMA array, respectively. It is common practice to use the terms "array" and "function" interchangeably in this regard, although this is not strictly correct. The author will follow common practice in this discussion and will use the terms intercheangably as there is rarely any confusion as to what is meant. The mathematics describing the author's approach is presented in section 4.3.

The polyenergetic nature of the beam is accounted for by modelling the beam as having ten spectral components. The adequacy of the selected components for the spectrum of a 10 MV beam was checked by doing open field Monte Carlo simulations which used the Electron Gamma Shower (EGS) Monte Carlo computing code. These simulations are described in section 4.4.

Total and primary polyenergetic dose spread arrays (PDSAs) have been generated for a high energy 10 MV radiotherapy photon beam using EGS. These simulations are described in section 4.5. By considering the attenuation of fluence per energy interval, PDSAs have been produced at radiological depths of 0 cm (the surface PDSA) and 40 cm (the beam hardened PDSA). The properties of DSAs at other depths (25 cm and 50 cm) are also discussed, as are the properties of a 3 MeV monoenergetic DSA. The 3 MeV DSA is of interest as this is the "most probable" energy of photons in a 10 MV X-ray beam (see section 4.4.1).

The radiotherapy X-ray beam computation method, which is introduced in section 4.3, involves a single superposition of the surface generated PDSA or beam hardened PDSA

with a polyenergetic TERMA. Percentage depth dose results from the simulations are compared in homogeneous media and the results are presented in section 4.7. The mean percentage difference between depth dose curves obtained using superposition of surface and beam hardened PDSAs is only 0.1%. The mean percentage difference from experimental data for these superposition curves is 2.8% down to 40 cm in a homogeneous phantom. The superposition process is shown to be forgiving to spectral differences when calculating the PDSA but sensitive to the incident photon energy spectrum used to calculate the TERMA.

Methods of scaling PDSAs to account for lung inhomogeneous regions are discussed in section 4.8 and simulations in the two lung phantoms (details of which are outlined in chapters 2 and 3) show good agreement with experimental results and Monte Carlo simulations.

4.2 DISCUSSION

The properties of dose spread arrays have been reported by various authors (Dean 1980, Mackie *et al* 1985a, 1988, Boyer and Mok 1985, 1986, Boyer *et al* 1989, Mohan *et al* 1986, Ahnesjö *et al* 1987, Ahnesjö and Mackie 1987, Ahnesjö 1989, Iwasaki 1990, Metcalfe *et al* 1989). These dose spread arrays (DSAs) have also been termed as energy deposition kernels, differential pencil beams and point spread functions by the authors cited above. The work of Mackie *et al* (1988) demonstrates the effectiveness of applying DSA data to find solutions to radiotherapy beam interaction phenomena.

The "superposition" methods developed by these authors employ convolution mathematics applied to DSAs to effectively model charged particle transport in three-dimensions. Superposition methods have been shown to closely match experimental data and Monte Carlo simulations in regions of electronic disequilibrium (Mackie *et al* 1985a, Mohan *et al* 1986, Metcalfe and Battista 1988, Ahnesjö 1989). In contrast, other currently employed algorithms such as scatter function and effective pathlength methods, which only model photon transport, display inaccuracy in such regions (Kornelson and Young 1982, Cunningham 1982, Mohan and Chui 1985a, Mackie *et al* 1985b, Metcalfe and Beckham 1988).

Further improvements in the speed of convolution techniques using Fourier transforms have been demonstrated (Boyer 1984, Boyer *et al* 1988, Field and Battista 1987, Murray *et al* 1989a). It is however more difficult to achieve correct range scaling using Fourier convolution techniques (Boyer and Mok 1986, Zhu and Boyer 1990, Ahnesjö 1989). Prudent programming of a parallel computing system has recently shown that convolution in

real space (not Fourier space) with range scaling is approaching the speed required for use in routine radiotherapy planning (Murray *et al* 1990).

The superposition methods of Mohan *et al* (1986) and Boyer *et al* (1989) model the polyenergetic nature of the high energy photon beams used in radiotherapy (see section 4.3). The penalty involved in this approach is that a separate convolution is required for each of the beam's spectral components. This increases the computation time for convolution approximately in proportion to the number of spectral components.

An alternative approach is to correct for the polyenergetic nature of the beam while maintaining a single convolution per beam. This method does not explicitly account for the effect of beam hardening on the DSA as it traverses tissue. Hence a detailed analysis of the effect of beam hardening on PDSAs and the final dose distribution is essential. The magnitude of these effects are quantified in sections 4.5 and 4.6 of this chapter.

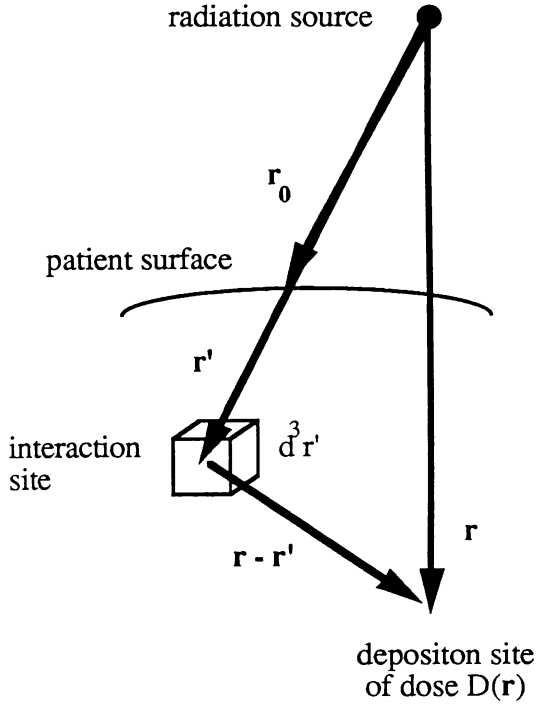

Figure 4.1: Vectorial framework for the superposition approach. The photon interacts at **r'** and dose is transported to **r** by charged particles.

4.3 THEORY OF SUPERPOSITION

The superposition system of mapping dose deposition in a homogeneous phantom calculates the dose D(**r**) to a point **r** from a photon interaction at point **r'** (Figure 4.1) using the superposition (convolution) integral of the primary fluence Φ and the energy spread function G. In this manner scattered charged particles ranging away from the initial interaction sites are accounted for. Therefore the dose deposition site and photon interaction sites are not coincident. In contrast, previously described methods (including scatter function and effective pathlength methods) assume "on the spot" energy deposition.

Unifying the implementations of Mackie *et al* (1984), Boyer and Mok (1985), and Metcalfe and Battista (1988), an energy spread function serves as the superposition kernel G describing energy spread from the primary interaction site. The components of this energy spread are energy of charged particles (positrons and electrons) from primary photon interactions $G_e(\mathbf{r} - \mathbf{r}')$, energy of charged particles from first scatter photon interactions $G_s(\mathbf{r} - \mathbf{r}')$ and energy from charged particles from multiple scatter photon interactions $G_{sm}(\mathbf{r} - \mathbf{r}')$. If Φ is the primary photon fluence at position **r'** and D is the dose to the volume element at position **r**, then for a monoenergetic photon beam in a homogeneous medium the dose is a convolution over the volume being irradiated d^3r', such that

$$D(\mathbf{r}) = \int_v \Phi(\mathbf{r}')\, G_e(\mathbf{r} - \mathbf{r}')\, d^3r' + \int_v \Phi(\mathbf{r}')\, G_s(\mathbf{r} - \mathbf{r}')\, d^3r' + \int_v \Phi(\mathbf{r}')\, G_{sm}(\mathbf{r} - \mathbf{r}')\, d^3r' \,. \qquad (4.1)$$

The assumptions involved here are:

(1) G_e, G_s, G_{sm}, are spatially invariant due to invariant photon energy and medium composition.
(2) The beam is directionally invariant as is the case for a non-diverging (infinite SSD) beam.

All three kernels can be summed:

$$G_T(\mathbf{r} - \mathbf{r}') = G_e(\mathbf{r} - \mathbf{r}') + G_s(\mathbf{r} - \mathbf{r}') + G_{sm}(\mathbf{r} - \mathbf{r}') \,, \qquad (4.2)$$

and thus the total kernel describing energy deposited by charged particles at D(**r**) is given by

$$D(\mathbf{r}) = \int_v \Phi(\mathbf{r}') \, G_T(\mathbf{r} - \mathbf{r}') \, d^3r' \qquad (4.3)$$

The term $G_T(\mathbf{r} - \mathbf{r}')$ represents the dose deposited at $\mathbf{r}$ due to a unit fluence at $\mathbf{r}'$. This term includes factors which convert from fluence (photons cm^{-2}) to energy per unit mass, by the inclusion of the mass attenuation coefficient $(\mu/\rho)_0$ multiplied by the beam energy E_0. For a monoenergetic beam of energy E_0 then

$$G_T(\mathbf{r} - \mathbf{r}') = \left(\frac{\mu}{\rho}\right)_0 E_0 \, H_T(\mathbf{r} - \mathbf{r}') \quad . \qquad (4.4)$$

The term $H_T(\mathbf{r} - \mathbf{r}')$ is the dose spread function which represents the fraction of energy released at $\mathbf{r}'$ that is deposited in a unit volume at $\mathbf{r}$, such that

$$H_T(\mathbf{r} - \mathbf{r}') = \frac{d\varepsilon(\mathbf{r} - \mathbf{r}')}{E_0} \quad , \qquad (4.5)$$

where $d\varepsilon(\mathbf{r} - \mathbf{r}')$ is the energy deposited per unit volume at $\mathbf{r}$ due to a photon interacting at $\mathbf{r}'$. Note that the energy released E_0 includes that of the scattered photons.

An equivalent approach to (4.3) is to place the energy transfer terms into the fluence part of the equation (that is the mass attenuation coefficient $(\mu/\rho)_0$ and the beam energy E_0 are multiplied by the fluence). This new quantity has been defined as the "**T**otal **E**nergy **R**eleased per unit **MA**ss" (TERMA) (Ahnesjö *et al* 1987). The TERMA $T(\mathbf{r}')$ at point $\mathbf{r}'$ is

$$T(\mathbf{r}') = \left(\frac{\mu}{\rho}\right)_0 E_0 \, \Phi(\mathbf{r}') \quad , \qquad (4.6)$$

and thus (4.3) can be rewritten as

$$D(\mathbf{r}) = \int_v T(\mathbf{r}') \, H_T(\mathbf{r} - \mathbf{r}') \, d^3r' \qquad (4.7)$$

For a dose spread function defined in an infinite volume, the energy released at the interaction site matches that deposited during the ranging process (Boyer and Mok 1985), that is:

$$\int_v H_T(\mathbf{r} - \mathbf{r}') \, d^3r' = 1.0 \quad . \qquad (4.8)$$

A problem with the approach outlined so far and described by (4.7) is that the model assumes the beam to be monoenergetic.

The differential pencil beam method of Mohan *et al* (1986), the convolution method of Boyer *et al* (1989) and the polyenergetic superposition method of Ahnesjö (1989) all adjust the superposition model by presenting fluence and dose spread information which is representative of a polyenergetic beam. This method defines two quantities: the probability of photons interacting (a similar quantity to TERMA); and several differential pencil beams or monoenergetic convolution kernels (similar to H). Converting to the nomenclature used in this paper the following equivalent relation is obtained:

$$D(\mathbf{r}) = \int_E \int_v T_E(\mathbf{r}', E)\, H(\mathbf{r} - \mathbf{r}', E)\, d^3r'\, dE \quad , \tag{4.9}$$

where $T_E(\mathbf{r}', E)$ is the TERMA per unit energy interval at E and $H(\mathbf{r} - \mathbf{r}', E)$ is the dose spread function for the energy E.

The major improvement of this superposition model is that it incorporates a superposition of each discrete beam energy component by integrating over the energy components. Though this is a rigorous way to cope with the polyenergetic beam hardening effect, it slows the process by a factor approximately proportional to the number of energy components used (for example the five component spectrum used by Boyer *et al* (1989) requires five convolutions and thus will slow this part of the computation process by approximately a factor of five).

The method used here involves computing the dose at points in a medium by convolving a single polyenergetic dose spread array (PDSA) with a single TERMA array derived from polyenergetic data. The PDSA is obtained from the fractional energy deposition at a position $\mathbf{r} - \mathbf{r}'$ from an interaction point. Note that the photon spectrum used to compute the PDSA is that at a reference position $\mathbf{r}'_{ref}$ in the medium. Therefore the modification of (4.9) which is used here is

$$D(\mathbf{r}) = \int_v \left[\int_E T_E(\mathbf{r}', E)\, dE \right] H_p(\mathbf{r}'_{ref}, \mathbf{r} - \mathbf{r}')\, d^3r' \quad , \tag{4.10}$$

where $H_p(\mathbf{r}'_{ref}, \mathbf{r} - \mathbf{r}')$ is the polyenergetic dose spread function as described in this paper and is equal to

$$H_p(\mathbf{r'}_{ref},\ \mathbf{r} - \mathbf{r'}) = \frac{\int_E d\varepsilon(\mathbf{r} - \mathbf{r'}, E)\, \frac{d\Phi}{dE}(\mathbf{r'}_{ref}, E) \left(\frac{\mu}{\rho}(E)\right) dE}{\int_E \frac{d\Phi}{dE}(\mathbf{r'}_{ref}, E) \left(\frac{\mu}{\rho}(E)\right) E\, dE} \quad . \qquad (4.11)$$

The term $d\varepsilon(\mathbf{r} - \mathbf{r'}, E)$ is the energy deposited due to an incident photon of energy E in a unit volume at $\mathbf{r}$ from a photon interaction at $\mathbf{r'}$. As $(d\Phi/dE)$ is the photon fluence per unit energy interval then $(d\Phi/dE)$ times (μ/ρ) is the number of interactions in a unit mass per unit energy interval at E. Therefore H_p is the energy fraction deposited at a point $\mathbf{r}$ normalised to the energy released at $\mathbf{r'}$.

For an incident photon of the ith energy component E_i, the probability of the interaction occurring varies with energy according to $(\mu/\rho)_i$. To allow for this the PDSAs are generated by weighting the incident photons by a factor proportional to $(\mu/\rho)_i$. Details of how this is done are given elsewhere (Metcalfe *et al* 1990b).

Note from (4.10) that the TERMA value at $\mathbf{r'}$ is calculated from an integral over the energy components at depth $\mathbf{r'}$. Accounting for beam hardening effects on the TERMA is trivial but is nevertheless essential because this defines the energy imparted to the medium at $\mathbf{r}$. Comparison with monoenergetic TERMA arrays of the same mean energy have been shown to differ from the polyenergetic TERMA arrays by up to 10% (see caption in Figure 4.4). Therefore the method accounts for the effect of beam hardening of the TERMA. Using (4.10) the effect of beam hardening with depth on the polyenergetic dose spread function is not accounted for, but it is shown in this chapter that this does not lead to significant errors. A time advantage is gained because only one superposition per beam is required.

Murray *et al* (1990) outline the times required to compute dose distributions using this method on eight T800 Inmos transputer modules. In brief, computation times of only a few seconds are required for convolution in Fourier space and computation times of about two minutes are required for superposition in real space, utilising a simple range scaling algorithm.

4.4 BEAM SPECTRA

4.4.1 Full Field Monte Carlo Verification of Surface Spectra

Bremsstrahlung X-rays produced in a linear accelerator by electrons slowing down during passage through the target have a continuous range of energy. The practice of referring to a beam by its nominal peak energy indicates little about the spectral spread of photons below this value. In some applications a nominal value of 30% is applied to obtain an average of the photon energy. For example, a 10 MV beam is often assigned an approximate mean energy of 3 MeV.

An excellent review of the differences in penetration characteristics which do occur between different linear accelerators of the same target and flattening filter design can be found in the British Journal of Radiology's Supplement 17 (1983). The differences are a function of the nominal energy of the electrons when they strike the target, and this can vary from machine to machine depending primarily on specific waveguide and klystron (or magnetron) characteristics.

Very little measured information about high energy spectra is available, mainly due to difficulties with the high photon fluence saturating detecting systems. Some analysis has been attempted using spectral analysis (Levy *et al* 1976, Nath and Schultz 1976) and attenuation analysis (Huang *et al* 1882a, 1982b). The devices and computations employed are complicated and computationally intensive, respectively.

The spectral data used to calculate polyenergetic TERMA and PDSAs for the studies described in this paper is the spectral beam information published for a 10 MV Clinac 18 by Mohan and Chui (1985b). They produced the spectrum by using a Monte Carlo simulation combined with geometric information about the target and flattening filter design. The spectral distribution used here is a simplified version of their originally published 23 component spectrum, in that it has ten components as shown in Table 4.1 (row 3). The distribution shows how the beam's spectral components are weighted toward the low end of the energy spectrum.

An electron *history* is divided up into a manageable number of *charged particle steps*, each one accounting for a combined effect of many individual collisions (Nahum 1989). Verification of the suitability of spectral information for the Waikato Hospital 10 MV photon beam was obtained by doing full field EGS Monte Carlo (Nelson *et al* 1985) simulations on a DEC VAX 6330 (Murray 1990). The simulations followed the histories of 4 million

incident photons down to 40 cm depth with the fractional electron energy loss per step being set dynamically using the parameter reduced electron step algorithm (PRESTA) (Bielajew and Rogers 1987). This code selectively looks for interfaces and sets the electron energy loss per step to a level which depends on the distance of the charged particle from surrounding interfaces. The simulation batches the results into a set of ten and from these data sets the error in the mean is estimated. This was found to be less than 1% in all positions down to 40 cm depth. The computing time for each simulation was about 40 CPU hours.

The percentage depth dose (%D) curves for two 5 x 5 cm beams are plotted in Figure 4.2. Two different incident beam spectra were used for each simulation. The surface spectrum components used for this first simulation are shown in Table 4.1 (row 3, $d_{ref} = 0$ cm). To show the effect of using a less appropriate spectrum, the process was repeated using the beam hardened spectrum shown in Table 4.1 (row 5, $d_{ref} = 40$ cm).

Note that each point shown on the graph represents the dose scored in cylindrical voxel elements which step down the central axis and are of dimensions 10 mm radius and 5 mm depth. The dose is normalised to the voxel containing maximum dose (D_{max}).

As shown in Figure 4.2 the results of the EGS simulation using the 0 cm 10 MV spectrum agree to within a mean difference of 1.2% with the experimental depth dose readings obtained for a similar beam from the Waikato Hospital Varian Clinac 18 linear accelerator, measured with a PTW ionization chamber in a Therados RFA-3 water tank (see (3.21) for details of mean difference calculation). This indicates that it is appropriate to use the spectral data of Mohan and Chui (1985b) to simulate a 10 MV beam from the linear accelerator provided the surface spectrum is used. Hence dose spread arrays and TERMA arrays were generated using this spectral information. In contrast, the results of the EGS simulation for the 40 cm 10 MV spectrum show too shallow a fall off and do not agree well with the experimental depth dose results. This is because the incident beam spectrum is too heavily weighted with high energy components.

To demonstrate the effect of beam hardening on the TERMA, data in Figure 4.3 is presented. This graph shows the percentage TERMA (%T) calculated using (4.6) and (4.15) and normalised to 100% at the surface, plotted against depth as calculated for the 0 cm 10 MV and 40 cm 10 MV spectrum. Note the differences between the curves are significant and reflect those in Figure 4.2. This suggests that the main difference in the depth doses generated using the different spectra for the two Monte Carlo simulations is due to beam hardening of the TERMA.

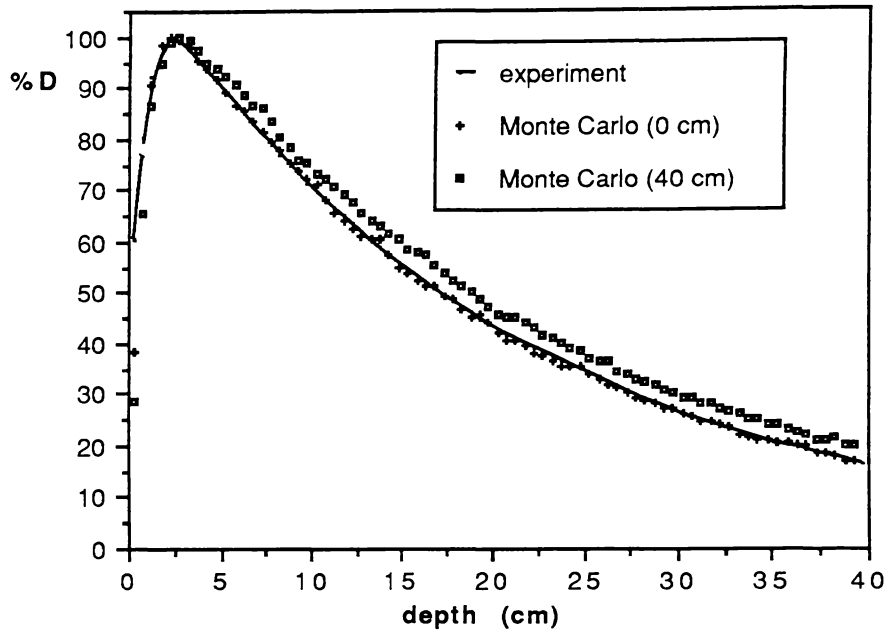

Figure 4.2: Central axis percentage depth dose (%D) curves generated using Monte Carlo (EGS) simulations which follows the histories of 4 million photons. The Monte Carlo simulations are for two different spectral distributions; that typical of a 10 MV surface spectrum (normalisation at D_{max} is 100% = 3.11 pGy MeV^{-1} cm^2) and that typical of a 10 MV beam which has traversed 40 cm of water (normalisation at D_{max} is 100% = 3.98 pGy MeV^{-1} cm^2). Experimental data collected using a PTW ionization chamber in a Therados water tank is also plotted on the graph. The beam size is 5 x 5 cm.

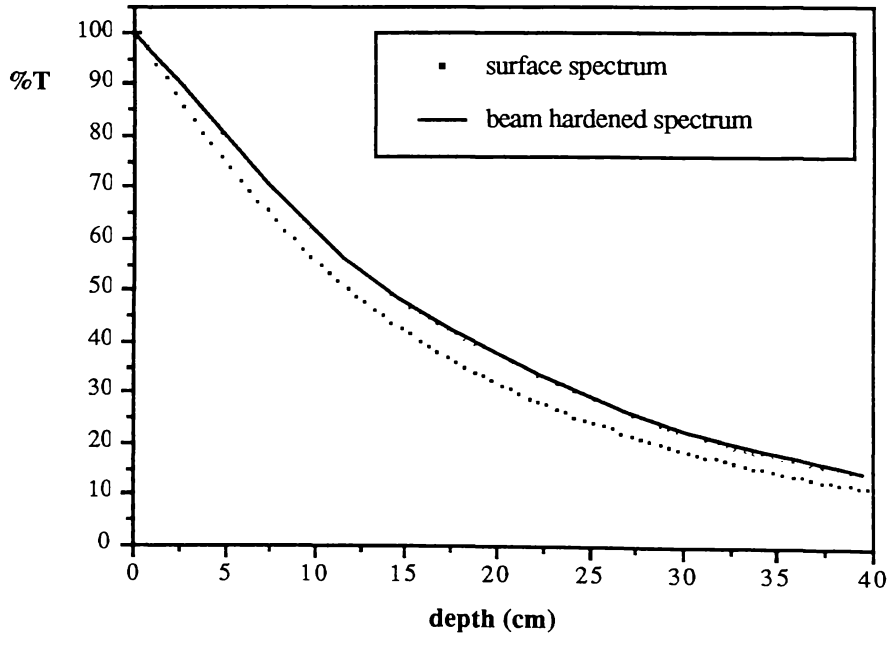

Figure 4.3: Percentage TERMA versus depth curves. The two TERMA curves are for the surface spectrum and beam hardened spectrum respectively. The curves have been normalised to 100% at the surface. Normalisation at the surface T_{max} for the surface spectrum is 100% = 6.03 pGy MeV^{-1} cm^2, and normalisation at the surface T_{max} for the beam hardened spectrum is 100% = 5.42 pGy MeV^{-1} cm^2.

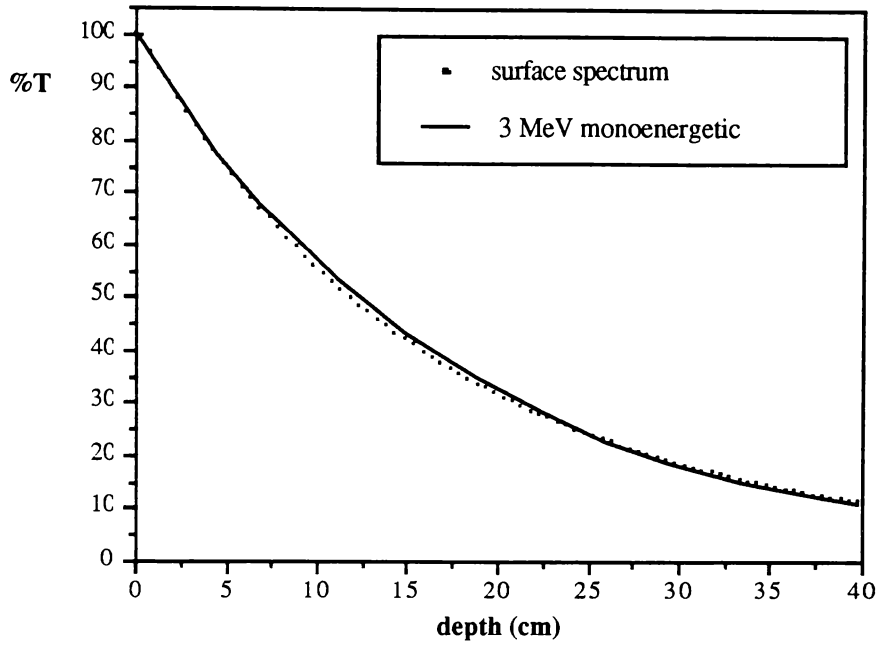

Figure 4.4: Percentage TERMA versus depth curves. The two TERMA curves are for the surface spectrum and 3 MV monoenergetic spectrum respectively. The curves have been normalised to 100% at the surface. It is difficult to see the differences on the graph but they are up to 6% at 40 cm. Calculation of data not shown on the graph at 50 cm showed a difference of 10% (These differences were assessed using (3.21) in section 3.4.3.2).

To observe the effect of monoenergetic versus polyenergetic spectral assumptions on the relative TERMA, a graph of relative TERMA produced using a nominal 3 MeV monoenergetic beam is plotted against depth in Figure 4.4. This graph also includes a plot of relative TERMA against depth produced by using the polyenergetic beam spectrum. Comparison of the curves in Figure 4.4 shows that the difference between the monoenergetic and polyenergetic TERMA curves is 2% at 10 cm and increases to 6% at 40 cm. This shows that a polyenergetic calculation of the TERMA is preferred.

4.4.2 Change of Beam Spectrum with Depth

It is possible to account for beam hardening effects on fluence (and therefore TERMA) as follows. For a polyenergetic beam where there is a range of photon energies from 0 to E_{max}

$$\Phi(\mathbf{r}') = \int_0^{E_{max}} \frac{d\Phi(\mathbf{r}')}{dE} dE \qquad (4.12)$$

where $d\Phi(\mathbf{r}')/dE$ is the photon fluence in a unit energy interval at E. For a discrete number of N spectral components:

$$\Phi(\mathbf{r}') = \sum_{n=1}^{N} \Phi_n(\mathbf{r}') \tag{4.13}$$

where

$$\Phi_n(\mathbf{r}') = \left(\frac{\mathbf{r_0}}{\mathbf{r}'}\right)^2 \Phi_n(\mathbf{r_0})\, e^{-(\mu/\rho)_n |\, \mathbf{r}' - \mathbf{r_0}\, |} \quad , \tag{4.14}$$

and therefore the description of the photon fluence reduction in terms of the discrete polyenergetic spectrum is

$$\Phi(\mathbf{r}') = \left(\frac{\mathbf{r_0}}{\mathbf{r}'}\right)^2 \sum_{n=1}^{N} \Phi_n(\mathbf{r_0})\, e^{-(\mu/\rho)_n |\, \mathbf{r}' - \mathbf{r_0}\, |} \tag{4.15}$$

Note that n = 1 is the first spectral energy component, N is the total number of spectral components, $\Phi_n(\mathbf{r_0})$ is the discrete photon fluence at the surface for the nth spectral component and $(\mu/\rho)_n$ is the attenuation coefficient for the nth spectral component. An inverse square correction $(\mathbf{r_0}/\mathbf{r}')^2$ is also included to account for intensity reduction of the fluence with distance from the source.

Now define $F_n(\mathbf{r_0})$ as the fraction of photons in the nth spectral component at the surface, such that

$$F_n(\mathbf{r_0}) = \frac{\Phi_n(\mathbf{r_0})}{\sum_{j=1}^{N} \Phi_j(\mathbf{r_0})} \tag{4.16}$$

and at $\mathbf{r}'$

$$F_n(\mathbf{r}') = \frac{\Phi_n(\mathbf{r}')}{\sum_{j=1}^{N} \Phi_j(\mathbf{r}')} \quad . \tag{4.17}$$

Now substituting (4.14) into (4.17), and replacing $\Phi_n(\mathbf{r_0})$ with $F_n(\mathbf{r_0})$ using (4.16) then

$$F_n(\mathbf{r}') = \frac{F_n(\mathbf{r_0})\, e^{-(\mu/\rho)_n |\, \mathbf{r}' - \mathbf{r_0}\,|}}{\sum_{j=1}^{N} F_j(\mathbf{r_0})\, e^{-(\mu/\rho)_j |\, \mathbf{r}' - \mathbf{r_0}\,|}} \quad . \tag{4.18}$$

A normalised photon spectrum at any depth may now be found from the normalised spectrum at the surface. Values used for F_n have been calculated for the ten component spectrum as it is attenuated down to 25, 40 and 50 cm depth and these values are listed in Table 4.1 (rows 4, 5 and 6). The data in Table 4.1 shows that there is a higher relative proportion of low energy spectral components for the surface spectrum than for the spectrum at depth. This is due to the more rapid attenuation of the low energy components with depth. The normalised fluence at any depth may then be used to generate the PDSAs using the method outlined in section 4.3. In this manner the effect of changing energy fluence with depth is accounted for.

Energy E_n (MeV)	0.5	1.5	2.5	3.5	4.5	5.5	6.5	7.5	8.5	9.5
$(\mu/\rho)_n$*	.0969	.0575	.0445	.0368	.0321	.0289	.0284	.0251	.0237	.0227
$\%F_n$, d_{ref} = 0 cm	17.5	22.0	20.4	12.9	9.2	7.1	4.9	3.2	1.9	0.9
% F_n, d_{ref} = 25 cm	5.1	16.6	21.1	16.0	12.8	10.7	7.5	5.3	3.4	1.5
% F_n, d_{ref} = 40 cm	2.0	12.8	19.5	16.8	14.4	12.7	8.9	6.6	4.2	2.1
% F_n, d_{ref} = 50 cm	1.2	10.4	18.3	16.8	15.2	13.7	9.8	7.5	4.8	2.3
% F_n 3 MeV MDSA	100% and $(\mu/\rho)_n$* = 0.397									

Table 4.1: Spectral data and mass attenuation coefficients used in generating fluence information and also used in the 5 x 5 cm full field Monte Carlo simulation.
* Attenuation coefficients are from Johns and Cunningham (1983).

4.5 DOSE SPREAD ARRAYS

4.5.1 Polyenergetic Dose Spread Array Profiles in Polar Co-ordinates

Sets of DSA data were formed by simulating 250 000 photons interacting at a point at the origin of a polar co-ordinate system and following their dose deposition histories. Figure 4.5 shows the DSA scoring geometry used in the EGS simulation. A scoring voxel is defined as the ring shaped region formed by the intersection of a concentric radial shell and a discrete polar angular interval. The radial shells have a thickness of 1 mm and the angular intervals span 5 degrees. The "voxel radius" r_i is defined as the distance from the origin to the centre of the shell, and the "polar angle" θ_i is defined as the angle to the centre of the voxel.

Important parameters used in the EGS simulation are outlined in Table 4.2.

PARAMETER NAME	DESCRIPTION	VALUE
EI	Incident photon energies	Spectra see table 4.1
	Number of photons incident	250 000
ESTEPE	Maximum electron energy loss per step	0.02
ECUT'	Ek local energy deposition cut-off	50 keV
AE'	Minimum discrete collision energy loss	50 keV
AP	Minimum discrete radiative energy loss	50 keV
PCUT	Photon local deposition energy cut off	50 keV

Table 4.2: EGS parameters used in MDSA and PDSA Monte Carlo simulations. Vax 6330-CPU time for each simulation was approximately 12 hours.

The EGS simulation gives results in terms of energy deposition per voxel volume as a fraction of the energy released at the interaction site. Because the voxels are of unequal volume, the result is then divided by voxel volume to give values which are defined as fractional energy deposition per unit volume (Ahnesjö 1989), in units of cm^{-3} .

In Figures 4.6 and 4.7, DSA values produced from the EGS simulation are plotted against distance from the interaction site for a particular angular interval centred at θ_i (for example in Figure 4.6 θ_i = 2.5 degrees). The vertical axis of the graphs are $H(r_i, \theta_i)$ which is the fractional energy deposition per unit volume, and the horizontal axis is the voxel radius r_i of the shell in which the energy is deposited. These graphs have been called "DSA profiles".

Shown in both Figures 4.6 and 4.7 are DSA data produced from three different EGS simulations. In one simulation 3 MeV mononchromatic dose spread array (MDSA) data is produced (this is the mean weighted energy of the 10 MV beam); the other two simulations produced PDSA data using spectral components encountered at two depths, d_{ref} = 0 cm and d_{ref} = 40 cm respectively. Graphs for two angular intervals are shown with θ_i = 2.5 degrees in Figure 4.6 and θ_i = 47.5 degrees in Figure 4.7. The graphs indicate the reduction of dose deposition with angle and a rapid reduction of dose deposition as the distance from the interaction site increases. As expected, most of the energy is deposited downstream of the interaction site.

Note that the DSAs produced using the polyenergetic beam are significantly different from those produced using the monoenergetic beam. For example, at the location r_i = 8 mm in the polar interval centred at 2.5 degrees, the MDSA line starts to dip below the PDSA lines and the dose deposition is much lower at about r_i = 14 mm, which appears to be the maximum range of electrons from primary interactions. Note at greater angles the difference between initial dose deposition is even greater (see Figure 4.7). This is because the dominant Compton scattering angles are more obvious for the MDSA profile than for the PDSA profile. These results demonstrate that the use of MDSA data is probably inadequate for the superposition process. This assumption is confirmed in the next section.

Using the beam hardened spectrum to generate a PDSA profile also induces relative energy deposition differences between the PDSA profiles. Note the PDSA profile data for the beam hardened spectrum falls off more slowly than that of the surface spectrum (see Figures 4.6 and 4.7). The magnitude of this effect is not clearly shown on the plots because of the log scale on the vertical axis (which is unavoidable due to the rapid energy deposition fall off). Note that these differences lead to very small spatial differences of about 1 mm between the profiles. Once again this is because of the rapid energy fall off.

To examine the effect of beam hardening, further PDSAs were produced for depths of 25 cm and 50 cm (see Table 4.1, rows 4 and 6). This data was in turn compared with the PDSA for the spectrum at the surface. The results are shown in Figure 4.8 for the polar angle 47.5 degrees. These results demonstrate that beam hardening induces relative dose differences close to the interaction site.

It is important to realise that the actual contributions to dose at larger distances from the interaction voxel are several orders of magnitude lower than those close to the interaction voxel. The difference in dose is caused by harder spectra. Note, for example, that the beam hardened DSAs show slightly more energy deposition at a greater voxel radius than the surface DSA. The insignificance of this difference to the accuracy of the superposition process is outlined in section 4.6.

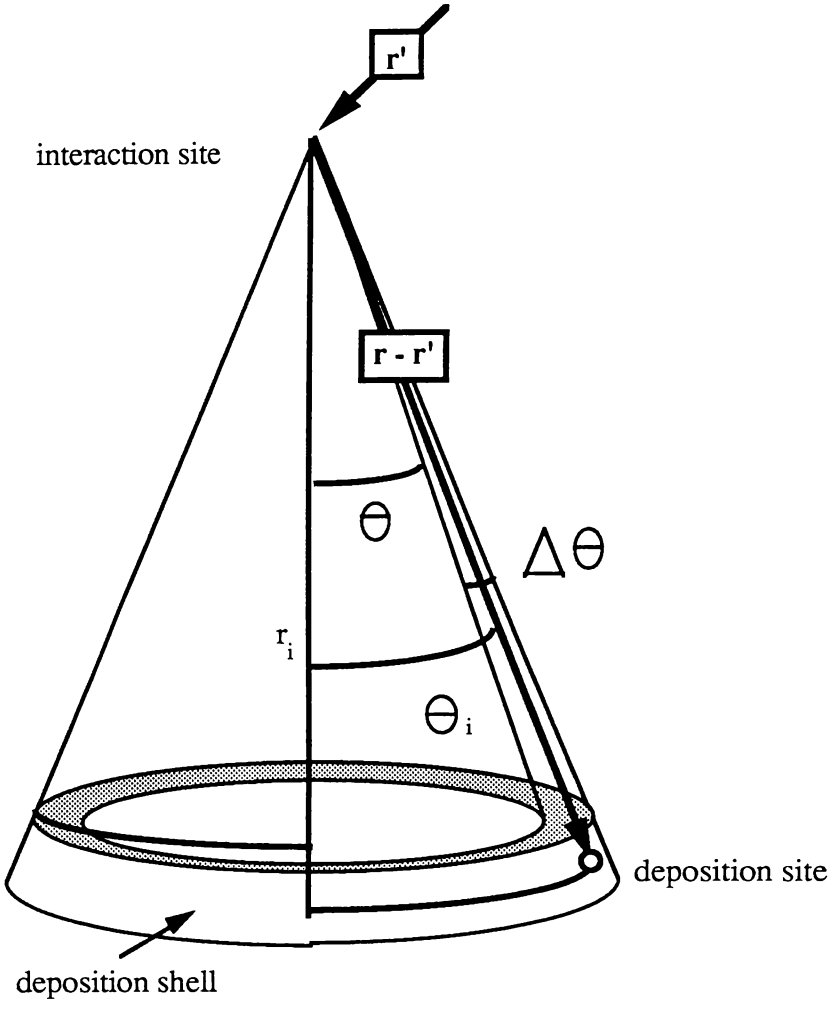

Figure 4.5: Polar geometry describing the DSA scoring co-ordinate framework used in the EGS simulations. The photon interacts at the primary interaction site and dose is scored in a shell of mean voxel radius r_i. The dose is scored into a volume defined by the polar voxel interval within the angle θ and $\theta+\Delta\theta$ which has a mean shell angle θ_i.

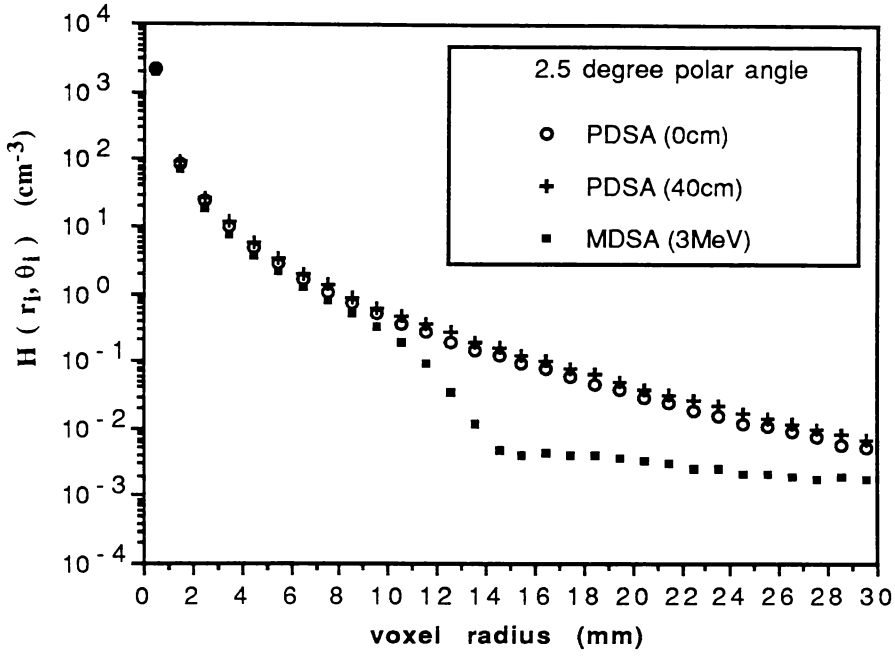

Figure 4.6: Total PDSA profiles showing relative dose plotted against voxel radius r_i for the θ_i = 2.5 degrees polar angle. The PDSAs were generated using the surface polyenergetic spectra (see Table 1, row 3) and the beam hardened 40 cm PDSA (see Table 4.1, row 5). Also included is a profile for a 3 MeV MDSA.

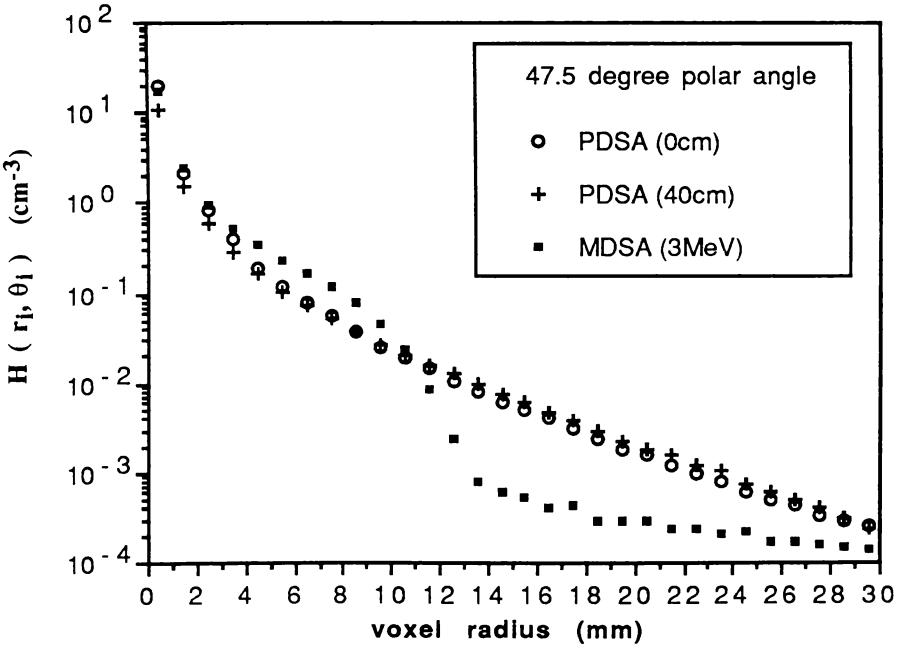

Figure 4.7: Total PDSA profiles showing relative dose plotted against voxel radius r_i for the θ_i = 47.5 degrees polar angle. The PDSAs were generated using the surface polyenergetic spectra (see Table 1, row 3) and the beam hardened 40 cm PDSA (see Table 4.1, row 5). Also included is a profile for a 3 MeV MDSA.

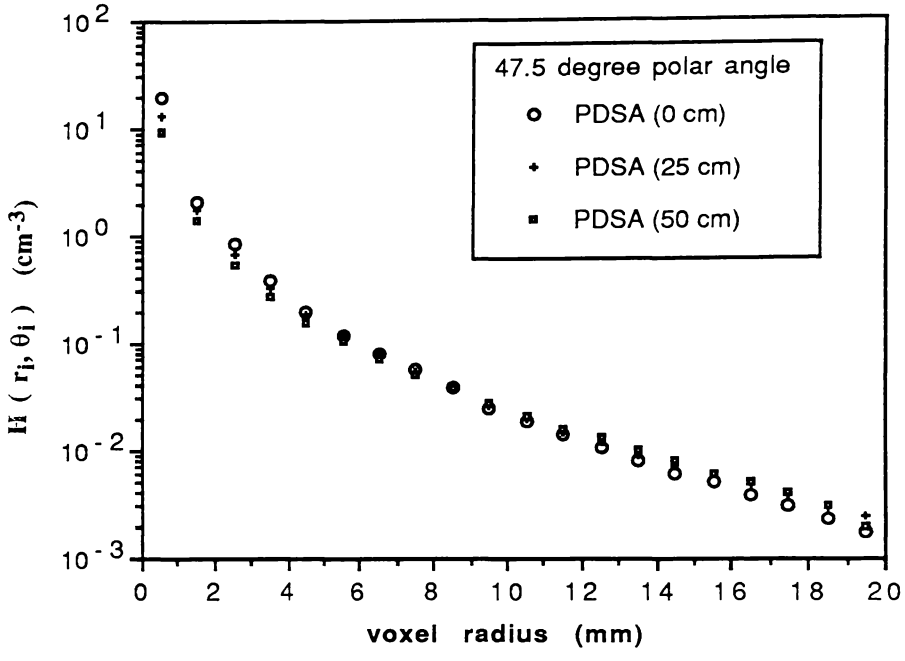

Figure 4.8: Total PDSA profiles showing relative dose plotted against voxel radius r_i for the $\theta_i = 47.5$ degrees polar angle. The PDSAs were generated using the surface polyenergetic spectra (see Table 1, row 3) and the beam hardened 25 and 50 cm PDSA (see Table 4.1, rows 4 and 6).

4.5.2 Primary Polyenergetic Dose Spread Array Profiles

The process described above was repeated for the 0 cm and 40 cm PDSAs, except only dose from primary photon interactions at the origin which led to charged particle transport was scored. Mackie *et al* (1988) call these primary dose spread arrays or primary deposition kernels.

This data is shown because it gives an indication of dose deposition from charged particle transport. From this data the effective radius of energy deposition by charged particles has been calculated. If the total PDSAs are used then the range estimate would include the long tail of the DSA due to scattered photon interactions (this increases the mean range estimate by about 50%). The graphs of Figures 4.9 and 4.10 show the "primary DSA profiles" for two angular intervals, the interval centred at $\theta_i = 2.5$ degrees (figure 4.9) and the interval centred at $\theta_i = 47.5$ degrees (Figure 4.10).

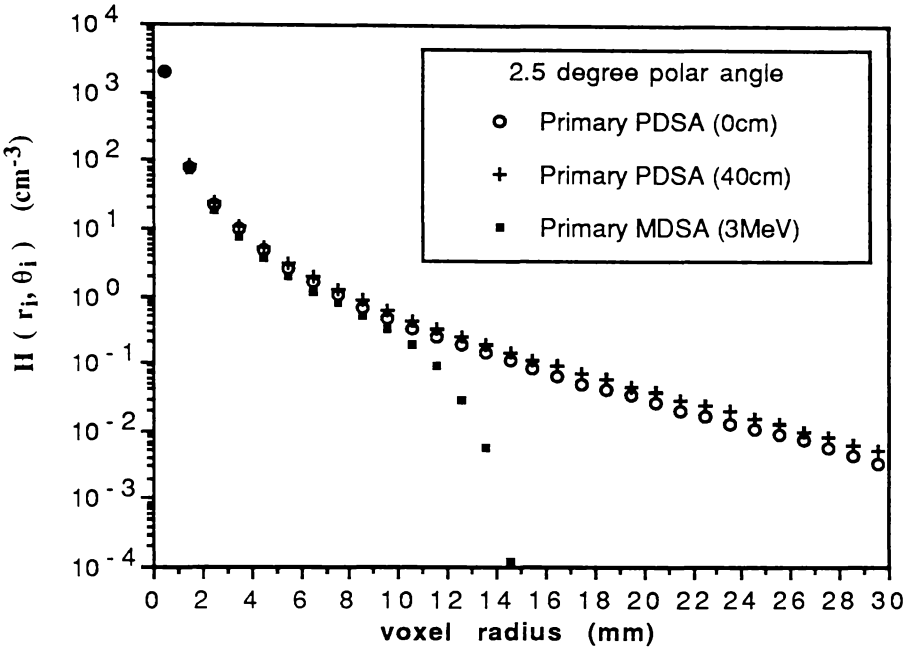

Figure 4.9: Primary PDSA profiles showing relative dose plotted against voxel radius r_i for the θ_i = 2.5 degree polar interval compared with primary MDSA profiles produced using a monoenergetic 3 MeV beam.

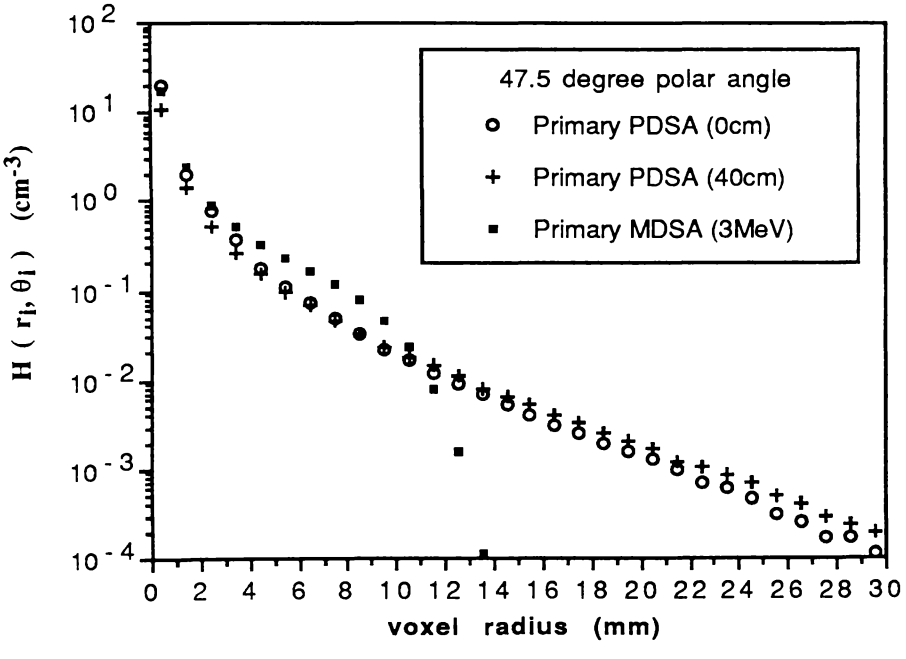

Figure 4.10: Primary PDSA profiles showing relative dose plotted against voxel radius r_i for the θ_i = 47.5 degree polar interval compared with primary MDSA profiles produced using a monoenergetic 3 MeV beam.

Note that the energy deposition close to the interaction voxel is very similar to the values obtained for the total DSA profiles. However, the profiles diverge from those of Figures 4.6

and 4.7 further from the interaction voxel because the flat tail due to secondary photon interactions is not present in these profiles. The difference between the surface and beam hardened PDSA primary profiles is once again small, however the fall off is much less rapid for both of the polyenergetic profiles than the monoenergetic DSA profile. This is because of the much broader range of electron energies present in the case of the PDSA, leading to a less defined electron range.

4.5.3 Effective Range of Energy Deposition for Primary PDSAs

Mackie *et al* (1988) have shown that the assumption of dose deposition at the geometric voxel centre is not valid when an accurate assessment of primary DSA charged particle range is required. For this reason a method has been developed for calculating the effective range within the EGS simulation, using the position of each charged particle step. This avoids the need to calculate the effective voxel centre as is the case when energy scored per voxel is used to calculate the range (Mackie *et al* 1988).

This has been achieved using the position of each charged particle step relative to the primary interaction point. Energy ε_n is deposited for the nth step, and the effective charged particle range r_{eff} is given by

$$r_{eff} = \frac{\sum_{n=1}^{N} \varepsilon_n \, (x_n^2 + y_n^2 + z_n^2)^{1/2}}{\sum_{n=1}^{N} \varepsilon_n} , \qquad (4.19)$$

where x_n, y_n, and z_n are the cartesian co-ordinates describing the particle's position and the interaction occurs at (x, y, z) = (0, 0, 0). To ensure that energy is deposited on average at the centre of the charged particle step, the position of energy scoring alternates between the beginning and end of the steps for each successive particle history.

Similarly the effective longitudinal range z_{eff} can be established as

$$z_{eff} = \frac{\sum_{n=1}^{N} \varepsilon_n \, z_n}{\sum_{n=1}^{N} \varepsilon_n} , \qquad (4.20)$$

and the lateral range y_{eff} is defined here as

$$y_{eff} = \frac{\sum_{n=1}^{N} \varepsilon_n (x_n^2 + y_n^2)^{1/2}}{\sum_{n=1}^{N} \varepsilon_n} . \qquad (4.21)$$

A summary of the range calculation results is given in Table 4.3. MDSA results show good agreement with the calculations of Mackie *et al* (1988) for a 3 MeV dose spread array for all range calculations. The table also indicates the longer effective range of the PDSAs compared to the MDSA. The difference in mean ranges between the surface and beam hardened PDSAs is small (less than 1.5 mm) for all component range calculations. Note that Mackie *et al* (1988) use a different definition of lateral range to calculate y_{eff} which produces slightly different results. Mackie determines y_{eff} from r_{eff} and z_{eff} using Pythagoras' theorem, $(y_{eff})^2 = (r_{eff})^2 - (z_{eff})^2$. The effective position of energy deposition is therefore defined as a circular region centred a distance z_{eff} from the primary interaction site along the direction of the incident photons, with radius y_{eff}. A simple illustration of the difference between (4.21) and Mackie's definition of y_{eff} can be made by considering the case where energy deposition is restricted to being uniformly deposited on a spherical shell of radius r_{eff}, centred at the primary interaction site. In this case, $z_{eff} = 0$ since the distribution is symmetrical about $z = 0$, therefore by Mackie's definition $y_{eff} = r_{eff}$. Using (4.21), y_{eff} will be less than r_{eff} since $(x_n)^2 + (y_n)^2$ ranges between 0 and $(r_{eff})^2$. The definition in (4.21) is obviously more realistic in this case, since Mackie's method calculates y_{eff} as the maximum lateral range. Results calculated using Mackie's method are also shown in Table 4.3.

Type of DSA	z_{eff}	r_{eff}	y_{eff}	y'_{eff}
primary surface PDSA	5.73	6.67	2.79	3.41
primary 40 cm PDSA	7.15	8.24	3.35	4.09
primary mono. 3 MeV DSA	3.95	4.81	2.28	2.74
primary mono. 3 MeV DSA$^+$	3.968	4.803	-----	2.705

Table 4.3: The effective depth of penetration z_{eff}, the effective range r_{eff} and the effective lateral distance y_{eff} of charged particle transport generated by primary dose spread arrays. The term y'_{eff} is the lateral range calculated using another method (Mackie *et al* 1988). The units of range are in mm. $^+$ Data from (Mackie *et al* 1988)

4.5.4 Isoline DSA Distributions

In order to get a better indication of spatial energy distributions of DSAs, they are represented in isolines of relative dose deposition (units cm^{-3}) (ie. lines of equal relative dose deposition). The plots shown in Figures 4.11, 4.12 and 4.13 are the isolines plotted for polar angle θ_i versus voxel radius r_i.

Figure 4.11 shows the isoline distribution for the 3 MeV MDSA and Figure 4.12 shows the isoline distribution for the surface spectrum 10 MV PDSA. Both distributions show that most energy is distributed down stream from the interaction site, although the 3 MeV MDSA plot shows less penetration. To more clearly demonstrate the differences, a single isoline for different DSAs are presented in Figure 4.13, the least penetrative is the 3 MeV MDSA, due to the absence of high energy recoil electrons. The surface 10 MV PDSA and beam hardened 10 MV PDSA show very small spatial differences, with the surface PDSA being slightly less penetrating than the beam hardened PDSA.

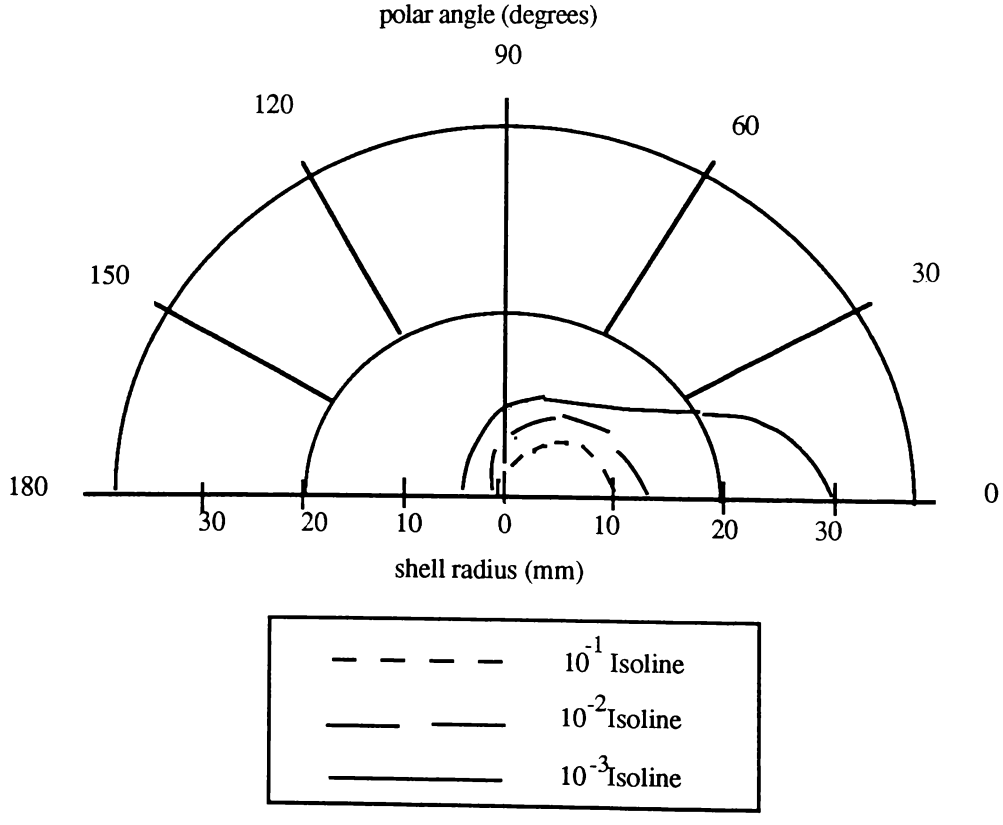

Figure 4.11: Isoline distributions showing levels of equal energy deposition within a mean polar angle versus mean shell radius. MDSA 3 MeV isoline distribution showing 10^{-1}, 10^{-2}, 10^{-3} levels (units cm^{-3}).

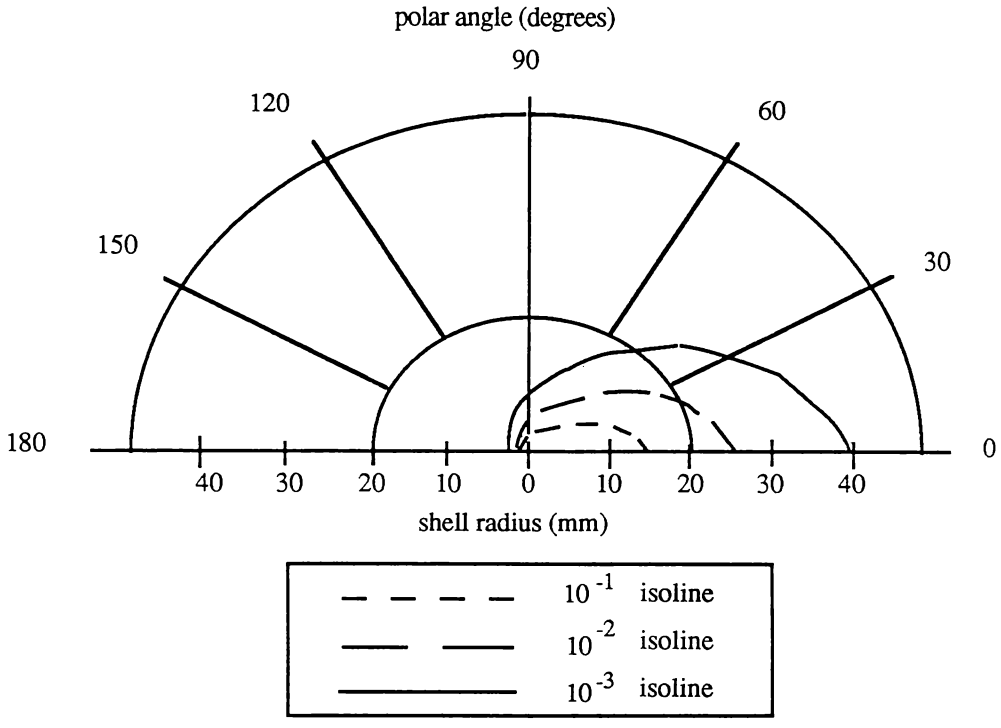

Figure 4.12: Isoline distributions showing levels of equal energy deposition within a mean polar angle versus mean shell radius. Surface 10 MV PDSA distribution showing 10^{-1}, 10^{-2}, 10^{-3} levels (units cm^{-3}).

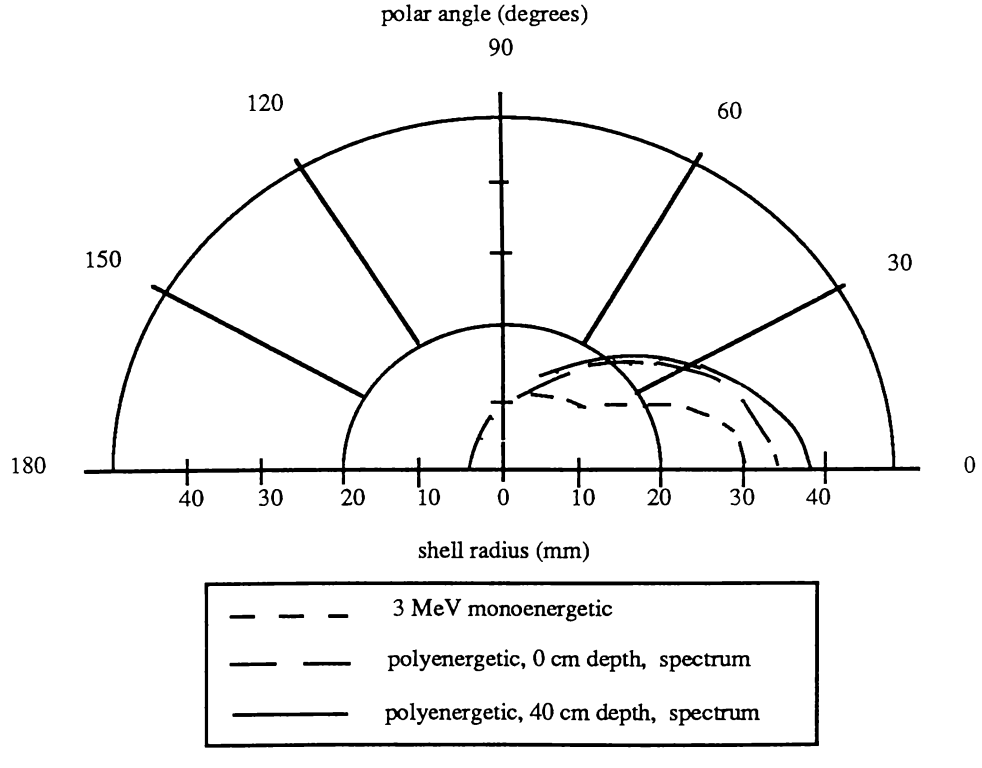

Figure 4.13: Different DSAs intercompared as isoline distributions, showing the 10^{-3} isoline level for the 3 MeV MDSA, total 0 cm depth 10 MV PDSA and total 40 cm depth 10 MV PDSA respectively.

4.5.5 DSAs in Cartesian Co-ordinates

In order to carry out superposition one can use polar arrays directly (Mohan *et al* 1986) or Cartesian arrays of data. The computation method for superposition presented here uses Cartesian arrays. The cartesian arrays are fomulated by "forcing" primary photons to interact within a voxel and "scoring" the dose in other voxels (Mackie 1983).

A very small part of these Cartesian DSAs used in the superposition are shown in Figure 4.14. The energy is deposited in $(5\ mm)^3$ Cartesian voxels and is shown across the central axis of a symmetric quadrant. The upper numeric values shown in Figure 4.14 are the fractional energy deposition per unit volume for the surface 10 MV PDSA and the lower numeric values in each voxel are the fractional energy deposition per unit volume due to the beam hardened 10 MV PDSA. This representation clearly shows that most energy is deposited in the interaction voxel but a significant amount of energy is also deposited in the other voxels. The fractional energy deposition in the interaction voxel is higher for the surface 10 MV PDSA than the beam hardened 10 MV PDSA but the differences in the other voxels are small.

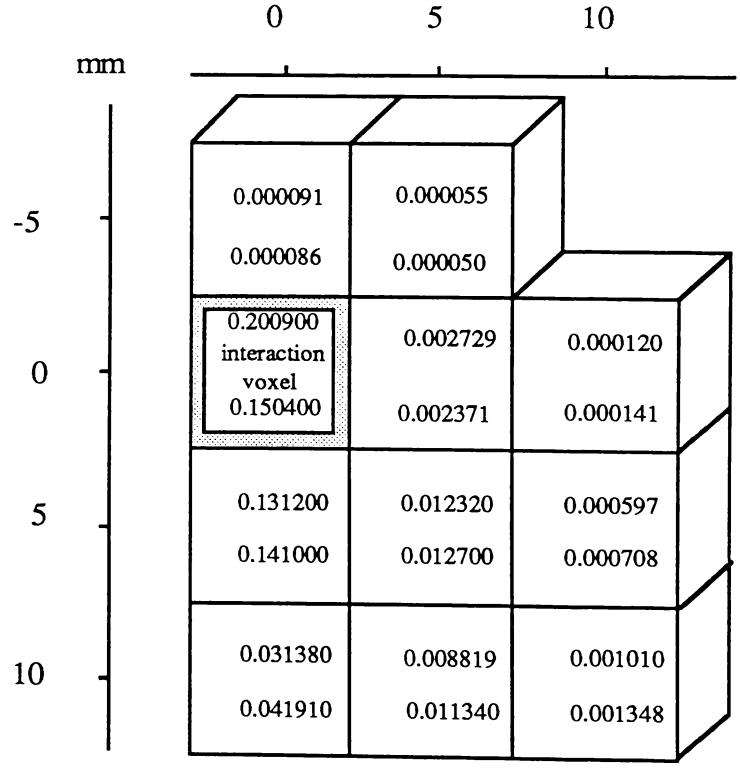

Figure 4.14: Two-dimensional single quadrant representation of DSAs scored in Cartesian co-ordinates. The upper values in each voxel refer to the dose deposition values obtained using the 0 cm depth, 10 MV PDSA spectrum. The lower values in each voxel refer to the values obtained using the 40 cm depth, 10 MV PDSA spectrum (units cm^{-3}).

4.6 SUPERPOSITION RESULTS IN THE HOMOGENEOUS ENVIRONMENT

The superposition program used to test the effect of beam hardening on the superposition process was developed by Murray *et al* (1989, 1990), and further details of profile measurement tests are provided in these papers. For details of comparisons in the build up region of the beam, the work of Harper is relevant (Harper 1990, Harper *et al* 1990). The program can perform superposition in Fourier space or real space. The calculations outlined in this section used Cartesian dose spread arrays generated in Cartesian co-ordinates which were "superposed" using real space superposition.

Figure 4.15 shows the central axis percentage depth dose (%D) curve for a 5 x 5 cm beam generated by superposition of the surface spectrum PDSA with a surface spectrum TERMA (which alters due to beam hardening with depth), the process is described by (4.10). Other field sizes produce similar results but for the sake of brevity these are not examined here. Also shown on the graph are depth dose readings obtained using a PTW (0.1cc) thimble ionization chamber in a Therados RFA3 water tank. The results show a mean difference (see (3.21)) of 1.2% down to 20 cm and 2.8% down to 40 cm. Shown in Figure 4.16 is the curve generated by superposition of a beam hardened PDSA with a surface spectrum TERMA. These results differ from the experimental results by 2.9% down to 40 cm.

Note the computed depth dose results obtained using superposition of the surface and hardened PDSAs in figures 4.15 and 4.16 are virtually the same, with the mean difference between these two curves being only 0.1%. This shows that the accuracy of the spectrum used to calculate the PDSA has very little effect on the resulting superposition calculated depth dose curve. It is shown next, however (Figure 4.17), that an MDSA calculated from a single assumed equivalent energy is not adequate for accurate superposition results.

The small difference in results using the two PDSAs indicates that the use of a single PDSA is adequate to model beam depth dose characteristics in a homogeneous water medium down to 40 cm depth. This demonstrates that not accounting for beam hardening of the PDSA component does not cause a significant error in percentage depth dose calculation.

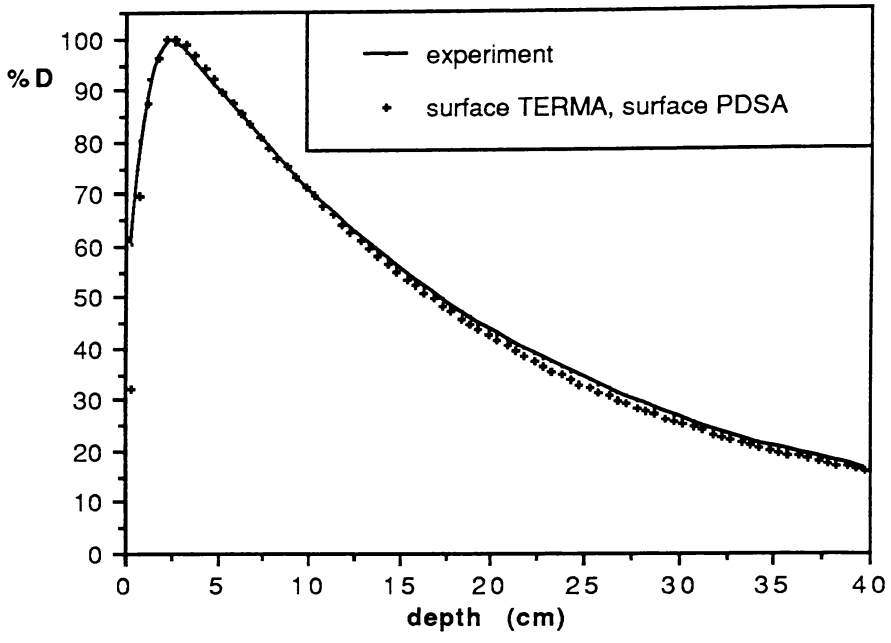

Figure 4.15: The central axis percentage depth dose (%D) curve for a 5 x 5 cm beam generated by superposition of the surface PDSA with a surface spectrum TERMA (normalisation at D_{max} is 100% = 3.13 pGy MeV^{-1} cm^{-2}). The data for an experimental depth dose curve obtained using a PTW ion chamber is also shown.

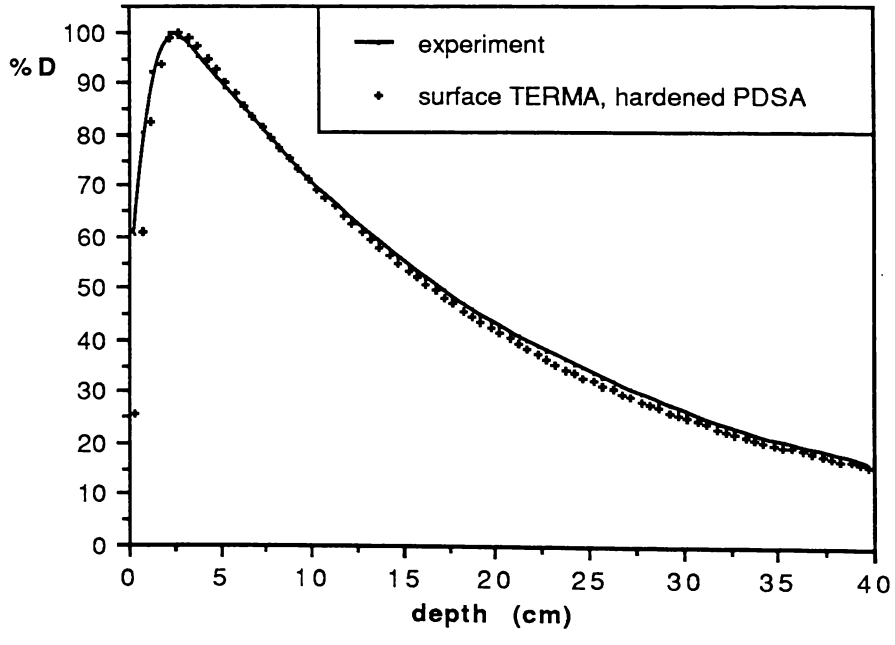

Figure 4.16: The central axis percentage depth dose (%D) curve for a 5 x 5 beam generated by superposition of the PDSA produced by a beam hardened 40 cm spectrum with a surface spectrum TERMA (normalisation at D_{max} is 100% = 3.30 pGy MeV^{-1} cm^{-2}). The data collected using a PTW ion chamber is also shown.

Shown in Figure 4.17 is a central axis depth dose curve generated by superposition of the 3 MeV monoenergetic DSA (MDSA) with the polyenergetic TERMA. Also shown is the experimental depth dose curve obtained. Comparison of the curves shows that the curve produced by superposition of an MDSA is too sharp in the build up region and the depth dose (fall off) region shows a mean difference from experimental data of 8%. It is obvious from the inaccuracy in results shown in Figure 4.17 that superposition involving the use of an MDSA does not produce sufficiently accurate depth dose information for radiotherapy treatment planning.

The graph of Figure 4.18 shows the depth dose curve obtained by superposition of the 0 cm 10 MV PDSA with TERMA calculated using the 40 cm 10 MV spectrum. This depth dose curve shows a mean difference of 8.2% from the experimental results. It is obvious from the inaccuracy in results shown that superposition involving the use of the wrong spectrum for the TERMA calculation does not produce sufficiently accurate depth dose information for radiotherapy treatment planning. It is also apparent from this result that it is the spectrum used for calculating the TERMA which most affects the shape of the depth dose curves.

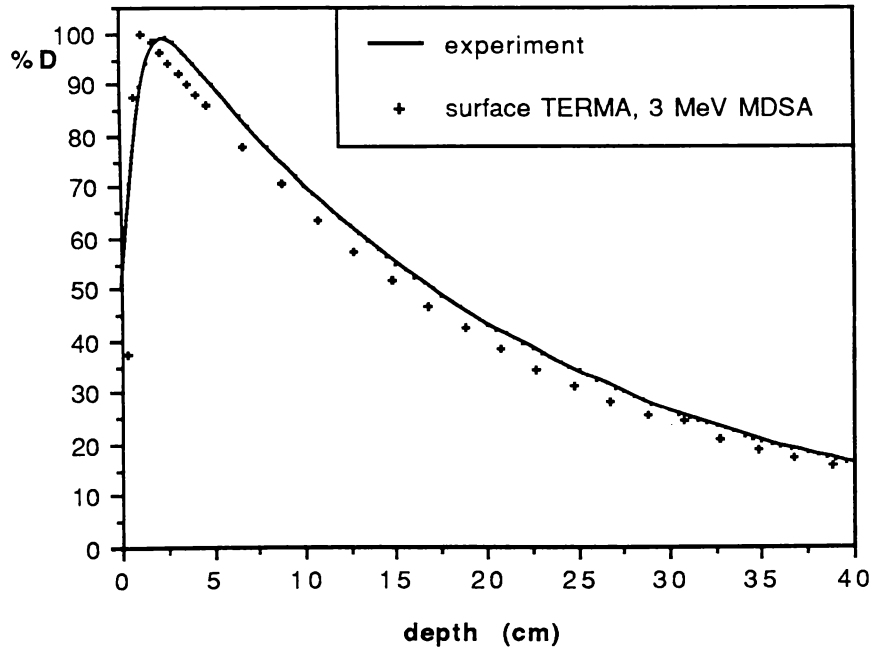

Figure 4.17: The central axis percentage depth dose (%D) curve for a 5 x 5 cm beam generated by superposition of the 3 MeV MDSA with a surface spectrum TERMA. Also plotted is the experimental central axis depth dose curve obtained using a PTW ionization chamber in a Therados water tank.

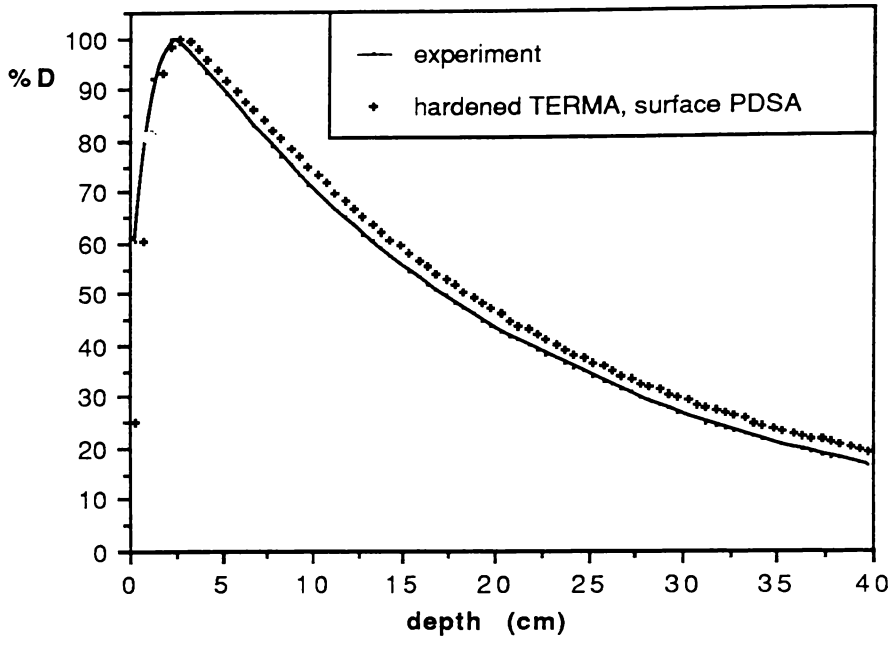

Figure 4.18: The central axis percentage depth dose (%D) curve for a 5 x 5 beam generated by superposition of the 0 cm 10 MV PDSA with the 40 cm 10 MV spectrum used to calculate the TERMA (normalisation at D_{max} is 100% = 2.83 pGy MeV^{-1} cm^{-2}). Also plotted is the experimental central axis depth dose curve obtained using a PTW ionization chamber in a Therados water tank. A comparison of results shows that the superposition data points do not coincide well with the experimental data. This is because the spectrum used to calculate the TERMA is not correct for this beam.

4.7 SUPERPOSITION IN THE INHOMOGENEOUS ENVIRONMENT

It is obvious that TERMA and DSA arrays obtained for a unit density medium must be scaled according to medium density when dose calculations are to be done in inhomogeneous media. This can be done by using three-dimensional ray tracing techniques.

In practice some modifications are required to this ideal in the interests of computing speed. Detail of the superposition of PDSAs in low density media has been outlined in detail by Hoban *et al* (1990a). In brief, the method uses a three-dimensional ray trace of the TERMA array using a method described by Siddon (1985) combined with a z-direction ray trace used to ascertain scaling information for the DSAs. The z direction ray trace for the DSAs is done to reduce computing time and has no effect on the accuracy in slab inhomogeneities where interfaces are perpendicular to the beam. The method uses interpolation between sets of DSA data scored in density steps. Expressed in cartesian co-ordinates, the dose to a voxel at $i+\Delta i$, $j+\Delta j$, $k+\Delta k$ due to an interaction voxel i, j, k is given by (Hoban *et al* 1990a):

$$D(i + \Delta i, j + \Delta j, k + \Delta k; i, j, k) = TER(i, j, k) \frac{1}{\bar{\rho}} H(\bar{\rho}, \Delta i, \Delta j, \Delta k) \quad , \quad (4.22)$$

where TER is the total energy released and H is the energy spread array. The term $\bar{\rho}$ is calculated as the mean path length in the z direction, such that

$$\bar{\rho} = \frac{\left[\sum_{i=0}^{\Delta k} f_i \, \rho \, [k + i] \right]}{\sum_{i=0}^{\Delta k} f_i} \quad . \quad (4.23)$$

Note that the weighting factor f_i has been set at 0.5 for voxel f_0 and f_k (as this is to the mean of each voxel), and 1 for all intervening voxels. This is known as equal voxel weighting and this method was used in all results shown in Figures 4.19 - 4.25. The method is similar to that developed by Mackie (1985). Hoban *et al* (1990a) has also found some increase in interaction voxel weighting is required in the DSA ray trace to account for the electron scattering mechanism. This affect appears to be more marked at low densities as the electrons curved paths approximate less and less to rectilinear scaling. The method of giving more weight to the interaction voxel improves the results in the phantom A by about 2% but in phantom B the improvement is only about 1%. This is because the lower lung density has a larger effect on the linear scaling approximation.

In order to test the accuracy of the implementation in disequilibrium situations the two lung phantom constructed out of polystyrene and cork (density 0.2, phantom A), and muscle (MS10, density 1.0) and lung (LN10/75, density 0.3, phantom B) analog material following the recipes of White *et al* (1977, 1986) were tested. Ionization readings were recorded in the central axis using a Baldwyn Farmer type ionization chamber (with the build up cap removed), in the two lung phantom configurations of dimensions shown in Figures 2.6 and 2.10 respectively .

Shown in Figures 4.19 - 4.24 are ionization chamber readings directly converted to depth dose readings normalised to D_{max}. This can be referred to as an experimental depth dose curve because the ionization fluence correction ratio for the chamber within the lung analog when taken as a ratio to that in tissue analog (TG 21, 1983) defined as $P_{flue,het}/ P_{flue,hom}$ was calculated to be less than 2% using the radial build up factor method of Rice *et al* (1988) (see Appendix 2). The accuracy of the experimental results is further verified by the close agreement of the data points obtained from a full field Monte Carlo simulation of 8.2 million

incident photons, which is also shown on the graph plot of Figure 4.21. The mean difference between the Monte Carlo and experimental results for data points within the lung regions is 1.6%.

Figures 4.19 and 4.20 indicate the range scaled superposition results obtained using the superposition method in the low density cork/polystyrene phantom for 5 x 5 cm and 10 x 10 cm beams respectively. The simulations show close agreement with the experimental results.

Figures 4.21 and 4.22 indicate the range scaled superposition results obtained using the superposition method in lung/muscle analog phantom for 5 x 5 cm and 10 x 10 cm beams respectively. The simulations show close agreement with the experimental results. The mean percentage difference between the superposition and experimental data, shown in Figure 4.22, in the lung regions for the 5 x 5 cm simulation is 2.0%. The percentage difference between the superposition and Monte Carlo results in the lung regions is 1.6%. Therefore the superposition results show good agreement with experiment and Monte Carlo simulations respectively.

Lines produced using the E-TAR (Sontag and Cunningham 1978) and the Batho dSAR (Wong and Henkelman 1983) correction methods are also shown in chapter 3 and compared to the experimental results. For the convenience of the reader some results from chapter 3 are re-presented in Figure 4.23 along with superpositon and experimental results for a 5 x 5 cm field, 10 MV in the lung phantom B. The difference in the data points and for experimental results within the lung regions was calculated using (3.22). For the E-TAR correction the difference is 3.5% and for the Batho correction the difference is 12.3%, whereas for the superposition method the difference is only 2.0%. Despite the match being better in the central axis for E-TAR than for Batho, this method has previously been shown to be more inaccurate than this, particularly at higher X-ray energies and lower lung densities (Metcalfe and Battista 1988).

To further test the accuracy of the superposition method experimental results for mid lung off-axis profiles are compared with the superposition simulation method. The results of such a study are shown in Figures 4.24 and 4.25 for phantom A and B respectively. The profile shapes produced using superposition follow the experimental results quite well. For example the results show percentage differences at 5 cm off-axis of 6.4% and 4.3%, respectively. This is an improvement in accuracy of a factor of three over the results presented in chapter 3 for methods which use penumbral forming functions.

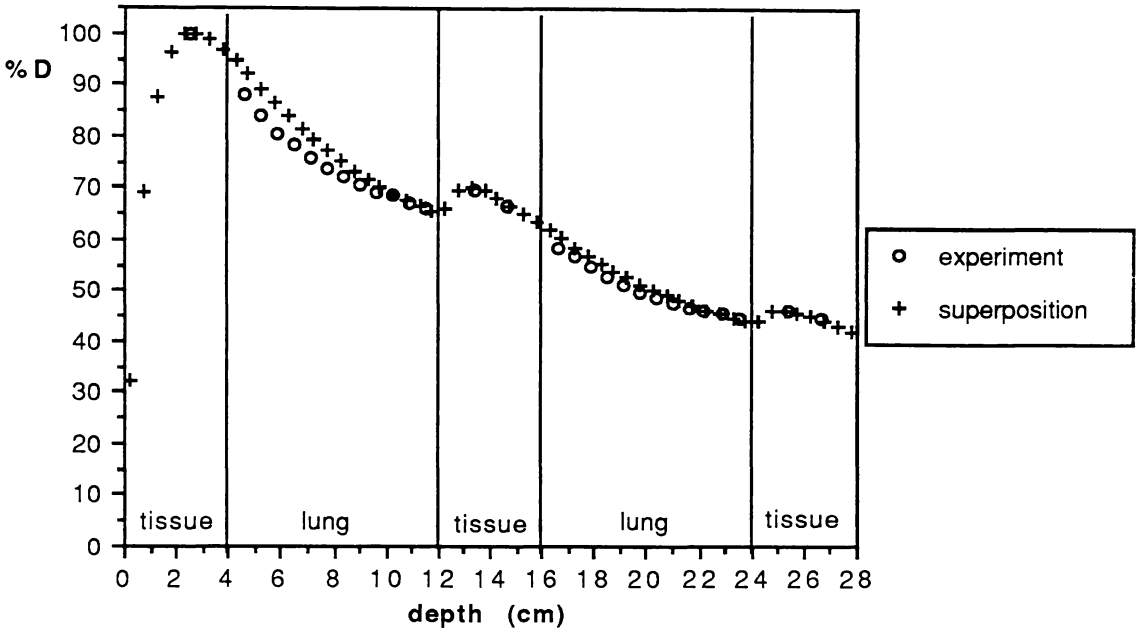

Figure 4.19: Depth dose plots of superposition and experimental measurements:
Beam energy 10 MV, field size 5 x 5 cm, phantom A.
Mean difference 2.3%, mean lung difference 2.7%, maximum difference 6.2%.

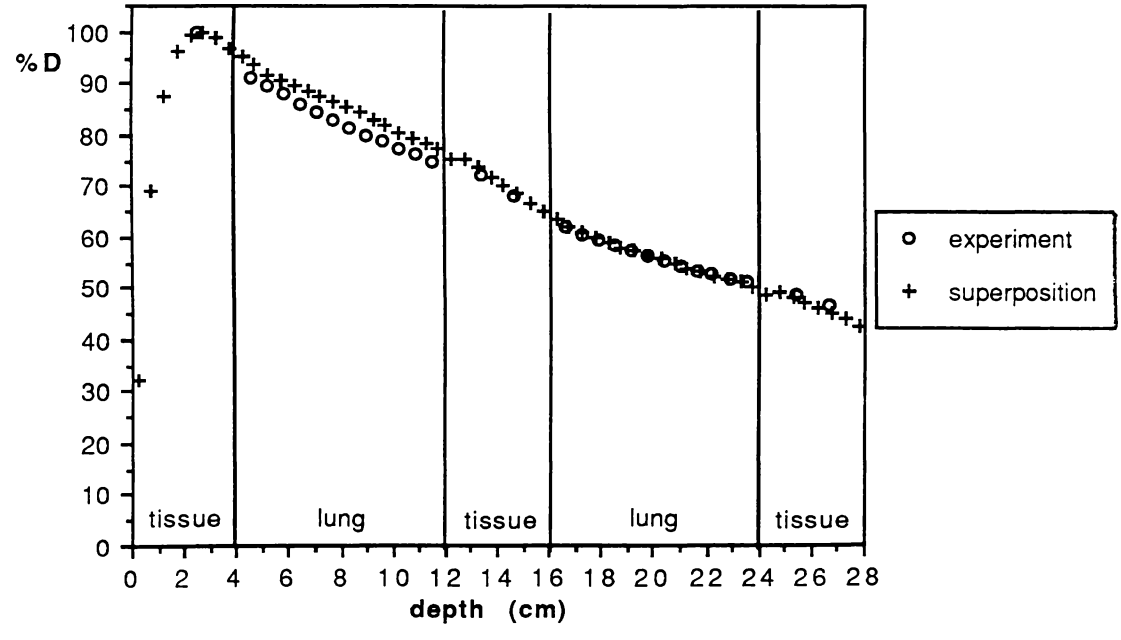

Figure 4.20: Depth dose plots of superposition and experimental measurements:
Beam energy 10 MV, field size 10 x 10 cm, phantom A.
Mean difference 1.9%, mean lung difference 2.0%, maximum difference 4.6%.

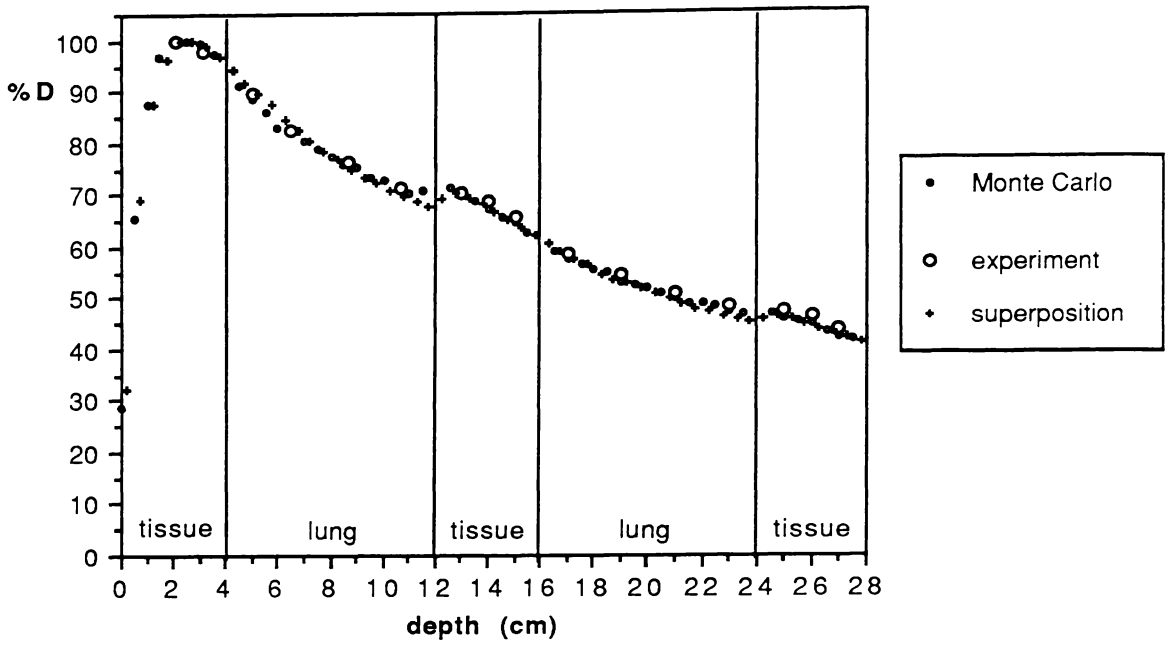

Figure 4.21: Depth dose plots of superposition, Monte Carlo and experimental measurements:
Beam energy 10 MV, field size 5 x 5 cm, phantom B.
Mean difference 2.0%, mean lung difference 2.0%, maximum difference 4.8%.

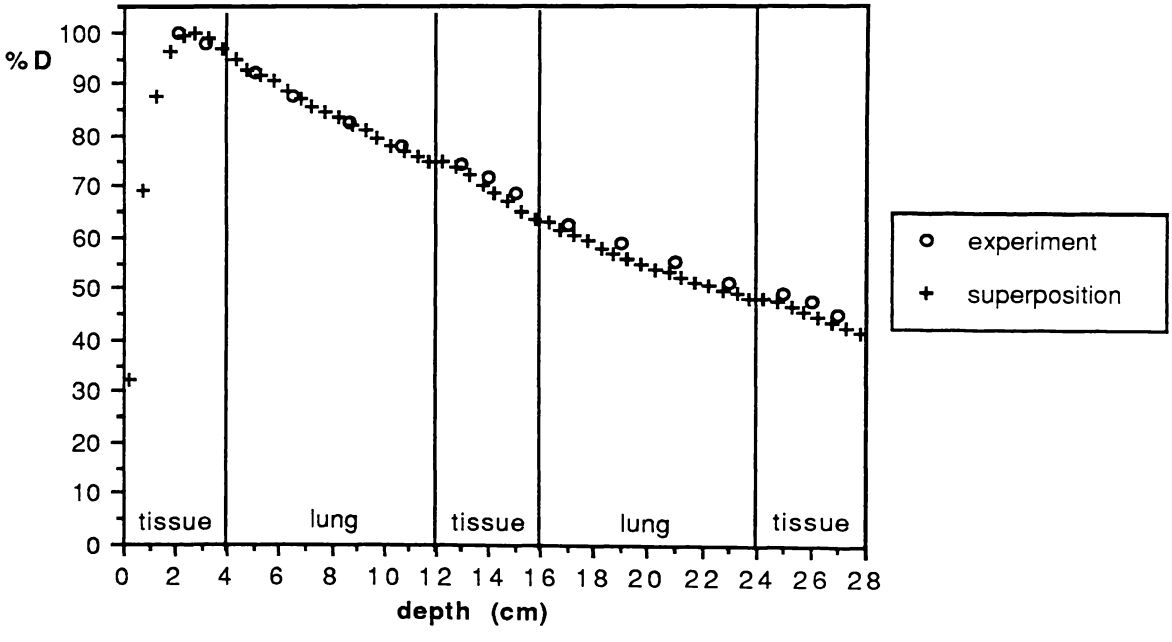

Figure 4.22: Depth dose plots of superposition and experimental measurements:
Beam energy 10 MV, field size 10 x 10 cm, phantom B.
Mean difference 2.9%, mean lung difference 2.5%, maximum difference 7.0%.

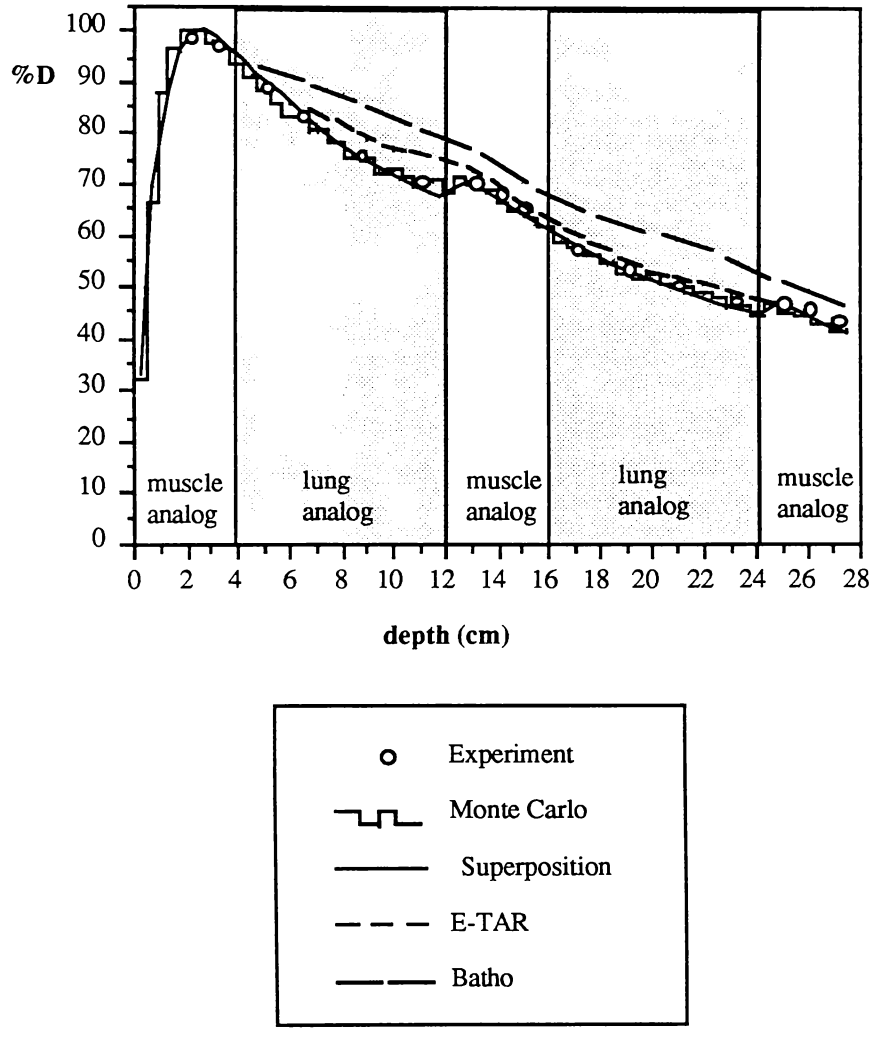

Figure 4.23: Percentage depth dose curves: Comparisons of some data presented in chapters 3 and 4: Data points for Monte Carlo (EGS), superposition, E-TAR and Batho(dSAR) are shown: Beam energy 10 MV, field size 5 x 5 cm, phantom B.

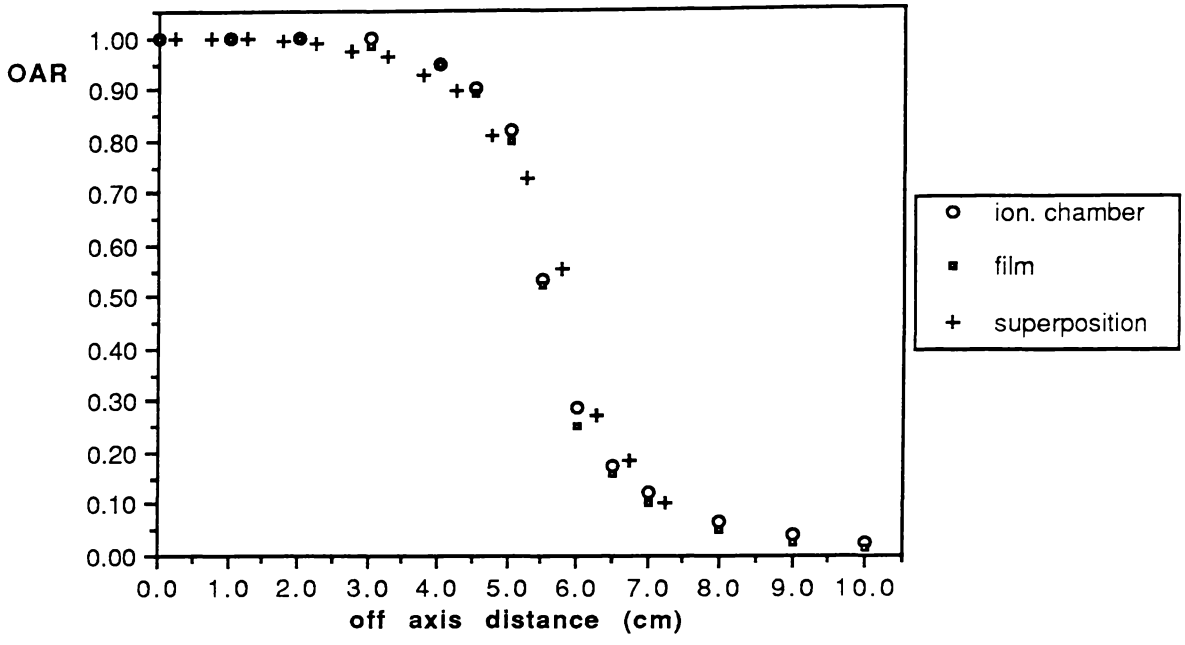

Figure 4.24: Dose profile of off axis ratio versus off axis distance as predicted by superposition:
Also measured with ionization chamber and film at, mid lung, 8 cm depth:
Beam energy 10 MV, field size 10 x 10 cm, phantom A.
Difference at 5 cm is 6.4%.

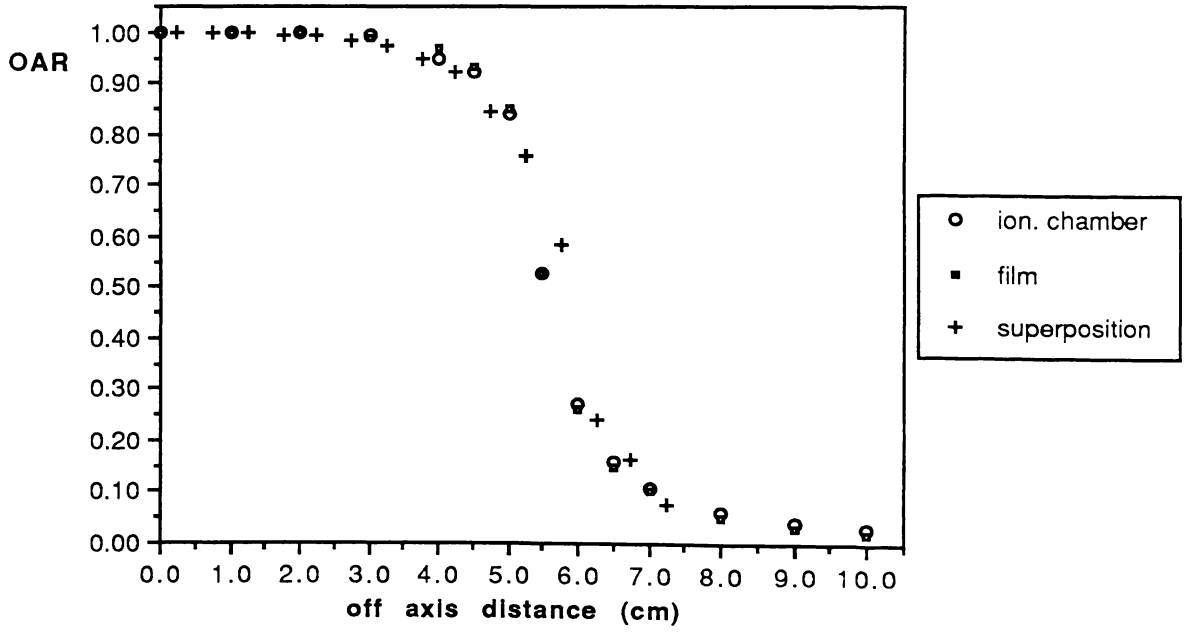

Figure 4.25: Dose profile of off axis ratio versus off axis distance as predicted by superposition:
Also measured with ionization chamber and film at, mid lung, 8 cm depth:
Beam energy 10 MV, field size 10 x 10 cm, phantom B.
Difference at 5 cm is 4.3%.

4.8 CONCLUSIONS

Figure 4.15 indicates that using monoenergetic beam assumptions to model a polyenergetic beam is not sufficiently accurate for radiotherapy planning purposes as recommended by ICRU # 24 (1976). The results show that the MDSAs produced are not adequate models of a polyenergetic beam.

The results in Figures 4.17 and 4.18 show that a calculation of polyenergetic TERMA is a very accurate way to account for attenuation in a polyenergetic beam and this computation should be used in preference to monoenergetic TERMA. It is apparent that since the TERMA is affected in this manner then the DSAs are also affected by beam hardening and this was studied using the EGS Monte Carlo code to generate PDSAs with four different polyenergetic spectra.

By comparing "primary" PDSAs produced at two different depths (0 cm and 40 cm), the effect of beam hardening on the PDSA has been quantified. Calculations outlined in section 4.5.3 show the mean electron range due to the surface primary PDSA is 6.67 mm and the mean electron range of the beam hardened primary PDSA is 8.24 mm. In comparison a 3 MeV primary monoenergetic dose spread array (MDSA) has a much smaller mean electron range of 4.81 mm (see Table 4.3). These electron range calculations show differences of about 1.5 mm between the surface PDSA and the beam hardened PDSA respectively. In contrast the 3 MeV PDSA has a much shorter range.

The superposition process (see Figure 4.17) does give accurate depth dose results down to 40 cm depth using a single surface spectrum dose spread array convolved with a depth dependent polyenergetic TERMA. The correct selection of the spectrum is not critical for the PDSAs but is important when calculating the TERMA.

Work in this chapter provides additional confidence that the convolution method can be used to predict radiation therapy dose. A major conclusion, namely that one needs to account for hardening of the primary photon intensity but that the convolution kernel is relatively invariant with respect to changes in spectrum varifies the assumption made previously by Mackie *et al* (1985a, 1987). The results indicate that production of several DSAs from different spectrum is not essential and this result has major implications in reducing computing time required for the convolution process.

As far as the author is aware this is the first time that the characteristics of PDSAs have been studied in detail. The implications are that point spread distributions typical of that produced by radiotherapy X-ray beams have been visualised and their properties (eg. effective charged particle range) characterised.

Methods of scaling PDSAs and TERMA to account for low density lung inhomogeneous regions show good agreement with experimental results and Monte Carlo simulations, even in regions of lateral electronic disequilibrium. The mean difference between experiment and superposition simulation tested in the two lung phantoms tests is better than 3% in most situations (see Figures 4.19 - 4.25 for details). Note the E-TAR and Batho results show inferior accuracy to the superposition results in all situations tested and reported in this thesis.

With standard methods, the penumbra simply follows the same shape in all media. It should also be remembered that disagreement occurs in the penumbral region even when transient equilibrium is achieved in the centre of these fields at larger field sizes. This effect leads to an isodose flaring effect which is not accounted for by methods which use empirical penumbral forming functions (as do most TAR methods). This flaring is only correctly modelled using superposition and Monte Carlo methods (Ahnesjö 1989). Figure 4.26 is presented which clearly shows the effect of penumbral flaring in lung.

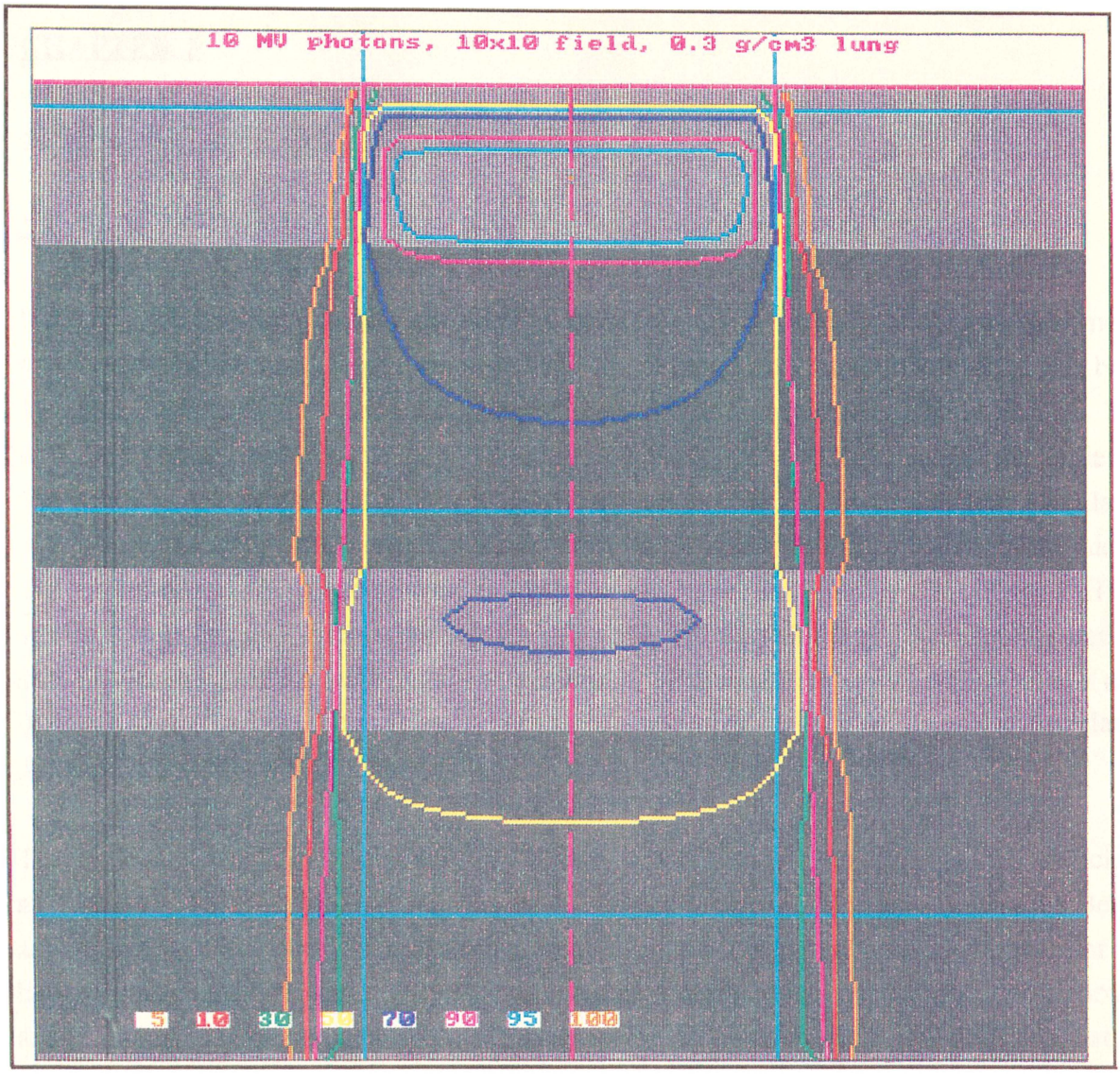

Figure 4.26: Isodose lines showing "penumbral flaring" of a 10 MV X-ray beam in lung as predicted using the superposition scaling method of Hoban *et al* (1990a). The Isodose lines are normalised to 100% at D_{max}. The phantom lung density is 0.3 (ie. phantom B) and the field size is 10 x 10 cm. The flaring clearly indicates that disequilibrium occurs in the penumbral region of standard sized fields in low density media. The figure was produced on the Transputer Treatment Planning System at the University of Waikato.

CHAPTER 5

SUMMARY AND FUTURE PROJECTS

5.1 THE PRODUCTION OF BODY ANALOGS AND PHANTOMS

Bone, muscle and lung analog materials have been manufactured in-house, and dosimetry phantoms have been produced (as described in chapter 2). A method using CT has been developed to check that the analogs match the radiation properties of body tissues. The relative electron densities and ratio of electron cross sections are calculated from elemental compositions of the analogs. Using the data, theoretical CT numbers have been calculated and these numbers were compared with experimental CT numbers for the analogs produced. The experimental CT numbers were found by scanning the samples on a Seimens DRH CT scanner. Results presented in chapter 2 show the maximum difference between theoretical and experimental CT numbers for the analogs is 18 Hounsfield units, which relates to a ΔN_{CT} of less than 1%. Comparison of analog CT numbers with CT numbers for the related patient tissues also shows a close match.

The in-house manufacture of epoxy resin based analogs shows benefit provided sufficient analog has to be manufactured and a suitable laboratory for manufacture is available. Being able to mould the analogs to the required configurations directly is another advantage of in-house production. The CT quality assurance method outlined is advisable for both in-house and commercially acquired analogs, as this provides the physicist with essential information about the radiological properties of the analog.

The production of these analogs has already lead to several useful phantoms being produced for radiological physics applications in CT and radiotherapy. The lung phantom produced was used in subsequent experiments to assess the accuracy of effective path length, Tissue Air Ratio, Monte Carlo and superposition calculations.

5.2 E-DEPTH, BATHO AND E-TAR CORRECTIONS IN LUNG REGIONS

The accuracy of inhomogeneity corrections in a two lung phantom geometry has been discussed in chapters 3 and 4. The photon beam methods reviewed in chapter 3 show inaccuracy in lung, because they fail to account for charged particle transport. The E-depth correction shows large differences (MPD about 10%) for the majority of beam energies and field sizes tested. This is because the method fails to model photon scatter and charged particle transport.

The Batho and E-TAR corrections show small differences (MPD about 3%) in the central axis depth dose regions of 10 x 10 cm field sizes even at 10 MV. This is because these methods account for photon scatter in their scaling procedures. However, the Batho and E-TAR methods display large differences in their off-axis profiles (eg. percentage difference at off-axis distance 5 cm in phantom B is 12.6% for 10 x 10 cm field at 10 MV). This is because these methods use penumbral forming functions which fail to account for loss of electron equilibrium at the penumbral edge of the beam.

The failure to account for charged particle transport leads to electron disequilibrium extending to the centre of the field for 5 x 5 cm fields tested. This leads to MPDs in the central axis of between 3.5 and 6.3% for E-TAR at 10 MV and between 8.8% and 10.0% for Batho (dSAR) at 10 MV. The differences depend on the field size, phantom type, beam energy and correction method employed.

The guideline for dose accuracy recommended by ICRU (1976) is that the total error in dose delivered be less than 5% and the contribution to this error from beam models be less than 2%. Therefore in terms of this guideline all methods reviewed in chapter 3 are inadequate in the central axis region for 5 x 5 cm fields in lung, and are inadequate in the penumbral region in lung for 10 x 10 cm fields.

5.3 PROPERTIES OF POLYENERGETIC DOSE SPREAD ARRAYS

By comparing "primary" PDSAs produced at two different depths (0 cm and 40 cm) in chapter 3, the effect of beam hardening on the PDSA has been quantified. Calculations show the mean electron range due to the surface primary PDSA is 6.67 mm and the mean electron range of the beam hardened primary PDSA is 8.24 mm. In comparison a 3 MV primary monochromatic dose spread array (MDSA) has a much smaller mean electron range of 4.81 mm.

5.4 SUPERPOSITION METHOD ACCURACY IN WATER AND LUNG

Percentage depth dose results from the simulations are compared in homogeneous media and the results are presented in section 4.6. The mean percentage difference between depth dose curves obtained using superposition of surface and beam hardened PDSAs is only 0.1%. The mean percentage difference from experimental data for these superposition curves is 2.8% down to 40 cm in a homogeneous phantom. The superposition process is shown to

be forgiving to spectrally induced differences in the PDSA but sensitive to spectrally induced changes in the TERMA.

Methods of scaling PDSAs to account for lung inhomogeneous regions are discussed in section 4.8 and simulations in the two lung phantoms show good agreement with experimental results and Monte Carlo simulations.

Figures 4.21 and 4.22 indicate the range scaled superposition results obtained using the superposition method in lung/muscle analog phantom for 5 x 5 cm and 10 x 10 cm fields respectively. The simulations show close agreement with the experimental results. The mean percentage difference between the superposition and experimental data, shown in Figure 4.21, in the lung regions for the 5 x 5 cm simulation is 2.0%. The percentage difference between the superposition and Monte Carlo results in the lung regions is 1.6%. Therefore the superposition results show good agreement with experiment and Monte Carlo simulations respectively.

To test the accuracy of the method experimental results for mid lung off-axis profiles are compared with the superposition simulation method, the results are shown in Figures 4.24 and 4.25 for phantom A and B respectively. The profile shapes produced using superposition follow the experimental results quite well. For example the results show percentage differences at 5 cm off-axis of 6.4% and 4.3%, respectively. This is an improvement in accuracy of a factor of three over the results presented in chapter 3 for methods which use penumbral forming functions. Note the E-TAR and Batho results show inferior accuracy to the superposition results in all situations tested and reported in this thesis.

5.5 RELATED AND FUTURE PROJECTS

Charged particle contamination affects the shape of the dose build up curve in the first superficial centimeters. A correction for this contamination has not been shown in the depth dose curves presented in this thesis. However a colleague has already isolated the electron contamination component (Harper 1990, Harper *et al* 1990). It should be a relatively easy task to overlay a set of contamination data into the final isodose distributions.

Most of the programs tested in chapter 4 were developed on a Vax 6220 at the University of Waikato and have also been adapted so that they now run on a Multicomputer system called the Transputer Treatment Planning System (TTPS) at a considerably faster speed. A member of the research group has been responsible for the majority of this implementation

(Murray *et al* 1990). This researchers current interests also involve the improvement of the EGS Monte Carlo resource which he has implemented on both Vax and TTPS systems (Murray 1990). These Monte Carlo programs were used extensively for the production of DSAs and full X-ray beam simulations presented in chapter 4 of this thesis. It is envisaged that many more EGS Monte Carlo simulations will be employed in future work by the group.

The effect of voxel weighting on the ray trace and ultimate accuracy in low density media has not been discussed in detail here, although it is briefly mentioned in section 4.7. The approximation of rectilinear range scaling of DSAs does cause small inaccuracies in lung (1 to 2%) that may increase as density is reduced (eg. in air cavities). A member of the research group has studied this effect in more detail elsewhere (Hoban *et al* 1990a). It is also expected that this researcher, in combination with the author of this thesis, will further study the accuracy of the superposition scaling method in non slab geometries as well as in bone.

This researcher (Peter Hoban) is also continuing to study the intricacies of charged particle transport in relation to electron beams. He has recently implemented two pencil beam scaling methods for electron beam planning onto TTPS. Both methods are 3-Dimensional. One method is based on the Fermi-Eyges generated pencils and the other is based on Monte Carlo generated pencils.

Accurate three-dimensional photon (and electron algorithms) have been produced by members of our research group. TTPS has already been used as a planning aid in some specific CT patient situations. The next challenge is to account for beam manipulation requirements in a more routine fashion, for example beam angulation, weighting, compensators, blocks all have to be accounted for so that TTPS may be used for routine planning of Radiotherapy Cancer patients. The future prospects of this project are truly exciting.

APPENDIX 1

Example Of How to Calculate R_σ, ρ_e^w and Z_{eff} for Bone Analog Material

To calculate R_σ at 71 keV the mass attenuation coefficients at this energy for the composite elements are found from Tables (Jackson and Hawkes 1981). The A/Z ratios are found from the periodic table. Percentage by mass of elements are from White *et al* (1977). A summary of the data is shown in Table A1.1.

ELEMENT	% BY MASS (% f_j)	$(A/Z)_j$	$(\mu/\rho)_j$
H	7.90	1.008	0.3165
C	63.79	2.001	0.1666
N	4.23	2.001	0.1736
O	9.88	2.000	0.1736
Cl	14.20	2.085	0.3037

Table A1.1: Percentage by mass $\%f_j$, atomic to mass number ratio $(A/Z)_j$, and attenuation coefficients $(\mu/\rho)_j$ for constituent elements in bone analog material.

To calculate R_σ then for water

$$\left[\sum_{i=1}^{N} f_i \left(\frac{\mu}{\rho}\right)_i \left(\frac{A}{Z}\right)_i\right]_w = (0.112)(1.008)(0.3165) + (0.888)(2.0)(0.1736)$$

$$= 0.3440 \quad . \qquad \text{(A1.1)}$$

Also for the bone analog substance

$$\left[\sum_{j=1}^{N} f_j \left(\frac{\mu}{\rho}\right)_j \left(\frac{A}{Z}\right)_j\right]_s = (0.079)(1.008)(0.3165) + (0.6379)(2.001)(0.1666)$$

$$+ (0.0423)(2.001)(0.1736) + (0.0988)(2.000)(0.1736)$$

$$+ (0.1420)(2.085)(0.3037)$$

$$= 0.3768 \quad . \qquad \text{(A1.2)}$$

Then from (2.20)

$$R_\sigma = \frac{\left[\sum_{i=1}^{N} f_i \left(\frac{\mu}{\rho}\right)_i \left(\frac{A}{Z}\right)_i\right]_w}{\left[\sum_{j=1}^{N} f_j \left(\frac{\mu}{\rho}\right)_j \left(\frac{A}{Z}\right)_j\right]_s} = \frac{0.3440}{0.3768} = 0.9330 \quad . \qquad \text{(A1.3)}$$

The mass density was measured as $\rho = 1.16$ then

$$\rho_e^w = 1.81\,\rho \left(\sum_{i=1}^{N} f_i \left(\frac{Z}{A}\right)_i\right) = 1.14 \quad . \qquad \text{(A1.4)}$$

Therefore

$$N_{CT} = \frac{1000}{R_\sigma}(\rho_e^w - R_\sigma) = \frac{1000}{0.9330}(1.14 - 0.9330) = 222 \text{ HU} \quad . \qquad \text{(A1.5)}$$

The N_{CT} value calculated using the method outlined above is shown in Table 2.7. In order to calculate Z_{eff} using (2.27). The expression is repeated here for convenience:

$$\alpha_i = \frac{f_i\left(\frac{Z}{A}\right)_i}{\sum_{j=1}^{q} f_j\left(\frac{Z}{A}\right)_j} \quad . \qquad \text{(A1.6)}$$

The denominator is given by

$$\sum_{j=1}^{q} f_j\left(\frac{Z}{A}\right)_j = 0.5357 \qquad \text{(A1.7)}$$

and the numerator for one of the elements (hydrogen) is given by

$$f_1\left(\frac{Z}{A}\right)_1 = (0.079)(0.992) = 0.0784 \quad . \qquad \text{(A1.8)}$$

Therefore repeating the summation for the constituent elements as outlined in (2.21) and including Z_i with the exponent (a = 2.94) the expression is

$$Z_{eff} = \left(\sum_{i=1}^{q} \alpha_i (Z_i)^a \right)^{\frac{1}{a}} = 9.26 \quad . \qquad \text{(A1.9)}$$

The effective atomic number relative to water Z_{eff}^{w} is the ratio of the substances effective atomic number $Z_{eff,s}$ to the effective atomic number of water $Z_{eff,w}$, such that

$$Z_{eff}^{w} = \frac{Z_{eff,s}}{Z_{eff,w}} = \frac{9.26}{7.40} = 1.25 \quad . \qquad \text{(A.10)}$$

APPENDIX 2

Calculation of P_{flue} using Radial Build up Factors

The ratio $P_{flue,het}/P_{flue,hom}$ can be calculated from taking the ratio of radial build up factors (RBFs) (Rice *et al* 1988) such that

$$\frac{P_{flue,het}}{P_{flue,hom}} = \frac{RBF(r_1)}{RBF(r_2)} \quad , \qquad \text{(A2.1)}$$

where RBF(r) is the ratio of dose at d_{max} for a field of radius r relative to the dose at d_{max} for a field size large enough to ensure electronic equilibrium (approximately at $r = d_{max}/2\rho$). The term r_1 is the effective radius in g/cm^2 of the field without the detector present. The term r_2 is the effective field radius with the detector present.

The appropriate RBFs have been calculated using a superposition calculation method outlined in chapter 4. The superposition results for different field sizes are shown in Figure A2.1 and as the most important field sizes are for small radii then a more detailed graph is shown in Figure A2.2 (this shows part of the data in Figure A2.1 in more detail).

For a 5 x 5 cm field the effective field radius r_1 is

$$\begin{aligned} r_1 &= \sqrt{\frac{5x5}{\pi}}\,\rho \\ &= 2.82\,(0.2) \\ &= 0.564\ g/cm^2 \quad . \end{aligned} \qquad \text{(A2.2)}$$

For the Baldwin Farmer chamber used in chapter 3 in the 0.2 density cork phantom the equivalent thickness of the chamber wall is $t = 0.0375\ g/cm^2$. The equivalent thickness of the cork replaced by the detector wall is $t' = t\rho$, therefore r_2 is equal to

$$\begin{aligned} r_2 &= t + \rho\,(r_1 - t') \\ &= 0.0375 + 0.2\,(2.82 - 0.0375) \\ &= 0.594\ g/cm^2 \end{aligned} \qquad \text{(A2.3)}$$

Therefore the ratio $P_{flue,het}/ P_{flue,hom}$ is

$$\frac{P_{flue,het}}{P_{flue,hom}} = \frac{RBF(0.57)}{RBF(0.59)}$$
$$= \frac{0.770}{0.785}$$
$$= 0.98 \quad . \qquad \text{(A2.4)}$$

Repeating the calculation for the 0.3 density lung analog material (LN 10/75) gives a $P_{flue,het}/ P_{flue,hom}$ ratio equal to

$$\frac{P_{flue,het}}{P_{flue,hom}} = \frac{RBF(0.85)}{RBF(0.87)}$$
$$= \frac{0.920}{0.930}$$
$$= 0.99 \quad . \qquad \text{(A2.5)}$$

These estimates of the $P_{flue,het}/ P_{flue,hom}$ ratios are the maximum deviation from unity, because the effective radius of the beam is calculated from the density of the low density medium only, whereas in reality a significant number of electrons reaching the cavity come from the denser overlying layer (see Hoban *et al* 1990a, Figure 5 for details). Therefore the effective field radius is always more than the radius used in these calculations. This implies that the respective RBFs will fall further up the graph in Figure A2.2, and the ratio will be closer to unity. A more complex calculation could be undertaken involving ray tracing to more accurately predict equivalent field radius. Because the effect is very small it was felt that an estimate of the maximum effect was an adequate approximation, note RBFs are an assessment of the maximum magnitude of the error. Because the magnitude of the effect is not predicted at all positions then no correction for P_{flue} was applied in the results shown in chapters 3 and 4.

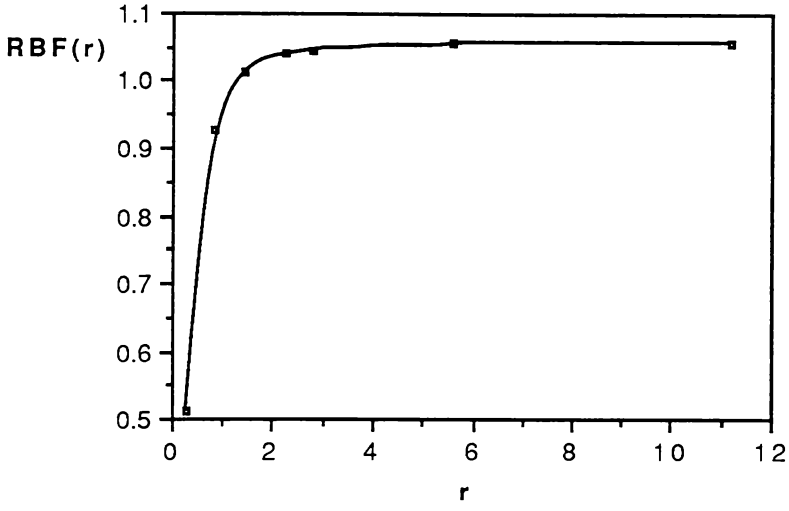

Figure A2.1: Radial build up factor RBF versus field radius r in g/cm^2 for 10MV X-rays. The RBF values were obtained by performing a superposition calculation. Electron equilibrium is reached at about r=1.25 g/cm^2 and the dose output still increases beyond this radius due to scattered photons.

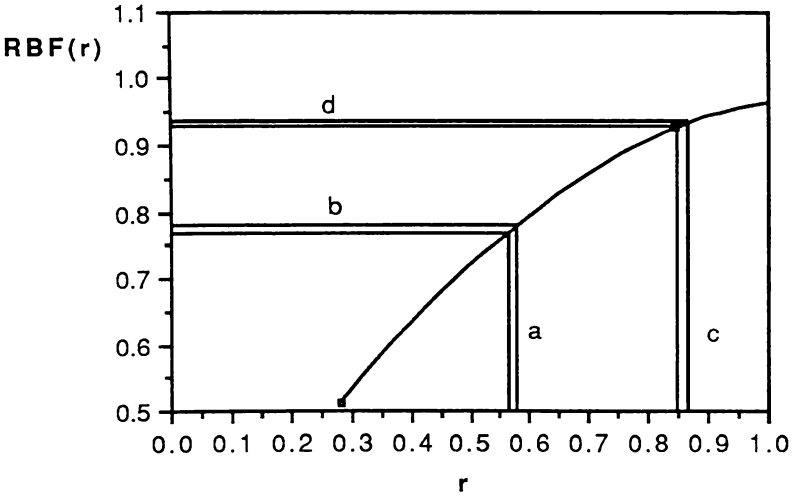

Figure A2.2: Radial build up factor RBF versus field radius r in g/cm^2 for 10MV X-rays. More detailed results were required for small radii fields so Figure A2.1 is reproduced up to a radius of r = 1 g/cm^2. The lines near a are the radius with and without the detector present in 0.2 cork, and the lines near b are the respective RBF values. The lines near c are the radius for 0.3 lung analog with and without the detector present, and the lines near d are the respective RBFs in this case. The difference between the lines at b is 2% and between the lines at d is 1%. These results are consistent with (A2.4) and (A2.5), respectively.

APPENDIX 3

PUBLICATIONS

Australas Radiol 1988; 32: 371-379

Radiotherapy Planning Accuracy in Terms of C.T. Numbers and Inhomogeneity Correction Techniques

P.E. METCALFE, MSc. AND W.A. BECKHAM, MSc.(MED PHYS).

Department of Scientific Services,
Waikato Hospital, Private Bag, Hamilton, New Zealand.

INTRODUCTION

The following is an analysis of how accurately relative electron densities for Radiotherapy planning may be derived from true C.T. numbers and how adequately the effective depth inhomogeneity correction method[1] handles these data. However, the error analysis is defined with sufficient generality for the same analysis to be applied to other dose calculation algorithms.

Parameters which contribute to errors in Radiotherapy planning from C.T. data are outlined in Figure 1. The structure of this paper is reflected in the figure.

1. C.T. Derived Electron Densities

A. Atomic Number Bone Assumptions

Samples of known electron density and effective atomic number[2,3] were placed in plugs in an acrylic phantom (30 cm diameter) on the Seimens DR-H C.T. scanner. The resultant C.T. number (Nct) versus relative electron density (p_e^w) calibration graph is shown in Figure 2. Other variables which have been shown to effect C.T. number[4] are size and position of the scanned sample object. On the Seimens DR-H these effects have been shown to produce an uncertainity in p_e^w of less than 1.5% for all situations tested. The x on y regression lines are represented by equations 1-3. Workers[2,3] have used both $CaCl_2$ and K_2HPO_4 in bone equivalent solutions. As was seen in Figure 2 the plots of C.T. number verses p_e^w for these two solutions are reasonably close. Bone was assumed to lie between these two values. The equation of this line is given by equation 4.

$$\text{When } Z_{eff} = Z_{eff}^{water}$$

$$\rho_e^w(\text{tissue}) = \frac{N_{CT}}{1000} + 1 \quad (1)$$

$$\text{When } Z_{eff} = Z_{eff}^{CaCl_2}$$

$$\rho_e^w(CaCl_2) = \frac{0.38N_{CT}}{1000} + 1 \quad (2)$$

$$\text{When } Z_{eff} = Z_{eff}^{K_2HPO_4}$$

$$\rho_e^w(K_2HPO_4) = \frac{0.55N_{CT}}{1000} + 1 \quad (3)$$

$$Z_{eff}^{bone} = \tfrac{1}{2}(Z_{eff}^{CaCl_2} + Z_{eff}^{K_2HPO_4})$$

$$\rho_e^{bone} = \frac{0.465\,N_{CT}}{1000} + 1 \quad (4)$$

$$\Delta Dp = Dp(\rho_e^w(\text{bone})) - Dp(\rho_e^w(\text{tissue})) \quad (5)$$

$$\frac{\partial \mu(x,y,z)}{\partial z} = 0 \quad (6)$$

$$\Delta Dp = Dp - D_E \quad (7)$$

Key Words:
Computed tomography
radiotherapy planning,
inhomogeneity correction.

Accepted for publication on 28th July, 1987.

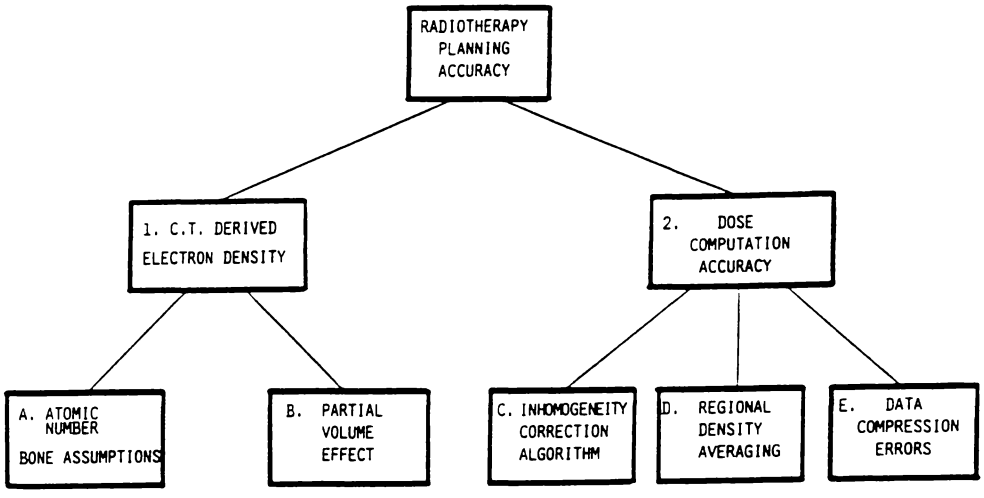

FIGURE 1 — Error analysis structure chart.

The error in dose due to incorrect density is defined in equation 5. The dose Dp is ideally measured in a phantom, or it can be modelled using a simulation with an appropriate correction alogrithm.

A worst case bone error estimate is simulated using the effective depth algorithm on a head of femur model shown in Figure 3.

Values of Dp are presented in Table 1 for two cases, that of no bone calibration when converting C.T. numbers to p_e^w and that for using a bone calibration in the conversion. It is apparent from these results that bone calibration is essential to reduce errors in dose calculation.

TABLE 1

Effect of non-use of Bone Calibration

	Dp Cobalt-60	Dp 10MV photons
Calibration	31.5[1]	44.4
No calibration	25.8	39.2
ΔDp	5.7	5.2

Notes:

1. Figures are given as a percentage of Dmax
2. Assume N_{CT} = 700 for observed bone.

   p_e^w(bone) = 1.33 p_e^w(tissue) = 1.7

   This leads to two values of p_e^w depending on whether a calibration is used or not.

B. Partial Volume Effect

Inherent in the C.T. scanning process is the principle that a two dimensional pixel set is produced from a three dimensional set of voxels, hence constant attenuation is assumed across the slice width (as described by equation 6).

To study the effect for bony structures cones of Teflon were produced with different edge angles. Only the edge pixels of the structures are affected, provided the structure passes fully across the slice width. However, a major effect on average C.T. number estimation occurs if the structure partially fills the slice width, in which case serious discrepancies between actual and apparent values of p_e^w are introduced. As long as structures pass fully through the slice width, derived values of p_e^w can be relied upon. We are not able to consistently predict the effect in patient anatomy situations, although errors from this source can be minimised by choosing scans where, for example, spinal processes "look well defined" across the scan plane. If this is done then the criterion that the structure falls within the slice width is satisfied. Where scanners have accurate scan position estimation from scout views, positioning of eg. the vertebra totally within the slice width is made easier.

Assuming one can minimize the partial volume effects a decision has to be made as to what to do with the p_e^w value gained for in this case the vertebra. Obviously some consideration

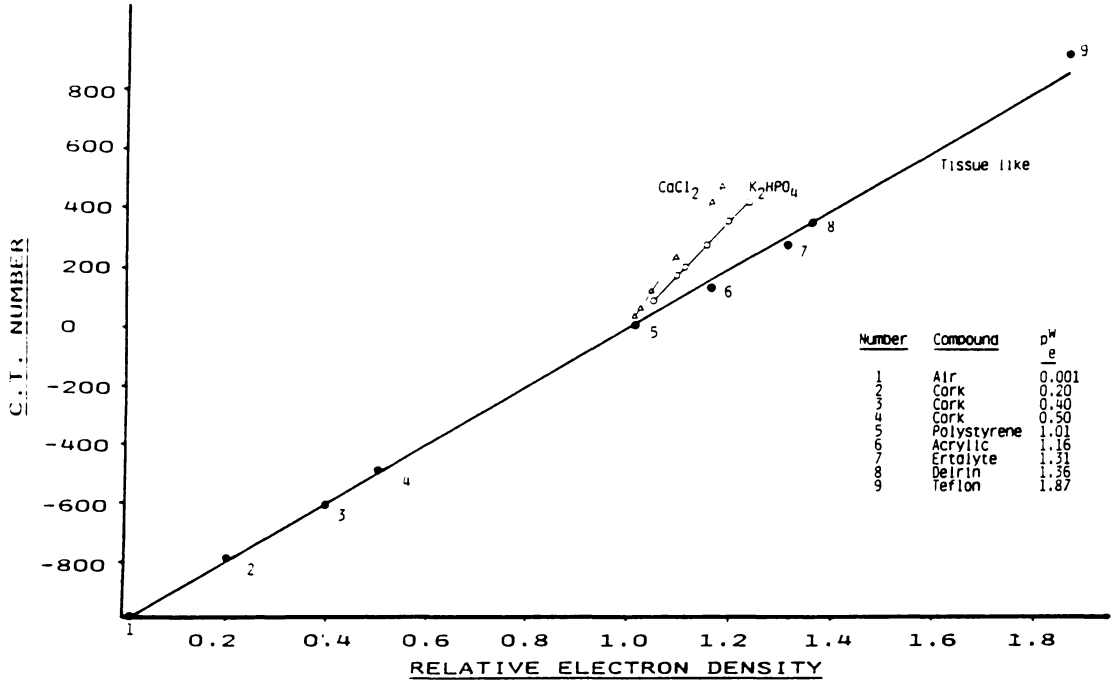

FIGURE 2 — C.T. number versus relative electron density (125 kVp) calibration.

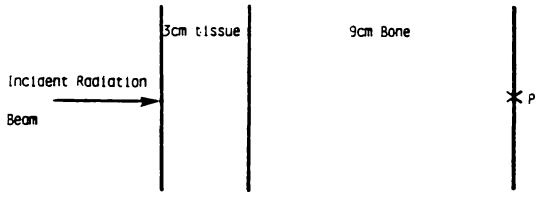

FIGURE 3 — Bone simulation, head of femur interface.

must be given to the fact that the spine is not a continuous length of bone of electron density as determined from the vertebrae but that it is interruped by less dense spinal discs. An average ρ^w_e value is required. More work needs to be done to assess this.

2. Dose Computation Accuracy

C. Inhomogeneity Correction Algorithm

A "cork/polystyrene" phantom was pro duced to simulate the effect of high energy photon beams passing through patient "lung type" tissue. Computer generated "effective depth", Batho[6] and E-TAR[7]dose data is compared with in-phantom ionisation chamber readings. The phantom configuration is shown

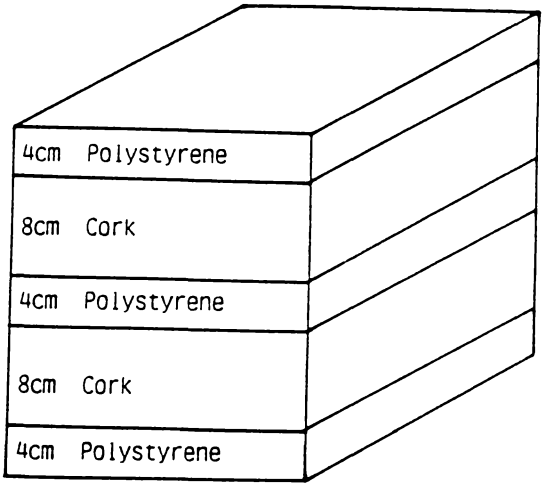

FIGURE 4 — Lung phantom configuration.

in Figure 4. This phantom configuration more closely models a beam traversing typical patient chest wall and lungs[8] than other commonly used lung phantom configurations outlined in the literature[9].

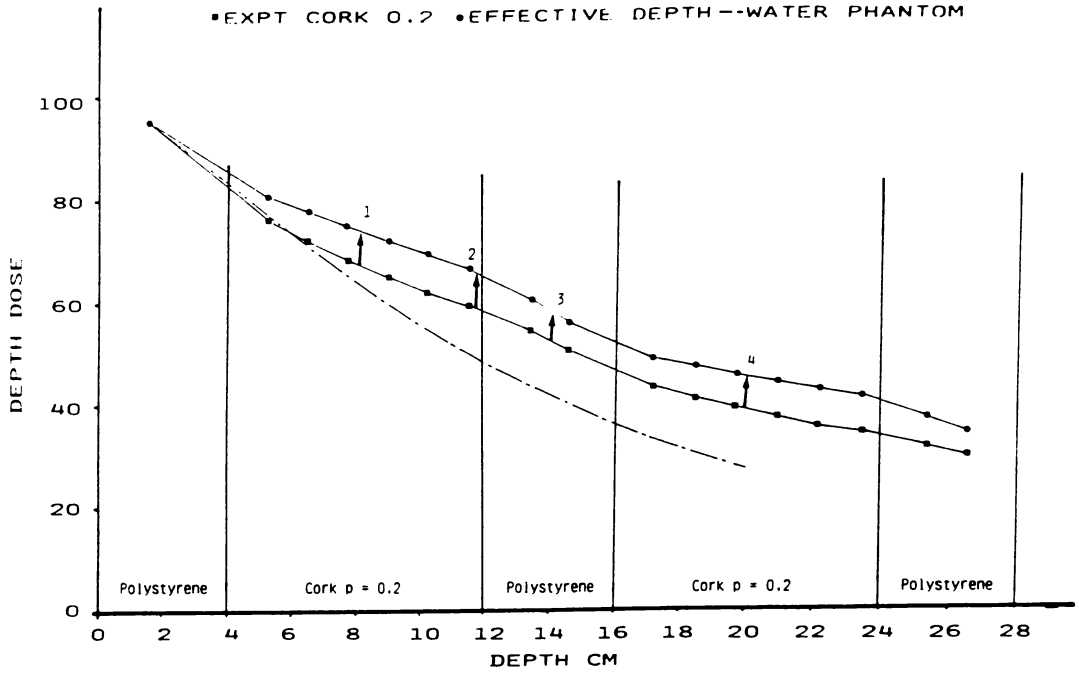

FIGURE 5 — Cobalt-60 depth dose comparison 10 cm. field between effective depth algorithm and experimental measurements.

A consistent difference between experiment and effective depth calculation was observed for 5, 10, 25 cm² Cobalt-60 field sizes tested.

As shown in Figure 5 the error in dose at different points due to inadequacies in the correction algorithm are defined in equation 7. Dp is the dose to a point as calculated by the algorithm and D_E is the dose obtained from ionisation chamber measurements. The error analysis is presented in table 2 for 4 positions. The main reason for the difference, Dp, is because the effective depth method merely scales full scatter depth dose data and does not attempt to correct for lack of scatter in the lung medium. The phenomenon is better coped with by empirical scatter weighting techniques such as equivalent tissue air ratio methods (E-TAR), Figure 6.

As shown in Figure 7 this effect is reduced for the effective depth correction method for 10 MV photon square fields of 10 cm² and above due to the backscatter being a smaller component of the beam at these higher energies. However, at small field sizes and high energies as shown in Figure 8 another phenomenon becomes significant: a non-equilibrium in central axis is set up due to

TABLE 2

Errors due to inadequate correction algorithm

Mode/position	Dp	D_E	ΔDp
Cobalt-60 10 square			
1	75	68	+ 7
2	65	58	+ 7
3	58	53	+ 5
4	45	38	+ 7
Linac 10 MV, 10 square			
1	86	83	+ 3
2	77	74	+ 3
3	69	69	0
4	57	55	+ 2
Linac 10 MV, 5 square			
1	85	73	+12
2	76	66	+10
3	70	68	+ 2
4	58	50	+ 8

Notes:

1. Positions are as defined in figures 5, 7 and 8.

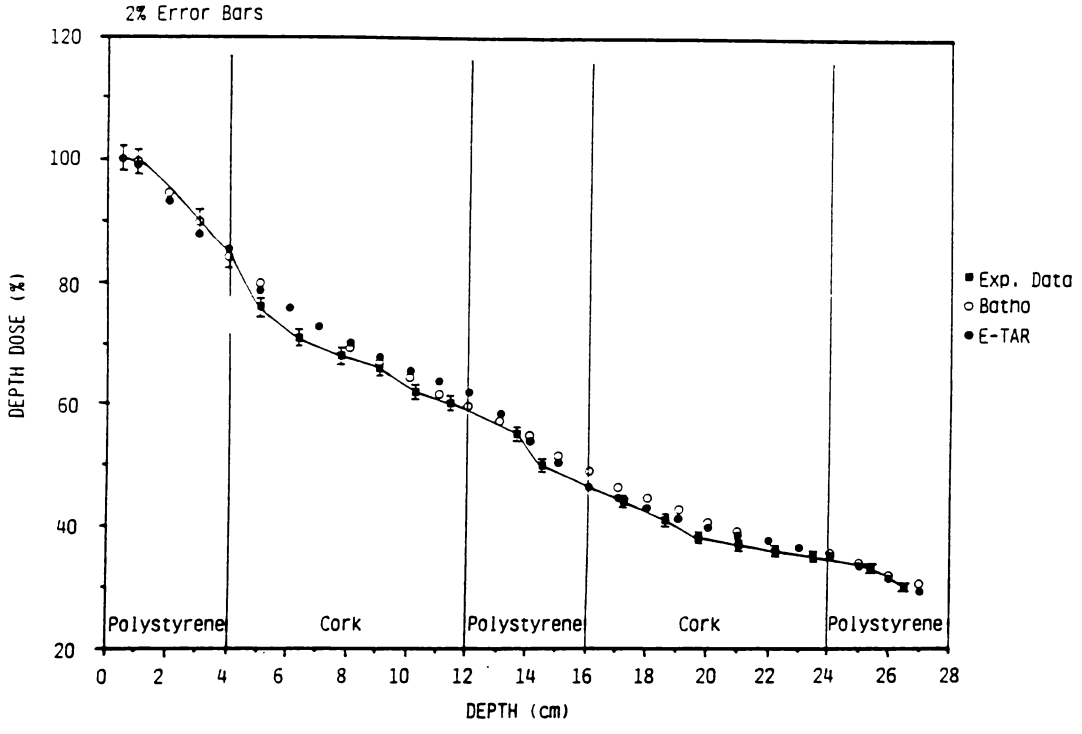

FIGURE 6 — Depth dose comparison "Cobalt-60, 10x10 field".

the electron range from the Kerma site to the dose deposition site being greater than the field width[10], a problem not solved by E-TAR type methods (Figure 1). Convolution techniques handle this problem[11,12] but require more development before implementation into commercial systems becomes a reality.

D. Regional Density Averaging

The density texture across the lung is significant[12]. To assess this effect on dose two different cork densities were tested as shown in Figure 8.

Investigation showed that using a typical lung density value causes systematic dose errors, whereas calculating a lung specific average density causes relatively small errors. Pixel correction for density variations across the lung is ideal, but may not be essential.

E. Data Compression Errors

Due to the limits imposed on computing facilities it is sometimes necessary to compress some of the information contained in the C.T. scanner data. Compromise is often necessary in the picture matrix size. If the scanner's matrix is 512 x 512 pixels then it may be necessary to compress the matrix to 256 x 256 or even 64 x 64 for the radiotherapy computer. Obviously then when it comes to contour mapping, eg. boundary between bone and soft tissue, the coarser matrix may lead to uncertainties in boundary position. Figure 11 shows the effect of changing chest wall thickness at 5 cm depth in lung 1. Note that spatial accuracy is less important for photon beams than electron beams.

It may also be necessary to reduce the fineness of the density scale applied to a given pixel. Some scanners may have up to 12 bits to define density. Due to computer memory restriction this may have to be reduced, and as a result may lead to problems in differentiating between tissues of reasonably similar densities.

SUMMARY

The use of C.T. scanners in radiotherapy planning is becoming widespread. It is essential therefore that adequate assessment of the reliability of the C.T. acquired data for planning purposes is carried out. It is also important that

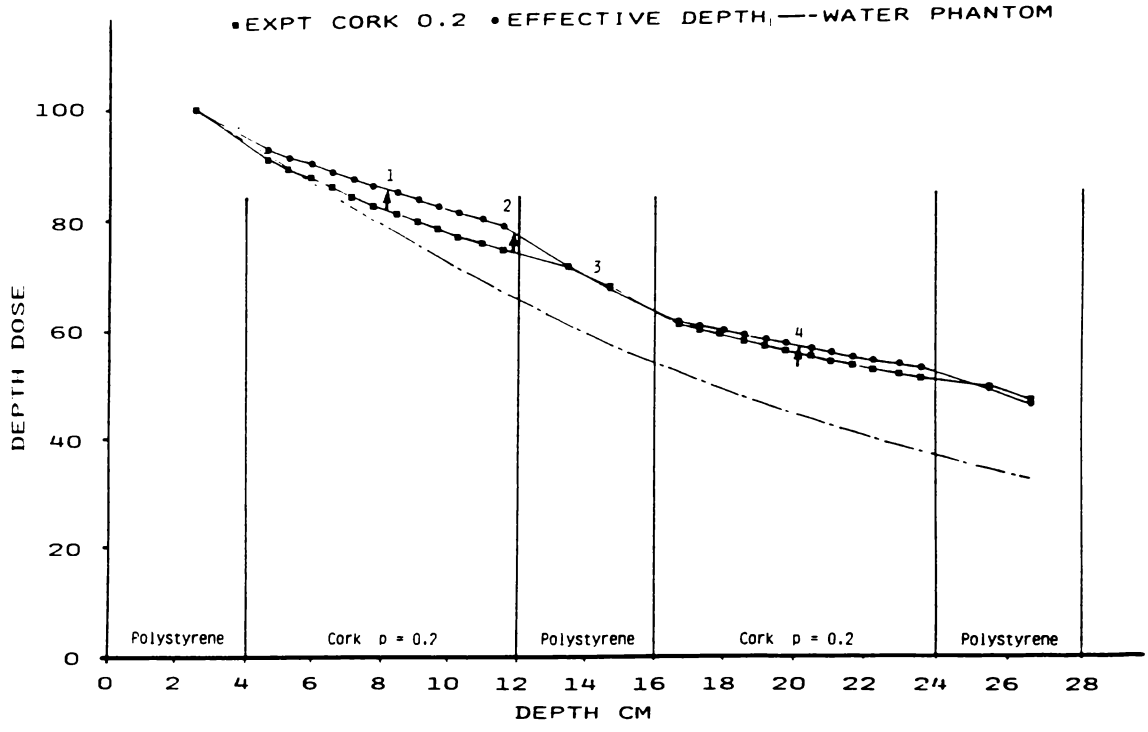

FIGURE 7 — Linac 10MV depth dose comparison 10 cm. field between effective depth algorithm and experimental measurements.

all makes of C.T. scanner be assessed due to their varying characteristics.

Dose computation inaccuracies have to be considered also if one is to get an estimate of the overall accuracy of a given radiotherapy planning technique. In general, it would appear that until the convolution techniques become commercially available the Radiotherapy computer is now the primary source of dose calculation error, due to inadquacies in commonly used inhomogeneity correction algorithms.

ABSTRACT

A protocol is described for assessing the accuracy of radiotherapy plans produced using C.T. derived electron density information. Essentially there are two main sources of error, those coming from various C.T. related inaccuracies and those from inaccuracies in the radiotherapy dose calculation algorithms. The various subdivisions of these two sources of inaccuracy are discussed in detail.

More specifically this paper deals with the effective depth method of inhomogeneity correction, but sufficient generality is applied to the discussion to enable the same analysis to be applied to other dose calculation algorithms.

It would appear that with state of the art C.T. scanning that the area which introduces the greatest errors is now radiotherapy computing accuracy. Until convolution correction techniques become commercially available this will probably continue to be the case.

ACKNOWLEDGEMENTS

The authors wish to thank the C.T. staff at Waikato Hospital for their help. We also appreciate the conceptual guidance of M. Pracy and his reading of the manuscript. We are grateful to J.J. Battista, Cross Cancer Institute, Canada, for the use of the VAX planning system to prepare the data for Figures 6 and 9.

Thanks are due to E. Graham for his construction of phantoms and to B. Parkinson for typing the manuscript.

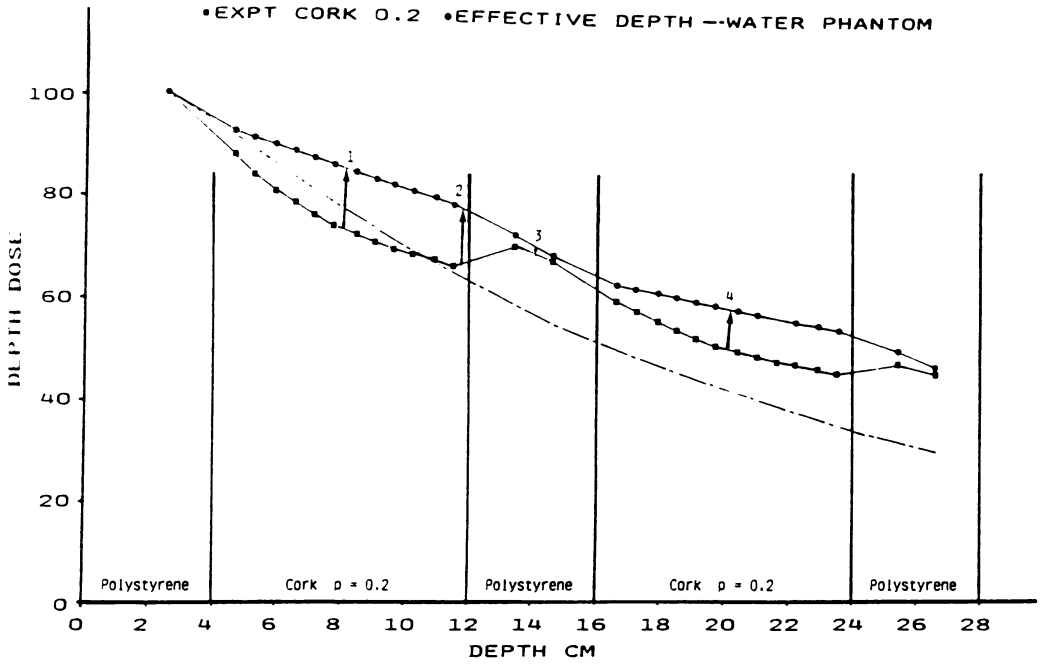

FIGURE 8 — Linac 10MV depth dose comparison 5 cm. field between effective depth algorithm and experimental measurements.

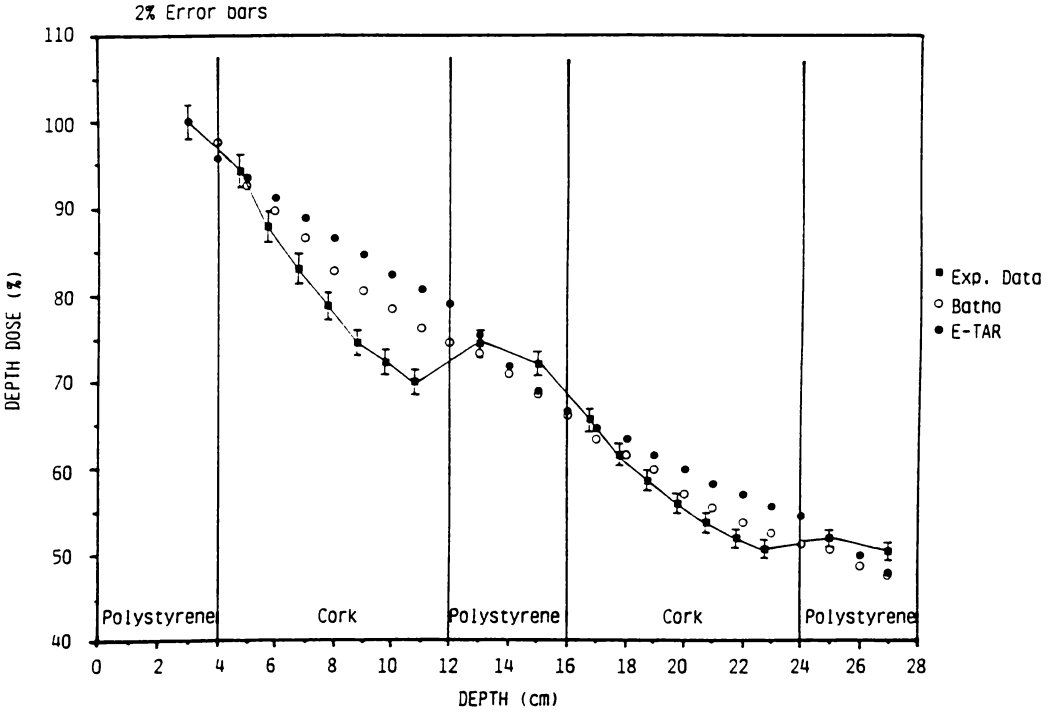

FIGURE 9 — Depth dose comparison "15MV, 5x5 field".

Figure 10: COBALT -60 DEPTH DOSE COMPARISON, 10cm² FIELD VARYING CORK DENSITY

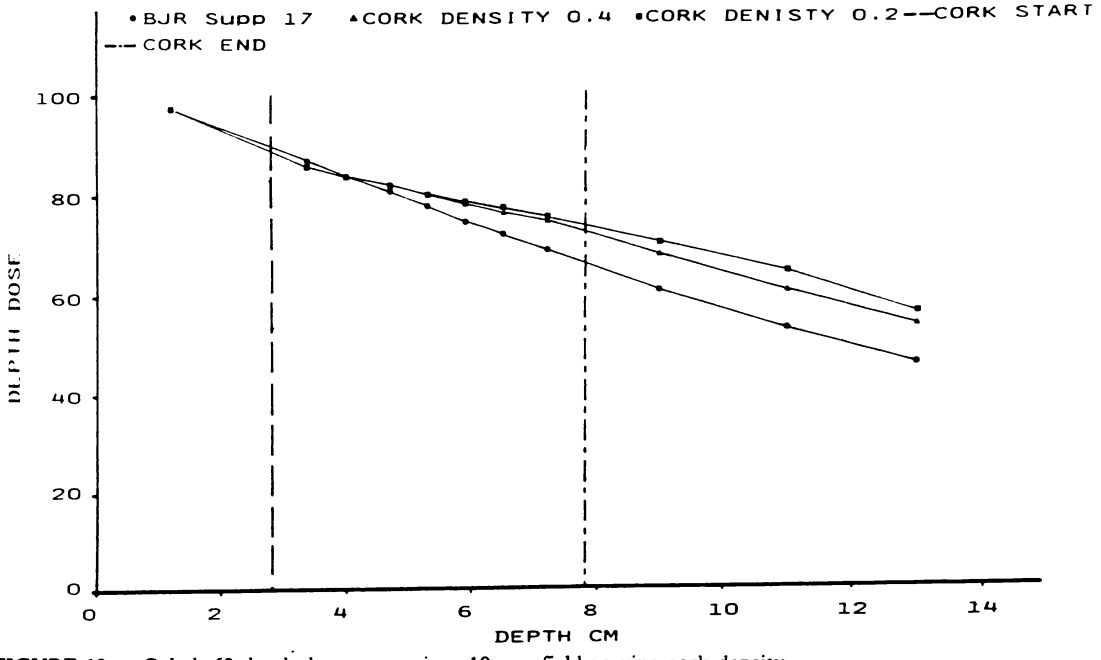

FIGURE 10 — Cobalt-60 depth dose comparison 10 cm. field varying cork density.

REFERENCES

1. Milan J and Bently RE. The Storage and Manipulation of Radiation Dose Data in a Small Digital Computer. British Journal of Radiology 1974; 45 : 115-121.
2. Huizenga H and Storchi PRM. The Use of Computed Tomography Numbers in Dose Calculations for Radiation Therapy. Act Radiologica 1985; 24 : 509-519.
3. McCullough EC and Homes TW. Acceptance Testing of Computerised Radiation Therapy Planning Systems: Direct Utilization of C.T. Scan Data. Med Phys 1985; 12 : 237-242.
4. Mahaworasilpa T and Southon FGC. C.T. Vertebral Bone Mineral Measurement — Intrinsic Errors of Single kV. Australasian Physical and Engineering Sciences in Medicine, 1986; 9 : 23-28.
5. Glover GH and Pelc NJ. Non Linear Partial Volume Artifacts in X-ray Computed Tomography. Med Phys 1980; 7 : 238-248.
6. Batho HF. Lung Corrections in Cobalt-60 Beam Therapy. J Can Assoc Radiol 1964; 15 : 79-83.
7. Sontag MR and Cunningham JR. The Equivalent Tissue-Air Ratio Method for Making Absorbed Dose Calculations in a Heterogeneous Medium. Radiology 1978; 129 : 787-794.
8. Van Dyk J. Lung Dose Calculations Using Computerised Tomography: Is there a need to Pixel Based Procedures? Int J Radiation Oncology Biol Phys 1983; 9 : 1035-1041.
9. Cunningham JR. Tissue Inhomogeneity Corrections in Photon Beam Treatment Planning. In Progress in Medical Radiation Physics; Vol 1.
10. Mackie TR, El-Khatib E, Battista J, Scrimger J, Van Dyk J and Cunningham JR. Lung Dose Corrections for 6- and 15- MV X-rays. Med Phys 1985; 12 : 327-332.
11. Mackie TR, Scrimger JW and Battista JJ. A Convolution Method of Calculating Dose for 15-MV X-rays. Med Phys 1985; 12 : 188-196.
12. Boyer AL and Mok EC. Calculations of Photon Dose Distribution in an Inhomogeneous Medium Using Convolutions. Med Phys 1986; 13 : 503-509.
13. Wegener OH, Koeppe P and Oeser H. Measurement of Lung Density by Computer Tomography. Journal of Computer Assisted Tomography 1978; 2 : 263-273.

Figure 11: EFFECT OF CHEST WALL THICKNESS ON MID-LUNG DOSE, 10cm² FIELDS

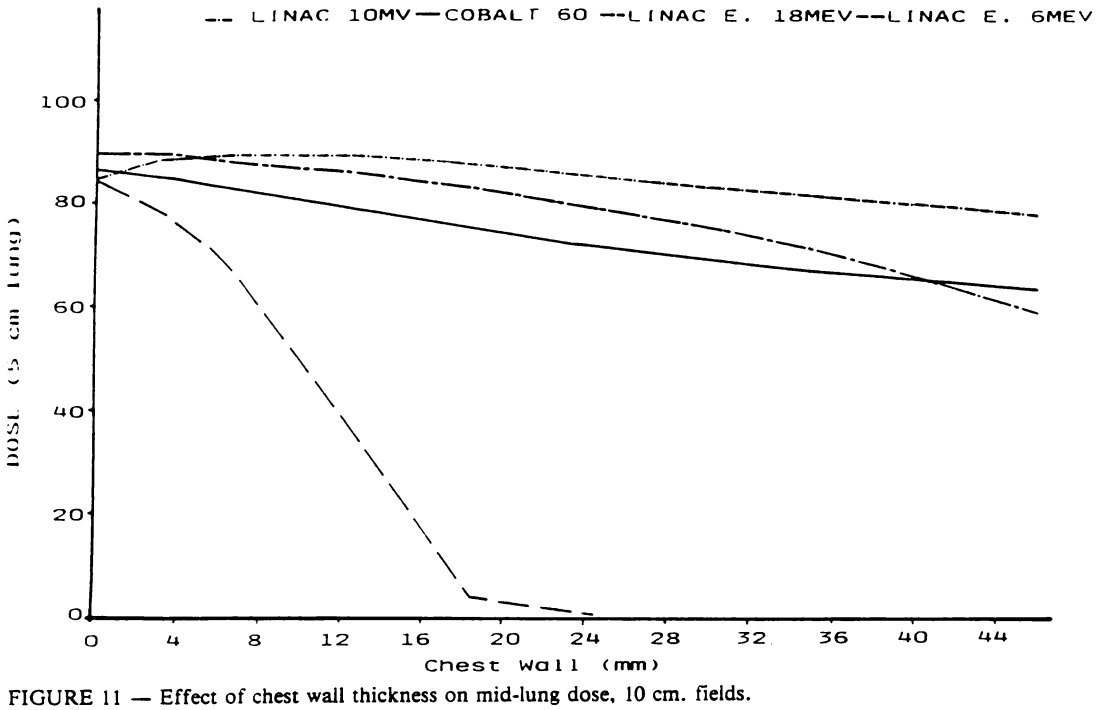

FIGURE 11 — Effect of chest wall thickness on mid-lung dose, 10 cm. fields.

Australasian Physical & Engineering
Sciences in Medicine (1988) Vol. 11 No. 3

THE EFFECT OF PATIENT DENSITY VARIATION ON RADIOTHERAPY DOSE CALCULATIONS*

P.E. Metcalfe[1], W.A. Beckham[1], B.H. Long[2], J.J. Battista[3],

[1]Waikato Hospital, Hamilton, New Zealand, [2]Cross Cancer Institute, Edmonton, Canada, [3]London Regional Cancer Centre, London, Ontario, Canada

Abstract

Inaccurate density assessment of tissue regions within the patient can contribute significantly to errors in dose during radiotherapy planning. The impact of inaccurate patient density information on dose has been quantified for photon (Co-60) and electron (18 MeV) beams.

Spatial maps of isodose differences are presented to visualise the magnitude and location of density-induced errors.

The algorithms for dose calculation used in this study were the Equivalent-TAR (E-TAR) for Cobalt-60 photons and the Fermi-Eyges Hogstrom (FEH) pencil beam for 18 MeV electrons. Dose trends were studies in a "spinal bone" and a "two lung" phantom.

Inhomogeneity correction factor (CF)versus density graphs are presented which show dose errors of 7.0% in mid-lung for the electron beam if typical densities are used and 1.5% if accurate CT densitometry information is employed. For the photon beam, the mid-lung error is 0.9% using typical densities in contrast with 0.2% if CT data are employed. Bone phantom tests confirm similar advantages in using CT densitometry.

A protocol is discussed for improving the accuracy of electron density information obtained from CT scans by using a crescent-shaped phantom placed beneath the patient for continuous quality assurance.

Keywords

Radiotherapy, Computerised Treatment Planning, Computed Tomography

Introduction

Dosimetry protocols can ensure the accurate measurement and prediction of absorbed dose from radiotherapy photon and electron beams at points in a homogeneous water phantom (1). However, the human body is inhomogeneous, with structures of variable density such as lungs and bones which can affect the dose distribution within a patient to a level well beyond the required 5% accuracy (2).

The errors which arise during the radiotherapy treatment planning process are due to a combination of inaccurate electron density information obtained from either X-ray or CT images and inadequate corrections for tissue inhomogeneities as outlines in a companion article (3). This article concentrates on quantifying the error contribution arising only from inaccurate density assignments.

It should be noted that practical constraints often limit the availability and suitability of CT for radiotherapy planning purposes. The majority of treatment plans are still produced using cross sectional contours reconstructed from conventional X-ray simulation techniques. For these patients "average" densities are assigned within inhomogeneous regions (the average being a sample population average). In contrast, the protocols of choice when CT scans are available make optimum use of more patient-specific densitometry.

Density calibration curves can be used to determine electron density of pixels in a CT image and dose computation algorithms can make use of this information. Vector-based algorithms use the tissue contours and average "in-vivo" density calculated within the contoured regions. For pixel-based algorithms, the contouring is avoided as individual pixel densities are used directly; this is the most advanced use of CT density information in radiotherapy planning today.

The conversion of CT data to accurate electron density information (e cm^{-3}) is usually achieved by scanner calibration performed on a periodic basis. Using samples of known electron density and atomic number placed in phantoms, suitable calibration graphs are produced.

An alternative calibration method is presented which uses a modified crescent-shaped phantom placed beneath the patient during a scan. This work is an extension of the studies of Cann (4) and accounts for a wider range of tissue densities as encountered in radiotherapy. The

* *Presented AAPM conference Michigan-Detroit, USA, 1987 and EPSM conference Auckland, New Zealand, 1987*
Manuscript first received 29 June 1988. Revised August 1988.

procedure described may also have applications in diagnostic soft tissue densitometry (for example lung density monitoring).

The phantom provides continuous calibration, slice-by-slice, of electron density information for use later at the radiotherapy planning computer. The phantom design incorporates three soft tissue and three bone analogs which are inserted to monitor calibration over a wide dynamic range of density. A recent design by another worker (5) incorporates only two samples which results in a more compact phantom at the expense of having "assumed linearity" on the basis of two sample points.

Methods and results

Radiotherapy Dose Errors Caused by Using Conventional X-ray Projection

It is of interest to compare the resultant errors in planned dose caused by different density assignments. To assess the effect of incorrect density on calculated dose we have injected the density uncertainty data from previous publications into radiotherapy dose computation algorithms. These tests are designed to indicate the magnitude and spatial extent of errors which accumulate when "average" density assumptions are applied within geometric contours obtained by either conventional simulation X-ray imaging (or CT scans in which the density information has been discarded).

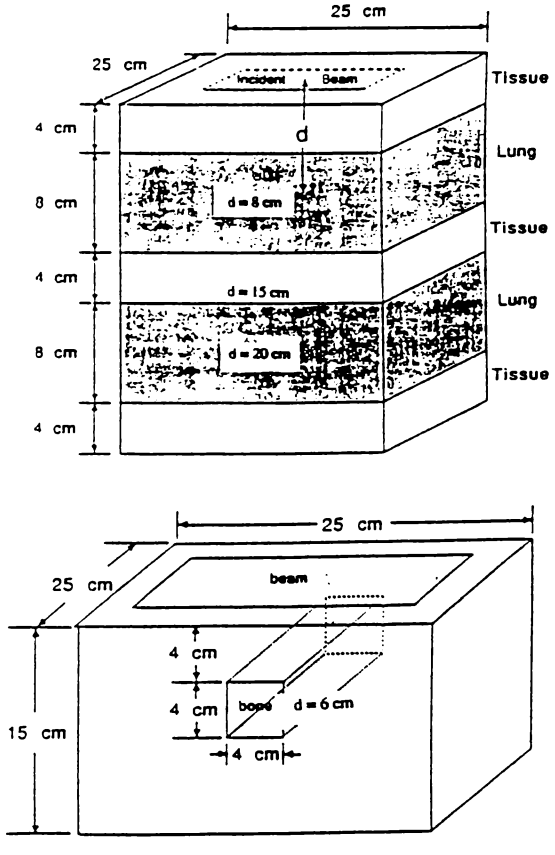

Fig. 1: Body Phantoms Used in Dose Versus Density Experiments
(a) "Two-Lung" Phantom
(b) "Bone" Phantom

The algorithms for dose calculation used to study the density effect were the Equivalent-TAR (E-TAR) (6) for Cobalt-60 photons, the accuracy of which is discussed in the companion article (3) and the Fermi-Eyges Hogstrom (FEH) (7) pencil beams for 18 MeV electrons, the accuracy of which has also been the subject of a recent detailed study (8). Within the constraints of the phantom configurations used here and the beam energies chosen, these algorithms produce accurate dose results. The phantoms used to model these dose trends include a "two-lung" phantom shown in Figure 1(a) and a "bone" phantom shown in Figure 1(b).

Based on a survey of lung densities "in-vivo" by Van Dyk et al (9), it is reasonable to assume the range of lung density which we have chosen (0.25 to 0.45) encompasses expected lung density variations encountered in a sample of radiotherapy patients.

Dose errors in radiotherapy plans due to these assigned lung densities are visualised in two dimensions using spatial maps of dose differences. As shown in Figure 2 for 18 MeV electrons (corrected with the FEH algorithm), two plans (Figures 2(a) and 2(b)) with different lung density are compared and the resultant subtraction of dose levels is shown (Figure 2(c)). Increases in dose of up to 25% occur for this electron beam due to the increase in the electron range caused by a lung density reduction (0.45 to 0.25).

For a Cobalt-60 photon beam (corrected with the E-TAR algorithm), Figure 3 indicates that dose differences of only 4% occur for the same density change. This smaller error is, however, over a more significant volume of lung. This error in dose is systematic and as total errors in dose are cumulative, this still represents a significant contribution to the total error in dose delivered. Such a large contribution to the total dose error should still be avoided if the 5% total error guideline in dose delivered is to be met (2). However, it is evident that the penetration of a photon beam (Figure 3) is less influenced by density than the penetration of an electron beam (Figure 2).

Dose Differences From C.T. Derived Density

As predicted in the next section, an uncertainty in density of about 0.025 is expected from CT scan data. This is a considerable improvement over the density ranges used with contours which use "standard lung" and bone densities.

Since difference maps do not clearly show up the effect of such small density changes on dose, a more sensitive approach was required. Hence Figures 4 and 5 were produced to show comparisons of inhomogeneity correction factors at a point (mid lung and mid bone respectively) for electron and photon beams. These results confirm the relative insensitivity of photon beam dose to density changes when compared with electron beams.

Results obtained at other depths are shown in Figure 6. The correction factor varies with the depth in phantom. Therefore one can only specify an approximate gradient

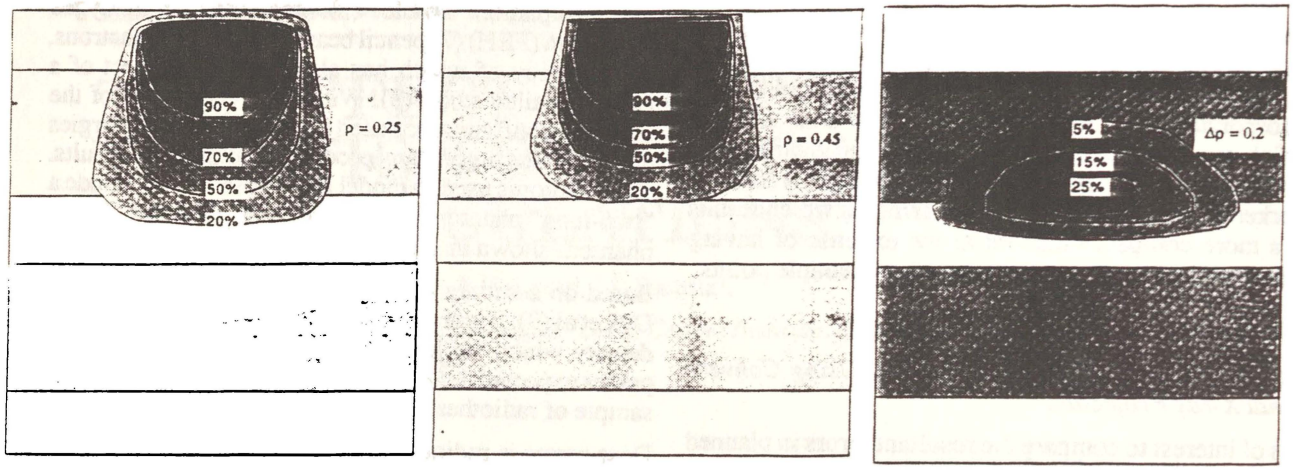

Fig. 2: Electron Isodose Distributions: 18 MeV, FEH algorithm, 10 sq. cm field, 100 cm SSD
(a) Lung Density 0.25: (b) Lung Density 0.45: (c) Dose Difference Map (a-b)

of dose change per unit density change. To determine this gradient for the curves of Figure 4, 5 and 6 the correction factor CF_ρ is defined as the correction factor for dose at a point on the beams central axis in the lung or bone phantom as related to ρ of this regions (Note: ρ = ρ_e the relative electron density to water in equations 1 to 3).

Polynomial regression of the curves superimposed in Figure 4, 5 and 6 show good fits to the data of CF_ρ versus ρ. The results are summarised in equation 5 with the appropriate coefficients listed in Table 1. This curve fit enables errors to be calculated between any two extreme values of [ρ1,ρ2].:

$$CF_\rho = A\rho^4 + B\rho^3 + C\rho^2 + D\rho + E \qquad (1)$$

The percentage change in correction factor ($\%\Delta CF_{\Delta\rho}$) is defined as the change in CF over a density interval between [ρ1,ρ2]: These values can be used in equation 1 substituting ρ = ρ1 and ρ = ρ2 respectively where Δρ = ρ1 - ρ2:

$$\%\Delta CF_{\Delta\rho} = \frac{CF_{\rho 1} - CF_{\rho 2}}{\frac{1}{2}(CF_{\rho 1} + CF_{\rho 2})} \times 100\% \qquad (2)$$

The relationship of percentage CF change per unit CT number (N_{CT} in Hounsfield units) is established:

$$\frac{\%\Delta CF_{\Delta\rho}}{\Delta N_{CT}} = \frac{(\%\Delta CF_{\Delta\rho})}{\left(\frac{1}{R_\gamma}\right)(\Delta\rho)} \qquad (3)$$

Equation 3 gives a useful relationship between the effect of a change in N_{CT} on change in CF because as shown in the next section Rγ, as defined in equation 5, varies significantly with atomic number of material. It is assigned unity for lung and approximately 0.55 for bone tests (see Figure 7 (b)). Hence equation 3 shows that as the bone curve (N_{CT} versus ρ) has approximately twice the gradient of the soft tissue curve.

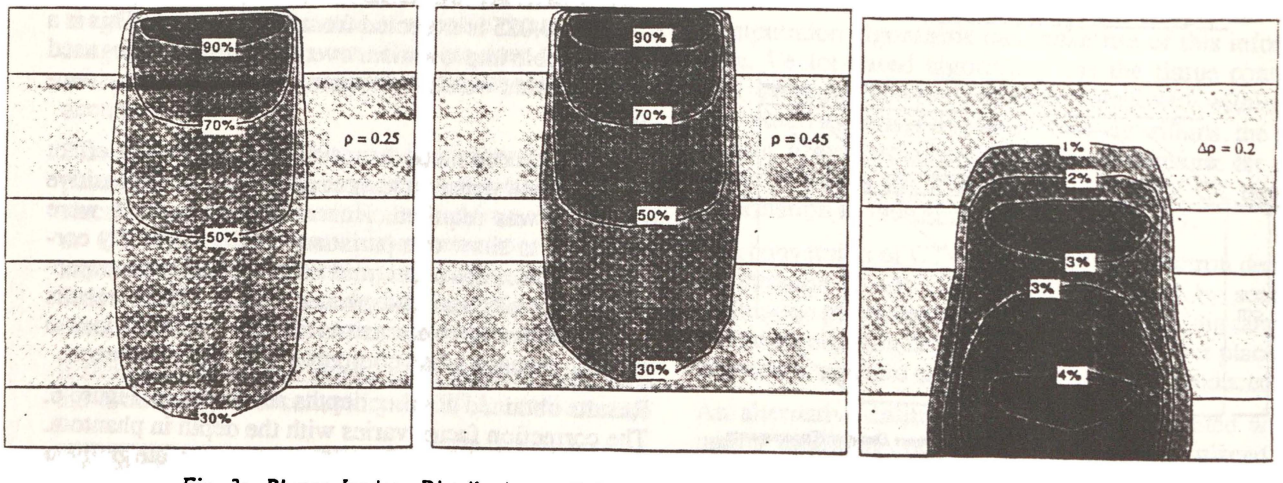

Fig. 3: Photon Isodose Distributions: Cobalt-60, E-TAR algorithm, 10 sq. cm field, 80 cm SSD
(a) Lung Density 0.25: (b) Lung Density 0.45: (c) Dose Difference Map (a-b)

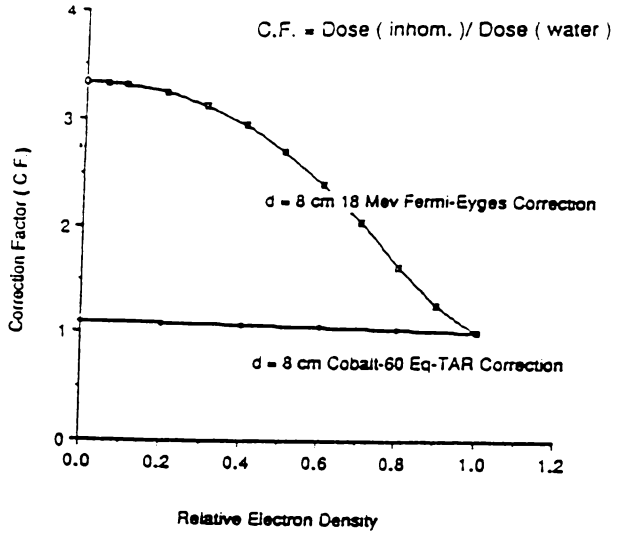

Fig. 4: Effect of Density Change on Mid-Lung Dose (See phantom Figure 1(a)) at one depth for Cobalt-60 Photons and 18 MeV Electrons

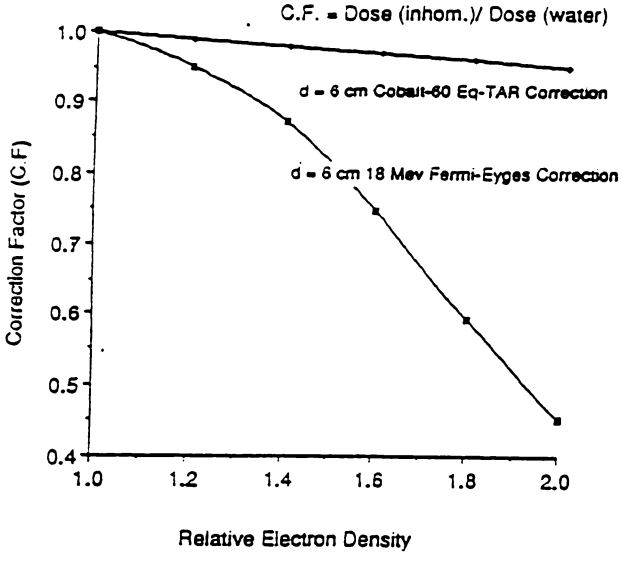

Fig. 5: Effect of Density Change on Mid-Spine Dose (See phantom Figure 1(b)) at one depth for Cobalt-60 Photons and 18 MeV Electrons

The error in dose depends on the density range parameters [ρ1,ρ2]. Table 2 shows some typical values of ρ1 and ρ2 for bone and lung situations as encountered in Figures 4, 5 and 6 and gives indications of the associated change in dose with these density changes.

Use of equation 2 for the lung density ranges quoted in the previous section will give an indication of extreme range. Whilst [0.25, 0.45] is an extreme range of lung density variation nobody attempting an approximation would use either value and in the absence of CT information they are most likely to select a mean value of 0.35. The density range [0.35, 0.45] was therefore used in

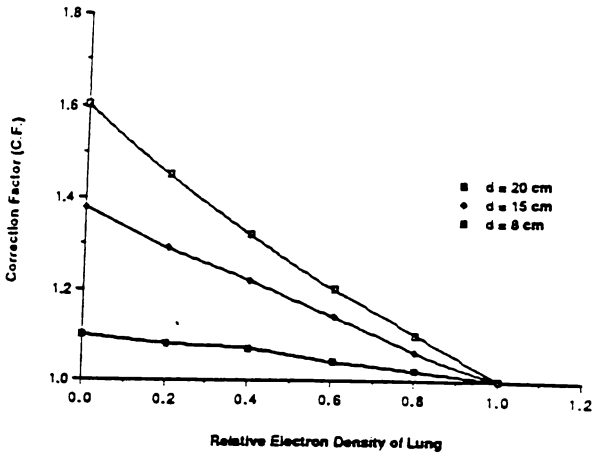

Fig. 6: Effect of Density Change on Lung Dose Three Different Phantom Depths for (10 x 10cm) Cobalt-60 Photons (see phantom Figure 1(a))

Table 2 to indicate the likely error due to using non CT data for lung density assessment. For example, applying this range to equations 1 and 2 an error of 7.0% is observed, mid-lung for the electron beam, if arbitrary density information is used but much smaller errors of less than 1.5% are observed if CT patient specific data are used.

The order of magnitude of these results indicates that the dose error which can be expected from CT data is within the required accuracy (2) provided care is taken with CT number versus electron density calibration (particularly with regard to the bone calibration line). Two different calibration methods are discussed in the next section.

CT Calibration Methods

Calibration plots for a Siemens DRH and a General Electric 8800 scanner, as shown in Figures 7(a) and 8(b) were obtained from data included in Table 3. In this case the electron density relative to water (ρ_e^w) are related to mass density (ρ_m):

$$\rho_e^w = \rho_m \qquad (4)$$

The relationship of CT number (N_{CT}) to electron density relative to water is quasi-independent of beam energy, only if the effective atomic number (Z_{eff}) of the substance matches that of water (and hence soft tissues). This assumption is valid for the lung analogs made of cork which conformed to the Hounsfield regression line fit shown in Figure 7(a).

For the other compounds of different atomic number (Polystyrene, Acrylic, Ertalyte and Delrin) the electron densities are calculable since the chemical formula and mass density are available. Electron densities and atomic numbers were calculated for such compounds, using the formulae of McCullough (10)) and the results of calculations for the samples are provided in Table 3(a): for the DHR and 3(b) for the GE8800.

Bone exhibits extra photoelectric absorption due to its yet higher atomic number. These have been investigated

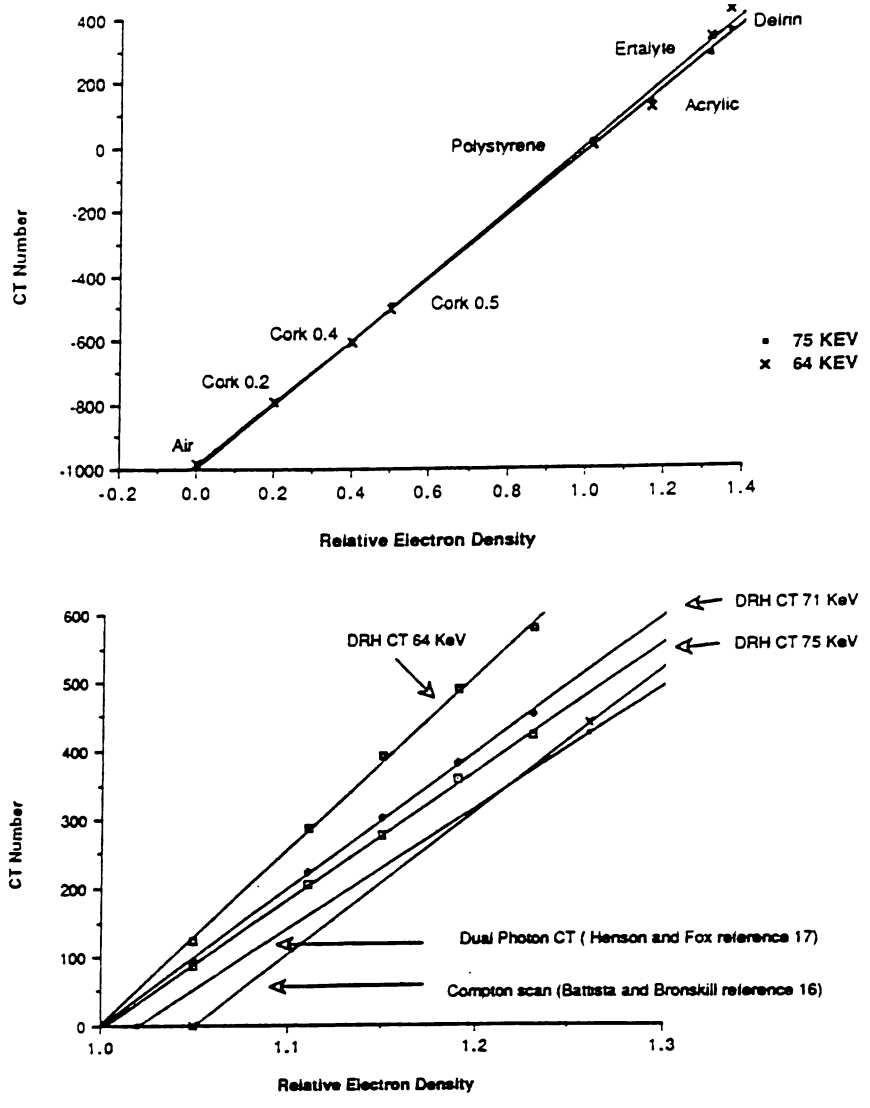

Fig. 7: Tissue Calibration Curves
(a): Calibration of N_{CT} Versus Relative Electron Density (75 keV, 64 keV) Siemens DRH Tissue Calibration Line
(b): Calibration of N_{CT} Versus Relative Electron Density Siemens DRH Bone Calibration at (75 keV, 71 keV, 64 keV) compared to other calibration methods.

here using liquid solutions with various concentrations of mono hydrogen di-potassium phosphate (K_2HPO_4). The method used to ascertain the electron densities and effective atomic numbers from the solution concentrations also followed the guidelines of McCullough (10) also and the results are listed in Table 3.

In comparing Figures 7(a) and (b) it is interesting to note the energy dependance of N_{CT} for the analogs with the greater atomic numbers. Figure 7(b) shows that liquid analogs are limited to electron density levels below ρ_e^w = 1.3, because the solutions become saturated. Due to this upper limit on density and also long term instability of liquid solution, our future studies will focus upon the use of solid bone analogs as proposed by White et al (11, 12, 13, 14).

The samples listed in Table 3(a) were studied on a Siemens DRH scanner. Due to a change in the primary beam attenuation filter (from 0.4 to 0.2 mm Copper) the opportunity arose to examine the effect of tube kilovoltage on sample calibration. Three effective energies were studied (75, 71 and 64 keV) as determined by the use of "effective KeV liquids" (15). It was found that the change in X-ray spectra had little effect on the soft tissue analog calibration lines (Figure 7(a)) but a more significant effect on the bone analog line gradients (Figure 7(b)). This is attributed to the energy dependance of the enhanced photoelectric effect observed in samples of greater atomic number.

Intercomparison of these plots with "in-vivo" data obtained independently by Compton scanning (16) and a dual photon CT method (17) as shown in Figure 7(b) indicates that the K_2HPO_4 compound closely models the slop of the "in-vivo" data. The offset relative to the "in-vivo" data is in part due to uncertainties in the experimental data of 5% for the dual photon case and 10% for the Compton scan data. By introducing the following linear relationship we can obtain the regression lines for the different samples; where $R\gamma$ represents the experimental regression line gradient (see Figure 7(b)).

$$\rho_e^w = R_\gamma\left(\frac{1}{1000} N_{CT}\right) + C \qquad (5)$$

The results in Figure 7(b) show variation of N_{CT} with beam energy and suggest that a periodic calibration technique or continuous "on-line" calibrations will ensure that a change in effective energy is accounted for by the recalibration.

Independent scanner calibration with phantoms requires access to valuable CT scanner time which could be used instead to scan patients. A novel approach to this problem is to introduce a slice-by-slice method of CT calibration.

Implementation of Slice-by-Slice Calibration On a GE 8800 CT Scanner

The crescent shaped phantom design used for density quality assurance is shown in Figure 8(a). Soft tissue and bone analog calibration lines for the GE8800 are shown in Figure 8(b) to indicate the variation in N_{CT} for samples placed either in a body phantom or the crescent phantom.

The reproducibility of lung and bone analog N_{CT} was also measured when placed in various other body phantom configurations. In summary the ΔN_{CT} dependence on sample position and patient size within the image plane is less than 16 HU for cylindrical phantom tests and less than 25 HU for body phantom configurations. The difference in the CT numbers is due in the first case to beam hardening across the image plane and in the second case to cylindrical geometry assumed during the system calibration and image reconstruction process.

Further details of the variations expected for this scanner are also detailed elsewhere (18) and the magnitude of these effects for several different scanner models has been outlined previously in a paper by Mahaworasilpa and Southon (19). Using a crescent phantom underlying the patient is an acceptable way to monitor CT calibration of density within the patient at least for radiotherapy planning purposes.

Conclusions

Large variations (15%) in scanner calibration have been reported by other authors (20). This paper shows that if periodic calibration checks are not implemented a change in CT beam energy can significantly affect bone density assessment.

This variation in tube energy was however due to tube replacement and it is doubtful whether current CT scanners under normal operating conditions will exhibit major changes in calibration, such is the consistency of these devices. It is likely therefore that an initial detailed CT calibration is adequate provided CT tube or detector devices are not modified.

Accurate densitometry is essential for radiotherapy treatment planning with electron beams and is less criti-

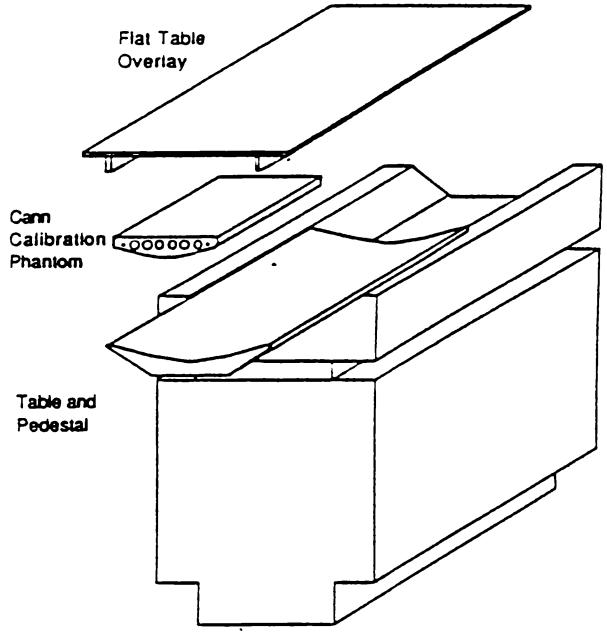

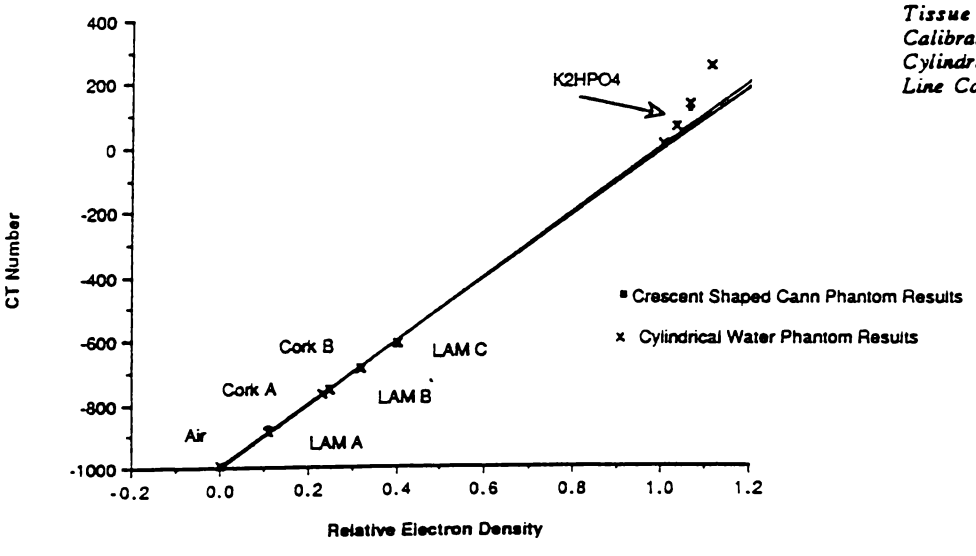

Fig. 8:
(a) Crescent shaped Cann phantom used in on-line density Quality Assurance for Radiotherapy planning purposes.
(b) Calibration of N_{CT} Versus Relative Electron Density (72 keV), GE8800 Tissue and Bone Analog Calibration Line. Crescent Versus Cylindrical Phantom Calibration Line Comparison.

cal for photon beams. The magnitude of dose errors due to density effects have been quantified and effective protocols have been proposed to reduce their extent.

Acknowledgements

We thank Mr Ernest Mah for his comments and for programming assistance with dose difference maps and the electron beam algorithm.

The primary author wishes to thank Dr W.H. Round and Martin Pracy for encouraging his further research in this area. Also Tracy Metcalfe for helping prepare the manuscript.

Table 1: Regression Coefficients Relating Cuves in Figures 8, 9, 10 to Equations 5 and 6

This table provides data used in equation 1 and enables errors to be calculated between any two ranges of density selection [ρ1,ρ2]

Phantom Type	Beam Type	Depth (cm)	Cofficients A	B	C	D	E	Reference Figure
"Two-Lung"	18 Mev	8	5.384	-8.881	1.717	-0.571	3.345	4
	Cobalt	8	-0.006	0.039	-0.085	-0.042	1.095	4,6
		15			0.073	-0.457	1.385	6
		20		-0.066	0.257	-0.787	1.597	6
"Bone"	18 MeV	6			-0.334	-0.438	0.902	5
	Cobalt	6				-0.051	1.051	5

Table 2: Errors expected in terms of (%ΔCF) In the Lung and Bone Phantoms

Phantom	Beam	Depth (cm)	Conventional X-ray ρ1	ρ2	%ΔCF		CT Densitometry ρ1	ρ1	%ΔCF	
"Two-lung"	18MeV	8	0.35	0.45	7.0	*	0.35	0.375	1.5	**
	Cobalt	8	0.35	0.45	0.9	*	0.35	0.375	0.2	**
		15	0.35	0.45	3.3	*	0.35	0.375	0.8	**
		20	0.35	0.45	4.6	*	0.35	0.375	1.0	**
"Bone"	18MeV	6	1.25	1.45	10.5	*	1.25	1.264	0.3	***
	Cobalt	6	1.25	1.45	1.0	*	1.25	1.264	0.1	***

Footnotes

* These changes relate to a density varation of 0.1 as expected using population averaged density assignments for lung and a varation of 0.2 arbitrarily assigned for bone.

** These changes relate to an N_{CT} variation of 25 HU using $R\gamma$ of 1.0 in equation (3). ($\Delta\rho = 0.025$)

*** These changes relate to an N_{CT} variation of 25 HU using $R\gamma$ of 0.55 in equation (3) ($\Delta\rho = 0.014$)

Table 3(A): Electron Density, Effective Atomic Number and N_{CT} for a Siemens DRH CT Scanner

Compound (Formula)	Mass Density	Electron Density	Effective Atomic No:	Concentration (mg/ml)	C.T. Scanner (N_{CT}) 75 keV	71keV	64 keV
AIR	0.001	0.001	1.02	-	-985.6	-	-984.2
CORK	0.2	0.2++	1.0++	-	-789.2	-	-789.4
CORK	0.4	0.4++	1.0++	-	-606.3	-	-605.5
CORK	0.5	0.5++	1.0++	-	-491.5	-	-501.9
POLYSTYRENE (C_8H_8)	1.04	1.01	0.77	-	8.3	-	1.6
ACRYLIC ($C_5H_8O_2$)	1.19	1.16	1.02	-	128.1	-	115.2
ERTALYTE ($C_5H_4O_2$)	1.29	1.31	0.89	-	274.6	-	327.2
DELRIN (CH_2O)	1.41	1.36	0.94	-	348.5	-	412.4
(K_2HPO_4)	1.06	1.05	1.15	75	88.2	96.1	122.1
(K_2HPO_4)	1.13	1.11	1.29	180	204.0	223.5	286.9
(K_2HPO_4)	1.18	1.15	1.36	250	276.0	302.6	391.5
(K_2HPO_4)	1.23	1.19	1.42	325	359.3	383.1	488.5
(K_2HPO_4)	1.27	1.23	1.47	400	424.3	454.0	580.5

Table 3(B): Electron Density, Effective Atomic Number and N_{CT} for a GE 8800 CT Scanner

Compound (Formula)	Mass Density	Electron Density	Effective Atomic No:	Concentration (mg/ml)	C.T. Scanner (N_{CT}) C.T. Scanner GE 8800 (72KeV) Cann Phantom	Body Phantom
AIR	.001	.001	1.02	-	-992.5	-995.0
LAM+	0.11	.11++	1.0++	-	-875.1	-884.8
CORK	0.23	.23++	1.0++	-	-766.9	-766.4
LAM+	0.25	.25++	1.0++	-	-748.2	-753.4
CORK	0.32	.32++	1.0++	-	-683.2	-690.2
LAM+	0.40	.40++	1.0++	-	-619.7	-608.9
WATER	1.0	1.0	1.0	-	-3.1	5.4
(K_2HPO_4)	1.03	1.03	1.11	50	64.1	61.1
(K_2HPO_4)	1.07	1.06	1.19	100	113.3	129.1
(K_2HPO_4)	1.13	1.11	1.31	200	252.6	248.1

Footnotes:

\+ LAM= Lung analog material, manufacturer claims contains approximately 6% H, 68% C, 9% N, 17% 0.

++ Lack of detailed chemical formulae, requires equation 4 to be invoked. Evidence that this approximation is valid for these samples provided by the linear relation between N_{CT} and density as shown in Figures 7(a) and 8(b).

References

1. Task group 21, Radiation Therapy Committee, American Association of Physicists in Medicine, *A protocol for the determination of absorbed dose from high energy photon and electron beams.* Med Phys., (1983), 10, 6, 741-771.
2. ICRU, Report #24, *Determination of absorbed dose in a patient irradiated by beams of X or gamma rays in radiotherapy procedures* (1976), 46
3. Metcalfe P.E., Battista J.J. *Accuracy of inhomogeneity corrections in lung irradiated with high energy X-rays.* Australasian Phys. Eng. Sci. Med. (1988) 11, 2, 67-75.
4. Cann C.E., Genant H.K. *Precise measurement of vertebral mineral content using CT.* J. Comput. Assist. Tomogr. (1980) 4, No. 4.
5. Kalendar W.A., Suess C. *A new calibration phantom for quantitative computed tomography.* Med. Phys. (1987) 14, 5, 863-866.
6. Sontag M.R., Cunningham J.R. *The Equivalent Tissue-Air-Ratio method for making absorbed dose calculations in heterogeneous medium.* Radiology, (1978) 129, 3, 787-794.
7. Hogstrom K.R. *Evaluation of electron pencil beams dose calculations.* AAPM presentation (Abstract) Med. Phys. (1985) 12. No. 4.
8. Cygler J., Battista J.J., Scrimger J.W., Mah E., Antolak J. *Electron dose distributions in experimental phantoms: A comparison of 2D pencil beam calculations.* Phys. Med. Biol. (1987) 32, 9, 1073-1086.
9. Van Dyk J., Keane T.J., Rider W.D. *Lung density as measured by computerised tomography: Implications for radiotherapy.* Int. J. Radiation Oncology Biol. Phys., (1982) 8, 1363-1372.
10. McCullough E.C., Holmes T.W. *Acceptance testing radiation treatment planning systems.* Med. Phys. (1985) 12, 5, 237-242.
11. Woodard H.Q., White D.R. *The composition of body tissues.* Brit. J. Radiol. (1986), 59, 1209-1219.
12. White D.R., Constantinou C., Martin R.J. *Foamed epoxy resin-based lung substitutes.* Brit. J. Radiol. (1986) 59, 787-790.
13. White D.R., Martin R.J. Darlison R. *Epoxy resin based tissue substitutes.* Brit. J. Radiol. (1977) 50, 814-821.
14. Woodard H.W. *Bone models for use in radiation dosimetry.* Brit. J. Radiol. (1982) 55, 277-282.
15. White D.R., Speller R.D. *The measurement of effective photon energy and linearity in computerised tomography.* Brit. J. Radiol. (1980) 53, 5-11.
16. Battista J.J., Bronskill M.J. *Compton scatter imaging of Transverse sections: an overall appraisal and evaluation of radiotherapy planning.* Phys. Med. Biol., (1981) 26, 1, 89-99.
17. Henson P.W., Fox R.A. *The electron density of bone for inhomogeneity correction in radiotherapy planning using CT numbers.* Phys. Med. Biol. (1984) 29, 4, 351-359.
18. Hangartner T.N., Battista J.J., Overton T.R. *Performance evaluation of density measurements of axial and peripheral bone with X-ray and gamma-ray computed tomography.* Phys. Med. Biol. (1987) 32, 11, 1393-1406.
19. Mahaworasilpa T., Southon F.C.G. *CT Vertebral Bone Mineral Measurement - Instrinsic errors of single KV.* Australasian Phys. Eng. Sci. Med. (1986) 9, 1, 23-28.
20. Levi C., McCullough E.C., Hattery R.R. *The unreliability of CT numbers as absolute values.* Amer. J. Roentengology, (1982) 139, 443-447.

Australasian Physical & Engineering
Sciences in Medicine (1988) Vol. 11 No 2

ACCURACY OF INHOMOGENEITY CORRECTIONS IN LUNG IRRADIATED WITH HIGH ENERGY X-RAYS*

P.E. Metcalfe[1] and J.J. Battista[2],
[1]*Waikato Hospital, Hamilton, New Zealand*
[2]*Cross Cancer Institute, Edmonton, Canada*

Abstract

Dosimetry results obtained using a "two lung" phantom are compared with dose computations produced by superposition (1), equivalent TAR and regional Batho methods. The TAR methods show reasonable agreement with dosimetry results at cobalt 60 energy, but errors as high as 17% were observed in the lung phantom at a higher photon energy (15MV). We discuss the TAR algorithm assumptions which do not allow for electronic disequilibrium and thus lead to significant errors in dose prediction accuracy. A superposition technique which shows better agreement with the experimental data at high energies is presented. This shows promise within the bounds of certain computing time constraints which are quantified.

Key Words

Radiotherapy, Computerised Treatment Planning, Superposition, Convolution, Tissue-Air-Ratio

Introduction

Monte Carlo methods provide accurate dose results for beams incident on inhomogeneous media (2). However, the computing time required to simulate the history of several million particles to achieve accurate results is unacceptable for routine use in radiotherapy patient beam planning.

Hence semi-empirical approximations (3) have been devised which predict dose distributions from broad photon beam interactions with body inhomogeneities of various complexity. These algorithms generally represent a compromise between dose accuracy and computing time constraints.

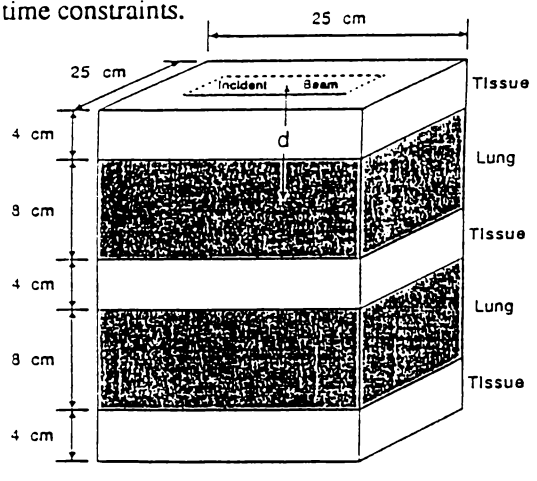

Fig.1 Two Lung Phantom (Oblique Chest)

*Presented AAPM conference Michigan-Detroit, USA, 1987 and EPSM conference Auckland, New Zealand, 1987
Manuscript received 5 April 1988, revised 9 May 1988.

This article quantifies errors in dose computation which occur in lung by comparing dose computations with dosimetry results in a "two-lung" model shown in figure 1. This arrangements approximates the situation of a therapy beam laterally traversing the chest wall and lungs in the patient thorax region (4).

The density of the materials used in the phantom have been accurately measured to minimise the uncertainty in dose caused by inaccurate density assessment. Appraisal of the latter effect is the subject of a companion article (5).

Theory

Correction Factors For Tissue Inhomogeneities

Correction methods are often compared in terms of inhomogeneity correction factors (CF) which relate the dose in an inhomogeneous medium to the dose in an all water medium:

$$CF = \frac{\text{Dose to inhomogneous medium}}{\text{Dose to homogeneous medium}} \qquad (1)$$

This pertubation approach produces a convenient way of adjusting doses in a homogeneous medium, which are precalculated by the multiplication factor (CF) to give an estimate of the degree of perturbation due to interaction with the inhomogeneous media.

The BATIIO Correction

The Batho power law method of dose computation uses tissue-air-ratios raised to an exponent based on density differences. The method corrects for changes in primary photon fluence and approximates scattered radiation effects (6). The inhomogeneity is assumed to be slab extending well beyond the beam boundaries. The original method only calculated dose beyond inhomogeneities (7) but Sontag and Cunningham (8) subsequently

extended the technique to calculate dose within inhomogeneities. The technique used in this article is based on a further small modification by El-Khatib and Battista (9) which improves the accuracy of this method within lung by using tissue-phantom-ratios (TPR).

$$CF = \frac{[TPR(d_1, r)]^{\rho_2 - \rho_1}}{[TPR(d_2, r)]^{1-\rho_1}} \quad (2)$$

TPR = Tissue - phantom - ratio

ρ_1 = relative electron density of medium 1

ρ_2 = relative electron density of medium 2

d_1 = distance from calculation point to top of inhomogeneity

d_2 = distance from calculation point to skin surface

r = beam radius at depth of calculation point

As with all TAR (TPR) methods, the Batho method inherently assumes full electron beam equilibrium and it is this assumption which leads to the errors in dose prediction for high energy X-rays.

The Equivalent (TAR) Correction

The Equivalent tissue air ratio (E-TAR) method developed by Sontag and Cunningham (10) was the first algorithm which attempted to correct for the scattered radiation component by using multiple slice CT pixel density information. This was achieved by scaling the beam size in proportion to the lateral electron density distribution and associated photon scattering. At present, it is the "benchmark" to which other algorithms are compared since it is the most advanced algorithm commercially implemented and shows a good compromise between dose accuracy and speed of computation.

This algorithm and the superposition approach outlined in the next section both rely on O'Connors range scaling theorem(11) which predicts that the dose to a point in a unit density medium is the same as the dose to a point in a non-unit density medium provided the beam radius (r) and depth (d) are appropriately scaled. The inhomogeneity correction factor is defined using the E-TAR method as:

$$CF = \frac{TAR(d', \tilde{r})}{TAR(d, r)} \quad (3)$$

The derivation of suitable ways to scale d' and $\tilde{r}$ to account for primary and scatter contributions are dealt with as follows. Using standard ray tracing the radiological beam depth (d') is the geometric depth scaled by the average density ($\bar{\rho}$) lying along a beam ray where the path length is made up of n pixels:

$$d' = d\bar{\rho} \quad (4)$$

$$\bar{\rho} = \sum_{i=1}^{n} \frac{1}{n} \rho_i \quad (5)$$

As the scatter increases with beam size, the beam radius is scaled in a complicated fashion to account for the relative "scattering power" of the neighbouring voxels to the dose voxel in question:

$$\tilde{r}' = r\tilde{\rho} \quad (6)$$

where:

$$\tilde{\rho} = \frac{\sum_i \sum_j \sum_k \rho_{ijk} W_{ijk}}{\sum_i \sum_j \sum_k W_{ijk}} \quad (7)$$

The E-TAR algorithm is three dimensional in conception but only two dimensional in implementation. The three dimensional summation of W_{ijk} has not been attempted as it is considered too time consuming for available computing resources. Hence present day commercial implementations use a two dimensional simplification of the method, relying on the "assumption" of separability:

$$W_{ijk} = W_k W_{ij} \quad (8)$$

where:

$$\tilde{\rho}'_{2D} = \frac{\sum_i \sum_j \left(\sum_k \rho_{ijk} W_k \right) W_{ij}}{\sum_i \sum_j W_{ij}} \quad (9)$$

and

$$W_k = \Delta SAR\ (d_{ref}, r_1) - \Delta SAR\ (d_{ref}, r_2) \quad (10)$$

r_1 = radius of large field size and

r_2 = radius of small field size

This reduces the method to a two dimensional method with some weighting applied from the third dimension by placing the lateral density information in an effective scattering slice at an average location away from the calculation plane (see Figure 2).

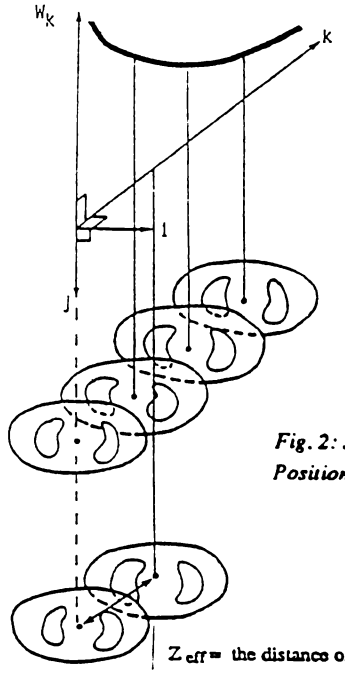

Fig. 2: Schematic of Scatter Plane Positioning for E-TAR Correction

Regardless of its two or three dimensional implementation, however, the accuracy of the algorithm relies on the calculation of weighting factors. The calculation of W_{ij} includes the consideration of first and multiple scattering, separated into first and multiple scatter components.

Accurate experimental measurement of such differential scatter-air-ratios has proven difficult due to the small dose differences which need to be detected (12). Weighting factors are thus calculated using semi-analytic principles described in the original work (13, 14, 15). These derivations assume electron equilibrium and this leads to the errors in dose prediction accuracy shown later in Figure 5.

Lateral Electron Disequilibrium

This phenomenon has been characterised by other researchers (16, 17, 18) but a brief discussion is included here. Due to electrons ranging longitudinally and laterally from the site of photon interactions, the site of energy deposition (dose) is different from the site of energy release (KERMA). If the beam width and phantom depth are greater than the longitudinal and lateral range of the electrons set in motion, then the same aggregate electron energy enters a dose site as leaves the site. In this case electronic equilibrium is said to exist. the phenomenon is sketched in Figure 3 which shows that disequilibrium occurs near the edge of photon fields. The latter effect is small in unit density media but it is nevertheless observable in the penumbral isodose lines of high energy photon beams. These effects are generally accounted for in a water medium through the use of empirical beam edge shaping functions.

In a lower density medium, the electron range is extended at high energies (eg. 15MV X-rays) to sometimes exceed the field width. In this situation electron lateral disequilibrium extends across the entire field width leading to a "dose void" along the central axis, as is described in this article.

The SUPERPOSITION Correction (Deposition Viewpoint)

The superposition system of mapping dose deposition in a homogeneous phantom implies that the dose to a point $\bar{r}$, $(D(\bar{r}))$, from a photon interaction at point $\bar{r} - \bar{r}'$ can be represented by the superposition integral (convolution integral in real space) of the primary fluence (ϕ) and the energy spread function (G). In this manner scattered electrons ranging away from the initial interaction sites are accounted for. Therefore, the dose deposition site and (KERMA) interaction sites are not coincident, unlike previously described methods which assume "on the spot" energy absorption.

Following the implementation of Mackie et al (1) we use a Greens function which serves as the superposition Kernel describing energy spread from the primary interaction site. The subcomponents of this energy spread are electrons from primary KERMA interaction $G_e(\bar{r} - \bar{r}')$, first scatter $G_s(\bar{r} - \bar{r}')$ and multiple scatter $G_m(\bar{r} - \bar{r}')$. Schematic representation of this relationship is shown in Figure 4 and the mathematical description is given in equations 11 and 12. If ϕ_p is the photon fluence at position $(\bar{r}')$ and D is the dose to the volume element at position $(\bar{r})$ then:

$$D(\bar{r}) = \int \phi_p(\bar{r}')\, G_e(\bar{r} - \bar{r}')\, d\bar{r}' + \int \phi_p(\bar{r}')\, G_s(\bar{r} - \bar{r}')\, d\bar{r}' + \int \phi_p(\bar{r}')\, G_m(\bar{r} - \bar{r}')\, d\bar{r}' \qquad (11)$$

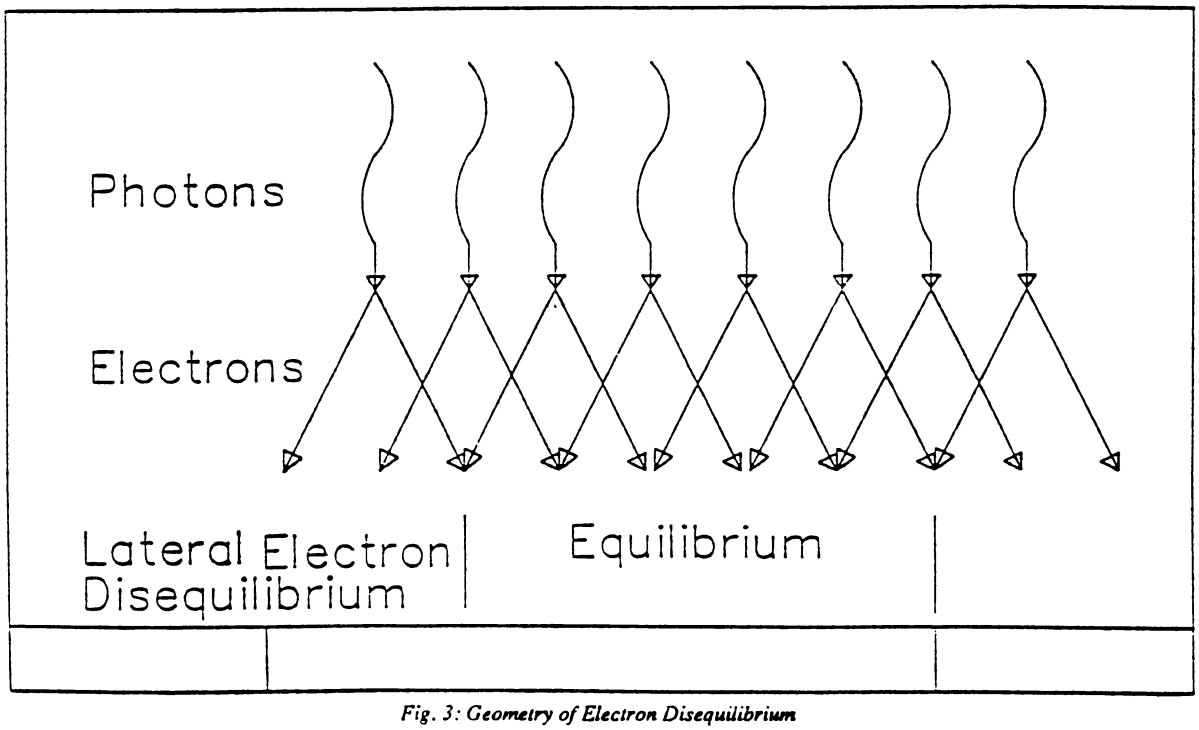

Fig. 3: Geometry of Electron Disequilibrium

By invoking the "Superposition" principle all three kernels can be summed such that the total Greens function kernel describing electron energy deposited at D(r) is given by

$G_T = G_e + G_s + G_m$:

$$D(\bar{r}) = \int \phi_p(\bar{r}') G_T(\bar{r} - \bar{r}')\, d\bar{r}' \qquad (12)$$

The Kernels are obtained by Monte Carlo techniques, such as (MOCA) (1) or electron gamma shower codes (EGS) (19,20,21,22) as discussed further in appendix 1. These yield an accurate mapping of charged particle transport which can be manipulated to account for the lateral disequilibrium in non unit density media. The computer implementation uses discrete summation over Cartesian coordinates for voxel elements:

$$D(i',j',k') = \sum_{i'}\sum_{j'}\sum_{k'} \phi_p(i',j',k')\, G(i-i', j-j', k-k') \qquad (13)$$

The advantage of this approach is that the dose at all locations (i,j,k) is incremented progressively as photon "impulse" locations (i',j',k') are scanned, yielding ultimately the complete three dimensional dose distribution. The disadvantage is the difficulty in properly modifying the Greens function (as generated in the homogeneous media) to account for inhomogeneities.

In this application O'Connors range scaling assumption as discussed previously has been used on a ray-by-ray basis (along $\bar{r} - \bar{r}'$) to approximate the change of the Greens function by the density.

Methods

Batho, E-TAR and superposition computations were performed on a VAX 11/780 computer running the Alberta Treatment Planning (ATP) software (23). Comparisons were made for two photon energies (Cobalt-60 - Theratron-80 and 15MV X-rays - Siemens Mevatron XX) along the beam central axis. Dosimetry was performed by placing an ionisation chamber at various positions in a cork-polystyrene sandwich phantom described in Figure 1.

Measurements were performed at the two participating institutions. The Cobalt-60 data were obtained with a Baldwin Farmer type (Nuclear Enterprises, 0.6ml, 2571 graphite) ionisation chamber in cork with a relative electron density of 0.2, whereas the 15MV readings were recorded using a Baldwin farmer type Capintec (PR-06, 0.65ml) ionisation chamber in cork with an electron density of 0.25.

All "in-cork" measurements were recorded without a build-up cap in order to avoid inducing a false electronic equilibrium. The 2% error bars shown in Figures 3 and 5 represent the experimental uncertainty using this technique due to positioning errors and changing spectra in regions of severe disequilibrium. A recent publication (24) indicates that the mismatch between chamber wall

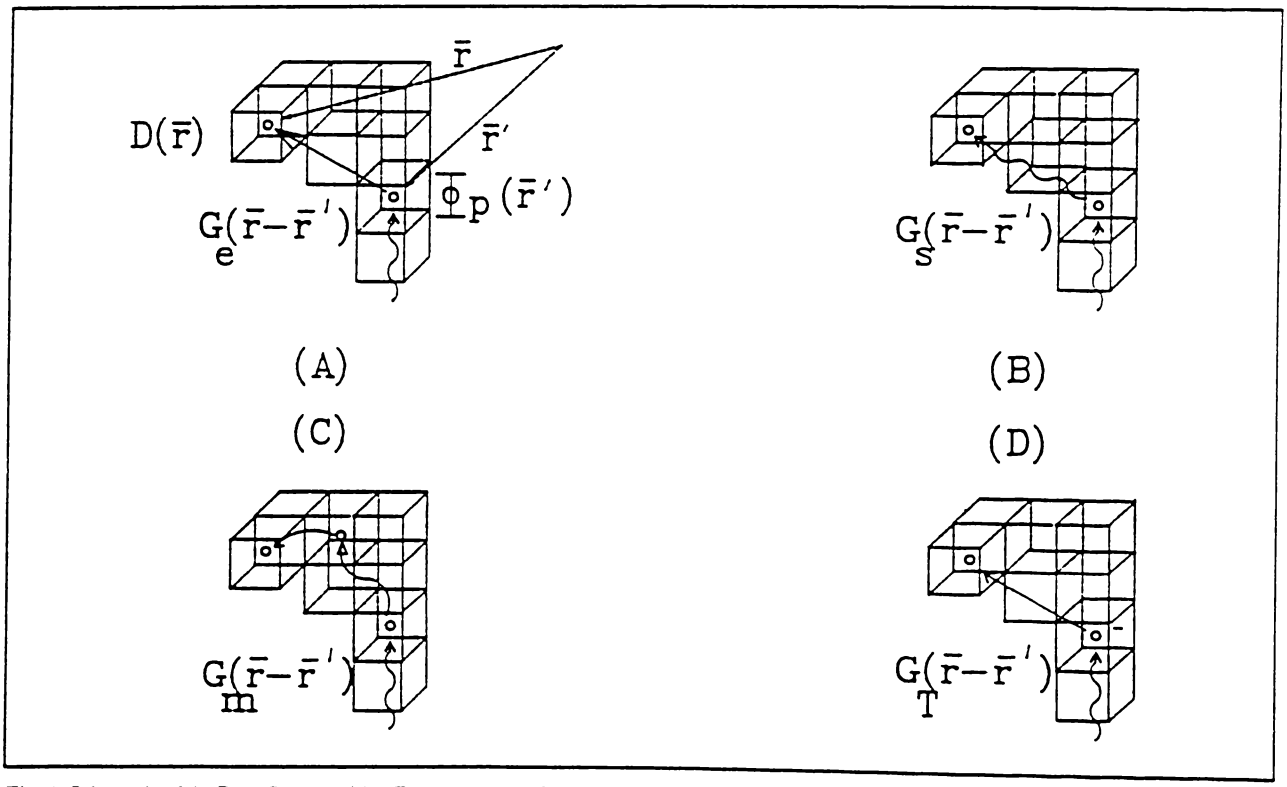

Fig. 4: Schematic of the Dose Superposition Framework (a): Greens Function Describing Electron Ranging From Primary KERMA (b): Greens Function Describing First Scatter (c): Greens Function Describing Multiple Scatter (d): Greens Function Describing Total Dose Transport

and a low density medium causes very small errors in dose prediction and this article confirms that using the simple ratio of ionisation chamber readings is valid for the ionisation chambers used in this study.

Results

Central axis depth dose results shown in Figure 5 indicate that the TAR(TPR) based algorithms closely model the experimental results at Cobalt energy (1.25 MeV) for this phantom configuration. The results indicate that the Batho and E-TAR corrections are adequate for all data points to within the 2% experimental uncertainty. Similar results were obtained for other field sizes (5cm square and 25cm square) but these are not reported here.

A similar accuracy was also achieved along the central axis of 15MV X-ray fields for sizes greater than 10cm square. However for a smaller field size (5cm square) both TAR(TPR) algorithms are inaccurate by as much as 17% as shown in Figure 6. This is due to the disequilibrium effect caused by lateral electron scattering as described previously (16,17,18).

Results of the superposition algorithm are also shown in Figure 6, indicating superior performance, although there is some disagreement in the second deeper lung. It is speculated that this may be due to beam hardening which is significant at this depth. This could be overcome by either doing repeated superpositions for each beam spectral component or by simply modifying the fluence component by a depth by depth KERMA weighted attenuation coefficient rather than "an effective attenuation" coefficient. This would better account for poly-

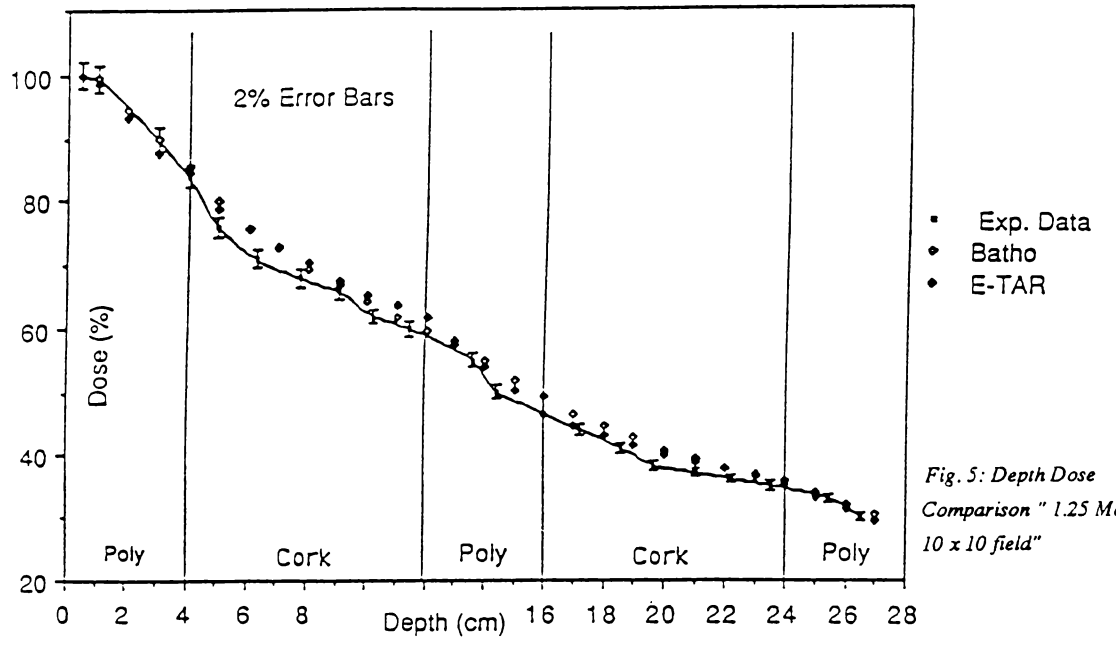

Fig. 5: Depth Dose Comparison " 1.25 MeV, 10 x 10 field"

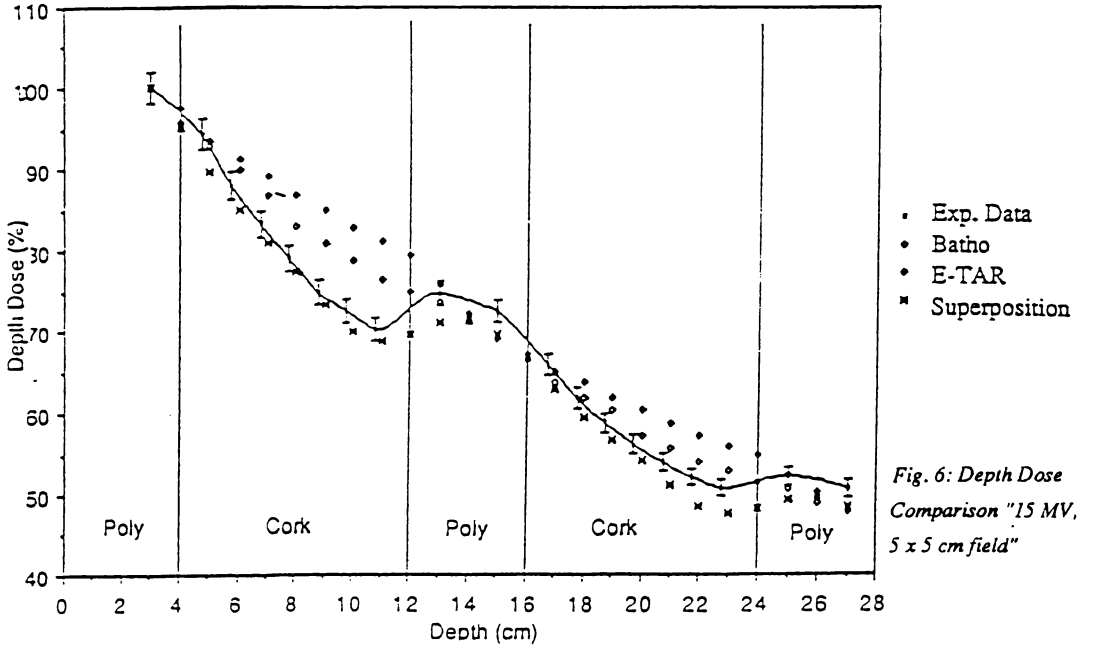

Fig. 6: Depth Dose Comparison "15 MV, 5 x 5 cm field"

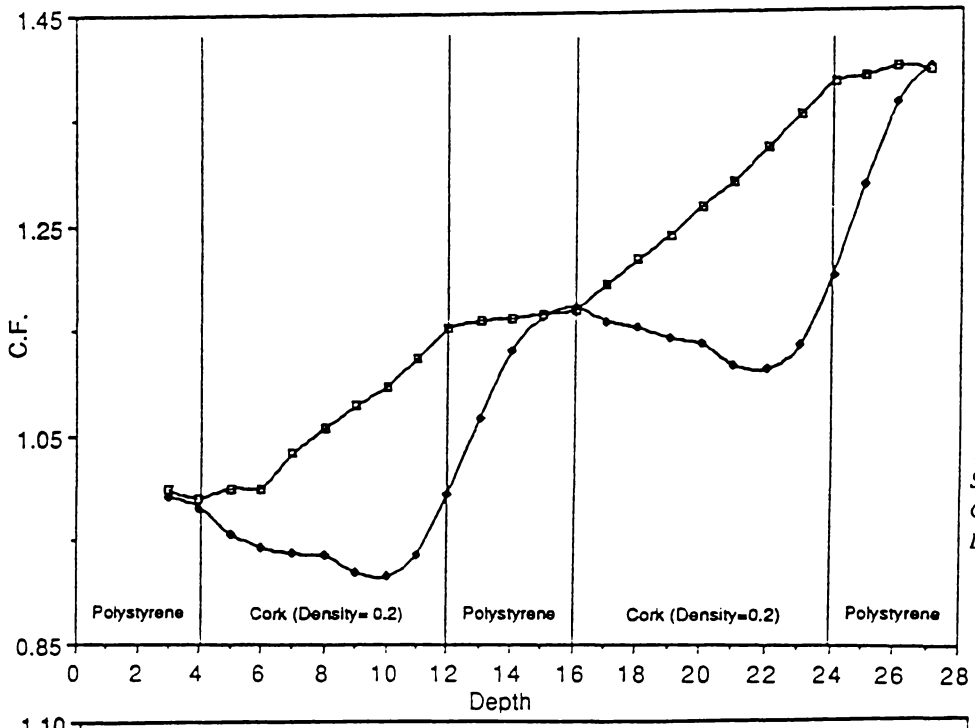

Fig. 7: Comparison of Superposition and E-TAR Corrections (a): Lung Density 0.2

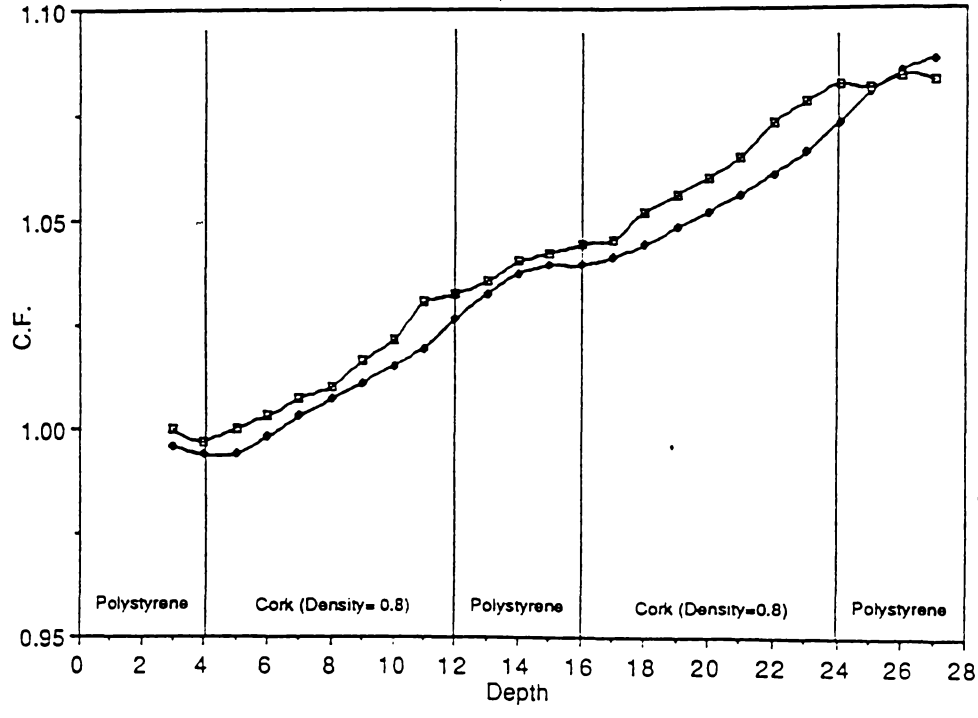

Fig. 7: Comparison of Superposition and E-TAR Correction (b): Lung Density 0.8

chromatic beam components, although may be an insignificant effect (1). It also appears that this implementation of the algorithm is insensitive to very localised density changes at tissue interfaces, probably due to the coarse voxel arrays which hold the spread kernels (1cm³); this tends to "smear" the localised dose perturbation. This limitation can be overcome by performing the computation with a finer Cartesian grid. As the lung density is increased and the disequilibrium effect becomes less significant, one would expect the TAR(TPR) and Superposition Corrections to converge as was indeed found in Figures 7a and 7b.

The computing implementation of the superposition technique is intrinsically three dimensional. Thus, field length and width are accounted for in the computation; this has advantages over the TAR(TPR) methods which rely on equivalent square field data. Figure 8 indicates the errors introduced by implied field symmetry when simplified two dimensional algorithms are applied. This result suggests that three dimensional algorithms need to be incorporated into planning systems for optimum dose accuracy.

Number of Dose Voxels	:	Dose Matrix	CPU Time(minutes)
700		5x5x28	3.11
1008		3x12x28	6.15
1372		7x7x28	10.21
2800		10x10x28	34.00
4096		16x16x16	50.00*
32768		32x32x32	492.00*

*T.R. Mackie (29),
Vax 11/780 processor, 4 Megabytes of Main Memory, Kernel size 1 cm

Table 1: CPU Timing Results for Superposition in Real Space

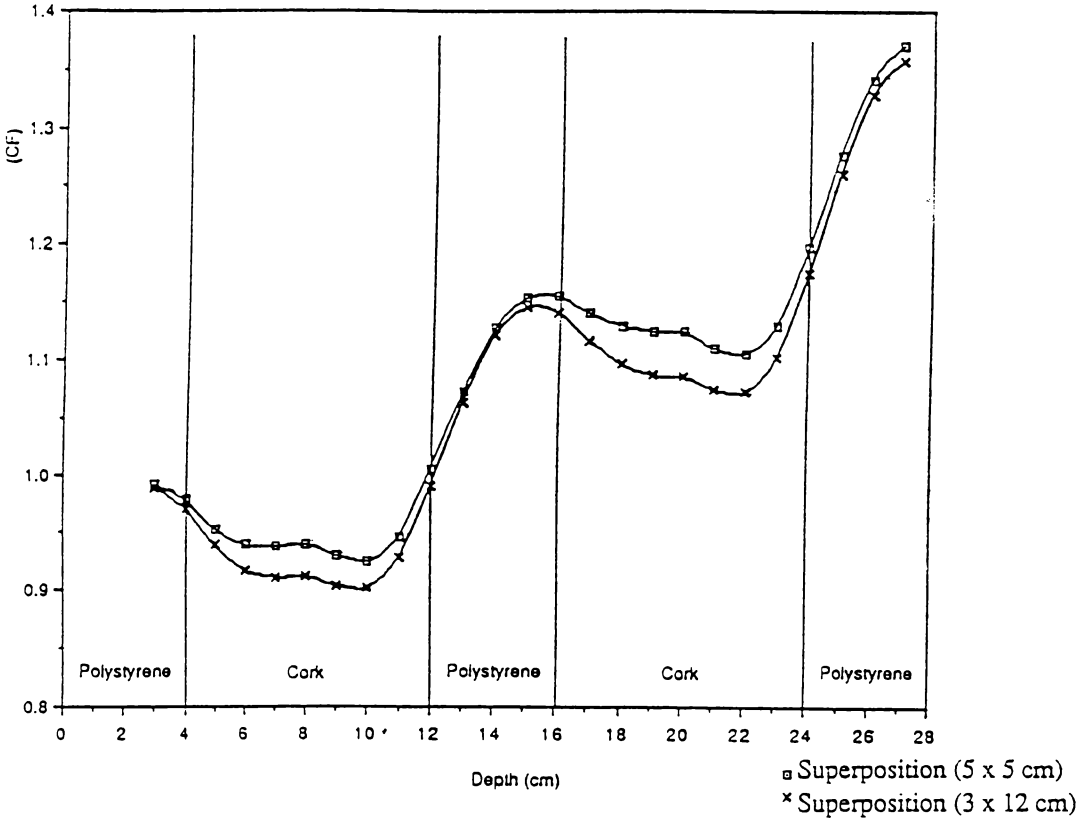

Fig. 8: Superposition Performance Comparison "15 MV 5 x 5 versus 12 x 3 cm fields"

Computational Speed

Timing tests summarised in Table 1, indicate the computing time required for the superposition algorithm using present day hardware. A coarse matrix was used to generate the central axis results shown in Figure 6 in only 3.11 minutes. However as previously pointed out, further optimisation of this technique is required to attain sufficient spatial resolution in high dose gradient regions such as tissue interfaces and the beam penumbra.

The technique slows markedly as the number of voxels increases. This is because the real space superposition of a primary fluence distribution $\phi_p(i',j',k')$ with a scatter kernel $G(\Delta i,\Delta j,\Delta k)$ requires $i^2 \times j^2 \times k^2$ multiplications. Two dimensional implementations reduce the computing times by two orders of magnitude but this compromises dose accuracy as shown for example in Figure 8.

Another suggested approach to increasing the speed of the process is called "nesting" superposition, whereby the matrix size is adjusted for each scatter component. This technique has precedent, as it is already used in E-TAR implementations where the scatter weights are applied on a coarser grid. Present research at the Waikato University centre if focused on speeding up the process. By using a more powerful computer (a VAX 8530) speed gains of a factor of eight have been achieved for a find grid three dimensional dose matrix (64 x 64 x 8) and using the nesting approach could further significantly reduce these times. As tests are incomplete this will be the subject of a future publication. Further improvements of

speed may also be obtainable by the introduction of even faster computer hardware such as "transputers", which may more quickly handle the large multiplications involved.

Perhaps the most efficient increase in computation speed is promised by reducing the superposition integral to a convolution product (25) and performing a convolution in Fourier space (26) using the fast fourier transform.

Computing tests performed by Field and Battista (25) in a homogeneous phantom show that a strict convolution of two 32 x 32 x 32 dose spread arrays using the transform reduces computing time by a factor of 36. This result although less optimistic than that of Boyer's (27) nevertheless indicates better than an order of magnitude improvement in computation speed for 3 dimensional calculations. Unfortunately convolution in Fourier space is valid only if the Greens function is spatially invariant (27,28). Since inhomogeneities introduce non-linearities into the Kernels, no obvious solution to this problem exists and further research is warranted.

Conclusion

Implementation of the superposition technique combined with O'Connors scaling does account for lateral disequilibrium of electrons and leads to an improved dose accuracy superior to that presently achieved with TAR(TPR) based methods. Superior accuracy is also due to its inherent three dimensional approach which may become more important as three dimensional planning of beam positioning and dose distributions evolves. However there remains time constraints for routine planning applications which have yet to be overcome.

Appendix 1:

Discussion of Monte-Carlo Techniques

Dose spread array data are obtained by using Monte-Carlo techniques. The exact "scoring" technique has been discussed in previous articles (1,21,29) so will not be further outlines here.

However Monte-Carlo codes which are employed in the procedure do warrant brief discussion. At least 10^6 charged particles per cm^2 are set in motion by a pencil beam of monochromatic photons. Like many statistical techniques a large number of histories are necessary to reduce the statistical error in the results.

Both MOCA and EGS take into account the photoelectric, Compton and pair production effects. At the 15MV energy studied here the codes have been shown to produce virtually identical results (29).

EGS is however more adaptable over a wide photon energy range, partly because it distinguishes positrons from electrons, whereas MOCA transports positrons as though they were electrons. Also MOCA employs the continuous slowing down of electrons approximation to delta rays and does not account for bremsstrahlung.

MOCA is adequate at the energies tested in this article but for the above reasons the new data base produced by Mackie et al (21) which contains dose spread arrays for energies from 0.1 to 50 MeV is produced using the EGS code. This is because of its greater accuracy over this large energy range.

Acknowledgements

The authors would like to thank T. Rock Mackie for the use of his original superposition program and for inspiration.

Thanks to Peter Hoban for helpful discussions about the paper.

Thanks also to the respective institutions which encouraged the scientific exchange which led to this publication.

References

1. Mackie T.R., Scrimger J.W., Battista J.J. *A convolution method of calculating dose for 15-MV X-rays.* Med. Phys., (1985), 12, 188-196.
2. Raeside D.E. *Monte Carlo Principles and Applications*, Phys. Med. Biol., (1976), 21(2), 181-187.
3. Cunningham J.R. *Radiotherapy planning dose calculations.* Canadian College of Physicists in Medicine Symposium, (Extended Abstract) Toronto, 1987.
4. Van Dyk J. *Lung dose calculations using computed tomography: Is there a need for pixel based procedures.* Int. J. Radiation Oncology Biol. Phys., (1983), 9, 1035-1041.
5. Metcalfe P.E., Beckham W.A., Long B.H., Battista J.J. *Quality assurance of C.T. densitometry for Radiotherapy Dose calculations*, Submitted for publication, ACPSM Journal, 1988.
6. Wong J.W., Henkelman R.M. *A new approach to pixel based photon dose calculations in heterogeneous media.* Med. Phys., (1983), 10(2), 199-208.
7. Batho H.F. *Lung corrections in cobalt-60 beam therapy. J.* Canadian Ass. of Radiologists, (1964), 15, 79-83.
8. Sontag M.R., Cunningham J.R. *Corrections to absorbed dose calculations for tissue inhomogeneities.* Med Phys., (1977), 4, 431-436.
9. El-Khatib E., Battista J.J. *Improved lung dose correction using tissue maximum ratios in the Batho correction.* Med Phys. , (1984), 11(3), 279-286.
10. Sontag M.R., Cunningham J.R. *The equivalent Tissue-Air ratio method for making absorbed dose calculations in heterogeneous medium.* Radiology, (1978), 129(3), 787-794,.

11. O'Connor J.E. *The variation of scattered X-rays with density in an irradiated body.* Phys. Med. Biol., (1957), 1, 352-369.

12. Wong J.W., Henkelman R.M., Andrews J.W., Van Dyk J., Johns H.E. *Effect of small inhomogeneities on dose in a Cobalt-60 beam.* Med. Phys., (1981), 8(6), 783-791.

13. Johns H.E., Cunningham J.R. The Physics of Radiology, 4th Edition Chapter 6, 167-216, 1983.

14. Sontag M.R. *Photon beam dose calculations in regions of tissue hetrogeneity using computed tomography,* Ph.D. Thesis, Toronto University, Appendix A1, 83-90, 1979.

15. Cunningham J.R. *Scatter - Air - Ratios.* Phys. Med. Biol., (1972), 17(1), 42 - 51.

16. Kornelson R.O., Young M.E.J. *Changes in the dose-profile of a 10 MV x-ray beam within and beyond low density material.* Med. Phys., (1982), 9, 114-116.

17. Young M.E.J., Kornelson R.O. *Dose corrections for low-density tissue inhomogeneities and air channels for 10-MV x-rays.* Med. Phys., (1983), 10. 450-455.

18. Mackie T.R., El-Khatib E., Battista J.J., Scrimger J., Van Dyk J., Cunningham J.R. *Lung dose corrections for 6- and 15MV x-rays.* Med. Phys., (1985), 12(3), 327-332.

19. Rogers D.W.O., Bielajew A.F. *The use of EGS for Monte Carlo calculations in medical physics,* NRC Canada Report, PXNR-2693, 1984.

20. Nelson W.R., Hirayama H., Rogers D.W.O. *The EGS4 Code System, Stanford Linear Accelerator Centre Publication,* Report - 265, 1985.

21. Mackie T.R, Bielajew A.F., Rogers D.W.O., Battista J.J. *Generation of photon energy deposition kernels using the EGS Monte Carlo Code.* Phys. Med. Biol. (1988), 33(1), 1-20.

22. Mohan R., Chui C. *Differential pencil beam dose computation model for photons.* Med. Phys., (1986), 13(1), 64-73.

23. Battista J.J., Field C., Santon L., Barnett R. *Radiotherapy planning on a VAX 11/780 computer.* Proceedings of the IEEE, 8th conference, computers in radiotherapy (1984), 489-492.

24. Mauceri T., Kase K. *Effects of ionisation chamber construction on dose measurements in a heterogeneity.* Med. Phys., (1987), 14, 4, 653-656.

25. Field C., Battista J.J. *Photon Dose Calculations Using convolution in Real and Fourier Space: Assumptions and Time Estimates.* Presented 9th ICCR Conference, Holland, 1987.

26. Boyer A.L. *Shortening the calculation time of photon dose distributions in an inhomogeneous medium.* Med. Phys., (1984), 11, 552-554.

27. Bracewell R. *The fourier transform and its applications.* (McGraw-Hill) New York, 110, 1965.

28. Boyer A.L., Mok E.C. *Calculation of photon dose distributions in an inhomogeneous medium using convolutions.* Med. Phys., (1986), 13(4), 503-509.

29. Mackie T.R. *The study of megavoltage x-ray beams.* Ph.D. Thesis Vol. 2, University of Alberta, 348, 1985.

Australasian Physical & Engineering
Sciences in Medicine (1989) Vol. 12 No.3

MODELLING POLYCHROMATIC HIGH ENERGY PHOTON BEAMS BY SUPERPOSITION

P.E. Metcalfe[1], P.W. Hoban[2], D.C. Murray[2], W.H. Round[2]

[1] *Scientific Services, Waikato Hospital, Hamilton, New Zealand*
[2] *Physics Department, University of Waikato, Hamilton, New Zealand*

Abstract

A unified three dimensional superposition approach to dose calculations used in treatment planning of polychromatic high energy photon beams in radiotherapy is developed. The approach we have used involves computing the dose at all points in a medium by superposing the dose spread array (DSA) from the interaction of a photon at a point in the medium with an array of data representing the TERMA (photon fluence times the photon energy) at points in the beam. The polychromatic nature of the beam is accounted for by modelling the beam as having ten spectral components. A "polychromatic dose spread array" (PDSA) for an interaction from a beam with this spectrum was derived. The TERMA array is calculated from a weighted average of the TERMA arrays for the ten photon energies to give a "polychromatic TERMA array". Thus the method accounts for the effect of beam hardening of the TERMA. But it does not account for the effect of beam hardening on the PDSA since a single PDSA (usually for the spectrum at the surface of the medium) is used at all depths. However, by considering measured and calculated beam central axis data, this model is shown to be adequate for computing depth doses for beams in a homogeneous medium penetrating to extreme radiological depths. A computation time advantage is gained because only one superposition per beam is required.

Key Words:

Radiotherapy, computerised treatment planning, superposition, convolution, polychromatic dose spread arrays, Monte Carlo.

Introduction

Present commercial computer algorithms based on the "scatter function" (tissue-air-ratio or TAR) model[1] are inadequate as high energy photon beam models.[2] The deficiencies of this method are outlined further in Appendix A. The inability of these models to cope with electron disequilibrium situations has been outlined by several authors.[3,4,5] Their work indicates there is a need for a more rigorous model which combines accuracy with acceptable computation speed.

The "superposition" methods which employ convolution mathematics show acceptable agreement with experimental data in regions of electronic disequilibrium.[6,7,8,9] Further improvements in the speed of these techniques are possible using Fourier transforms[10,11], although the requirement of an invariant kernel makes it difficult to provide an adequate inhomogeneity correction technique some success using this process at low photon energies has been reported by Boyer and Mok.[7] Recent computer hardware improvements as outlined in a complementary article by Murray *et al*[12] suggest that these methods, either with or without Fourier transform techniques, may soon be able to be used in routine radiotherapy planning.

Only the method of Mohan *et al* [8], however, rigorously models the polychromatic nature of the high energy photon beams used in radiotherapy. The penalty involved in this approach is that a convolution is required for each spectral component. This increases the computation time significantly. An alternative approach developed here includes correcting for the polychromatic nature of the beam while maintaining a single convolution per beam.

The Superposition Approach

The superposition system of mapping dose deposition in a homogeneous phantom calculates the dose D(r) to a point r from a photon interaction at point r' (Figure 1) using the superposition (convolution)

Received 28 March; accepted in final form 27 June, 1989

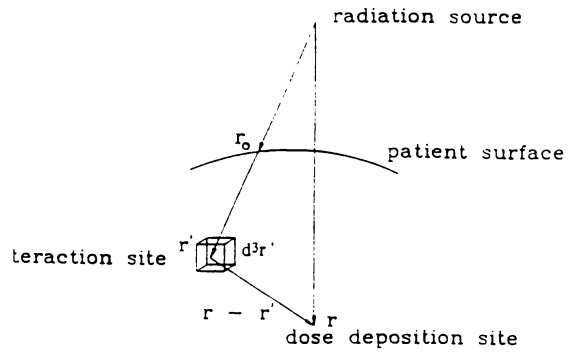

Figure 1: Vectorial framework for the superposition approach, the photon interacts at r' and dose is transported to r by any one of the interactions outlined in Equation 1.

integral of the primary fluence Φ and the energy spread function G. In this manner scattered charged particles ranging away from the initial interaction sites are accounted for. Therefore, the dose deposition site and photon interaction sites are not coincident. In contrast, previously described methods (including scatter function and effective pathlength methods) assume "on the spot" energy absorption.

Unifying the implementations of Mackie *et al* [6], Boyer and Mok[13], and Metcalfe and Battista[9], an energy spread function serves as the superposition kernel G describing energy spread from the primary interaction site. The components of this energy spread are energy from charged particles (positrons and electrons) from primary photon interactions $G_e(r - r')$, energy from charged particles from first scatter photon interactions $G_s(r - r')$ and energy from charged particles from multiple scatter photon interactions $G_{sm}(r - r')$. If Φ is the primary photon fluence at position **r'** and D is the dose to the volume element at position **r**, then for a monoenergetic photon beam in a homogeneous medium the dose is a convolution over the volume being irradiated, d^3r', such that

$$D(r) = \int_v \Phi(r')\, G_e(r - r')\, d^3r' + \int_v \Phi(r')\, G_s(r - r')\, d^3r' + \int_v \Phi(r')\, G_{sm}(r - r')\, d^3r' . \quad (1)$$

The assumptions involved here are:

(1) G_e, G_s, G_{sm}, are spatially invariant due to invariant photon energy and medium composition.

(2) The beam is directionally invariant as is the case for a non-diverging (infinite SSD) beam.

All three kernels can be summed

$$G_T(r - r') = G_e(r - r') + G_s(r - r') + G_{sm}(r - r') \quad (2)$$

and thus the total kernel describing energy deposited by charged particles at D(**r**) is given by

$$D(r) = \int_v \Phi(r')\, G_T(r - r')\, d^3r' . \quad (3)$$

The term $G_T(r-r')$ represents the dose deposited at **r** due to a unit fluence at **r'**. This term includes factors which convert from fluence (photons cm^{-2}) to energy per unit mass by the inclusion of the mass attenuation coefficient $(\mu/\rho)_0$ multiplied by the beam energy E_0. For a monochromatic beam then

$$G_T(r - r') = \left(\frac{\mu}{\rho}\right)_0 E_0\, H_T(r - r') \quad (4)$$

The term $H_T(r-r')$ is the dose spread function which represents the fraction of energy released at **r'** that is deposited in a unit volume at **r**.

An equivalent approach to Equation 3 is to place the energy transfer terms into the fluence part of the equation (that is the mass attenuation coefficient $(\mu/\rho)_0$ and the beam energy E_0 are multiplied by the fluence). This new quantity has been defined as the "Total Energy Released per unit MAss" (TERMA).[14] TERMA is the total energy Removed from the incident beam and it should not be confused with the "Kinetic Energy Released per unit MAss" (KERMA). The TERMA includes the kinetic energy imparted to electrons and the energy of the residual photon. The TERMA T(r') at point **r'** is

$$T(r') = \left(\frac{\mu}{\rho}\right)_0 E_0\, \Phi(r') , \quad (5)$$

thus Equation 3 can be rewritten as

$$D(r) = \int_v T(r')\, H_T(r - r')\, d^3r' . \quad (6)$$

For a dose spread function defined in an infinite volume, the energy released at the interaction site matches that deposited during the ranging process[13], that is:

$$\int_v H_T(r - r')\, d^3r' = 1.0 \quad (7)$$

A problem with the approach outlined so far is that the model assumes the beam to be monochromatic.

The differential pencil beam (DPB) method of Mohan *et al* [8] adjusts the superposition model by presenting fluence and dose spread information which is representative of a polychromatic beam. This method defines two quantities: the probability of photons

interacting (a similar quantity to TERMA); and the DPB (similar to H) of the dose distribution. Converting to the nomenclature used in this paper the following equivalent relation is obtained

$$D(\mathbf{r}) = \int_E \int_v T_E(\mathbf{r}', E)\, H_E(\mathbf{r} - \mathbf{r}', E)\, d^3\mathbf{r}'\, dE \quad , \qquad (8)$$

where $T_E(\mathbf{r}', E)$ is the TERMA per unit energy interval at E and $H_E(\mathbf{r}-\mathbf{r}', E)$ is the dose spread per unit energy interval.

The major improvement of this superposition model is that it incorporates a superposition of each discrete beam energy component and then an integration over the energy components. Though this is the most rigorous way to cope with the polychromatic beam hardening effect, it slows the process by a factor proportional to the number of energy components used (for example a ten component spectra will slow the process by a factor of ten).

The method we have used involves computing the dose at points in a medium by superposing an array of data representing the dose spread function (the dose spread array or DSA) from the interaction of a photon at a point in the medium with an array of data representing the TERMA at points in the beam. The polychromatic nature of the beam is accounted for by modelling the beam as having ten spectral components. A "polychromatic dose spread array" or PDSA for an interaction from a beam with this spectrum was derived. The TERMA array is calculated from a weighted average of the TERMA arrays for the ten photon energies to give a "polychromatic TERMA array". Thus the method accounts for the effect of beam hardening of the TERMA. But it does not account for the effect of beam hardening on the PDSA since a single PDSA (usually for the spectrum at the surface of the medium) is used at all depths.

This model is shown to be adequate for modelling a beam in a homogeneous medium penetrating to extreme radiological depths. A time advantage is gained because only one superposition per beam is required. This method is examined later in the paper to show that it provides accurate depth dose data to extreme radiological depths. A complementary paper by Murray *et al*[12] outlines the times required to compute dose distributions using this method.

Beam Spectra

Bremsstrahlung X-rays produced in a linear accelerator by electrons slowing down during passage through the target have a continuous range of energy. The practice of referring to a beam by its nominal peak energy indicates little about the spectral spread of photons below this value. In some applications a nominal value of 30% is applied to get an average of the photon energy. For example, a 10 MV beam is often assigned an approximate mean energy of 3 MeV.

An excellent review of the differences in penetration characteristics which do occur between different linear accelerators of the same target and flattening filter design can be found in the British Journal of Radiology's Supplement 17.[15] The differences are a function of the nominal energy of the electrons when they strike the target, and this can vary from machine to machine depending primarily on specific waveguide and klystron characteristics.

Very little measured information on high energy spectra is available mainly due to difficulties with the high photon fluence saturating detecting systems. Some analysis has been attempted using spectral analysis[16,17] and attenuation analysis.[18,19] The devices and computations employed are complicated and computationally intensive, respectively.

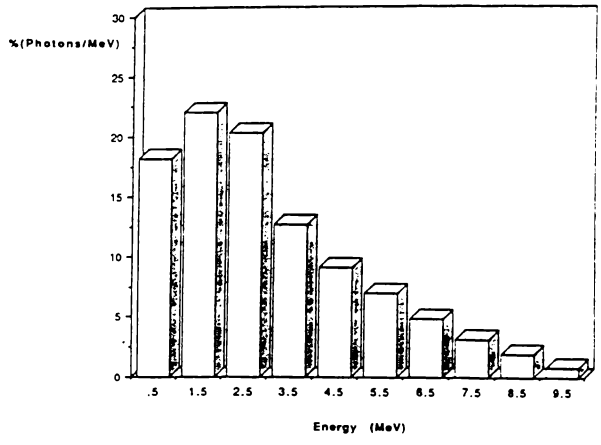

Figure 2: Ten component 10MV photon spectrum, a simplification of that published by Mohan and Chui.[20]

The data used to calculate polychromatic TERMA and DSAs for the the studies described in this paper is the spectral beam information published for a 10 MV Clinac 18 by Mohan and Chui.[20] They produced the expected spectrum by using a Monte Carlo simulation. The spectral distribution is a simplified version of the original spectra in that it has a ten component spectra as shown in Figure 2. The distribution shows how the beam's spectral components are weighted toward the low end of the energy spectrum. Verification of the suitability of this spectral information for the Waikato Hospital 10MV photon beam was obtained by using the Waikato University implementation of the "electron gamma shower" (EGS) Monte Carlo simulation code as supplied by the Stanford Linear Accelerator Centre (SLAC), Nelson *et al*[21], and implemented at Waikato by Murray *et al* .[12]

Table 1

EGS PARAMETERS USED IN 5X5 CM FULL PHOTON BEAM SIMULATION

PARAMETER NAME	DESCRIPTION	VALUE
EI	Incident photon energies	Spectral see table 2(A)
NCASE	Number of photons incident	6.75 million
ESTEPE	Maximum fraction of electron energy loss per step	0.05
TIME	Vax 6220-CPU simulation time	108 hours
ECUT'	Electron kinetic energy local energy deposition cut-off	50 keV
AE'	Minimum delta ray energy	50 keV
AP	Minimum scattered photon energy	50 keV
PCUT	Photon energy local deposition cut-off	50 keV

An EGS simulation was run on a VAX 6220. It simulates the percentage depth dose (%D) properties of a 5x5 cm beam. The EGS parameters used in the simulation are outlined in Table 1 and the spectral components used are shown in Table 2. The results of the simulation which followed the histories of 6.75 million incident photons over a computing time of 108 CPU hours are shown in Figure 3. Note that each point shown on the graph represents the dose scored in a cylindrical voxel element of 8mm radius and 5mm depth. The dose is normalised to the voxel containing maximum dose (D_{max}). The results of the EGS simulation agree to within a 3% mean error with the depth dose readings obtained for a similar beam from the Waikato Hospital's Varian Clinac 18 linear accelerator measured with a PTW ionisation chamber in a Therados RFA-3 water tank (see Appendix B, Equation B2 for details of error analysis). This indicates that it is appropriate to use the simplified spectral data of Mohan and Chui[29] to simulate a 10MV beam from our linear accelerator.

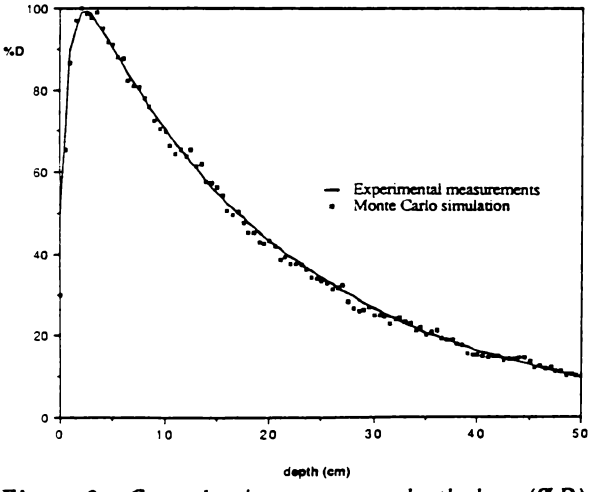

Figure 3: Central axis percentage depth dose (%D) curves showing a comparison between a Monte Carlo (EGS) simulation which follows the histories of 6.75 million photons and experimental data collected using a PTW ionisation chamber in a Therados water tank. The beam size is 5x5 cm.

Fluence and Terma

Let the relative fluence at a depth r' of a monochromatic beam of energy E_0 be $\Phi(r')$. If $\Phi(r')$ is the relative primary fluence at the surface, then

$$\Phi(r') = \Phi(r_0)\, e^{-\mu |r' - r_0|} \qquad (9)$$

where μ is the linear attenuation coefficient.

For a polychromatic beam where there is a range of photon energies from 0 to E_{max}, then

$$\Phi(r') = \int_0^{E_{max}} \frac{d\Phi(r')}{dE}\, dE \ , \qquad (10)$$

where $d\Phi(r')/dE$ is the number of photons in a unit energy interval.

To acquire a discrete summation equivalent, each energy interval is assigned a mean energy E_n, and an energy fluence weighting F_n which defines the relative number of photons per energy interval (see

Figure 2). Then taking the discrete sum of energies from 0 to E_{max}, the fluence is

$$\Phi(r',E_n) = \left(\frac{r_0}{r'}\right)^2 \sum_{n=1}^{N} F_n \Phi_{E_n} e^{-\mu_n |r' - r_0|} \qquad (11)$$

where n=1 is the first spectral energy component and N is the total number of spectral components, $\Phi_{En}(r_\theta)$ is the discrete photon fluence at the surface for the nth spectral component and μ_n is the attenuation coefficient for the nth spectral component (note μ_n is the same as $(\mu/\rho)_n$ for unit density material). An inverse square correction $(r_\theta/r')^2$ is also included to account for intensity reduction of the fluence with distance from the source.

The polychromatic TERMA is given by

$$T(r') = \left(\frac{r_0}{r'}\right)^2 \sum_{n=1}^{N} \left(\frac{\mu}{\rho}\right)_n E_n F_n \Phi_{E_n} e^{-\mu_n |r' - r_0|} . \qquad (12)$$

The values used for F_n and E_n are listed in Table 2(a) for the ten spectral components used.

To observe the effect of monochromatic and polychromatic spectrum assumptions on the expected fluence, the relative fluence produced using a nominal 3MeV monochromatic beam is graphed against depth in Figure 4(a) along with a graph of relative fluence against depth produced by using the polychromatic beam spectrum. Comparison of the curves in Figure 4(a) shows that the error in the monochromatic fluence curve is about 15% at points beyond 10cm (see Appendix B, Equation B1). This indicates that the assumption that the fluence of a beam can be modelled as monochromatic is invalid and that it should be modelled as being polychromatic.

To observe the effect of monochromatic versus polychromatic spectral assumptions on the relative TERMA, a graph of relative TERMA produced using a nominal 3MeV monochromatic beam is plotted against depth in Figure 4(b). This graph also includes a plot of relative TERMA against depth produced by using the polychromatic beam spectrum. Comparison of the curves in Figure 4(b) shows that the difference between the monochromatic and polychromatic TERMA curves is 2% at 10cm and increases to 10% at 50 cm. This indicates the assumption that the beam must be modelled as being polychromatic rather than monochromatic is not as vital when calculating TERMA as it is when calculating fluences. But the error is still significant enough to require that a polychromatic beam assumption is made where possible.

Dose Spread Arrays

The effects of assuming a polychromatic or a monochromatic beam on DSAs are studied in this section. Several EGS Monte Carlo simulations were

Table 2:

(A) SPECTRAL DATA USED IN GENERATING FLUENCE AND PDSA INFORMATION

ALSO USED IN GENERATING 5X5 CM FULL FIELD MONTE CARLO SIMULATION:

Attenuation coefficients (Johns and Cunningham[25]:
spectral components N = 10

EI =Energy E_n	0.5	1.5	2.5	3.5	4.5	5.5	6.5	7.5	8.5	9.5
% F_n, row 1 (d= 0cm)	17.5	22.0	20.4	12.9	9.2	7.1	4.9	3.2	1.9	0.9
% F_n, row 2 (d= 25cm)	5.1	16.6	21.1	16.0	12.8	10.7	7.5	5.3	3.4	1.5
% F_n, row 3 (d = 50cm)	1.2	10.4	18.3	16.8	15.2	13.7	9.8	7.5	4.8	2.3
μ_n	.0969	.0575	.0445	.0368	.0321	.0289	.0284	.0251	.0237	.0227

(B) 3MEV MONOCHROMATIC DATA USED IN GENERATING FLUENCE

AND MDSA INFORMATION

Attenuation coefficients (Johns and Cunningham[25]:
spectral components N = 1

(E_0)	3.0
μ_0	.0397

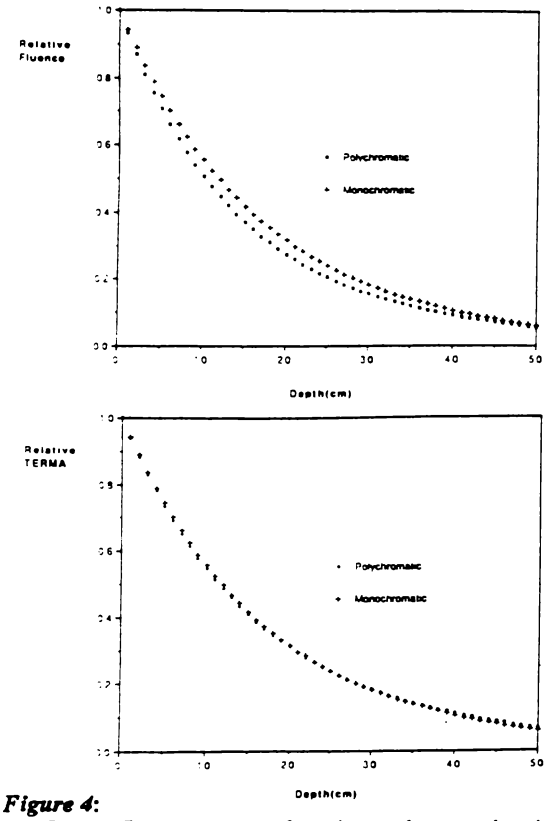

Figure 4:
(a) Depth fluence curves for photon beams showing a comparison of the relative fluence curve produced using a 3MeV monochromatic beam with the relative fluence curve produced using the polychromatic 10MV spectra.

(b) Depth TERMA curves for photon beams showing a comparison of the relative TERMA curve produced using a 3MeV monochromatic beam with the relative TERMA curve produced using the polychromatic 10MV spectra.

run whereby a monochromatic DSA (MDSA) for a 3MeV photon beam was produced using the spectral information outlined in Table 2(b). This was compared with PDSAs produced using the spectral components outlined in Table 2(a).

Sets of DSA data were formed by forcing 250 000 photons to interact at a point and following the dose deposition histories. Figure 5 shows the DSA polar scoring coordinate geometry used in the EGS implementation. The radial shells are separated into 5 degree angular intervals ($\Delta\theta$ = 5 degrees). Energy is scored in radial shells of 1mm length (Δs = 1 mm) and these shells radiate out from the interaction voxel along a distance to the centre of the shell which is defined as the "shell depth s" and an angle which lies between θ and $\theta + \Delta\theta$. Important parameters used in the EGS simulation are outlined in Table 3. The EGS simulation gives results in terms of energy deposition per voxel volume normalised to energy released at the interaction site. These are then divided by voxel volume to give values of relative energy deposition per unit volume.

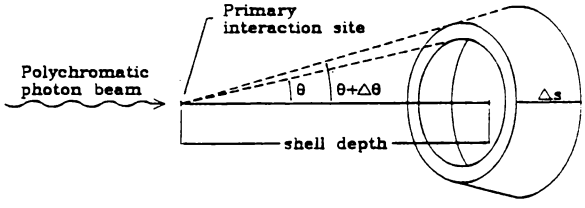

Figure 5: Polar geometry describing the DSA scoring coordinate framework used by EGS. The photon interacts at the primary interection site and dose is scored in a shell of depth s . The dose is scored into a volume defined by the polar voxel interval within the angle θ and $\theta+\Delta\theta$ and the length of the shell is Δs.

Table 3

EGS PARAMETERS USED IN MDSA AND PDSA BEAM SIMULATION

PARAMETER NAME	DESCRIPTION	VALUE
EI	Incident photon energies	PDSA Spectral see table 2(A) MDSA E_0 = 3 MeV
NCASE	Number of photons incident	250 000
ESTEPE	Maximum fraction of electron energy loss per step	0.02
TIME	Vax 6220-CPU simulation time	12 hours
ECUT'	Electron kinetic energy local energy deposition cut-off	50 keV
AE'	minimum delta ray energy	50 keV
AP	minimum scattered photon energy	50 keV
PCUT	photon energy local deposition cut-off	50 keV

The term H(r) in Equation 13 represents the relative fraction of energy released at r which is deposited at r' per cm³ of deposition volume. It is equivalent to a normalised relative dose. For an MDSA the equation which defines this is

$$H(r) = \frac{dE_0(r)}{E_0(r')\,dv} \quad , \qquad (13)$$

where dv is a small volume in the shell at depth s and angle θ (see Figure 5), and $dE_0(r)/E_0(r')$ is the fractional energy deposited in the volume dv of the energy $E_0(r')$ released at position r'.

The PDSA data could have been derived from several monochromatic EGS simulations by computing a weighted sum over the spectral components in much the same way as the fluence was derived, such that

$$H(r) = \sum_{n=1}^{N} F_n\, H(r, E_n) \qquad (14)$$

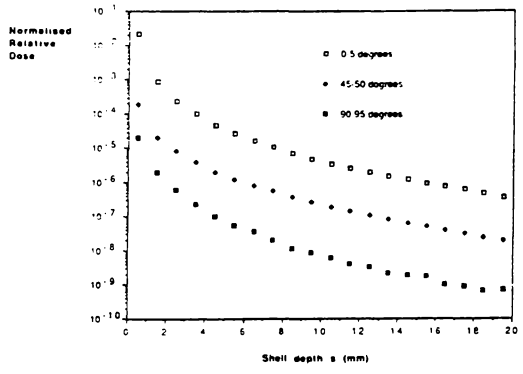

Figure 6: PDSA profiles showing relative dose plotted against shell depth for three polar angles, 0 - 5 degrees, 45 - 50 degrees and 90 - 95 degrees. The PDSAs were generated using the surface polychromatic spectra (see-Table 2a, row 1).

Note that this is not how the PDSAs were formulated here. Instead H(r) was obtained directly using the EGS simulation with the simplified polychromatic spectrum of Mohan and Chui[20] for a beam at the surface of a water phantom (see Table 2(a), F_n row 1, for details of the spectrum used). In Figure 6 graphs of the PDSA data produced from the EGS simulation are plotted against distance from the interaction site. The vertical axis of the graph is H(r) (cf. relative dose), and the horizontal axis the mean shell depth, s, of the shell in which the energy is deposited. We have called such graphs "DSA profiles". Data for three different shell angular intervals are shown on the graphs and indicate the reduction of dose deposition with angle and the rapid reduction of dose deposition as the distance from the interaction site increases. As expected, most of the energy is deposited downstream of the interaction site.

Shown in Figures 7(a) - (c) are DSA data produced from two different EGS simulations. In one simulation 3MeV MDSA data is produced; the other simulation was that which produced the PDSA data shown in Figure 6. Graphs for three angular intervals are shown, between θ = 0 and θ + Δθ = 5 degrees (Figure 7(a)), between θ = 45 and θ + Δθ = 50 degrees (Figure 7(b)) and between θ = 90 and θ + Δθ = 95 degrees (Figure 7(c)). Note that the DSAs produced using the polychromatic beam are significantly different from that produced using the monochromatic beam. They show a less defined electron range and less immediate deposition close to the interaction site. For example, at the location s = 5 mm in the polar interval 0-5 degrees close to the interaction

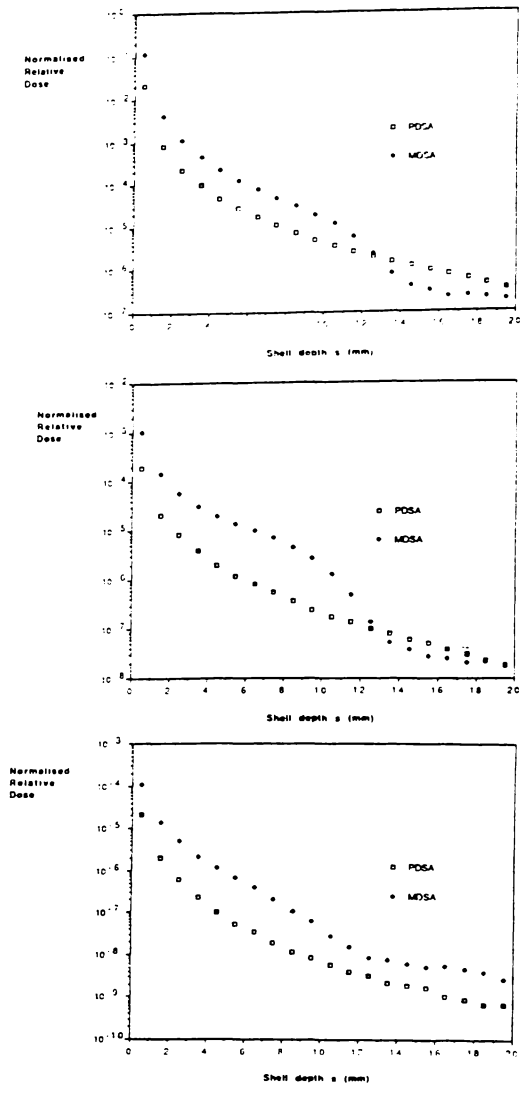

Figure 7: PDSA profiles showing relative dose plotted against shell depth for three polar angles compared with MDSA profiles produced using a monochromatic 3MeV beam (see-Table 2b).

(a) PDSA versus MDSA comparison at 0 - 5 degree polar interval.

(b) PDSA versus MDSA comparison at 45 - 50 degree polar interval.

(c) PDSA versus MDSA comparison at 90 - 95 degree polar interval.

voxel, the difference is almost a factor of ten and this reduces to a factor of five at the 45-50 degree angular interval. This demonstrates that the use of MDSA data is probably inadequate for the superposition process; an assumption confirmed in the next section.

To examine the effect of beam hardening, further PDSAs were then produced by EGS simulation using the spectra calculated from the spectrum of Mohan and Chui[20] for depths of 25cm and 50cm (see Table 2(a), F_n rows 2 and 3). These data were in turn compared with the PDSA for the spectrum at the surface (ie that of Mohan and Chui). The results are shown in Figure 8 for the polar angle 45-50 degrees. These results demonstrate that beam hardening induces relative dose differences of up to a factor of two between the distributions produced using the surface spectra and that produced using the 50cm deep spectra. This difference is caused by spectral beam hardening. The insignificance of this difference to the accuracy of the superposition process is outlined in the next section.

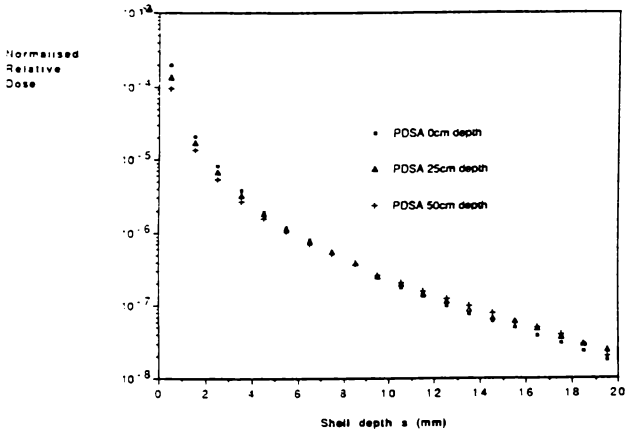

Figure 8: PDSA profiles showing relative dose plotted against shell depth for three different spectra at a single 45-50 degree polar interval. The spectra generated for use in the EGS simulations were those expected using the fluence attenuation equation 11, applied to depths of 0, 25 and 50cm (these spectral components are shown in Table 2a).

Superposition Results

Superposition was carried out using the newly developed framework whereby the superposition Equation 6 was used in conjunction with T as defined in Equation 12, and H as defined in Equation 14 (but actually obtained by performing a Monte Carlo simulation for a polychromatic beam). The beam spectrum chosen was that for a 0 cm depth (see table 2(a) F_n, row 1).

In Figure 9(a) is shown the central axis percentage depth dose (%D) curve for a 5x5 beam generated by superposition of the surface polychromatic spectra with the polychromatic TERMA. Also shown is the experimental depth dose curve obtained by using a PTW (0.1cc) thimble ionisation chamber in a Therados water tank. The reasons for the discrepancy in results in the build up region are outlined in a complementary article, see Murray *et al.*[12] Comparison of the superposition results with the experimental depth dose data gave a mean error of 2% (see Appendix B, Equation B2) in the depth dose (fall off region). The small error indicates that the use of a single PDSA is adequate to model beam depth dose characteristics in a homogeneous water medium down to an extreme radiological depth (50cm which may occur in the pelvic region). This demonstrates that not accounting for beam hardening of the polychromatic DSA component does not cause a significant error in percentage depth dose calculation.

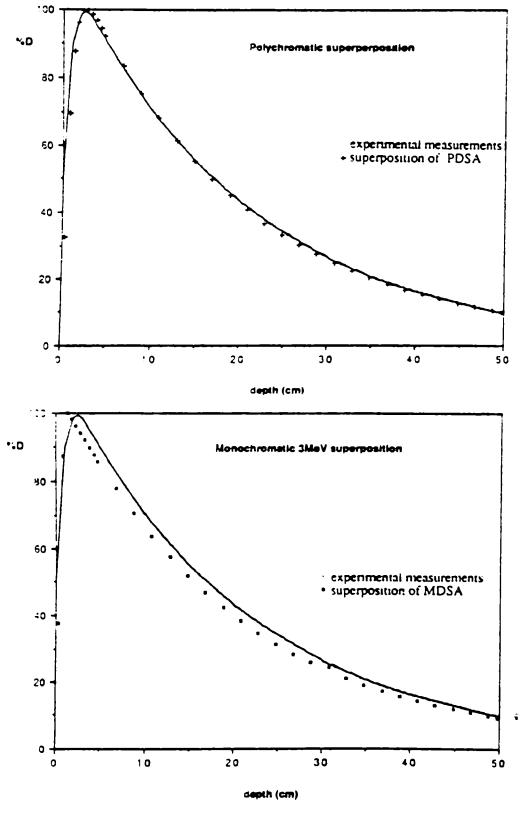

Figure 9:
(a) The central axis percentage depth dose (%D) curve for a 5x5cm beam generated by superposition of the surface polychromatic spectra (see figure 6)with the polychromatic TERMA (see figure 4(b)) is shown. Also plotted is the experimental central axis depth dose curve obtained using a PTW ionisation chamber in a Therados water tank. A comparison of results shows that the superposition data points coincide with the experimental data to within a mean error of 2% with the experimental data

(b) The central axis percentage depth dose (%D) curve for a 5x5cm beam generated by superposition of the 3MeV MDSA (see figure 7) with the polychromatic TERMA (see figure 4(b)) is shown. Also plotted is the experimental central axis depth dose curve obtained using a PTW ionisation chamber in a Therados water tank. A comparison of results shows that the superposition data points coincide with the experimental data to within a mean error of 8% with the experimental data

Shown in Figure 9(b) is a central axis depth dose curve generated by superposition of the 3MeV monochromatic DSA (MDSA) with the polychromatic TERMA. Also shown is the experimental depth dose curve obtained. Comparison of the curves shows that the curve produced by superposition of an MDSA is too sharp in the build up region and the depth dose (fall off) region shows a mean error of 8%. It is obvious from the inaccuracy in results shown in Figure 9(b) that superposition involving the use of an MDSA does not produce sufficiently accurate depth dose information for radiotherapy treatment planning.

Conclusions

Figures 4,7, and 9(b) indicate that using monochromatic beam assumptions to model a polychromatic beam is not sufficiently accurate for radiotherapy planning purposes as recommended by ICRU # 24.[22] The results show that the MDSAs produced[13,23] are not adequate models of a polychromatic beam. However it is assumed that the use of equation 14 would ensure the monochromatic data available could be of use in producing PDSAs without the requirement of further Monte Carlo simulations.

These results show that a calculation of polychromatic TERMA is a very accurate way to account for attenuation in a polychromatic beam and this computation should be used in preference to monochromatic TERMA. It is apparent that since the TERMA is affected in this manner then the DSAs are also affected by beam hardening and this was studied using the EGS Monte Carlo code to generate PDSAs for three different polychromatic spectra. Though the differences in PDSAs are noticeable (see Figure 8) the superposition process (see Figure 9(a)) does give accurate (to within 2%) depth dose results down to 50cm depth using a single surface spectrum dose spread array convolution with a depth dependant polychromatic TERMA.

Methods of scaling PDSAs and TERMA to account for inhomogeneous regions such as lung and bone are not dealt with in this publication and are the subject of further research.[24]

Acknowledgement

The authors acknowledge financial assistance from the Cancer Society of New Zealand (National, Waikato and Bay of Plenty Divisions) and the Waikato Hospital.

References

(1) Meredith W.J., Neary G.J. *The production of isodose curves and the calculation of energy absorption from standard depth dose data* B.J.R., 17, 75, 1944.

(2) Mohan R., Chui C. *Validity of the concept of separating primary and scatter dose* Med. Phys., 12 (6), 726 - 730, 1985.

(3) Kornelson R.O., Young M.E.J. *Changes in the dose - profile of a 10MV X-ray beam within and beyond low density material* Med. Phys., 9 (1), 114 - 116, 1982.

(4) Mackie T.R., El-Khatib E., Battista J.J., Scrimger J., Van Dyk J., Cunningham J.R. *Lung dose corrections for 6 and 15 MV X-rays* Med. Phys., 12 (3), 327 - 332, 1985.

(5) Metcalfe P.E., Beckham W.A. *Radiotherapy planning accuracy in terms of CT Numbers and inhomogeneity correction techniques.* Aust. Rad., 32 (3), 371 - 379, 1988.

(6) Mackie T.R., Scrimger J.W., Battista J.J. *A convolution method of calculating dose for 15MV X-rays* Med. Phys., 12, 188 - 196, 1985.

(7) Boyer A.L., Mok E.C. *Calculation of photon dose distributions in an inhomogeneous medium using convolutions* Med. Phys., 13 (4), 503 - 509, 1986.

(8) Mohan R., Chui C., Lidofsky L. *Differential pencil beam dose computation model for photons* Med. Phys., 13 (1), 64 - 73, 1986.

(9) Metcalfe P.E., Battista J.J. *Accuracy of inhomogeneity corrections in lung irradiated with high energy X-rays* Aust. Phys. Eng. Sci. Med. , 11 (2), 67 - 75, 1988.

(10) Boyer A.L. *Shortening the calculation time of photon dose distributions in an inhomogeneous medium* Med. Phys., 11, 552 - 554, 1984.

(11) Field C., Battista J.J. *Photon dose calculations using convolution in real and Fourier space: Assumptions and Time Estimates* Presented 9th ICCR Conference, Holland, 1987.

(12) Murray D.C., Hoban P.W., Metcalfe P.E., Round W.H. *3-D superposition for radiotherapy treatment planning using fast Fourier transforms* Aust. Phys. Eng. Sci. Med. ,12, XXX-YYY, 1989.

(13) Boyer A.L., Mok E.C. *A photon dose distribution model employing convolution calculations* Med. Phys., 12 (2), 169 - 177, 1985.

(14) Ahnesjo A., Andreo P., Brahme A. *Calculation and application of point spread functions for treatment planning with high energy photon beams* Acta Oncologica, 26 (1), 49 - 55, 1987

(15) British Journal of Radiology, Supplement 17 *Central axis depth dose data for use in radiotherapy* B.J.R. Supplement. 1983

(16) Levy L.B., Waggener R.G., Wright A.E. *Measurement of primary bremsstrahlung spectrum from an 8MeV linear accelerator* Med. Phys., 3 (5), 173 - 175, 1976.

(17) Nath R., Schultz R.J. *Determination of high energy x-ray spectra by photoactivation* Med. Phys., 3 (3), 133 - 141, 1976.

(18) Huang P.H., Kase K.R., Bjarnguard B.E. *Simulation studies of 4 MV x-ray spectra by numerical analysis of transmission data* Med. Phys., 9 (5), 695 - 703, 1982

(19) Huang P.H., Kase K.R., Bjarnguard B.E. *Reconstruction of 4 MV bremsstrahlung spectra from measured transmission data* Med. Phys., 10 (6), 778 - 785, 1982

(20) Mohan R., Chui C. *Energy and angular distributions of photons from medical linear accelerators* Med. Phys., 12 (5), 592 - 597, 1985.

(21) Nelson W.R., Hirayama H., Rogers D.W.O. *The EGS4 Code System* Stanford Linear Accelerator Centre Publication , Report - 265 , 1985.

(22) ICRU 24 *Determination of absorbed dose in a patient irradiated by beams of X or gamma rays* International Commission on Radiation Units and measurements, Washington DC, 1976.

(23) Mackie T.R., Bielajew A.F., Rogers D.W.O., Battista J.J. *Generation of photon energy deposition kernels using the EGS Monte Carlo code* Phys. Med. Biol ., 33 (1), 1 - 20, 1988

(24) Hoban P.W., Metcalfe P.E., Round W.H. *Dose spread arrays for high energy photon beams* Proceedings EPSM conference, (Abstract 69), Brisbane, Australia 1988.

(25) Johns H.E., Cunningham J.R. *The physics of radiology* 4th Edition, Appendix A, 723, 1983.

Appendix A:

Re-examination of the Scatter Function Model

In effect, the present "scatter function" model of dose deposition states that the beam can be represented by two components. That is the dose deposition due to primary photons TAR(d,0) at depth d and beam size 0, and the dose deposition due to scattered photons SAR(d,S) at depth d and beam size S:

$$TAR(d,S) = TAR(d,O) + SAR(d,S) . \quad (A1)$$

If the dose and fluence site are now represented using a vectorial framework (see Figure 1) then the assumption of the scatter function model is that:

$$Dose(\mathbf{r}) = Primary\ Dose(\mathbf{r}) + Scatter\ Dose(\mathbf{r}) . \quad (A2)$$

This model implies that **the dose deposition site is at the same position as the dose interaction point.** Thus in the scatter function model it is assumed that the photon electron interaction site and the site where electrons deposit their energy are spatially coincident, that is:

$$\mathbf{r} = \mathbf{r}' . \quad (A3)$$

This assumption is not correct for high energy photon beams, because high energy electrons have a significant range. For example the mean range in tissue for electrons of 3MeV is about 2.0 cm and this range extends in low density media.

The "on the spot" energy deposition assumption is the major model inadequacy of the scatter function method. This assumption requires electronic equilibrium to exist for it to be accurate. The number of disequilibrium situations now encountered in day to day radiotherapy treatment planning situations is increasing due to the replacement of Cobalt-60 machines with higher energy accelerators, and so the need to replace this model in dose calculations where disequilibrium may occur (in regions of interfaces, inhomogeneities and beam boundaries) is paramount. The logical replacement framework is a superposition approach since this accounts for dose deposition at sites remote from the original interaction.

Appendix B:

Error Assessment Method

The errors quoted relate to normalised errors. This means that all data points are given an equal weighting of importance in error assessment. This is a very critical way to assess errors especially in regions of extreme radiological depth. For assessing the TERMA error

$$\%\text{error} = \frac{\sum_{n=1}^{N}\left[\left(\left|\frac{T_{monochromatic} - T_{polychromatic}}{T_{polychromatic}}\right|\right) x\ 100\right]}{N} \quad \text{(B1)}$$

where N is the number of sample points and T represents the TERMA calculated for monochromatic and polychromatic beam respectively. Assessment of fluence error was undertaken using equation B1 by replacing T with Φ, respectively.

For assessing the error of Monte Carlo and superposition simulations

$$\%\text{error} = \frac{\sum_{n=1}^{N}\left[\left(\left|\frac{D_{simulation} - D_{experiment}}{D_{experiment}}\right|\right) x\ 100\right]}{N} \quad \text{(B2)}$$

where N is the number of sample points and D is the percentage dose due to the simulation and experimental data respectively.

IN PRINT - ACCEPTED FOR PUBLICATION IN THE JOURNAL:
PHYSICS IN MEDICINE AND BIOLOGY, AN IOP PUBLICATION
VOLUME 35

BEAM HARDENING OF 10 MV RADIOTHERAPY X-RAYS : ANALYSIS USING A CONVOLUTION/SUPERPOSITION METHOD

P. E. Metcalfe[1,2,3], P. W. Hoban[1], D. C. Murray[1], W. H. Round[1]

[1] Physics Department, University of Waikato, Hamilton, New Zealand
[2] Scientific Services, Waikato Hospital, Hamilton, New Zealand
[3] Current Address, Medical Physics Dept.,Wollongong Hospital, N.S.W., Australia

ABSTRACT

Total and primary polyenergetic dose spread arrays (PDSAs) have been generated for a high energy 10 MV radiotherapy photon beam using the electron gamma shower (EGS) Monte Carlo code. By considering the attenuation of fluence per energy interval, PDSAs have been produced at radiological depths of 0 cm (the surface PDSA) and 40 cm (the beam hardened PDSA).

By comparing primary PDSAs produced at these different depths, the effect of beam hardening on the PDSA has been quantified. Calculations show the mean electron range due to the surface primary PDSA is 6.67 mm and the mean electron range of the beam hardened primary PDSA is 8.24 mm. In comparison a 3 MeV primary monoenergetic dose spread array MDSA has a much smaller mean electron range of 4.81 mm.

A radiotherapy X-ray beam computation method is introduced which involves a single superposition of the surface generated PDSA or beam hardened PDSA with a polyenergetic TERMA. The mean percentage difference between depth dose curves obtained using superposition of surface and beam hardened PDSAs is only 0.1%. The mean percentage difference from experimental data for these superposition curves is 2.8% down to 40 cm in a homogeneous phantom. The superposition process is shown to be forgiving to spectral differences when calculating the PDSA, but sensitive to the incident photon energy spectrum used to calculate the TERMA.

Key Words:
radiotherapy, computerised treatment planning, superposition, convolution
dose spread arrays, Monte Carlo, beam hardening, beam spectrum.

1. INTRODUCTION

The properties of dose spread arrays (DSAs) have been reported by various authors (Dean 1980, Mackie *et al* 1985a, 1988, Boyer and Mok 1985, 1986, Boyer *et al* 1989, Mohan *et al* 1986, Ahnesjö *et al* 1987, Ahnesjö and Mackie 1987, Ahnesjö 1989, Metcalfe *et al* 1989). These dose spread arrays (DSAs) have also been termed as energy deposition kernels, differential pencil beams and point spread functions by the authors cited above. The work of Mackie *et al* (1988) demonstrates the effectiveness of applying DSA data to find solutions to radiotherapy beam interaction phenomena.

The "superposition" methods developed by these authors employ convolution mathematics applied to DSAs to effectively model charged particle transport in three dimensions. Superposition methods have been shown to closely match experimental data and Monte Carlo simulations in regions of electronic disequilibrium (Mackie *et al* 1985a, Mohan *et al* 1986, Metcalfe and Battista 1988, Ahnesjö 1989). In contrast, other currently employed algorithms such as scatter function and effective pathlength methods, which only model photon transport, display inaccuracy in such regions (Kornelson and Young 1982, Cunningham 1982, Mohan and Chui 1985a, Mackie *et al* 1985b, Metcalfe and Beckham 1988).

Further improvements in the speed of superposition techniques using Fourier transforms have been demonstrated (Boyer 1984, Boyer *et al* 1988, Field and Battista 1987, Murray *et al* 1989). It is however more difficult to achieve correct range scaling using Fourier convolution techniques (Boyer and Mok 1986, Ahnesjö 1989). Prudent programming of a parallel computing system has recently shown that real space superposition with range scaling is approaching the speed required for use in routine radiotherapy planning (Murray *et al* 1990).

The superposition methods of Mohan *et al* (1986) and Boyer *et al* (1989) rigorously model the polyenergetic nature of the high energy photon beams used in radiotherapy. The penalty involved in this approach is that a separate convolution is required for each of the beam's spectral components. This increases the computation time for convolution approximately in proportion to the number of spectral components.

An alternative approach is to correct for the polyenergetic nature of the beam while maintaining a single convolution per beam. This method does not explicitly account for the effect of beam hardening on the DSA as it traverses tissue. Hence a detailed analysis of the effect of beam hardening on polyenergetic dose spread arrays (PDSAs) and the final dose distribution is essential. The magnitude of this effect is quantified in this paper.

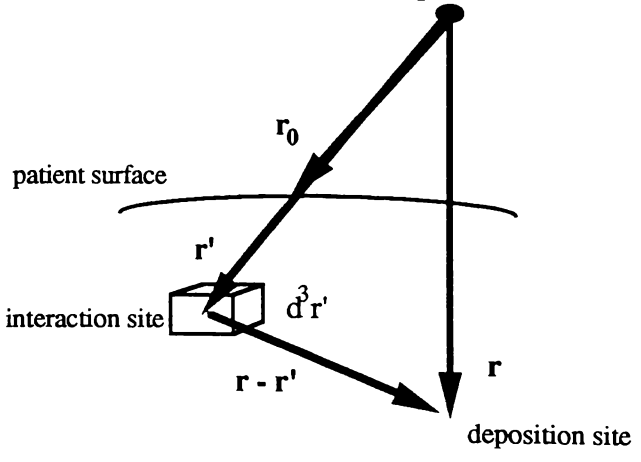

Figure 1(a): Vectorial framework for the superposition approach. The photon interacts at **r'** and dose is transported to **r** by charged particles.

2. THEORY OF SUPERPOSITION

The superposition system of mapping dose deposition in a homogeneous phantom calculates the dose D(**r**) to a point **r** from a photon interaction at point **r'** (Figure 1(a)) using the superposition (convolution) integral of the primary fluence Φ and the energy spread function G.

In this manner scattered charged particles ranging away from the initial interaction sites are accounted for. The components of the total energy spread function G_T are energy from charged particles (positrons and electrons) from primary photon interactions, energy from charged particles from first scatter photon interactions and energy from charged particles from multiple scatter photon interactions. If Φ is the primary photon fluence at position **r'** and D is the dose to the volume element at position **r**, then for a monoenergetic photon beam in a homogeneous medium the dose is a convolution over the volume being irradiated v , such that

$$D(\mathbf{r}) = \int_v \Phi(\mathbf{r}')\, G_T(\mathbf{r} - \mathbf{r}')\, d^3\mathbf{r}' \quad . \tag{1}$$

The term $G_T(\mathbf{r}-\mathbf{r}')$ represents the dose deposited at **r** due to a unit fluence at **r'**. This term includes factors which convert from fluence (photons cm^{-2}) to energy per unit mass by the inclusion of the mass attenuation coefficient $(\mu/\rho)_0$ multiplied by the beam energy. For a monoenergetic beam of energy E_0 then

$$G_T(\mathbf{r} - \mathbf{r}') = \left(\frac{\mu}{\rho}\right)_0 E_0\, H_T(\mathbf{r} - \mathbf{r}') \quad . \tag{2}$$

The term $H_T(\mathbf{r}-\mathbf{r}')$ is the dose spread function which represents the fraction of energy released at **r'** that is deposited in a unit volume at **r**, such that

$$H_T(\mathbf{r} - \mathbf{r}') = \frac{d\varepsilon(\mathbf{r} - \mathbf{r}')}{E_0} \quad , \tag{3}$$

where $d\varepsilon(\mathbf{r} - \mathbf{r}')$ is the energy deposited per unit volume at **r** due to a photon interacting at **r'**. Note that the energy released includes that of the scattered photons.

An equivalent approach to (1) is to place the energy transfer terms into the fluence part of the equation (that is the mass attenuation coefficient $(\mu/\rho)_0$ and the beam energy E_0 are multiplied by the fluence). This new quantity has been defined as the "**T**otal **E**nergy **R**eleased per unit **MA**ss" (TERMA) (Ahnesjö *et al* 1987). The TERMA T(**r'**) at point **r'** is

$$T(\mathbf{r}') = \left(\frac{\mu}{\rho}\right)_0 E_0\, \Phi(\mathbf{r}') \quad , \tag{4}$$

and thus (1) can be rewritten as

$$D(\mathbf{r}) = \int_v T(\mathbf{r}')\, H_T(\mathbf{r} - \mathbf{r}')\, d^3\mathbf{r}' \quad . \tag{5}$$

A problem with the approach outlined so far is that the model assumes the beam to be monoenergetic.

The differential pencil beam method of Mohan *et al* (1986) and the convolution method of Boyer *et al* (1989) adjust the superposition model by presenting fluence and dose spread information which is representative of a polyenergetic beam. These methods define two quantities: the probability of photons interacting (a similar quantity to TERMA); and the differential pencil beams or several monoenergetic convolution kernels (similar to H). Converting to the nomenclature used in this paper the following equivalent relation is obtained

$$D(\mathbf{r}) = \int_E \int_v T_E(\mathbf{r}', E)\, H(\mathbf{r} - \mathbf{r}', E)\, d^3r'\, dE \quad , \tag{6}$$

where $T_E(\mathbf{r}', E)$ is the TERMA per unit energy interval and $H(\mathbf{r} - \mathbf{r}', E)$ is the dose spread function for the energy E.

The major improvement of this superposition model is that it incorporates a superposition of each discrete beam energy component by integrating over the energy components. Though this is the most rigorous way to cope with the polyenergetic beam hardening effect, it slows the process by a factor approximately proportional to the number of energy components used (for example the five component spectrum used by Boyer *et al* (1989) requires five convolutions and thus will slow this part of the computation process by about a factor of five).

The method we have used involves computing the dose at points in a medium by convolving a polyenergetic dose spread array (PDSA) with a TERMA array derived from polyenergetic data. The PDSA is obtained from the fractional energy deposition at a position $\mathbf{r}-\mathbf{r}'$ from an interaction point. Note that the photon spectrum used to compute the PDSA is that at a reference position $\mathbf{r}'_{ref}$ in the medium. Therefore the modification of (6) which we have used is

$$D(\mathbf{r}) = \int_v \left[\int_E T_E(\mathbf{r}', E)\, dE \right] H_p(\mathbf{r}'_{ref}, \mathbf{r} - \mathbf{r}')\, d^3r' \quad , \tag{7}$$

where $H_p(\mathbf{r}'_{ref}, \mathbf{r} - \mathbf{r}')$ is the polyenergetic dose spread function as described in this paper and is equal to

$$H_p(\mathbf{r}'_{ref}, \mathbf{r} - \mathbf{r}') = \frac{\int_E d\varepsilon(\mathbf{r} - \mathbf{r}', E)\, \frac{d\Phi}{dE}(\mathbf{r}'_{ref}, E) \left(\frac{\mu}{\rho}(E)\right) dE}{\int_E \frac{d\Phi}{dE}(\mathbf{r}'_{ref}, E) \left(\frac{\mu}{\rho}(E)\right) E\, dE} \quad . \tag{8}$$

The term $d\varepsilon(\mathbf{r} - \mathbf{r}', E)$ is the energy deposited due to an incident photon of energy E in a unit volume at $\mathbf{r}$ from a photon interaction at $\mathbf{r}'$. As $(d\Phi/dE)$ is the photon fluence per unit energy interval then $(d\Phi/dE)$ multiplied by (μ/ρ) is the number of interactions in a unit mass per unit energy interval at energy E. Therefore H_p is the energy fraction deposited at a point $\mathbf{r}$ normalised to the energy released at $\mathbf{r}'$.

For an incident photon of the ith energy component E_i, the probability of the interaction occuring varies with energy according to $(\mu/\rho)_i$. To allow for this the PDSAs are generated by weighting the incident photons by a factor proportional to $(\mu/\rho)_i$. This is done in the EGS code by setting the particle weight parameter WTIN to equal $(\mu/\rho)_i$.

Note from (7) that the TERMA value at **r'** is calculated from an integral over the energy components at depth **r'**. Accounting for beam hardening effects on the TERMA in the computation is trivial but is nevertheless essential because this defines the energy imparted to the medium at **r**. Comparison with monoenergetic TERMA arrays of the same mean energy have been shown to differ from the polyenergetic TERMA arrays by up to 10% (Metcalfe *et al* 1989). Therefore the method accounts for the effect of beam hardening of the TERMA. Using (7) the effect of beam hardening with depth on the polyenergetic dose spread function is not accounted for, but it is shown in this paper that this does not lead to significant errors. A time advantage is gained because only one superposition per beam is required.

Murray *et al* (1990) outline the times required to compute dose distributions using this method on eight T800 Inmos transputer modules. In brief, computation times of only a few seconds are required for convolution in Fourier space and computation times of about two minutes are required for superposition in real space, utilising a simple range scaling algorithm.

3. BEAM SPECTRA

3.1 Full Field Monte Carlo Verification of Surface Spectra

The spectral data used to calculate polyenergetic TERMA and PDSAs for the studies described in this paper is the spectral beam information published for a 10 MV Clinac 18 by Mohan and Chui (1985b). They produced the expected spectrum by using a Monte Carlo simulation combined with geometric information about the target and flattening filter design. The spectral distribution we use is a simplified version of their originally published 23 component spectrum in that it has ten components as shown in Table 1 (row 3). The distribution shows how the beam's spectral components are weighted toward the low end of the energy spectrum.

Verification of the suitability of spectral information for our 10 MV photon beam was obtained by doing full field EGS Monte Carlo (Nelson *et al* 1985) simulations on a DEC VAX 6330. The simulations followed the histories of 4 million incident photons down to 40 cm depth with the electron step length being set dynamically using the parameter reduced electron step algorithm (PRESTA) (Bielajew and Rogers 1987). The simulation batches the results into a set of ten and from these data sets the error in the mean is estimated. This was found to be less than 1% in all positions down to 40 cm depth. The computing time for each simulation was about 40 CPU hours.

The percentage depth dose (%D) curves for two 5 x 5 cm beams are plotted in Figure 2. Two different incident beam spectra were used for each simulation. The surface spectrum components used for the first simulation are shown in Table 1 (row 3, d_{ref} = 0 cm). To show the effect of using an incorrect spectrum the process was repeated using the beam hardened spectrum (Table 4, row 4, d_{ref} = 40 cm).

Energy E_n (MeV)	0.5	1.5	2.5	3.5	4.5	5.5	6.5	7.5	8.5	9.5
$(\mu/\rho)_n$*	.0969	.0575	.0445	.0368	.0321	.0289	.0284	.0251	.0237	.0227
$\%F_n$, d_{ref} = 0 cm	17.5	22.0	20.4	12.9	9.2	7.1	4.9	3.2	1.9	0.9
$\%F_n$, d_{ref} = 40 cm	2.0	12.8	19.5	16.8	14.4	12.7	8.9	6.6	4.2	2.1

Table 1: Spectral data and mass attenuation coefficients used in generating fluence, TERMA and PDSA information. The data was also used in the 5x5 cm full field Monte Carlo simulation. * Mass attenuation coefficient data from Johns and Cunningham (1983)

Note that each point shown on the graph represents the dose scored in cylindrical voxel elements which step down the central axis and are of dimensions 10 mm radius and 5 mm thickness. The dose is normalised to the voxel containing maximum dose (D_{max}).

As shown in Figure 2 the results of the EGS simulation using the 0 cm depth, 10 MV spectrum agree to within a mean difference of 1.2% with the experimental depth dose readings obtained for a similar beam from our Varian Clinac 18 linear accelerator, measured with a PTW ionisation chamber in a Therados RFA-3 water tank. This indicates that it is appropriate to use the spectral data of Mohan and Chui (1985b) to simulate a 10 MV beam from our linear accelerator, provided the surface spectrum is used. Hence dose spread arrays and TERMA arrays were generated using this spectral information. In contrast the results of the EGS simulation for the 40 cm depth, 10 MV spectrum show a shallow fall off compared to the experimental depth dose results. This is because the incident beam spectrum is too heavily weighted with high energy components.

To demonstrate that the main difference in the depth doses generated using the different spectra for the two Monte Carlo simulations is due to beam hardening of the TERMA, Figure 3 is presented. This graph shows the percentage TERMA (%T), calculated using (4) and (11), normalised to 100% at the surface plotted against depth as calculated for the 0 cm depth, 10 MV and 40 cm depth, 10MV spectrum. Note the differences between the curves are significant and reflect those in Figure 2.

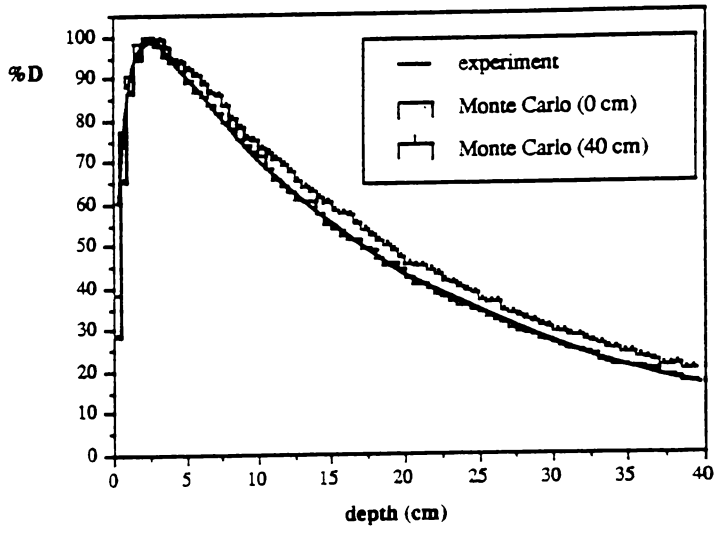

Figure 2: Central axis percentage depth dose (%D) curves showing a comparison between a Monte Carlo (EGS) simulation which follows the histories of 4 million photons. The Monte Carlo simulations are for two different spectral distributions; that typical of a 10 MV surface spectrum (normalisation at D_{max} is 100% = 3.11 pGy MeV^{-1} cm^2) and that typical of a 10 MV beam which has traversed 40 cm of water (normalisation at D_{max} is 100% = 3.98 pGy MeV^{-1} cm^2). Experimental data collected using a PTW ionisation chamber in a Therados water tank is also plotted on the graph. The beam size is 5 x 5 cm.

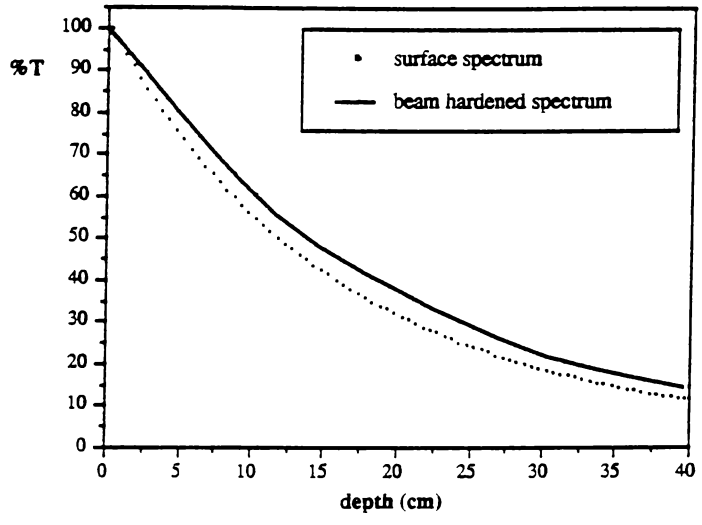

Figure 3: Percentage TERMA versus depth curves. The two TERMA curves are for the surface spectrum and beam hardened spectrum respectively. Normalisation at the surface T_{max} for the surface spectrum is 100% = 6.03 pGy MeV^{-1} cm^2, and normalisation at the surface T_{max} for the beam hardened spectrum is 100% = 5.42 pGy MeV^{-1} cm^2.

3.2 Change of Beam Spectrum with Depth

It is possible to account for beam hardening effects on fluence as follows. For a polyenergetic beam where there is a range of photon energies from 0 to E_{max}

$$\Phi(\mathbf{r}') = \int_0^{E_{max}} \frac{d\Phi(\mathbf{r}')}{dE}\, dE \qquad (9)$$

where $d\Phi(\mathbf{r}')/dE$ is the photon fluence in a unit energy interval at E. For a discrete number of spectral components

$$\Phi(\mathbf{r}') = \sum_{n=1}^{N} \Phi_n(\mathbf{r}') \quad . \qquad (10)$$

A normalised spectrum at depth $\mathbf{r}'$ is found by normalising each component at depth to the total fluence at depth $\mathbf{r}'$. If $F_n(\mathbf{r}')$ is the normalised component of fluence at $\mathbf{r}'$ then

$$F_n(\mathbf{r}') = \frac{F_n(\mathbf{r_0})\, e^{-(\mu/\rho)_n |\, \mathbf{r}' - \mathbf{r_0}\,|}}{\sum_{j=1}^{N} F_j(\mathbf{r_0})\, e^{-(\mu/\rho)_j |\, \mathbf{r}' - \mathbf{r_0}\,|}} \quad , \qquad (11)$$

where $F_n(\mathbf{r_0})$ is the normalised fluence component at the surface.

A normalised photon spectrum at any depth may now be found from the normalised spectrum at the surface. Values used for F_n have been calculated for the ten component spectrum as it is attenuated down to 40 cm depth, and the values for 0 cm and 40 cm spectra are listed in Table 1, rows 3 and 4 respectively. The data in Table 1 shows that there is a higher relative proportion of low energy spectral components for the surface spectrum than for the 40 cm depth spectrum. This is due to the more rapid attenuation of the low energy components with depth. The normalised fluence at any depth may then be used to generate the PDSAs using the method outlined in section 2, in this manner the effect of changing energy fluence with depth is accounted for.

4. DOSE SPREAD ARRAYS

4.1 Polyenergetic Dose Spread Array Profiles in Polar Coordinates

Sets of DSA data were formed by simulating 250 000 photons interacting at a point at the origin of a polar coordinate system and following their dose deposition histories. Figure 1(b) shows the DSA scoring geometry used in the EGS simulation. A scoring voxel is defined as the ring shaped region formed by the intersection of a concentric radial shell and a discrete polar angular interval. The radial shells have a thickness of 1 mm and the angular intervals span 5 degrees. The "voxel radius" r_i is defined as the distance from the origin to the centre of the shell, and the "polar angle" θ_i is defined as the angle to the centre of the voxel.

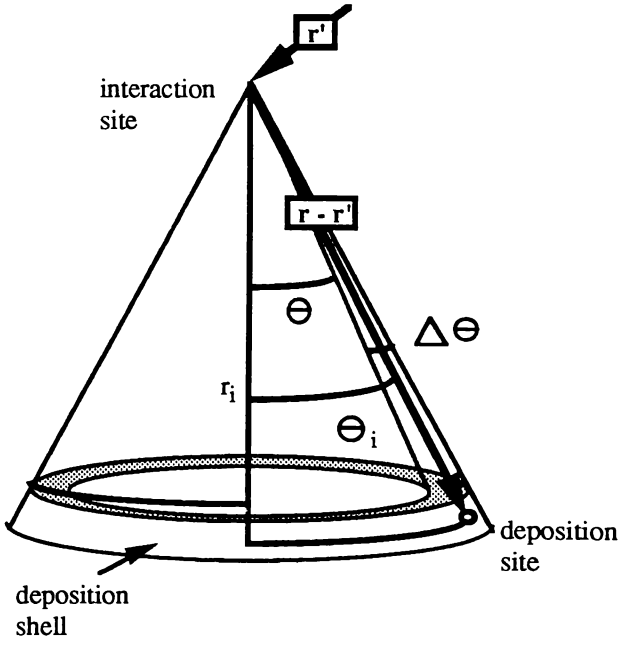

Figure 1(b): Polar geometry describing the DSA scoring coordinate framework used by EGS. The photon interacts at the primary interaction site and dose is scored in a shell of mean voxel radius r_i . The dose is scored into a volume defined by the polar voxel interval within the angle θ and $\theta+\Delta\theta$ which has a mean shell angle θ_i.

Important parameters used in the EGS simulation are outlined in Table 2. The EGS simulation gives results in terms of energy deposition per voxel volume as a fraction of the energy released at the interaction site. Because the voxels are of unequal volume, the result

is then divided by voxel volume to give values which are defined as fractional energy deposition per unit volume (Ahnesjö 1989), in units of cm^{-3}.

PARAMETER NAME	DESCRIPTION	VALUE
EI	Incident photon energies	Spectra see table 4.1
	Number of photons incident	250 000
ESTEPE	maximum electron energy loss per step	0.02
	Vax 6330-CPU approx. simulation time	12 hours
ECUT'	Electron kinetic energy deposition cut-off	50 keV
AE'	minimum delta ray kinetic energy loss	50 keV
AP	minimum discreet radiative energy loss	50 keV
PCUT	photon local deposition energy cut off	50 keV

Table 2: EGS parameters used in MDSA and PDSA Monte Carlo simulations.

In Figure 4, DSA values produced from the EGS simulation are plotted against distance from the interaction site for a particular angular interval centred at θ_i. The vertical axis of the graph is $H(r_i, \theta_i)$, which is the fractional energy deposition per unit volume, and the horizontal axis is the voxel radius r_i of the shell in which the energy is deposited. We have called such graphs "DSA profiles".

Shown in both Figures 4(a) and 4(b) is DSA data produced from three different EGS simulations. In one simulation 3 MeV monoenergetic dose spread array (MDSA) data is produced (this is the mean weighted energy of the 10 MV beam); the other two simulations produced PDSA data using spectral components encountered at two depths, $d_{ref} = 0$ cm and $d_{ref} = 40$ cm respectively. Graphs for two angular intervals are shown with $\theta_i = 2.5$ degrees in Figure 4(a) and $\theta_i = 47.5$ degrees in Figure 4(b). The graphs indicate the reduction of dose deposition with angle and the rapid reduction of dose deposition as the distance from the interaction site increases. As expected, much of the energy is deposited downstream of the interaction site.

Note that the DSAs produced using the polyenergetic beam are significantly different from that produced using the monoenergetic beam. They show a less defined electron range and less deposition close to the interaction site. For example, at the location $r_i = 8$ mm in the polar interval centred at 2.5 degrees the MDSA line starts to dip below the PDSA lines and the dose deposition is much lower at about $r_i = 14$ mm, which appears to be the maximum range of electrons from primary interactions. Note at greater angles the difference between initial dose deposition are even greater (see Figure 4(b)). This is because the dominant Compton scattering angles are more obvious for the MDSA profile than the PDSA profile. These results demonstrate that the use of MDSA data is probably inadequate for the superposition process. This assumption has been previously confirmed elsewhere (Metcalfe *et al* 1989).

There are also differences in relative energy deposition between the two PDSA profiles. The magnitude of this effect is not clearly shown on the plots because of the log scale on the vertical axis (which is unavoidable due to the rapid energy deposition fall off). Note that these differences lead to very small spatial differences of about 1 mm between the profiles. This is because of the rapid energy deposition fall off. It is important to realise that although the percentage difference between the 0 cm and 40 cm PDSAs increases with depth, the actual contributions to dose at larger distances from the interaction voxel are several orders of magnitude lower than those close to the interaction voxel. The difference is caused by harder spectrum. Note, for example, that the beam hardened PDSA shows energy deposition at a greater range than the surface PDSA. The insignificance of this difference to the accuracy of the superposition process is outlined in section 5.

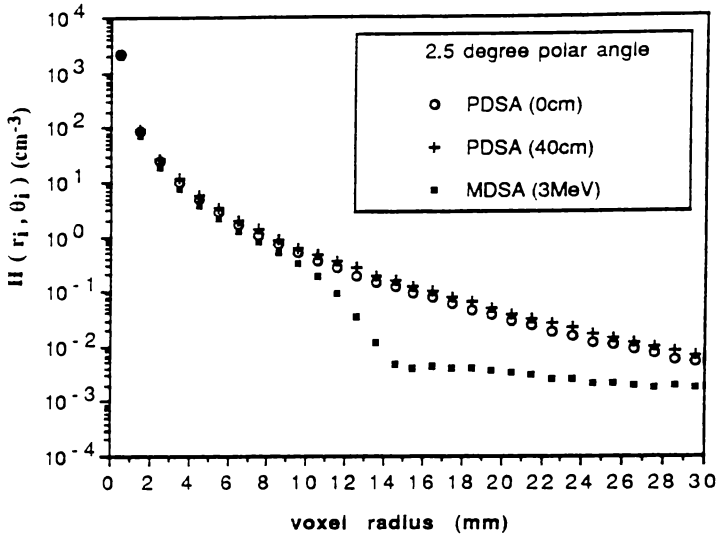

A

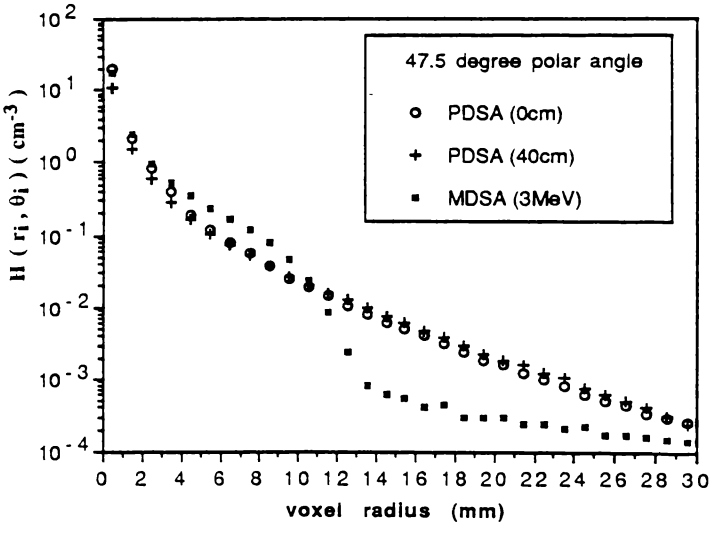

B

Figure 4:
Total PDSA profiles showing relative dose plotted against voxel radius r_i for two polar angles. The PDSAs were generated using the surface polyenergetic spectra (see Table 1, row 3) and the beam hardened PDSA (see Table 1, row 4). Also included is a profile for a 3 MeV MDSA.
(a) $\theta_i = 2.5$ degrees polar angle.
(b) $\theta_i = 47.5$ degrees polar angle.

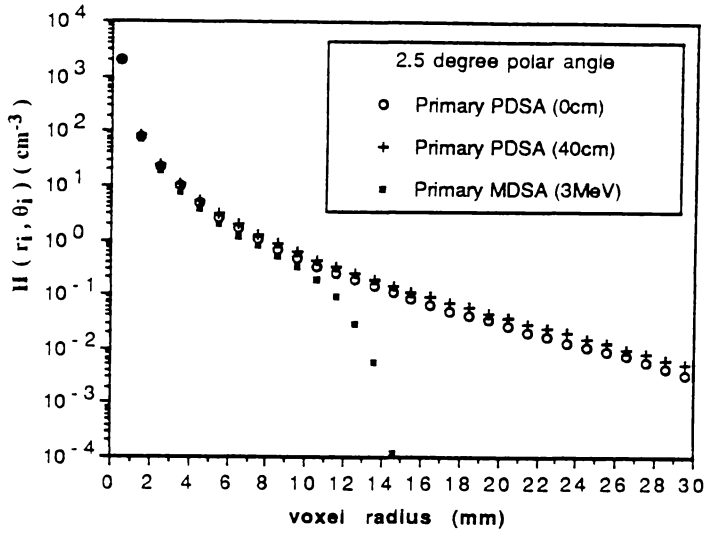

A

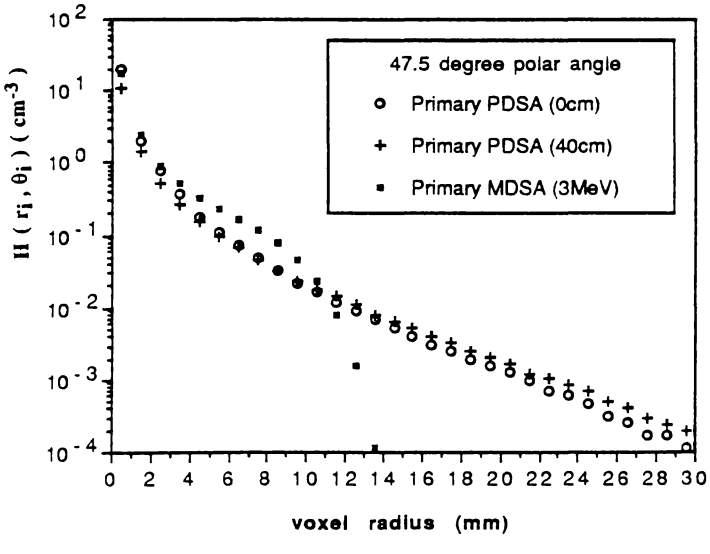

B

Figure 5:
Primary PDSA profiles showing relative dose plotted against voxel radius r_i for two polar angles compared with primary MDSA profiles produced using a monoenergetic 3 MeV beam.
(a) primary PDSAs versus primary MDSA comparison at $\theta_i = 2.5$ degree polar interval.
(b) primary PDSAs versus primary MDSA comparison at $\theta_i = 47.5$ degree polar interval.

4.2 Primary Polyenergetic Dose Spread Array Profiles in Polar Coordinates

The process described above was repeated, except only dose from primary photon interactions at the origin which led to charged particle transport was scored. Mackie *et al* (1988) call these primary dose spread arrays or primary deposition kernels.

This data is shown because it gives an indication of dose deposition from charged particle transport. The graphs of Figures 5(a) and 5(b) show the "primary DSA profiles" for two angular intervals, the interval centered at $\theta_i = 2.5$ degrees (Figure 5(a)) and the interval centred at $\theta_i = 47.5$ degrees (Figure 5(b)).

Note that the energy deposition close to the interaction voxel is very similar to the values obtained for the total DSA profiles. However, the profiles diverge from those of Figure 5 further from the interaction voxel because the flat tail due to secondary photon interactions is not present in these profiles. The difference between the surface and beam hardened PDSA primary profiles is once again small, however their fall off is much less rapid for both of the polyenergetic profiles than the monoenergetic DSA profile. This is because of the much broader range of electron energies present in the case of the PDSAs, leading to a less defined electron range.

It is important to note that for these graphs the geometric centre of the voxel has been used. It is valid to define the voxels at the geometric centre for these plots provided it is not assumed that the effective position of energy deposition is at this position.

4.3 Effective Range of Energy Deposition for Primary PDSAs

Mackie *et al* (1988) have shown that the assumption of dose deposition at the geometric voxel centre is not valid when an accurate assessment of primary DSA charged particle range is required. For this reason we have developed a method of calculating the effective range within the EGS simulation, using the position of each charged paticle step. This avoids the need to calculate the effective voxel centre as is the case when energy scored per voxel is used to calculate the range (Mackie *et al* 1988).

This has been achieved using the position of each charged particle step relative to the primary interaction point. Energy ε_n is deposited for the nth step, and the effective charged particle range r_{eff} is given by

$$r_{eff} = \frac{\sum_{n=1}^{N} \varepsilon_n (x_n^2 + y_n^2 + z_n^2)^{1/2}}{\sum_{n=1}^{N} \varepsilon_n}, \qquad (12)$$

where x_n, y_n, and z_n are the cartesian coordinates describing the particles position and the interaction occurs at (x,y,z) = (0,0,0). To ensure that energy is deposited on average at the centre of the charged particle step, the position of energy scoring alternates between the beginning and end of the step for each successive particle history.

Similarly the effective longitudinal range z_{eff} can be established as

$$z_{eff} = \frac{\sum_{n=1}^{N} \varepsilon_n z_n}{\sum_{n=1}^{N} \varepsilon_n} , \qquad (13)$$

and the lateral range y_{eff} is defined here as

$$y_{eff} = \frac{\sum_{n=1}^{N} \varepsilon_n (x_n^2 + y_n^2)^{1/2}}{\sum_{n=1}^{N} \varepsilon_n} . \qquad (14)$$

A summary of the range calculation results are shown in Table 3. MDSA results show good agreement with the calculations of Mackie *et al* (1988) for a 3 MeV dose spread array for all range calculations. The table also indicates the longer effective range of the PDSAs compared to the MDSA. The difference in mean ranges between the surface and beam hardened PDSAs is small (less than 1.5 mm) for all component range calculations. Note that Mackie *et al* (1988) use a different definition of lateral range to calculate y_{eff} which produces slightly different results. We have replicated this method for comparison and these results are in the column designated as y'_{eff}.

Type of DSA	z_{eff}	r_{eff}	y_{eff}	y'_{eff}
primary surface PDSA	5.73	6.67	2.79	3.41
primary 40 cm PDSA	7.15	8.24	3.35	4.09
primary mono. 3 MeV DSA	3.95	4.81	2.28	2.74
primary mono. 3 MeV DSA+	3.968	4.803	-----	2.705

Table 3: The effective depth of penetration z_{eff}, the effective range r_{eff} and the effective lateral distance y_{eff} of charged particle transport generated by primary dose spread arrays. Also included is y'_{eff}. The units of range are in mm. + Data from (Mackie *et al* 1988)

4.4 Isoline DSA Distributions

In order to get some indication of spatial energy distributions of total PDSAs, they can be represented in isoline distribution, ie. lines of equal fractional energy deposition per unit volume. Shown in Figure 6 are the lines plotted for polar angle θ_i versus voxel radius r_i.

To demonstrate the differences in DSA characteristics, a single isoline for different DSAs is presented in Figure 6. The least penetrative is the 3 MeV MDSA, due to the absence of high energy recoil electrons. The surface 10 MV PDSA and beam hardened 10 MV PDSA show very small spatial differences, with the surface PDSA being slightly less penetrating than the beam hardened PDSA.

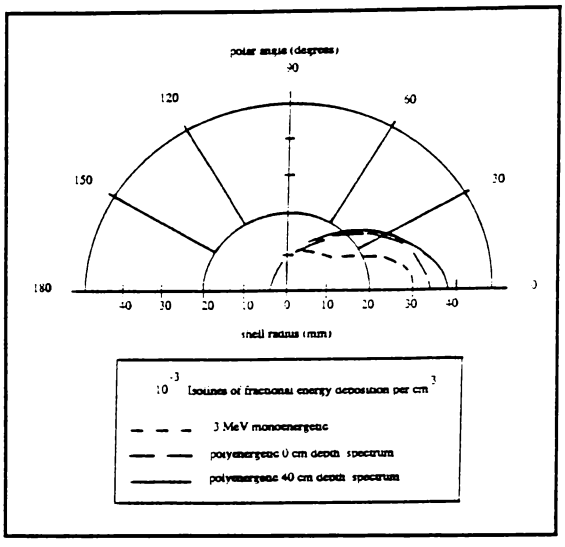

Figure 6: Isoline distributions showing levels of equal dose deposition within a mean polar angle versus mean shell radius. Different DSAs intercompared showing the 10^{-3} Isolines for the total 3 MeV MDSA, total surface 10 MV PDSA and total beam hardened 10 MV PDSA respectively (units cm^{-3}).

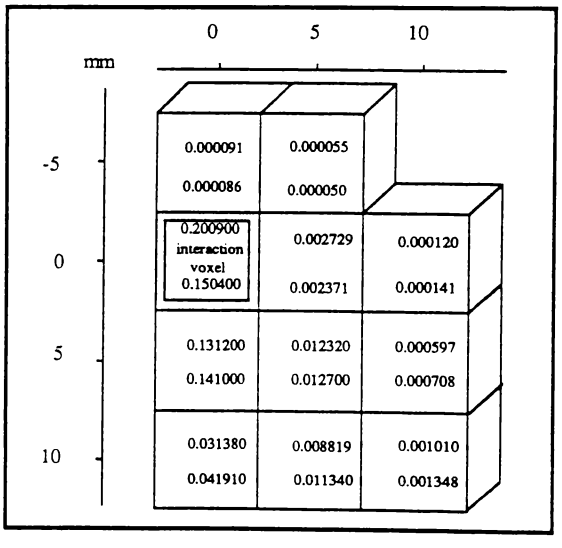

Figure 7: (a) Two dimensional single quadrant representation of "non-smeared" DSAs scored in Cartesian coordinates. The upper values in each voxel refer to the dose deposition values obtained using the surface 10 MV PDSA spectrum. The lower values in each voxel refer to the dose deposition values obtained using the 40 cm depth, 10 MV PDSA spectrum (units cm^{-3}).

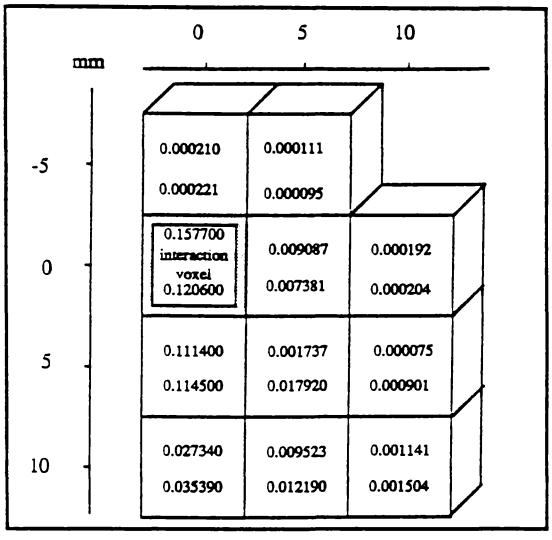

Figure 7: (b) Two dimensional single quadrant representation of "smeared" DSAs scored in Cartesian coordinates. The upper values in each voxel refer to the dose deposition values obtained using the surface 10 MV PDSA spectrum. The lower values in each voxel refer to the dose deposition values obtained using the 40 cm depth, 10 MV PDSA spectrum (units cm^{-3}).

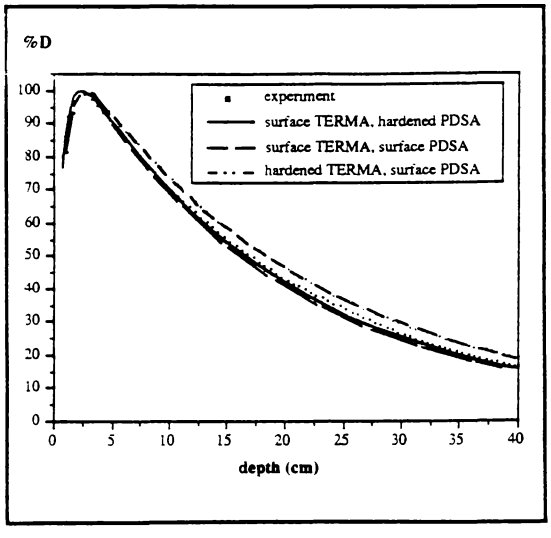

Figure 8: Percentage depth dose comparisons in homogeneous media. The central axis percentage depth dose (%D) curves for a 5x5 beam generated by superposition compared with experiment. The PDSAs used in these simulations were non-smeared.

5 RESULTS

5.1 DSAs in Cartesian Coordinates

In order to carry out superposition one can use polar arrays directly (Mohan *et al* 1986) or Cartesian arrays of data. The computation method for superposition at our institute uses Cartesian arrays. The cartesian arrays can be formed by "smearing" the photon interaction points evenly throughout the interaction voxel or alternately the cartesian arrays can be formulated as "non-smeared".

A very small part of these Cartesian DSAs used in the superposition are shown in Figure 7. The energy is deposited in $(5\ mm)^3$ Cartesian voxels is shown across the central axis of a symmetric quadrant. The upper numeric values shown in Figure 7(a) are the fractional energy deposition per unit volume for the non-smeared surface 10 MV PDSA and the lower numeric values in each voxel are the fractional energy deposition per unit volume due to the beam hardened non-smeared 10 MV PDSA. This representation clearly shows that most energy is deposited in the interaction voxel but a significant amount of energy is also deposited in the other voxels. The fractional energy deposition in the interaction voxel is higher for the surface 10 MV PDSA than the beam hardened 10 MV PDSA but the differences in the other voxels are small.

The comparison is repeated in Figure 7(b) for smeared surface and smeared beam hardened PDSAs respectively. For the smeared spread arrays there is less energy deposition in the interaction voxel and more energy is deposited in the surrounding voxels. Examination of these figures shows that smearing, non smearing and the spectrum significantly affects the dose deposited in the interaction voxel and surrounding voxels. But we have found that the use of any of these DSAs produces only a small percentage difference (0.3% at 10 cm depth and 1.3% at 20 cm depth) in depth dose results following superposition.

5.2 Superposition in the Homogeneous Environment

Superposition programs have been developed at our institute to test the effect of beam hardening on the superposition process. Further details of beam profile and build-up simulations are given elsewhere (Murray *et al* 1989, 1990). The programs can perform superposition in Fourier space or real space. The calculations outlined in this section used Cartesian dose spread arrays generated in Cartesian coordinates which were "superposed" using real space superposition.

Superposition was carried out using (7) which gives results in dose units of (MeV g^{-1}), this has been converted to dose per energy fluence (pGy MeV^{-1} cm^2) to comply with other work (Ahnesjö 1989). Because comparison with experimental results is required, the dose per energy fluence is normalised to 100% at D_{max} for the graphs which follow, and the conversion factor for the simulations is provided in the caption of each graph. Normalisation at D_{max} is adequate in this case because measurements using a thin window ionisation chamber under our beam have shown the contribution to dose at D_{max} from contamination electrons is less than 1% for a 5 x 5 cm field (Harper *et al* 1990).

In Figure 8 is shown the central axis percentage depth dose (%D) curve for a 5x5 cm beam generated by superposition of the surface spectrum PDSA with a surface spectrum TERMA (which alters due to beam hardening with depth), also shown on the graph are depth dose readings obtained using a PTW (0.1cc) thimble ionisation chamber in a Therados RFA3 water tank. The results show a mean difference of 1.2% down to 20 cm and 2.8% down to 40 cm. Also shown in Figure 8 is the curve generated by superposition of a beam hardened PDSA with a surface spectrum TERMA, these results differ from the experimental results by 2.9% down to 40 cm.

Note the depth dose results obtained using superposition of the surface and hardened PDSAs in Figures 8 are virtually the same and the mean difference between these two curves is only 0.1%. This shows that the spectrum from which the PDSA is formed has very little effect on the superposition. It has been shown previously however (Metcalfe *et al* 1989) that an MDSA calculated from a single energy is not adequate for accurate superposition results.

The graph of Figure 8 also shows the depth dose curve obtained by superposition of the 0 cm depth, 10 MV PDSA with TERMA calculated using the 40 cm depth, 10 MV spectrum. This depth dose curve shows a mean difference of 8.2% from the experimental results. It is obvious from the inaccuracy in results shown that superposition involving the use of the wrong spectrum for the TERMA calculation does not produce sufficiently accurate depth dose information for radiotherapy treatment planning. It is also apparent from this result that it is the spectrum used for calculating the TERMA which most affects the shape of the depth dose curves.

The small difference in results using the two PDSAs indicates that the use of a single PDSA is adequate to model beam depth dose characteristics in a homogeneous water medium down to 40 cm depth. This demonstrates that not accounting for beam hardening of the PDSA component does not cause a significant error in percentage depth dose calculation.

5.3 Superposition in the Inhomogeneous Environment

Detail of the superposition of PDSAs which produces accurate simulations in low density media using our method has been outlined in detail by Hoban *et al* (1990). In brief, the method uses a complete 3 dimensional ray trace of the TERMA array (Siddon 1985) combined with a z-direction ray trace used to ascertain scaling information for the DSAs. The method uses interpolation between sets of DSA data scored in density steps. The method is similar to that developed by Mackie (1985). Like Mackie we have also found some interaction voxel weighting is required in the DSA ray trace to more accurately account for the electron scattering mechanism. This affect appears to be more marked at low densities, as the electrons' curved paths approximate less and less to rectilinear scaling.

6. CONCLUSIONS

The effect of beam hardening on the structure of polyenergetic dose spread array distributions has been studied, using the EGS Monte Carlo code to generate PDSAs for two different polyenergetic spectra which modelled the 10 MV beam at 0 cm and 40 cm depth, respectively. These PDSAs display small differences which are clearly shown using DSA profile and Isoline distributions. Mean electron range calculations show differences of about 1.5 mm between the surface PDSA and the beam hardened PDSA respectively. In contrast the 3 MeV PDSA has a much shorter range.

The superposition process (see Figure 8) does give accurate depth dose results down to 40 cm depth using a single surface spectrum dose spread array convolution with a depth dependent polyenergetic TERMA. The correct selection of the spectrum is not critical for the PDSAs but is important when calculating the TERMA.

This paper provides additional confidence that the convolution method can be used to predict radiation therapy dose. The major conclusion, namely that one needs to account for hardening of the primary photon intensity but that the convolution kernel is relatively invariant with respect to changes in spectrum adds additional credence to this assertion made previously by Mackie *et al* (1987).

Methods of scaling PDSAs and TERMA to account for low density lung inhomogeneous regions also show good agreement with experimental results and Monte Carlo simulations even in regions of lateral electronic disequilibrium (Mackie *et al* 1985a, Hoban *et al* 1990,

Ahnesjö 1989). Improved scaling methods are the subject of continuing research at our institute. Development of the programs for routine use in the clinical environment is also presently in progress at our centre.

REFERENCES

Ahnesjö A., Andreo P., Brahme A. (1987) Calculation and application of point spread functions for treatment planning with high energy photon beams. *Acta Oncologica*, **26(1)**, 49-55.

Ahnesjö A. (1989) Collapsed cone convolution of radiant energy for photon dose calculation in heterogeneous media. *Med. Phys.*, **16(4)**, 577-554.

Ahnesjö A., Mackie T.R. (1987) Analytic description of Monte Carlo generated photon dose convolution kernels. *The use of computers in radiation therapy , Elsevier Science Publishers, Amsterdam.* 197-200.

Bielajew A.F., Rogers D.W.O. (1987) PRESTA: The parameter reduced electron step transport algorithm for electron Monte Carlo transport. *Nucl. Instrum. Methods.*, **B18**, 165.

Boyer A.L.(1984) Shortening the calculation time of photon dose distributions in an inhomogeneous medium. *Med. Phys.*, **11**, 552-554.

Boyer A.L., Mok E.C. (1985) A photon dose distribution model employing convolution calculations. *Med. Phys.*, **12(2)**, 169-177.

Boyer A.L., Mok E.C. (1986) Calculation of photon dose distributions in an inhomogeneous medium using convolutions. *Med. Phys.*, **13(4)**, 503-509.

Boyer A.L., Wackwitz R. Mok E.C. (1988) A comparison of the speed of three convolution algorithms. *Med. Phys.*, **15(2)**, 224-227.

Boyer A.L., Zhu Y., Wang L., Francois P. (1989) Fast Fourier transform convolution calculations of X-ray isodose distributions in homogeneous media. *Med. Phys.*, **16(2)**, 248-252.

Cunningham J.R. (1982) Tissue inhomogeneity corrections in photon beam treatment planning. Progress in Medical Radiation Physics, *Vol 1. Plenum publishers.*

Dean R.D. (1980) A scattering kernel for use in true three dimensional dose calculations. *Med. Phys.* (7), 429.

Field C., Battista J.J. (1987) Photon dose calculations using convolution in real and Fourier space: Assumptions and Time Estimates. *Presented 9th ICCR Conference, Holland*, 1987.

Harper N.R., Metcalfe P.E., Hoban P.W., Round W.H. (1990) Electron contamination from 4 and 10 MV X-ray beams. *Aust. Phys. Eng. Sci. Med. , Submitted for publication, May, 1990.*

Hoban P.W., Metcalfe P.E., Murray D.C., Round W.H.(1990) Superposition in low density media. *Aust. Phys. Eng. Sci. Med., June, 1990.*

Johns H.E., Cunningham J.R. (1983) The physics of radiology. *C.C. Thomas Publishers, Illinois.* 4th Edition, Appendix A, 723.

Kornelson R.O., Young M.E.J. (1982) Changes in the dose - profile of a 10 MV X-ray beam within and beyond low density material. *Med. Phys.*, **9(1)**, 114-116.

Mackie T.R. (1985) The study of megavoltage X-ray beams. *Phd Thesis, Vol 2. University of Alberta.*

Mackie T.R., Scrimger J.W., Battista J.J. (1985a) A convolution method of calculating dose for 15 MV X-rays. *Med. Phys.*, **12**, 188-196.

Mackie T.R., El-Khatib E., Battista J.J., Scrimger J., Van Dyk J., Cunningham J.R (1985b) Lung dose corections for 6 and 15 MV X-rays. *Med. Phys.*, **12(3)**, 327-332.

Mackie T.R., Ahnesjö A., Dickof P., Snider A. (1987) Development of a convolution/superposition method for photon beams. *The use of computers in radiation therapy, Elsevier Science Publishers, Amsterdam.* 107-110.

Mackie T.R., Bielajew A.F., Rogers D.W.O., Battista J.J. (1988) Generation of photon energy deposition kernels using the EGS Monte Carlo code. *Phys. Med. Biol .*, **33(1),** 1-20.

Metcalfe P.E., Battista J.J. (1988) Accuracy of inhomogeneity corections in lung irradiated with high energy X-rays. *Aust. Phys. Eng. Sci. Med.*, **11(2)**, 67-75.

Metcalfe P.E., Beckham W.A. (1988) Radiotherapy planning accuracy in terms of CT Numbers and inhomogeneity correction techniques. *Aust. Rad.*, **32(3)**, 371-379.

Metcalfe P.E., Hoban P.W., Murray D.C., Round W.H. (1989) Modelling polyenergetic high energy photon beams by superposition. *Aust. Phys. Eng. Sci. Med.*, **12(3)**, 138-149.

Mohan R., Chui C. (1985a) Validity of the concept of seperating primary and scatter dose. *Med. Phys.*, **12(6)**, 726-730.

Mohan R., Chui C. (1985b) Energy and angular distributions of photons from medical linear accelerators. *Med. Phys.*, **12(5)**, 592-597.

Mohan R., Chui C., Lidofsky L. (1986) Differential pencil beam dose computation model for photons. *Med. Phys.*, **13(1)**, 64-73.

Murray D.C., Hoban P.W., Metcalfe P.E., Round W.H. (1989) 3-D superposition for radiotherapy treatment planning using fast Fourier transforms. *Aust. Phys. Eng. Sci. Med.*, **12(3)**, 128-137.

Murray D.C., Hoban P.W., Metcalfe P.E., Round W.H. (1990) Superposition on a parallel processing computer. *Med. Phys., accepted for publication. July 1990.*

Nelson W.R., Hirayama H., Rogers D.W.O. (1985) The EGS4 Code System. *Stanford Linear Accelerator Center Publication , Report - 265.*

Siddon R.L. (1985) Fast calculation of the exact radiological path for a three-dimensional CT array. *Med. Phys.* **12(2)**, 252-255.

Australasian Physical & Engineering
Sciences in Medicine (1990) Vol. 13 No.3

THE PRODUCTION OF BODY ANALOGS FOR USE IN RADIATION PHYSICS*

P.E. Metcalfe[1,2], P.W. Hoban[2], N.R. Harper[2], D.C. Murray[2], W.H. Round[2]

[1] *Scientific and Information Services, Waikato Hospital, Hamilton, New Zealand.*
[2] *Department of Physics, University of Waikato, Hamilton, New Zealand.*

Abstract

Bone, muscle and lung analog materials have been produced in-house, and dosimetry phantoms have been produced. A method using computed tomography (CT) has been developed to check that the analogs produced match the radiation properties of body tissues. The relative electron densities and ratio of electron cross sections are calculated from elemental compositions of the analogs. Using these data the theoretical CT numbers are calculated and these numbers are compared with experimental CT numbers for the analogs produced. The experimental CT numbers are found by scanning the samples on a Siemens DRH CT scanner. Results show the maximum difference between theoretical and experimental CT numbers for the analogs is 18 Hounsfield units, which relates to a ΔN_{CT} of less than 1%. Comparison of analog CT numbers with CT numbers for the related patient tissues also shows a close match.

Key Words

Computed Tomography, Quantitative Computed Tomography, Body Analogs.

Introduction

Being able to tailor the exact density, atomic number and shape of radiation dosimetry phantoms has obvious advantages, and the use of commercial substances does not always give one this flexibility. Therefore in-house manufacture of lung, tissue and bone analogs for dosimetry phantoms was undertaken, and the manufacturing and quality assurance methods developed for this process are described here.

The in-house production of epoxy resin based body analogs is outlined in the next section. A quality assurance method which uses computed tomography (CT) scan data to analyse these analogs is also outlined. Several phantoms produced using this material are described and these include a two lung phantom, build-up caps and CT phantoms.

The analog materials manufactured are available in 30 x 30 x 1 cm slabs by a commercial supplier, (REM New Zealand Ltd. agents for Radiation Measurements Inc., Middleton Wisconsin, U.S.A. 1989). Their price was quoted as NZS560 per muscle or lung slab and NZS920 per bone slab. If purchased from the commercial supplier the analog material for the two lung phantom would have cost NZS15680 (ie. 28 slabs x $560). This cost was considered to be excessive considering the large amount of material which was required for the phantoms.

In contrast, in-house manufacture is relatively inexpensive. The cost for materials including resins, moulds and equipment to manufacture the analogs in-house is about NZS45 per slab. Hence the cost to produce the two lung phantom in-house worked out at NZS1260 (ie. 28 slabs x $45).

The in-house manufacture of solid bone analogs is just as advantageous as that of solid lung analogs. This is because no mass produced solid materials are suitable as bone analogs. In fact delrin, ertalyte and teflon are relatively poor bone analogs as their atomic numbers are much less than that of in vivo bone. Though the effective atomic number of the liquid analog K_2HPO_4 closely matches in vivo bone, the liquid analog solution reproducibility stability is a

* *Presented at the Aust. Phys. Eng. Sci. Med. 12th Annual Conference Hamilton, New Zealand, 1989.*
[1] *Current address, Medical Physics Dept., Cancer Care Centre, Wollongong Hospital, N.S.W.*
Received 7 May 1990; accepted in final form 8 August 1990.

problem. Also these analogs have to be housed in the required shape by some sort of vessel which cannot itself perturb the radiation beam. This is the main drawback when liquid analogs are used in radiotherapy phantoms.

Production of Moulds, Analogs and Phantoms

Bone, muscle and lung epoxy resin based analogs have been produced for use as dosimetry phantom material. The recipes and methods of White *et al* [2] have been followed in the manufacture of these substances. A method has been developed by White[3,4] to show that the radiation properties of these analogs match closely those of their respective equivalent human tissues. The mass stopping powers S/ρ, and mass attenuation coefficients μ/ρ, of these substances match those of their human tissue equivalents to within 3% over the x-ray energy range of 0.1 to 10 MeV[3,4].

Tables 1, 2, and 3 show the constituent elements required for production of bone, muscle and lung analog material respectively. Included in the tables is the code which White *et al* use to refer to these materials, for information about material description and supply (see column 1), and percentage by mass of constituents (see column 2), respectively.

The apparatus used for the manufacture of bone, muscle and lung analogs is shown in Figure 1. It consists of a powerful electric mixer (an electric drill motor) which turns a mixing propeller within a

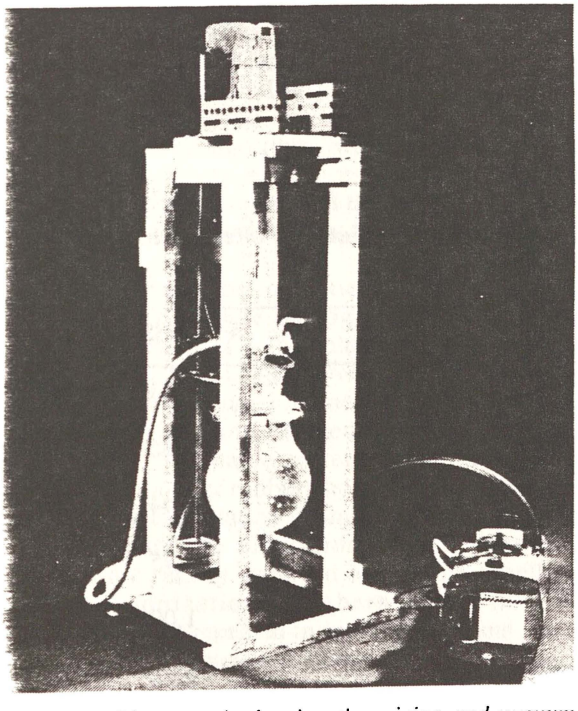

Figure 1: Photograph showing the mixing and vacuum apparatus used for the in-house manufacture of body analogs.

reaction vessel. The vacuum is provided by a vacuum pump, which is able to maintain a vacuum of 0.001 Torr. This is connected to the top of the reaction vessel by a flexible hose. An electric drill motor is connected to the mixing propeller by a connecting rod which feeds through a glass stirring gland. The gland is sealed by glycerol and the reaction vessel has a ground glass edge which means it can be vacuum sealed with grease. The apparatus is housed in a fume cupboard because the epoxy resin hardeners are extremely toxic.

The ingredients are combined on a percentage by mass basis. All ingredients are poured into the reaction vessel and are given a thorough manual mix. The reaction vessel is then attached to the mixing device. Automatic mixing is applied for a further 3 minutes and then the vacuum is applied to the reaction vessel. The pressure reduction in the vessel causes the fluid to rise in the vessel, but the rotating blades break the resulting foam and the trapped gases escape. This prevents bubbles forming in the mix. Mixing for 20 minutes under vacuum is essential to remove all the bubbles. The vacuum is then released and the mixing is stopped. The reaction vessel is then removed from the mixing device and the mixture is poured into the waiting mould.

The mixture settles in the mould and is left for 24 hours to harden. Complete curing is achieved by then heating the analogs in an oven at 70 degrees Celsius for a further two hours. At this stage the analog is set and can be removed from its mould. If the mixture is not exactly the desired shape then it can be reheated to 70 degrees Celsius, in which case it becomes slightly flexible and can be reset to the desired shape. If the mixture is not of the correct thickness it can be successfully faced off using a conventional milling machine.

The lung analog is made using the same process except the vacuum is not applied. The mixture is simply poured into waiting moulds and gently rises due to the expanding agent (Dow Corning 1107) which blows hydrogen bubbles into the mixture. The amount of large gas spaces left in the lung analog is reduced by the surfactant (Dow Corning 200/50). The type of MgO used is critical to the process. The more pure grades of MgO tend to collapse the mixture[2]. The MgO which we found most suitable was laboratory grade "MgO heavy". The curing process for the lung analog was supplemented by placing the material in an oven at 70 degrees Celsius for two hours. This speeds up the curing process and helps prevent the mixture from collapsing before it is set.

The moulds used to produce slab phantom material are constructed from acrylic and are screwed together such that the ends can be disassembled. This helps in the release process as does the addition of "mould release". To remove the analogs from the mould the sides are removed from the moulds and a chisel is

Table 1

Ingredients used to produce bone analog material for X-ray beam simulations (Whites code IB1).

MATERIALAND (SUPPLIER)	DESCRIPTION	% MASS
Araldite F (Ceiba Geigy)	Epoxy resin	47.0
Synolide 960 (TR Chemicals)	Hardener	28.2
Polyvynylchloride	PVC powder	24.8

Table 2

Ingredients used to produce muscle analog material for X-ray beam simulations (Whites code MS 10).

MATERIAL AND (SUPPLIER)	DESCRIPTION	% MASS
Araldite F (Ceiba Geigy)	Epoxy resin	47.5
Synolide 960 (TR Chemicals)	Hardener	28.5
Polyethylene	Powder 50 μm	15.0
Calcium carbonate	$CaCO_3$ powder	6.2
Phenolic micro-balloons	PMS low density powder	2.8

Table 3

Ingredients used to produce lung analog material for X-ray beam simulations (Whites code LN 10/75)

MATERIAL AND (SUPPLIER)	DESCRIPTION	% MASS
Araldite F (Ceiba Geigy)	Epoxy resin	33.71
Araldite epoxide 8	Hardener control	16.85
Araldite HY2996	Hardener	9.44
DC1107 (BDH chemicals)	Expander	0.75
DC 200/50	Surfactant	1.00
Phenolic micro-balloons	PMS low density powder	4.42
Polyethylene	Particulate filler powder	15.00
Magnesium oxide	Particulate filler powder	18.83

used to gently prize the rest of the analog from the base of the mould. The use of a hammer to dislodge the analogs from the moulds is not recommended as the analogs tend to shatter or crack.

Another release mould process was developed for the lung analogs, as they use a different hardener which does not release easily using mould release. The moulds were lined with "laboratory bench paper", with the plastic side facing the analog. The analog is removed from the mould once set and the paper peels from the analog.

Moulds for anthropomorphic and large cylindrical analog phantoms are formed by using a heat mould process which is commonly used in radiotherapy planning departments to create face masks for radiation therapy patients. The mould material is "cellulose acetate butyrate" and this is heat moulded into the required shape by using a dummy former. The dummy is removed and this space can be used to pour the analog material into. Dummy formers which have been successfully used include wood, acrylic cylinders, plaster casts and even Rando phantom cross sections.

Acrylic cylinders were used to mould CT phantoms and spinal process phantoms shown in Figure 2. The moulds are 1 mm thick acrylic and these were retained permanently around the analogs as the thin layer was found not to affect CT numbers or radiation dosimetry water tank measurements. The long cylinders produced were not only useful as the solid constituents of a Cann phantom[5,7] (see Figure 2a) but could also be used in a Therados water tank as cylindrical radiotherapy phantoms. The bone in particular is a good way of testing the accuracy of electron beam algorithms which until recently have been tested using substances such as teflon or lead which do not closely model the electron stopping and scattering powers of bone in electron beams[8].

Build-up caps for ionization chambers were also made using muscle analog material. The moulds used consisted of a thin plastic bottle as shown in Figure 2b. This is filled with analog material and then an aluminium ionization chamber former is used to create the desired space for ionization chambers. To enable easier release, the former is fitted into a thin rubber sheath (commonly used to water proof ionization chambers). When the analog has set hard the aluminium former plus rubber sheath are readily removed leaving an excellent fit for real ionization chambers to slot into. This process is also repeated in any slab phantom sections which need to house ionization chambers.

Build-up caps were produced out of muscle analog material to collect TAR data for high energy beams. The alternative method usually employed is to mill build-up caps out of acrylic (as polystyrene tends to be hard to mill in a lathe) and drill out a space for the ionization chamber. The new build-up caps produced were not only more tissue equivalent but

Figure 2: *A selection of phantoms produced in different shapes from body analog materials.*

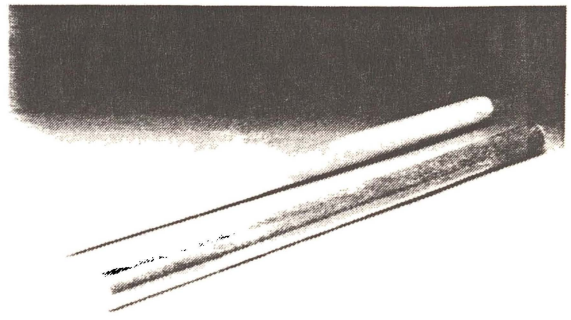

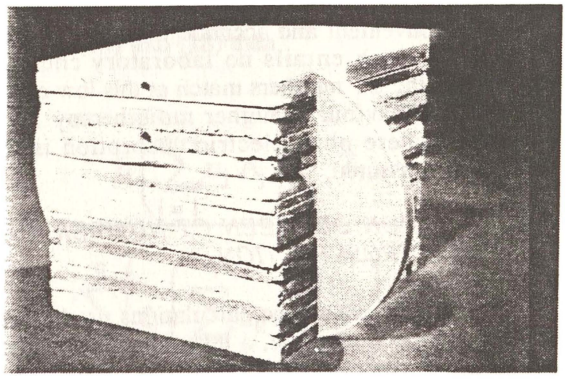

Figure 2a: *Cylindrical phantoms formed in thin acrylic pipes for use as radiotherapy phantoms and CT phantoms. The sample shown at bottom is muscle MS10, and at top is bone IB1 (see White et al[1,2] for codes)*

Figure 2b: *Build-up cap for use with a Baldwin Farmer ionization chamber. The centre of the photograph shows a build-up cap still in its plastic mould. The aluminium former used to create the space for ionization chambers is also shown, as is a completed build-up cap shown on the right of the photograph.*

Figure 2c: *The two lung phantom constructed for dosimetry tests using muscle analog (MS10) and lung analog (LN 10/75). The slabs make up layers of 4 cm muscle, 8 cm lung, 4 cm muscle, 8 cm lung, 4 cm muscle, respectively. The "wings" shown are included when the phantom is CT scanned as this reduces image reconstruction artifacts.*

they were also much easier to make by the moulding process described earlier.

The *two lung phantom* produced is shown in Figures 2c. It has been used in X-ray radiotherapy dosimetry tests as described elsewhere.[9] The phantom was built from components included in the CT analysis described. It consisted of muscle slabs ($\rho_e^w = 1.02$) to simulate muscle and lung slabs of density ($\rho_e^w = 0.3$) to simulate lung. It has the same geometric dimensions as the cork-polystyrene phantom mentioned previously[10,11,12] however the density of the lung analog ($\rho_e^w = 0.28$) is closer to the mean lung density ($\rho_e^w = 0.3$) for a sample of patients[13].

CT Quality Assurance Body Analog Composition

X-ray computed tomograpy (CT) scanners provide high contrast X-ray pictures and electron density information in the transverse axial patient plane[14,15]. The CT scanner used for tests in this paper was a Siemens DRH CT.

To ensure the analogs being manufactured closely matched the elemental compositions and therefore the radiation properties required, a convenient quality assurance method which uses CT analysis has been developed. Using the method described, experimental CT numbers for analogs are compared with the theoretical CT numbers expected from the analogs using the elemental compositions.

This is a convenient and accurate method of quality assurance which entails no laboratory chemical analysis. If the CT numbers match at this low energy then their behaviour at higher radiotherapy X-ray energies (where photoelectric absorption is less dominant) is assured.

THE RELATION BETWEEN CT NUMBER AND ELECTRON CROSS SECTION

In order to understand the calculations used in this quality assurance exercise, a theoretical way of calculating the expected CT numbers is developed as follows. The relationship defined by Hounsfield[14] between CT number N_{CT}, and linear attenuation coefficient μ, is

$$N_{CT} = \frac{1000(\mu_s - \mu_w)}{\mu_w} \quad , \qquad (1)$$

where μ_s (cm^{-1}) is the linear attenuation coefficient for a substance at a specific energy and μ_w is the linear attenuation coefficient of water at this energy.

The product of electron density ρ_e (electrons/cm3), and total electron cross section σ_e (cm^2/electron), is equal to μ[16,17]:

$$\mu = \rho_e \sigma_e \quad , \qquad (2)$$

where σ_e is the sum of component electron cross sections due to Rayleigh scattering σ_R, photoelectric absorption σ_τ, Compton scattering σ_C, and pair production σ_κ, such that

$$\sigma_e = \sigma_R + \sigma_\tau + \sigma_c + \sigma_\kappa \quad . \qquad (3)$$

The pair production term can be neglected as at diagnostic CT energies of less than 100 keV there would be no such contribution since 1.022 MeV is required, but it is included here for completeness.

Now let ρ_{es} and ρ_{ew} be the electron density for a substance and water respectively. Also defining σ_{es} and σ_{ew} as the total electron cross sections for a substance and water respectively, then by substituting (2) into (1) gives

$$N_{CT} = \frac{1000(\rho_{es}\sigma_{es} - \rho_{ew}\sigma_{ew})}{\rho_{ew}\sigma_{ew}} \qquad (4)$$

and this is equivalent to

$$\frac{\rho_{es}}{\rho_{ew}} = \frac{\sigma_{ew}}{\sigma_{es}}\left(\frac{N_{CT}}{1000} + 1\right) \qquad (5)$$

The term ρ_{es}/ρ_{ew} is the relative electron density of a substance to that of water, commonly called the relative electron density ρ_e^w. The ratio σ_{ew}/σ_{es} has been defined as the ratio of electron cross sections R_σ, by Battista and Bronskill[18]:

$$R_\sigma = \frac{\sigma_{ew}}{\sigma_{es}} = \frac{(\sigma_R + \sigma_\tau + \sigma_c + \sigma_\kappa)_w}{(\sigma_R + \sigma_\tau + \sigma_c + \sigma_\kappa)_s} \quad . \qquad (6)$$

Therefore (5) can be written as

$$\rho_e^w = R_\sigma\left(\frac{N_{CT}}{1000} + 1\right) \qquad (7)$$

or

$$N_{CT} = \frac{1000}{R_\sigma}(\rho_e^w - R_\sigma) \qquad (8)$$

To calculate R_σ using known elemental data, some terms first have to be defined.

For an ith element within a compound consisting of N elements it can be seen from (2) that

$$(\sigma_{es})_i = \left(\frac{\mu}{\rho}\right)_i\left(\frac{\rho}{\rho_{es}}\right)_i \quad , \qquad (9)$$

where ρ is the mass density and therefore ρ/ρ_{es}, is the inverse of the number of electrons of a substance per gram, and by rearranging a relation stated by McCullough[16], this is equal to:

$$\left(\frac{\rho}{\rho_{es}}\right)_i = \frac{1}{N_A}\left(\frac{A}{Z}\right)_i \quad , \qquad (10)$$

where N_A is Avogadro's number. By substituting (10) into (9) gives

$$(\sigma_{es})_i = \left(\frac{\mu}{\rho}\right)_i \frac{1}{N_A}\left(\frac{A}{Z}\right)_i \qquad (11)$$

Defining $(\sigma_{es})_i^{eff}$ as the effective cross section for a substance with elemental compositions of mass fraction f_i, then from (11), the relation is

$$(\sigma_{es})_s^{eff} = \left[\sum_{i=1}^{N} f_i \left(\frac{\mu}{\rho}\right)_i \frac{1}{N_A}\left(\frac{A}{Z}\right)_i\right]_s . \qquad (12)$$

Remembering from (6) that R_σ is the ratio of cross sections, then

$$R_\sigma = \frac{(\sigma_{es})_w^{eff}}{(\sigma_{es})_s^{eff}} = \frac{\left[\sum_{i=1}^{N} f_i \left(\frac{\mu}{\rho}\right)_i \left(\frac{A}{Z}\right)_i\right]_w}{\left[\sum_{j=1}^{N} f_j \left(\frac{\mu}{\rho}\right)_j \left(\frac{A}{Z}\right)_j\right]_s} . \qquad (13)$$

Values of $(\mu/\rho)_i$ were estimated for bone and muscle analogs at 71 keV using elemental μ/ρ values from Jackson and Hawkes[19]. Values of $(A/Z)_i$ were calculated from elemental A/Z values obtained by using the periodic table for chemical elements. Then R_σ can be calculated using (13) for body analogs and their equivalent humanoid tissues (see Table 5).

CALCULATING THE RELATIVE ELECTRON DENSITY

Now that a method for calculating R_σ has been presented then the only unknown in (8) is ρ_e^w. Knowing ρ and the atomic composition then ρ_e^w has been calculated[20]:

$$\rho_e^w = \frac{N_A \rho}{\rho_{ew}}\left[\sum_{j=1}^{N} f_j \left(\frac{Z}{A}\right)_j\right]_s , \qquad (14)$$

where N_A is 6.023×10^{23} mol^{-1} and ρ_{ew} is 3.33×10^{23} electrons/cm^3, then

$$\rho_e^w = 1.81\,\rho\left[\sum_{j=1}^{N} f_j \left(\frac{Z}{A}\right)_j\right]_s \qquad (15)$$

CALCULATING THE EFFECTIVE ATOMIC NUMBER

Another quantity of interest in assessing the radiation properties of analogs is the effective atomic number. This is assessed by using an adaptation of the methods developed by McCullough and Holmes[17] as follows.

The effective atomic number can be derived from[17]:

$$Z_{eff} = \left(\sum_{i=1}^{q} \alpha_i (Z_i)^a\right)^{\frac{1}{a}} , \qquad (16)$$

where

$$\alpha_i = \frac{n_i Z_i}{\sum_{j=1}^{q} (n_j Z_j)} . \qquad (17)$$

The term n_i is the number of ith atoms per molecule (ie. the empirical formula). But to use (14) directly from values of constituent fraction by mass f_i then α_i needs to be determined in terms of f_i. This can be done as follows. Describing f_i in terms of n_i

$$f_i = \frac{n_i A_i}{\sum_{j=1}^{q} n_j A_j} , \qquad (18)$$

therefore

$$n_i = f_i \left(\sum_{j=1}^{q} n_j A_j\right)\frac{1}{A_i} . \qquad (19)$$

Substitute (19) into (18) then

$$\alpha_i = \frac{f_i\left(\sum_{j=1}^{q} n_j A_j\right)\frac{1}{A_i} Z_i}{\sum_{j=1}^{q}\left(f_j\left(\sum_{k=1}^{q} n_k A_k\right)\frac{1}{A_j}\right) Z_j} , \qquad (20)$$

but as

$$\sum_{j=1}^{q} n_j A_j = \sum_{k=1}^{q} n_k A_k \qquad (21)$$

then (17) can be replaced by

$$\alpha_i = \frac{f_i\left(\frac{Z}{A}\right)_i}{\sum_{j=1}^{q} f_j \left(\frac{Z}{A}\right)_j} . \qquad (22)$$

By using (13) and (15), in combination with the composition data shown in Table 4, values of R_σ and ρ_e^w have been calculated respectively. Using (16) combined with (22) values of Z_{eff} have also been calculated for both analogs and human tissues as shown in Table 5. Note that in the calculation of Z_{eff} using (16) the exponent a which accounts for photoelectric effects at CT energies is set at 2.94 to conform with other publications[17].

Comparison of Calculations and Experimental Results

The values of N_{CT} calculated using (8) are shown in Table 6 for one nominal CT energy, 71 keV. Using the compositions of human bone, tissue and lung provided in the literature[1,21], (8) has been used once again to calculate the N_{CT} values expected for human tissue. Comparison of analog CT numbers and human tissue CT numbers in the table serves to show that at these energies the CT numbers of the analogs very closely match the CT numbers of the tissues for which they are substitutes.

As the calculation procedure is quite complicated, an example of the calculation for bone is provided in Appendix 1, this is also included for the convenience of readers who may wish to repeat the procedure with other analogs or in vivo human data. It is important to note the composition of real inner bone outlined in Table 4 (row 2) is used for the calculation of N_{CT} in Table 6 (row 2). This data is based on the estimate of White *et al*[1] that inner bone has an average composition of 22.4% hard bone and 77.6% red marrow.

To ensure the analog mix is close to the analog composition expected, samples of the analog were scanned using a Siemens DRH CT scanner and the

Table 4

The percentage by mass compositions ($\%f_i$) for bone, muscle and lung analog and human tissue respetively. Elemental compositions are based on data from White *et al*[1,2] and Woodard and White[21]

ANALOG / TISSUE	ELEMENT AND ($\%\ f_i$)
bone analog	H(7.90), C(63.79), N(4.23), O(9.88), Cl(14.20)
human bone	H(8.67), C(13.00), N(3.6), O(66.40), S(0.46), P(2.43), Ca(4.96), (Na, Mg, K,Trace)
muscle analog	H(9.15), C(70.66), N(4.28), O(13.34), Cl(0.11), Ca(2.46)
human muscle	H(10.20), C(14.30), N(3.40), O(71.00), K(0.40),Na(0.10), (P, S, Cl, Trace)
lung analog	H(8.36), C(60.41), N(1.67), O(17.33), Cl(0.15), Si(0.72), Mg(11.36)
human lung	H(10.30), C(10.1), N(2.90), O(75.50), Na(0.20), P(0.20), S(0.30), Cl(0.30), K(0.20)

Table 5

Mass density, relative electron density, ratio of cross sections and effective atomic numbers for body analogs and tissues. Values of ρ were obtained by weighing the samples.

SAMPLE	ρ	ρ_e^w	R_σ (71 keV)	Z_{eff}
bone analog++	1.16	1.14	0.9130	9.26
human bone	1.12	1.10	0.8982	9.32
muscle analog	1.03	1.02	0.9860	7.39
human muscle	1.05	1.04	0.9965	7.45
lung analog	0.30	0.28	0.9879	7.51
human lung	0.30	0.30+	0.9963	7.59

+ An electron density based on patient survey by Van Dyk *et al.*[13]
++ An example calculation for bone analog is provided in Appendix 1.

results of the experimental CT numbers obtained are shown in column 3 of Table 6.

The ΔN_{CT} value in column 4 of Table 6 represents the difference in Hounsfield units between the calculated and measured N_{CT} numbers, where

$$\Delta N_{CT} = | N_{CT}^{THEORY} - N_{CT}^{EXPERIMENT} | . \quad (23)$$

If this ΔN_{CT} difference is divided by the usual range of Hounsfield numbers, between air and bone from -1000 to +1000 then the difference in percentage terms can be estimated as

$$\%\Delta N_{CT} = \frac{\Delta N_{CT}}{2000} \times 100\% \quad (24)$$

When comparing the the analogs a worst difference of (ΔN_{CT} =18HU) was obtained. This is a $\%\Delta N_{CT}$ of 0.9%. Therefore the experimentally determined N_{CT} values shown in column 3 of Table 6 measured on the CT scanner are very close to the theoretically predicted N_{CT} values. Hence if the compound composition is known and the nominal energy of the CT beam is estimated[22], then the expected value of N_{CT} can be calculated. This estimate of CT number agrees closely with the samples scanned, and therefore the analogs produced closely match the elemental compositions expected using the original composition data.

The same procedure has been used for real body tissues. The N_{CT} values for real tissues also match closely those for their respective analogs. Comparing the CT numbers in the columns in Table 6 also shows there is a close match between the CT numbers of the tissues and their analogs.

N_{CT} values measured for these body analogs are compared with some other commercial materials commonly used in radiation dosimetry applications in Figure 3. A selection of the data introduced in a previous publication (Metcalfe *et al*[7]) for the likely bone line is compared with the N_{CT} value found for inner bone analog as shown in Figure 3. Also shown in Figure 4 is the Hounsfield regression line, note the muscle analog data point shown fits closely to this line. It is important not to get confused between the experimental Hounsfield regression line gradient R_γ defined elsewhere[7] and the ratio of cross sections R_σ defined in (13), the mathematical difference between these terms is outlined in Appendix 2.

Table 6

CT numbers for analogs and human tissue have been calculated and measured . CT numbers caiculated using (18) and (8), (column 2). These are compared with CT numbers measured on a Siemens DRH CT scanner at a nominal energy of 71 keV (column 3). The numbers in brackets refer to commercial samples from RMI which were tested.

SAMPLE	N_{CT} THEORY	N_{CT} EXPERIMENT	ΔN_{CT}
bone analog	222++	229 (238)	7
human bone	224	236+	12
muscle analog	34	16	18
human muscle	44	30	1
lung analog	-716	-720 (-718)	4
human lung	-699	-711+	12

(Units - Hounsfield units HU)

+ The human bone data and human lung data was obtained by sampling 5 patients whose soft bone and lung regions were CT scanned. It is recognised that bone density and composition varies greatly depending on site and patient. However the pelvic region is a frequent site for radiotherapy treatment so this was the bone area which was surveyed.

++ An example calculation for bone analog is provided in Appendix 1.

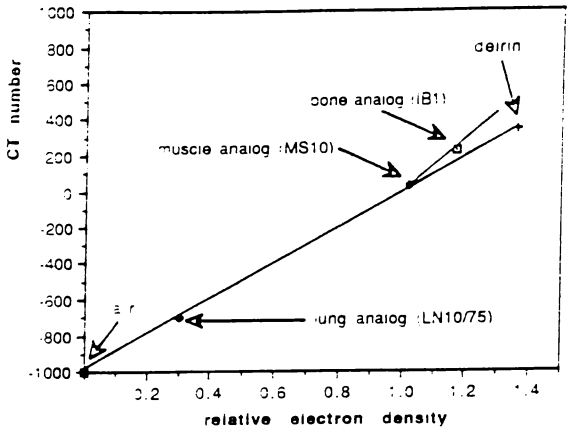

Figure 3: The CT number versus relative electron density for in-house manufactured body analogs compared with some other substances. The CT numbers were measured on a Siemens DRH CT scanner at 71 keV. The continuous narrow line is the Hounsfield line, where R_σ equals unity. The bracketed codes are those used by White et al (1,2) to describe these analogs.

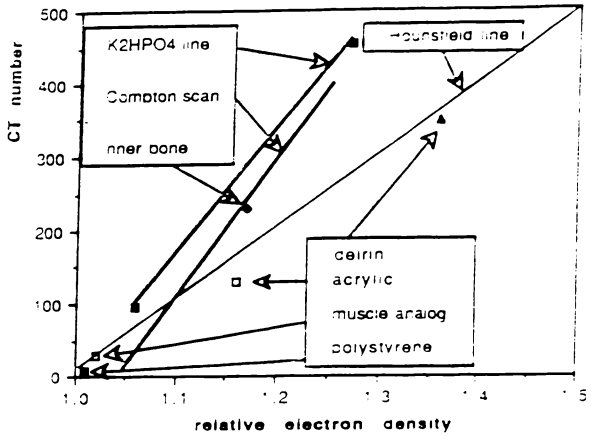

Figure 4: The CT number versus relative electron density for in-house manufactured muscle and bone analogs compared with other bone and tissue substitutes. The CT numbers were measured on a Siemens DRH CT scanner at 71 keV. The compton scan line is that for in vivo bone data from Battista and Bronskill (18).

Conclusions

The in-house manufacture of epoxy resin based analogs shows benefit provided sufficient analog has to be manufactured and a suitable laboratory for manufacture is available. Being able to mould the analogs to the required configurations directly is another advantage of in-house production. The CT quality assurance method outlined is advisable for both in-house and commercially acquired analogs, as this provides the physicist with essential information about the radiological properties of the analog.

The production of these analogs has already lead to several useful phantoms being produced for radiological physics applications in CT and radiotherapy. The phantoms produced are also being used to assess the accuracy of Monte Carlo and superposition calculations being carried out at our institute[9].

Acknowledgements

I wish to acknowledge Wayne Beckham, Jerry Battista and Brent Long for the many useful discussions about R_σ and Fionna Wilkinson and Linette Low for scanning the analogs. The commercial analog samples used for comparison in Table 6, were loaned to us by Wellington Hospital. Dr. D. H. White provided us with valuable extra information about lung analog production.

References

1. White D.R., Martin R.J., Darlison R. (1977). Epoxy resin based tissue substitutes. *B.J.R.* 50, 814 -821.

2. White D.R., Constantinou C., Martin R.J. (1986). Foamed epoxy resin-based lung substitutes. *B.J.R.* 59, 787 - 790.

3. White D.R. (1977). The formulation of tissue substitute materials using basic interaction data. *Phys. Med. Biol.* 22, 889 - 899.

4. White D.R. (1978). Tissue Substitutes in experimental radiation physics. *Med. Phys.* 5(6), 467 - 479.

5. Cann C.E., Gennant H.K.(1980). Precise measurement of vertebral mineral content using C.T. *J. Comput. Assist. Tomog.* 4(4).

6. Kalandar W.A., Suess C.A. (1987). A new calibration phantom for quantitative computed tomography. *Med. Phys.* 14(5), 863-866.

7. Metcalfe P.E., Beckham W.A., Long B.H., Battista J.J. (1988). The effect of patient density variation on radiotherapy dose calculations. *Aust. Phys. Eng. Sci. Med.* 11(3), 107-115.

8. Cygler J., Battista J.J., Scrimger J.W., Mah E., Antolak J. (1987). Electron dose distribution in experimental phantoms: A comparison of 2D pencil beam calculations. *Phys. Med. Biol.* 32(9), 1073-1086.

9. Metcalfe P.E., Hoban P.W., Murray D.C., Round W.H. (1990). Beam hardening of 10 MV Radiotherapy X-rays: Analysis using a convolution/superposition method. In-print *Phys. Med. Biol. accepted July 1990.*

10. Metcalfe P.E., Beckham W.A. (1988). Radiotherapy planning accuracy in terms of C.T. numbers and inhomogeneity correction techniques. *Aust. Rad.* 23(3), 371-379.

11. Metcalfe P.E., Battista J.J. (1988). Accuracy of inhomogeneity corrections in lung irradiated with high energy X-rays. *Aust. Phys. Eng. Sci. Med.* 11(2), 67-75.

12. Hoban P.W., Metcalfe P.E., Murray D.C., Round W.H. (1990). Superposition dose calculation in lung for 10 MV photons. *Aust. Phys. Eng. Sci. Med.* 13(2), 81-92.

13. Van Dyk J., Keane T.J., Rider W.D. (1982). Lung density as measured by computerised tomography: Implications for radiotherapy. *Int. J. Rad. Onc. Biol. Phys.* 8, 1363-1372.

14. Hounsfield G.N. (1973). Computerised transverse axial scanning (tomography): part 1 description of the system. *B.J.R.* 46, 1016-1022.

15. Brooks R.A. Di Chiro G. (1975). Theory of image reconstruction in computed tomography. *Radiology.* 117, 561-572.

16. McCullough E.C. (1975). Photon attenuation in computed tomography. *Med. Phys.* 2(6), 307-320.

17. McCullough E.C., Holmes T.S. (1985). Acceptance testing computerised radiation therapy treatment planning systems: Direct utilization of CT scan data. *Med. Phys.* 12(2), 237-242.

18. Battista J.J., Bronskill M.J. (1981). Compton scatter imaging of transverse sections: an overall appraisal and evaluation for radiotherapy planning. *Med. Phys. Biol.* 26(1), 89-99.

19. Jackson D.F., Hawkes D.T. (1981). Attenuation Coefficient data tables. *Physics Reports.* 70(3), 169-233.

20. Henson P.W. (1989). Determination of electron density, mass density and calcium fraction by mass of soft and osseous tissues by dual energy CT. *Aust. Eng. Phys. Sci. Med.* 12(1), 3-10.

21. Woodard H.Q., White D.R. (1986).The composition of body tissues. *B.J.R.* 59, 1209-1219.

22. White D.R., Speller R.D. (1980).The measurement of effective photon energy and linearity in comuterised tomography. *B.J.R.* 53, 5-11.

Appendix 1: Calculation of R_σ, ρ_e^w and Z_{eff} for Bone Analog Material

To calculate R_σ at 71 keV the mass attenuation coefficients at this energy for the composite elements are found from Tables (Jackson and Hawkes.)[19] The A/Z ratios are found from the periodic table. Percentage by mass of elements are from White *et al*[1,2]. A summary of the data is shown in Table A1.1.

To calculate R_σ then for water

$$\left[\sum_{i=1}^{N} f_i \left(\frac{\mu}{\rho}\right)_i \left(\frac{A}{Z}\right)_i\right]_w =$$

$$(0.112)(1.008)(0.3165) + \quad (A1.1)$$
$$(0.888)(2.0)(0.1736) \quad = 0.3440 \ .$$

Also for the bone analog substance

$$\left[\sum_{j=1}^{N} f_j \left(\frac{\mu}{\rho}\right)_j \left(\frac{A}{Z}\right)_j\right]_s =$$

$$(0.079)(1.008)(0.3165) \quad (A1.2)$$
$$+ (0.6379)(2.001)(0.1666)$$
$$+ (0.0423)(2.001)(0.1736)$$
$$+ (0.0988)(2.000)(0.1736)$$
$$+ (0.1420)(2.085)(0.3037) = 0.3768 \ .$$

Then from (13)

$$R_\sigma = \frac{\left[\sum_{i=1}^{N} f_i \left(\frac{\mu}{\rho}\right)_i \left(\frac{A}{Z}\right)_i\right]_w}{\left[\sum_{j=1}^{N} f_j \left(\frac{\mu}{\rho}\right)_j \left(\frac{A}{Z}\right)_j\right]_s} =$$

$$\frac{0.3440}{0.3768} = 0.9330 \ . \quad (A1.3)$$

The mass density was measured as $\rho = 1.16$ then

$$\rho_e^w = 1.81\,\rho_m \left(\sum_{i=i}^{N} \left(\frac{Z}{A}\right)_i \right) = 1.14 \cdot \quad \text{(A1.4)}$$

Therefore

$$N_{CT} = \frac{1000}{R_\sigma}(\rho_e^w - R_\sigma) = \quad \text{(A1.5)}$$

$$\frac{1000}{0.9330}(1.14 - 0.9330) = 222 \text{ HU} \cdot$$

The N_{CT} value calculated using the method outlined above is shown in Table 6. In order to calculate Z_{eff} using (16), we repeat the expression here for (22):

$$\alpha_i = \frac{f_i\left(\frac{Z}{A}\right)_i}{\sum_{j=1}^{q} f_j\left(\frac{Z}{A}\right)_j} \quad \text{(A1.6)}$$

Then the denominator is given by

$$\sum_{j=1}^{q} f_j\left(\frac{Z}{A}\right)_j = 0.5357 \quad \text{(A1.7)}$$

and the numerator for one of the elements (hydrogen) is given by

$$f_1\left(\frac{Z}{A}\right)_1 = (0.079)(0.992) = 0.0784 \quad \text{(A1.8)}$$

therefore repeating the summation for the constituent elements as outlined in (16) and including Z_i with the exponent ($a = 2.94$) the expression is

$$Z_{eff} = \left(\sum_{i=1}^{q} \alpha_i (Z_i)^a \right)^{\frac{1}{a}} = 9.26 \cdot \quad \text{(A1.9)}$$

Table A1.1

Percentage by mass $\%f_j$, atomic to mass number ratio $(A/Z)_j$, and attenuation coefficients $(\mu/\rho)_j$ for constituent elements in bone analog material.

ELEMENT	% BY MASS ($\%\ f_j$)	$(A/Z)_j$	$(\mu/\rho)_j$
H	7.90	1.008	0.3165
C	63.79	2.001	0.1666
N	4.23	2.001	0.1736
O	9.88	2.000	0.1736
Cl	14.20	2.085	0.3037

Appendix 2: The Difference Between R_γ and R_σ

It is important not to get confused between the experimental regression line gradient coefficient R_γ defined elsewhere and the ratio of cross sections R_σ defined in (13). Note that the equations describing these lines are not necessarily the same. For example R_γ may be representative of the bone line and is centered around the point of origin ($N_{CT} = 0$, $\rho_e^w = 1$), such that

$$N_{CT} = \frac{1000}{R_\gamma} (\rho_e^w - 1) \quad . \qquad (A2.1)$$

The mathematical difference is that R_σ is a line which is centered around the origin ($N_{CT} = 0$, $\rho_e^w = 0$), such that

$$N_{CT} = \frac{1000}{R_\sigma} (\rho_e^w - R_\sigma) \quad . \qquad (A2.2)$$

Figure A2.1 demonstrates the difference between the lines produced using (A2.1) and (A2.2), respectively.

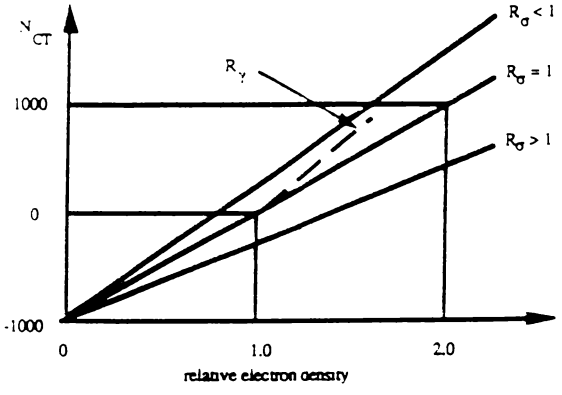

Figure A2.1: CT number versus relative electron density schematic of graph trends related to R_σ and R_γ

REFERENCES

Ahnesjö A., Andreo P., Brahme A. (1987). Calculation and application of point spread functions for treatment planning with high energy photon beams. *Acta Oncologica*, **26(1)**, 49-55.

Ahnesjö A., Mackie T.R. (1987). Analytic description of Monte Carlo generated photon dose convolution kernels. *The use of computers in radiation therapy*, 197-200.

Ahnesjö A. (1989). Collapsed cone convolution of radiant energy for photon dose calculation in heterogeneous media. *Med. Phys.*, **16(4)**, 554-577.

Attix F.H. (1979). The partition of KERMA to account for bremsstrahlung. *Health Phys.*, **36**, 347-354.

Batho H.F. (1964). Lung corrections in cobalt-60 beam therapy. *J. Canadian Ass. of Radiologists*, **15**, 79-83.

Battista J.J., Bronskill M.J. (1981). Compton scatter imaging of transverse sections: an overall appraisal and evaluation for radiotherapy planning. *Med. Phys. Biol.*, **26(1)**, 89-99.

Battista J.J., Field C., Santon L., Barnett R. (1984). Radiotherapy planning on a VAX 11/780 computer, *Proceedings of the IEEE, 8th conference, computers in radiotherapy,* 489-492.

Bielajew A.F., Rogers D.W.O. (1987). PRESTA: The parameter reduced electron step transport algorithm for electron Monte Carlo transport. *Nucl. Instrum. Methods.*, **B18**, 165.

Berger M.J., Seltzer S.M. (1966). Stopping power tables. *NASA SP3036. Washington D.C.*

Bleehen N.M., Glatstein E., Haybittle J.L. (1983). Radiation therapy planning. *Mercel Decker press, New York.*

Bloch P. (1988). A unified electron/photon dosimetry approach. *Phys. Med. Biol.*, **33(3)**, 373-376.

Boag J.W. (1950). Ionization measurements at very high intensities. *B.J.R.*, **20(300)**, 601-610.

Boag J.W. (1952a). Saturation curve for ionization measurements in pulsed radiation beams *B.J.R.*, **25(300)**, 649-650.

Boag J.W. (1952b). The saturation curve at high radiation intensities. *B.J. Appl. Phys.*, **3**, 222-229.

Boyer A.L. (1984). Shortening the calculation time of photon dose distributions in an inhomogeneous medium. *Med. Phys.*, **11**, 552-554.

Boyer A.L., Mok E.C. (1985). A photon dose distribution model employing convolution calculations. *Med. Phys.*, **12(2)**, 169-177.

Boyer A.L., Mok E.C. (1986). Calculation of photon dose distributions in an inhomogeneous medium using convolutions. *Med. Phys.*, **13 (4)**, 503-509.

Boyer A.L., Wackwitz R., Mok E.C. (1988). A comparison of the speed of three convolution algorithms. *Med. Phys.*, **15(2)**, 224-227.

Boyer A.L., Zhu Y., Wang L., Francois P. (1989). Fast Fourier transform convolution calculations of X-ray isodose distributions in homogeneous media. *Med. Phys.*, **16(2)**, 248-252.

Brahme A., Lax I., Andreo P. (1981). Electron beam dose planning using discrete Gaussian beams. *Acta Rad. Onc.*, **20(2)**, 147-158.

British Journal of Radiology Supplement **17**. (1983). Central axis depth dose data for use in radiotherapy. *B.I.R. Publishers.*

Brooks R.A., Di Chiro G. (1975). Theory of image reconstruction in computed tomography. *Radiology,* **117**, 561-572.

Bydder E. L., Crouch J. F., Metcalfe P.E. (1988). In house detector systems for a clinac 18 linear accelerator, *Aust. Phys. Eng. Sci. Med.,* **11(1)**, 27-35.

Cameron J.R., Suntheralingam N., Kenney G.N. (1968). Thermoluminescent dosimetry. *University of Wisconsin Press, Wisconsin.*

Clarkson J.J. (1941). A note on depth doses in fields of irregular shapes. *B.J.R.*, **14**, 265-268.

Coalter. G.C. (1984). Modification of high energy electron beams by small air cavities. *M.Sc. Thesis, University of Waikato.*

Cunningham J. R. (1972). Scatter-Air-Ratios. *Phys. Med. Biol.*, **17(1)**, 42-51.

Cunningham J.R. (1982). Tissue inhomogeneity corrections in photon beam treatment planning. Progress in medical radiation physics Vol 1. Edited by C.G. Orton. *Plenum publishers.*

Cunningham J.R. (1987). Radiotherapy planning dose calculations. Canadian College of Physicists in Medicine Symposium, *(Extended Abstract) Toronto.*

Cygler J., Battista J.J., Scrimger J.W., Mah E., Antolak J. (1987). Electron dose distribution in experimental phantoms: A comparison of 2D pencil beam calculations. *Phys. Med. Biol.*, **32(9)**, 1073-1086.

Day M.J. (1950). A note on the calculation of dose in X-ray fields. *B.J.R.*, **23**, 368-369.

Dean R.D. (1980). A scattering kernel for use in true three dimensional dose calculations. (Abstract) *Med. Phys.*, **7**, 429.

Dutriex J., Dutriex A., Tubana M. (1965). Electronic equilibrium and transition stages. *Phys. Med. Biol.*, **10(2)**, 177-190.

Dutriex J., Bernard M. (1966). Dosimetry at interfaces for high energy X and gamma rays. *B.J.R.*, **39**, 205-210.

Einstein A. (1905). On the electrodynamics of moving bodies. *Ann. Physik.*, **17**, 891.

Ekstrand K.E., Barnes W.H. (1990). Pitfalls in the use of high energy X-rays to treat tumours in the lung. *Int. J. Rad. Onc. Biol. Phys.*, **18**, 249-252.

El Khatib E., Battista J.J. (1984). Improved lung dose calculation using Tissue-Maximum -Ratios in the Batho correction. *Med. Phys.*, **11(3)**, 279-286.

Eyges L. (1948). Multiple scattering with energy loss. *Physical Review*, **74**, 1534-1535.

Field C., Battista J.J. (1987). Photon dose calculations using convolution in real and Fourier space: Assumptions and Time Estimates. *Proceedings 9th ICCR Conference*, Holland, 1987.

Frass B.A., McShan D.L., Diaz R.F., Ten Haken R.K., Aisen A., Gebarski S., Glazer G., Lichter A.S. (1987). Integration of magnetic resonance imaging into radiation therapy treatment planning. *Int. J. Rad. Onc. Biol. Phys.*, **13**, 1897-1908.

Geise R.A., McCullough E.C. (1977). The use of CT scanners in Megavoltage photon beam therapy planning. *Radiology*, **124**, 133-141.

Goitein M., Abrams M., Rowell D., Pollari H., Wiles J. (1983). Multi-dimensional treatment planning: II Beams eye-view, back projection and projection through CT sections. *Int. J. Rad. Onc. Biol. Phys.*, **9**, 789-797.

Greening J.R. (1981). Fundamentals of Radiation Dosimetry. *1st Edition, Adam Hilgar press, Bristol, England.*

Grussell E., Rikner G. (1984) Radiation damage induced dose rate non-linearity in an n-type silicon detector. *Acta. Radiol. Onc.*, **23(6)**, 465-469.

Gupta S.K., Cunningham J.R. (1966). Measurement if Tissue-Air-Ratios and scatter functions for large field sizes, for cobalt-60 radiation. *B.J.R.*, **39**, 7-11.

Harper N.R. (1990). The design, construction and use of a thin window ionization chamber. *M.Sc. Thesis, University of Waikato.*

Harper N.R., Metcalfe P.E., Hoban P.W., Round W.H. (1990) Electron contamination from 4 MV and 10 MV X-ray beams. *Aust. Eng. Phys. Sci. Med.*, submitted April.

Heitler W. (1960). The quantum theory of radiation. *Third edition, Clarendon press, Oxford,* 215.

Henson P.W., Fox R.A. (1984). The electron density of bone for inhomogeneity correction in radiotherapy planning using CT numbers. *Phys. Med. Biol.*, **29(4)**, 351-359.

Henson P.W. (1989). Determination of electron density, mass density and calcium fraction by mass of soft and osseous tissues by dual energy CT. *Aust. Eng. Phys. Sci. Med.*, **12(1)**, 3-10.

Hine G.J., Brownell G.L. (1956). Radiation Dosimetry. *Acedemic Press, New York,* 317.

Hogstrom K.R. (1985). Evaluation of electron pencil beam dose calculations. *Proceedings AAPM, Seattle* (Abstract) *Med. Phys.*, **12(4)**, 554.

Hoban P.W. (1988). Electron beam modelling in radiotherapy. *M.Sc. Thesis, University of Waikato.*

Hoban P.W., Metcalfe P.E., Murray D.C., Round W.H. (1990a). Superposition in low density media. *Aust. Eng. Phys. Sci. Med.*, **13 (2)**, 81-92.

Hoban P.W., Metcalfe P.E., Murray D.C., Round W.H. (1990b). A three-dimensional electron pencil beam method. *Aust. Phys. Eng. Sci. Med. Conference Adelaide. (Abstract in Proceedings) and private communication.*

Hounsfield G.N. (1973). Computerised transverse axial scanning (tomography): Part 1 description of the system. *B.J.R.*, **46**, 1016-1022.

Hubbell J.H., Veigele W.J., Briggs E.A., Brown R.T., Cromer D.T., Howerton R.J. (1975). Atomic form factors, incoherent scattering functions and photon scattering cross sections. *J. Phys. Chem. Ref. Data.* **4**, 471.

Huang P.H., Kase K.R., Bjarnguard B.E. (1982a). Simulation studies of 4 MV X-ray spectra by numerical analysis of transmission data. *Med. Phys.*, **9(5)**, 695-703.

Huang P.H., Kase K.R., Bjarnguard B.E. (1982b). Reconstruction of 4 MV bremsstruhlung spectra from measured transmission data. *Med. Phys.*, **10(6)**, 778-785.

Huizenga H., Storchi P.R.M. (1985). The use of computed tomography numbers in dose calculations for radiation therapy. *Acta. Rad. Onc.*, **24(6)**, 509-519.

IAEA International code of practice. (1987). Dosimetry protocol for absorbed dose. *IAEA Report.*, **277**.

International Commision on Radiological Units. (1971). Radiation Quantities and Units. *ICRU Report.*, **19**.

International Commision on Radiological Units. (1973). Measurement of absorbed dose in a phantom irradiated by a single beam of X or gamma rays. *ICRU Report.*, **23**.

International Commision on Radiological Units. (1976). Determination of absorbed dose in a patient irradiated with beams of X or gamma rays in radiation procedures. *ICRU Report.* **24**.

International Commission on Radiological Units. (1979). Average energy required to produce an ion pair. *ICRU Report.* **31**.

International Commission on Radiological Units. (1980). Radiation quantities and units. *ICRU Report* **33**.

Iwasaki A. (1990). Calculation of three-dimensional photon primary absorbed dose using forward and backward spread dose distribution functions. *Med. Phys.*, **17(2)**, 195-202.

Jackson D.F., Hawkes D.T. (1981). Attenuation coefficient data tables. *Physics Reports.* **70(3)**, 169-233.

Jette D.J. (1984a). The problem of electron beam calculation: I multiple scattering methods. *Am. Ass. Med. Dos.*, **9(3)**, 6-13.

Jette D.J. (1984b). The problem of electron beam calculation: II inhomogeneities and beam shaping. *Am. Ass. Med. Dos.*, **9(4)**, 12-17.

Johns H.E., Epp E.R., Cormack D.V., Fedoruk S.O. (1952). 1000 Curie Cobalt units for Radiation Therapy. *B.J.R.*, **25**, 296.

Johns H.E., Bruce W.R., Reid W.B. (1958). The dependence of depth dose on focal skin distance. *B.J.R.*, **31**, 254.

Johns H.E., Cunningham J.R. (1959). A precision Cobalt-60 unit for fixed and rotational therapy. *Amer. J. Roentgenol.*, **81**, 4.

Johns H.E., Cunningham J.R. (1981). The Physics of Radiology. *Third Edition, Thomas Sprinfield Press, Illinois.*

Johns H.E., Cunningham J.R. (1983). The Physics of Radiology. *Fourth Edition, Thomas Sprinfield Press, Illinois.*

Jones D.E.A. (1949). A note on back scatter and depth dose for elongated rectangular X-ray fields. *B.J.R.*, **22**, 342-345.

Karzmark C.J., Pering N.C. (1973). Electron linear accelerators for radiation therapy: History, principles and developments. *Phys. Med. Biol.*, **18(3)**, 321-354.

Karzmark C.J. (1984). Advances in linear accelerator design for radiotherapy. *Med. Phys.*, **11(2)**, 105-128.

Khan F.M., Gerbi B.J., Beibel F.C. (1986). Dosimetry of asymmetric X-ray collimators. *Med. Phys.*, **13(6)**, 936-941.

Klein O., Nishina Y. (1929). Uber die streuung von Strahlung durch freie Electronen nach der neuen relativistischen Quanten dynamic von Dirac: Translation - On the scattering of radiation by free electrons based on the relativistic quantum dynamics of Dirac. *Zs. f. Phys.*, **52**, 853-869.

Klevenhagen S.C. (1985). Physics of Electron Beam Therapy. *1st edition, Adam Hilgar press, Bristol England.*

Kornelson R.O., Young M.E.J.(1982). Changes in the dose-profile of a 10 MV X-ray beam within and beyond low density material. *Med. Phys.*, **9**, 114-116.

Lax I. (1986). Inhomogeneity corrections in electron-beam dose planning. Limitations with the semi infinite slab approximation. *Phys. Med. Biol.*, **31(8)**, 879-892.

Levy L.B., Waggener R.G., Wright A.E. (1976). Measurement of primary bremsstrahlung spectrum from an 8 MeV linear accelerator. *Med. Phys.*, **3(5)**, 173-175.

Mackie T.R. (1985). The study of megavoltage X-ray beams, *Ph. D Thesis*, University of Alberta .

Mackie T.R., Scrimger J.W., Battista J.J. (1985a). A convolution method of calculating dose for 15 MV X-rays. *Med. Phys.*, **12**, 188-196.

Mackie T.R., El-Khatib E., Battista J.J., Scrimger J., Van Dyk J., Cunningham J.R. (1985b). Lung dose corrections for 6 and 15 MV X-rays. *Med. Phys.*, **12(3)**, 327-332.

Mackie T.R., Ahnesjö A., Dickof P., Snider A. (1987). Development of a convolution/superposition method for photon beams. *The use of computers in radiation therapy, Elsevier Science Publishers, Amsterdam.* 107-110.

Mackie T.R., Bielajew A.F., Rogers D.W.O., Battista J.J. (1988). Generation of photon energy deposition kernels using the EGS Monte Carlo code. *Phys. Med. Biol.*, **33(1)**,1-20.

Mauceri T., Kase K. (1987). Effects of ionization chamber construction on dose measurements in a heterogeneity. *Med. Phys.*, **14(4)**, 653-656.

McCullough E.C. (1975). Photon attenuation in computed tomography. *Med. Phys.*, **2(6)**, 307-320.

McCullough E.C., Holmes T.W. (1985). Acceptance testing computerized radiation therapy treatment planning systems: Direct utilization of CT scan data. *Med. Phys.*, **12(2)**, 237-242.

Meredith W.J., Neary G.J. (1944). The production of isodose curves and the calculation of energy absorption from standard depth dose data. *B.J.R.*, **17**, 75-82.

Meredith W.J., Massey J.B. (1977). Fundamental physics of radiology. *Third edition, Wright and Sons Publishers, Bristol* , England, **69**.

Metcalfe P.E. (1982). Lung density physics. *M.Sc. Thesis, University of Waikato.*

Metcalfe P.E. (1988). Experimental verification of caesium brachytherapy line source emission using a semiconductor detector. *Med. Phys.*, **15(5)**, 702-706.

Metcalfe P.E., Battista J.J. (1988). Accuracy of inhomogeneity corrections in lung irradiated with high energy X-rays. *Aust. Phys. Eng. Sci. Med.*, **11(2)**, 67-75.

Metcalfe P.E., Beckham W.A. (1988). Radiotherapy planning accuracy in terms of C.T. numbers and inhomogeneity correction techniques. *Aust. Rad.*, **23(3)**, 371-379.

Metcalfe P.E., Beckham W.A., Long B.H., Battista J.J. (1988). The effect of patient density variation on radiotherapy dose calculations. *Aust. Phys. Eng. Sci. Med.*, **11(3)**, 107-115.

Metcalfe P.E., Hoban P.W., Murray D.C., Round W.H. (1989). Modelling polychromatic high energy photon beams by superposition. *Aust. Phys. Eng. Sci. Med.*, **12(3)**, 138-149.

Metcalfe P.E., Hoban P.W., Harper N.R., Murray D.C., Round W.H. (1990a). The production of body analog materials for use in medical radiation physics. *Aust. Phys. Eng. Sci. Med.*, **13(3)**, 117-128.

Metcalfe P.E., Hoban P.W., Murray D.C., Round W.H. (1990b). Beam hardening of 10 MV radiotherapy X-rays: Analysis using a convolution/superposition method. *Phys. Med. Biol., in-print,* **35**.

Milan J., Bentley R.E. (1974). The storage and manipulation of radiation dose data in a small digital computer. *B.J.R.*, **45**, 115-121.

Mitchell A.W., Johnson P.B. (1989). Methods for calculation of attenuation coefficient data in the diagnostic energy range. *Aust. Phys. Eng. Sci. Med. Conference Adelaide. (Abstract in Proceedings) and private communication.*

Mohan R., Chui C. (1985a). Validity of the concept of seperating primary and scatter dose. *Med. Phys.*, **12(6)**, 726-730.

Mohan R., Chui C. (1985b). Energy and angular distributions of photons from medical linear accelerators. *Med. Phys.*, **12 (5)**, 592-597.

Mohan R., Chui C., Lidofsky L. (1986). Differential pencil beam dose computation model for photons. *Med. Phys.*, **13(1)**, 64-73.

Mohan R. (1989). Three-dimensional radiation treatment planning. *Aust. Phys. Eng. Sci. Med.*, **12(2)**, 73-91.

Mould R.F. (1981). Radiotherapy treatment planning. *Adam Hilgar press, Bristol, England.*

Murray D.C., Hoban P.W., Metcalfe P.E., Round W.H. (1989). 3-D superposition for radiotherapy treatment planning using fast Fourier transforms. *Aust. Phys. Eng. Sci. Med.*, **12(3)**, 128-137.

Murray D.C. (1990). Using EGS4 Monte Carlo in medical radiation physics. *Aust. Phys. Eng. Sci. Med.*, **13(3)**, 132-147.

Murray D.C., Hoban P.W., Metcalfe P.E., Round W.H. (1990). Superposition on a parallel processing computer. *Med. Phys., in-print, accepted for publication, July, 1990.*

Nahum A.E. (1989). Electron and photon transport using the EGS4 Monte Carlo system: Lecture 7, electron interactions and Monte Carlo transport. *NPL report , Teddington, United Kingdom.*

Nath R., Schultz R.J. (1976). Determination of high energy X-ray spectra by photoactivation. *Med. Phys.*, **3(3)**, 133-141.

Nelson W.R., Hirayama H., Rogers D.W.O. (1985). The EGS4 Code System. *Stanford Linear Accelerator Centre Publication* , **265** .

NRL Dosimetry protocol. (1989). Absorbed dose determination in photon and electron beams: an adaptation of the IAEA international code of practice. *NRL Report* 1-26.

O'Connor J.E. (1957). The variation of scattered X-rays with density in an irradiated body. *Phys. Med. Biol.*, **1**, 352-369.

Perry D.J., Holt J.G. (1980). A model for calculating the effects of small inhomogeneities on electron beam dose distributions. *Med. Phys.*, **7(3)**, 207-215.

Pracy M. (1987). Automated photon field measurements for computer assisted radiotherapy treatment planning. *Phys. Med. Biol.*, **32**, 1509-1514.

Redpath A.T., Vickery B.L., Duncan W. (1977). A comprehensive readiotherapy planning system implemented in FORTRAN on a small interactive computer. *B.J.R.*, **50**, 51.

Rice R.K., Hansen J.L., Chin L.M., Mijnheer B.J., Bjarngard B.E. (1988). The influence of ionization chamber and phantom design on the measurement of lung dose in photon beams. *Med. Phys.*, **15(6)**, 884-890.

Rikner G. (1983). Silicon diodes as detectors in relative dosimetry of photon, electron and proton radiation fields. *PhD Thesis, University of Uppsala, Sweden.*

Rikner G., Grussell E., Hogstrom B., Jung B., Maripuu E. (1984). Variance measurements with two semiconductor dose detectors. *Acta. Radiol. Biol.*, **23(6)**, 471-475.

Rogers D.W.O., Ross C.K. (1988).The role of humidity and other correction factors in the AAPM TG 21 dosimetry protocol. *Med. Phys.*, **15(1)**, 40-48.

Siddon R.L. (1985). Fast calculation of the exact radiological path for a three dimensional CT array. *Med. Phys.*, **12(2)**, 252-255.

Slater J.C. (1948). The design of linear accelerators. *Reviews of modern physics.* **20(3)**, 473-518.

Sontag M.R., Cunningham J.R. (1977). Corrections to absorbed dose calculations for tissue inhomogeneities. *Med. Phys.*, **4**, 431-436.

Sontag M.R., Cunningham J.R. (1978). The Equivalent Tissue-Air-Ratio method for making absorbed dose calculations in heterogeneous medium. *Radiology*, **129(3)** , 787-794,

Sontag M.R. (1979). Photon beam dose calculations in regions of tissue heterogeneity using computed tomography, *Ph.D. Thesis*, Toronto University, Appendix A1, 83-90.

Task Group 21 (TG-21) (1983). A protocol for the determination of absorbed dose from high energy photon and electron beams. *Med. Phys.*, **10(6)**, 741-771.

Theraplan. (1989). Photon beam calculations. *Theraplan users manual Appendix 1.*

Van Dyk J. (1977). Practical dosimetric considerations of a 10 MV photon beam. *Med. Phys.*, **4**, 145.

Van Dyk J., Battista J.J., Rider W.D. (1979). The use of computed tomography in lung dose calculations for upper half-body irradiations. *B.J.R., supplement* **15**, 90-97.

Van Dyk J., Keane T.J., Rider W.D. (1982). Lung density as measured by computerised tomography: Implications for radiotherapy. *Int. J. Rad. Onc. Biol. Phys.*, **8**, 1363-1372.

Van Dyk J. (1983). Lung dose calculations using computed tomography: Is there a need for pixel based procedures. *Int. J. Rad. Onc. Biol. Phys.*, **9**, 1035-1041.

White D.R. (1977). The formulation of tissue substitute materials using basic interaction data. *Phys. Med. Biol.*, **22**, 889-899.

White D.R., Martin R.J., Darlison R. (1977). Epoxy resin based tissue substitutes. *B.J.R.*, **50**, 814-821.

White D.R. (1978). Tissue Substitutes in experimental radiation physics. *Med. Phys.*, **5(6)**, 467-479.

White D.R., Speller R.D. (1980). The measurement of effective photon energy and linearity in computerised tomography. *B.J.R.*, **53**, 5-11.

White D.R., Constantinou C., Martin R.J. (1986). Foamed epoxy resin-based lung substitutes. *B.J.R.*, **59**, 787-790.

Wickman G. (1974a). A liquid ionization chamber with high spatial resolution. *Phys. Med. Biol.*, **19(1)**, 66-72.

Wickman G. (1974b). Radiation quality independent liquid ionization chamber for dosimetry of electron radiation from medical linear accelerators. *Acta. Radiol. Onc.*, **13**, 37-47.

Wong J.W., Henkelman R.M., Fenster A., Johns H.E. (1981). Second scatter contribution to dose in a Cobalt-60 beam. *Med. Phys.*, **8(6)**, 775-782.

Wong J.W., Henkelman R.M. (1982). Reconsideration of the power law (Batho) equation for inhomogeneity corrections. *Med. Phys.*, **9(4)**, 521-529.

Wong J.W., Henkelman R.M. (1983). A new approach to CT pixel based photon dose calculations in heterogeneous media. *Med. Phys.*, **10(2)**, 199-208.

Wood R.G. (1981). Computers in radiotherapy planning. *Research Studies Press, New York.*

Woodard H.Q., White D.R. (1982). Bone models for use in radiotherapy dosimetry. *B.J.R.*, **55**, 277-282.

Yakiwczuk L. (1987). Analysis of the Equivalent Tissue-Air-Ratio method of photon dose computation. *M.Sc. Thesis*, University of Alberta, 1987.

Young M.E.J., Kornelson R.O. (1983). Dose corrections for low-density tissue inhomogeneities and air channels for 10 MV X-rays. *Med. Phys.*, **10**, 450-455.